Methods and algorithms of segmentation and deconvolution for quantitative analysis of Tissue Microarray images

Hoai Nam Nguyen

ANNÉE 2017

UNIVERSITÉ DE RENNES 1

UNIVERSITE BRETAGNE LOIRE

THÈSE / UNIVERSITÉ DE RENNES 1
sous le sceau de l'Université Bretagne Loire

pour le grade de
DOCTEUR DE L'UNIVERSITÉ DE RENNES 1
Mention : Traitement du Signal et Télécommunications
Ecole doctorale MathSTIC
présentée par

Hoài Nam NGUYỄN

préparée au Centre Inria Rennes – Bretagne Atlantique

Méthodes et algorithmes de segmentation et de déconvolution d'images pour l'analyse quantitative de Tissue Microarrays

Thèse soutenue à Rennes le 18 décembre 2017
devant le jury composé de :

Julie DELON
Professeur, Université Paris Descartes / Rapporteur

Grégoire MALANDAIN
Directeur de recherche, Inria / Rapporteur

Andrés ALMANSA
Directeur de recherche, CNRS / Examinateur

Guy CARRAULT
Professeur, Université de Rennes 1 / Examinateur

Cyril CAUCHOIS
Ingénieur de recherche, Innopsys / Examinateur

Pierre WEISS
Chargé de recherche, CNRS / Examinateur

Charles KERVRANN
Directeur de recherche, Inria / Directeur de thèse

For my parents, my wife and my son.

Remerciements

Je tiens à remercier en premier lieu mon directeur de thèse, Charles Kervrann, de m'avoir fait confiance et encouragé pendant ces dernières années malgré de nombreuses difficultés rencontrées notamment à la fin de cette longue période. Merci beaucoup de ta patience et tes conseils avisés qui m'ont beaucoup guidé lors de mes premiers jours à Inria.

Je remercie la société Innopsys d'avoir financé cette thèse. Je tiens à remercier sincèrement Vincent Paveau, qui n'a malheureusement pas pu venir à la soutenance, de ses efforts pour mener et maintenir ce projet de collaboration, sans lequel je n'avais pas l'opportunité de commencer mon doctorat.

Je souhaite dire ma gratitude à Julie Delon et Grégoire pour avoir accepté d'être rapporteur. Leurs remarques précieuses m'ont indiqué les limites de mes approches et m'ont ainsi ouvert les pistes à améliorer. Aux membres du jury, qui ont consacré leur temps pour un 18 décembre pas trop loin du Noël. Parmi eux, je tiens à remercier particulièrement Andrés Almansa de sa présence en vidéo-conférence bien qu'il soit encore malade. Merci à Guy Carrault, Cyril Cauchois et Pierre Weiss de leurs commentaires constructifs sur mes travaux. J'espère d'avoir la chance de collaborer avec vous dans l'avenir.

Merci également à mes amis vietnamiens à Inria pour les pauses-café et les coups de main dans diverses occasions. J'aimerais aussi remercier mes collègues (anciens et nouveaux) des épiques Serpico et Fluminance : Antoine, Tina, Thierry, Tristan, Philippe, Denis, Emmanuel, Anca, Léo, Vincent, Sandeep, Mayela, Xuân Quy, Cordelia, Ioanna, Valentin, etc., de m'avoir accompagné dès le début jusqu'à la fin. En particulier, je tiens à remercier Huguette Béchu, de ses aides pour les démarches administratives.

Enfin, merci de tout coeur à ma famille et ma belle-famille de m'avoir supporté, sans vous, je n'ai pas pu accomplir cette mission.

Contents

List of Figures

Résumé en français

Contexte et motivations

Introduits par Kononen et al. (1998), les "Tissue Microarrays" (TMAs) ou "puces à tissus" sont des lames histologiques sur lesquelles de nombreux échantillons tissulaires (micro-biopsies) inclus en paraffine sont organisés selon une structure de grille (appelée grille de TMA) pour faciliter l'identification de chacun d'eux. Cette technologie permet en effet d'analyser simultanément l'expression des gènes ou protéines de plusieurs centaines d'échantillons placés sur une même lame dans les mêmes conditions optimales de reproductibilité. Compatible avec les techniques courantes telles que l'immunohistochimie (IHC), l'hybridation in situ (ISH) ou l'hybridation in situ en fluorescence (FISH), l'utilisation des TMAs est une des méthodes les plus rapides et les plus efficaces pour valider et évaluer des nouveaux biomarqueurs. L'identification de biomarqueurs fiables joue désormais un rôle essentiel pour améliorer le diagnostic précoce de cancers.

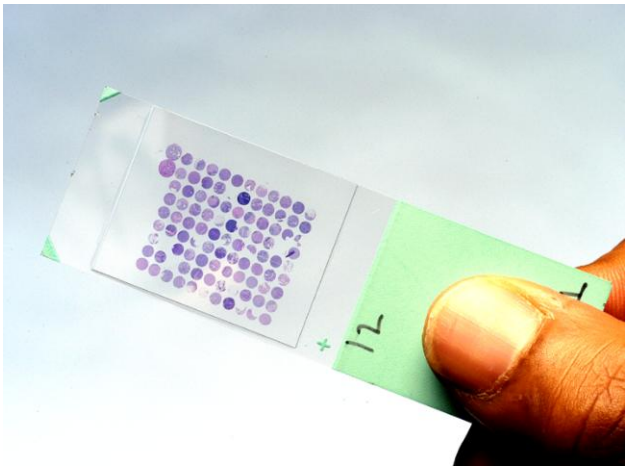

Figure 1: Une lame de Tissue Microarray (source: `http://tmalab.jhmi.edu/`)

Malheureusement, dans la plupart des laboratoires concernés, l'analyse de TMAs reste souvent très manuelle, de la numérisation des lames à l'interprétation des résultats. Elle exige encore trop de temps et doit être supervisée par un pathologiste, en général peu disponible. Ce manque d'automatisation ne permet pas d'exploiter tout le potentiel de la technologie TMA et limite la popularisation de cette technologie pour les activités de recherche ou pour les pratiques cliniques. Il est donc nécessaire de développer des outils automatisés, quantitatifs et dédiés aux TMAs

pour réduire le temps d'invervention humaine et permettre une analyse haut-débit, fiable et robuste.

Pour répondre à ce besoin, la société Innopsys, un des trois leaders mondiaux du marché des Microarrays, a développé et commercialisé une nouvelle génération de scanners en fluorescence appelée InnoScan 1100 AL[1]. Doté d'un système optique et mécanique soigneusement conçu, ce scanner est capable d'automatiser la numérisation de plusieurs lames insérées et d'effectuer des acquisitions simultanées de différentes couleurs (longueurs d'onde). La numérisation d'un grand nombre de lames est effectuée en un temps relativement court. Il représente un outil idéal pour les applications en grande échelle dans le domaine de la pathologie numérique et de la recherche contre le cancer. Afin de compléter cette offre en instrumentation, il s'avère indispensable de l'équiper aussi d'algorithmes de traitement d'images dédiés à l'analyse des TMAs pour faciliter l'interprétation des pathologistes.

Figure 2: De gauche à droite : le scanner InnoScan 1100 AL (source: `https://www.innopsys.com/`) et une image de TMA acquise en fluorescence.

Mon projet de thèse s'inscrit dans la cadre de la collaboration entre Inria et Innopsys. L'objectif est de développer des algorithmes originaux pour le traitement des images de tissus marqués en fluorescence produites par les scanners de la gamme InnoScan[2], notamment le prototype nommé InnoScan 1100 AL. Des développements conséquents portent sur plusieurs aspects tels que la problématique des Tissue Microarrays, l'imagerie en fluorescence, et les problèmes d'acquisition liés aux scanners dédiés en question. Plus précisément, ce travail de thèse visait à développer des méthodes pour la segmentation des échantillons de tissu, l'estimation de la déformation de la grille TMA, la correction des artéfacts de scan ainsi que l'amélioration de la résolution spatiale des images scannées. Les deux premières problématiques relèvent de l'identification automatique des échantillons de tissu, ce qui est extrême-

[1] Voir `https://www.innopsys.com/en/lifesciences-products/microarrays/innoscan/innoscan-1100-al` pour plus de détails du produit.

[2] `https://www.innopsys.com/en/lifesciences-products/microarrays/innoscan` .

ment important en analyse de TMA. Les deux dernières problématiques avaient pour objectifs d'améliorer la qualité visuelle des images brutes (à la sortie du scanner et avant tout prétraitement), un problème assez classique dans le domaine de traitement d'images. Néanmoins, chaque problématique a exigé un travail significatif de modélisation en tenant compte des caractéristiques des images de TMA, du processus d'acquisition d'images, des bruits électronique et photonique induits par le dispositif d'imagerie. À côté de ces travaux théoriques, les stratégies pragmatiques ont été également considérées dans certains cas pour pouvoir traiter non seulement un grand nombre d'images générées mais aussi des images de très grande taille (jusqu'à 44000×148000 pixels pour une lame entière imagée à la résolution maximale).

Le manuscrit est organisé de manière suivante. Le chapitre 2 aborde la problématique de la localisation des échantillons de tissu biologique présentés sur la lame de TMA et de l'estimation des coordonnées spatiales de chaque échantillon. Cette problématique, assez bien décrite en analyse de TMAs, dont la résolution est essentielle pour les utilisateurs (chercheurs et pathologistes), n'a pas reçu beaucoup d'attention dans le domaine de traitement d'images. Ensuite, le chapitre 3 introduit une méthode variationnelle, inspirée du calcul de flot optique, pour corriger les artéfacts de scan dus aux mauvais placements des pixels. Le problème de déconvolution d'images est traité dans le chapitre 4. De manière originale, pour la déconvolution des images en fluorescence, on introduit une nouvelle famille de régulariseurs convexes et adaptés à cette modalité d'imagerie. Enfin, le dernier chapitre résume les travaux réalisés dans le cadre de cette thèse et propose quelques perspectives.

Résumé des chapitres principaux

Chapitre 2 :

La première tâche en analyse de TMA vise à identifier chaque échantillon de tissu déposé sur la lame et de l'associer à des données cliniques. En terme de traitement d'images, il s'agit de localiser (segmenter) ces échantillons sur une image TMA de grande taille et d'estimer leur coordonnées spatiales disposées sur une grille régulière. Dans ce chapitre, on propose une nouvelle méthode de correction d'alignement en combinant la détection basée ondelettes, la segmentation par modèle paramétrique de forme et l'interpolation par spline ("plaque mince"). La méthode proposée est adaptée non seulement aux images de fluorescence mais aussi aux images en champ clair (*brightfield* en anglais). Elle est également robuste au bruit instrumental ainsi qu'aux déformations non linéaires de la grille TMA.

Chapitre 3 :

Dans ce chapitre, on traite le problème des artéfacts de scan qui se produisent sur les images acquises par les scanners de la gamme InnoScan développés par la société Innosys. Ce type d'artéfacts dus aux mauvais positionnements des pixels, est très similaire à ceux observés sur les images satellitaires de *whiskbroom* et *pushbroom*. Cependant, la situation est beaucoup plus compliquée dans le contexte des images

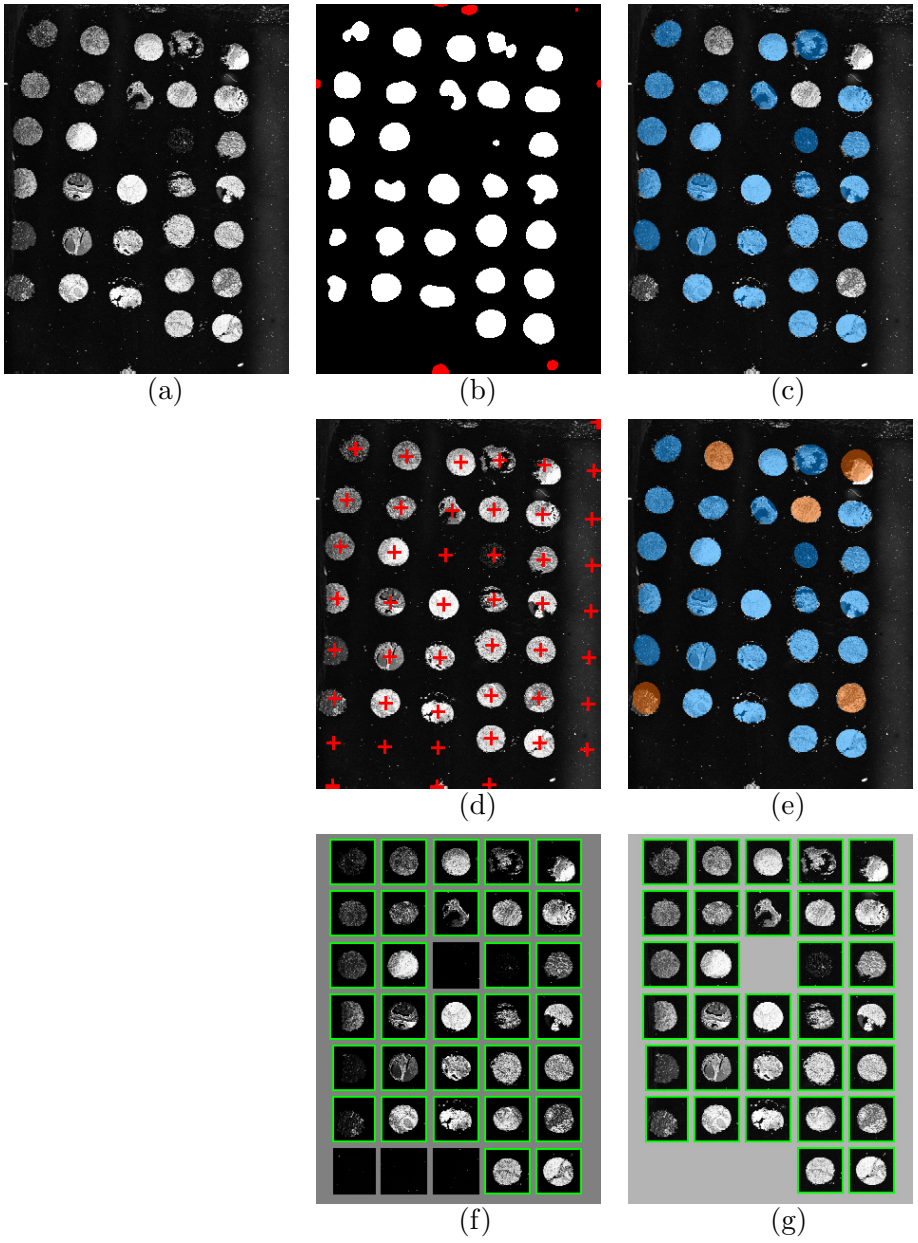

Figure 3: Exemple d'alignement de TMA. (a) Image de TMA en fluorescence, (b) résultat de détection, (c) segmentation des échantillons de tissu, (d) estimation de la déformation de la grille TMA, (e) échantillons segmentés (f) résultat d'alignement, (g) annotation manuelle.

biologiques, car les images contiennent les détails très fins avec les variations douces d'intensité. Pour cette raison, on considère une approche basée sur les méthodes variationnelles de flot optique pour estimer un champ de déplacement dense qui modélise les artéfacts de scan. Cette approche consiste à minimiser une fonction d'énergie composée d'un terme d'attache aux données non convexe et d'un terme de régularisation convexe. Le découplage de ce problème de minimisation en deux sous-problèmes est nécessaire pour séparer les termes convexe et non convexe. Pour minimiser la fonction d'énergie proposée, on considère la relaxation quadratique en introduisant une variable auxiliaire pour découpler la fonction originale en deux

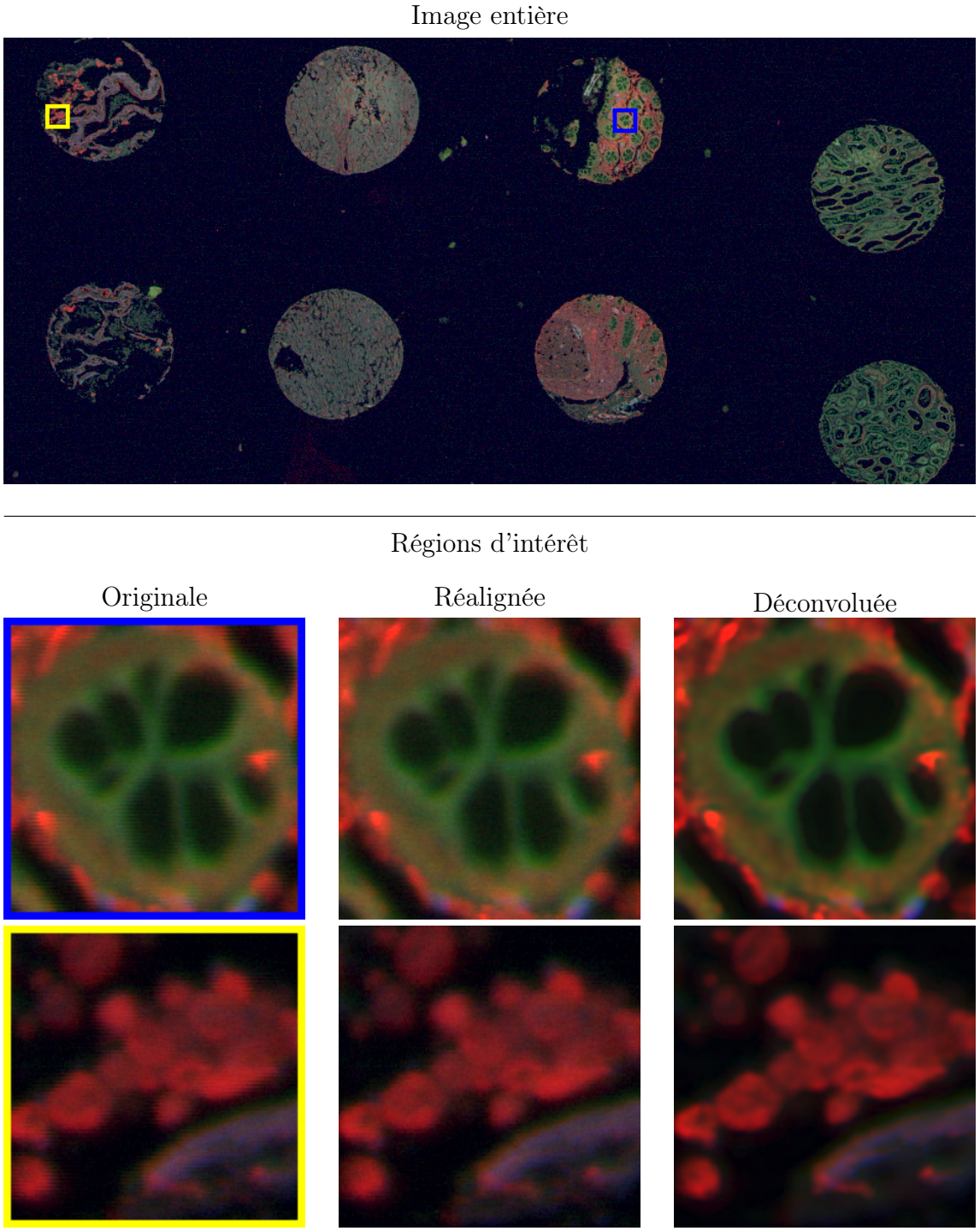

Figure 4: Exemple de correction d'artéfacts de scan et de déconvolution sur une image fluorescente de TMA acquise en trois couleurs.

parties: l'une est non convexe et peut-être minimisée en effectuant une recherche exhaustive; l'autre est convexe et facile à minimiser en utilisant les algorithmes d'optimisation standards. Les expériences réalisées sur les images synthétiques et réelles de fluorescence montrent que la correction des artéfacts de scan utilisant notre approche fournit des résultats prometteurs en terme de qualité visuelle.

Chapitre 4 :

En imagerie en fluorescence, quand la super-résolution est impossible, la seule méthode pour améliorer la résolution spatiale d'une image est la déconvolution. Dans ce chapitre, on introduit une nouvelle famille de régulariseurs convexes appropriés aux images fluorescentes. Cette famille de régulariseurs est généralisée à partir du concept de la variation parcimonieuse (*sparse variation*), qui associe la variation totale (*total variation*) et la norme L_1 de l'image pour rehausser des pixels dont l'intensité et le gradient sont non-nuls. On reformule donc le problème de déconvolution comme la minimisation d'une énergie composée par un terme d'attache aux données quadratique (sous l'hypothèse de bruit blanc Gaussien) et un terme de régularisation de cette famille sous certaines contraintes de positivité. Ce problème convexe peut être résolu, de manière efficace, par un algorithme primal-dual (proximal). Les résultats expérimentaux montrent que la méthode de déconvolution proposée (ainsi appelée SV déconvolution) est très compétitive en comparant avec celles de l'état-de-l'art comme la déconvolution basée sur la minimisation de la variation totale ou de la norme Schatten de la matrice Hessienne.

Chapter 1

Introduction

Context

Cancer is nowadays one of the biggest health issues of the modern society. Along with the continuously increasing number of new cancer cases detected every day, it is crucial to identify reliable biomarkers in order to improve the diagnosis, prediction and prognostication. The use of *tissue microarrays* (TMAs) [Kononen et al. 1998] has been proven to be an effective and efficient method for the evaluation and validation of novel tissue biomarkers. Then, what are tissue microarrays and why they are useful in cancer research?

A tissue microarray is a microscopy slide on which, up to thousands or more tissue samples are assembled according to a grid pattern (also called *TMA design grid*) in order to facilitate the identification of each sample. In comparison with conventional histo-pathological techniques that impose generally individual analysis of each tissue sample, the TMA technology allows, in contrast, simultaneous analysis of numerous samples at different levels (e.g., RNA, DNA, or protein level) in a single experiment under identical and standardized conditions while using only a single slide. It permits therefore to perform large-scale experiments where multiple markers are eventually tested on very large number of specimens, with substantially shorter time as well as lower material and labor cost. Furthermore, the application of TMAs in tissue-based researche also helps to preserve the limited and valuable tissue resource for future needs.

There is a wide range of immunohistochemical and molecular techniques that can be used with tissue microarrays as with regular tissue samples, including *immunohistochemistry* (IHC), *RNA in situ hybridization* (ISH), *fluorescence in situ hybridization* (FISH) and *immunofluorescence* (IF). For several decades, these techniques have required stained TMA slides to be observed under microscope and analyzed by pathologists. Unfortunately, results obtained with these microscopical analyses are in general irreproducible and subjected to observer variability in visual evaluation. To avoid these issues, digital images (*virtual slides*) which are acquired with dedicated devices are considered instead of physical slides, making a great evolution in the field of pathology – the era of digital pathology. Virtual slides, by the nature, not only provide the possibility of storage, viewing and manipulation in computers, but also enable automated and quantitative analysis (by using image

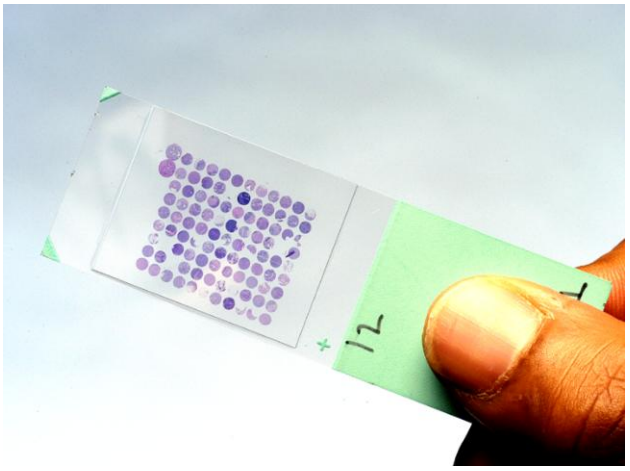

Figure 1.1: A Tissue Microarray slide (source: `http://tmalab.jhmi.edu/`).

processing algorithms). This computer-assisted approach to analyze TMAs represents so far a powerful and practical tool for pathologists to reduce interpretation errors and improve accuracy of diagnoses. It is especially useful for large-scale assays where a large number of TMAs and biomarkers may involve, since some quantitative information (e.g., annotated data) is provided through pre-processing by computers, thus easing the analyses of pathologists.

In the context of digital pathology, the workflow of TMA analysis is composed of following steps: (i) image acquisition of the TMAs which are stained according to the considered molecular technique; (ii) localization (segmentation) and identification of each tissue sample on the acquired images; and (iii) evaluation on the segmented (annotated) images. To our knowledge, there is not yet a standard platform dedicated to tissue microarrays which allows a totally automated workflow, or at least automated until human intervention for final evaluation. Indeed, the majority part of digital TMA image analysis is still performed manually in most biological laboratories, requiring a lot of time and a permanent supervision of a pathologist which is not always available for this tedious and time-consuming task. Consequently, in spite of its prominent potential, TMA technology encounters a major bottleneck for wide usage in basic research as well as routine clinical works, due to the lack of a convenient platform for automated and high-throughput analysis. The development of such a platform is highly recommended to accelerate and simplify the TMA analyzing process, thus reducing the working time of pathologists on the supervision and making them more available for their expertise (i.e. the discovery of new predictive biomarkers).

To meet this need, Innopsys – specialized in biological instrumentation – aims at providing a unified framework and a user-friendly environment for TMA analysis from fast image acquisition, protected data transfer and management to automated pre-processing (such as denoising, deconvolution, segmentation, etc.). They commercialize a new generation of fluorescence scanners named InnoScan 1100 AL[1]. Equipped with carefully designed mechanical, optical and electronic components,

[1] See `https://www.innopsys.com/en/lifesciences-products/microarrays/innoscan/innoscan-1100-al` for more technical details of the product.

the dedicated scanner is able to perform not only simultaneous acquisitions on different excitation channels but also programmed acquisition of a batch of multiple input specimen slides at very high spatial resolution while avoiding photo-bleaching. Moreover, thanks to its eligibility to any standard microscopy slide with various substrates – cells, tissue, proteins, DNA, glycans, peptides, and others – this specific device is potentially an adapted solution for large-scale application of multiplexed assay techniques which are commonly used in cancer research. Nevertheless, it also remains to integrate advanced image processing algorithms, especially those which are adapted for fluorescence images, in order to improve the visual quality of acquired images and facilitate the interpretation for further analyses.

Figure 1.2: From left to right: the scanner named InnoScan 1100 AL (source: `https://www.innopsys.com/`) and a fluorescence TMA image scanned using this device (by the courtesy of Innopsys).

The objective of this thesis in collaboration between Innopsys and Inria consists in investigating and developing methods and algorithms dedicated to TMA (and eventually other biological sample) images acquired by scanners and devices designed by the industrial partner (namely the range InnoScan[2], including the novel prototype InnoScan 1000 AL). More precisely, there are two major topics in which we are particularly interested: (i) challenges of digital TMA image analysis, and (ii) problems related to image acquisition with the scanner. For the first topic, we mainly focus on the localization (segmentation) of circular-shaped tissue samples in a bi-dimensional scanned TMA image and the estimation of their row and column coordinates according to a grid pattern. The aim is to correctly link each sample with its corresponding clinical data. This problem is also called *tissue microarray de-arraying* [Wang et al. 2011]. Meanwhile, other aspects of TMA image-based analysis (e.g., marker scoring, tumor recognition or tissue profiling, etc.) will not be covered in this dissertation and are subject to further studies. Regarding the imaging devices, beside classical problems in image processing such as denoising

[2] `https://www.innopsys.com/en/lifesciences-products/microarrays/innoscan` .

and deconvolution, the correction of pixel mispositioning (i.e. *jitter*) during scanning process is also discussed. Pixel mispositioning resulting in images with jagged shapes, represents in general a big issue, since the visual effect is disturbing due to rolling effect. The removal of this particular artifact is thus necessary to provide images which are visually more pleasant when compared to the jittered version. In the case of the InnoScan range, images acquired by those scanners not only suffer from the jittering effect which is common for all scanning platforms, but also are degraded by a blur due to the low-pass nature of the scanner's optical system. To address to this problem, a deconvolution algorithm is investigated to improve the image resolution.

Note that the algorithms developed during this thesis will be possibly integrated into industrial products. Accordingly, we need to take into account several practical constraints in the design of algorithms, including computational time, hardware requirements as well as implementation facility. It imposes us to design fast and low-memory-requirement algorithms using as-simple-as-possible approaches to ease the implementation. In addition, adhoc strategies such as subsampling or tiling can be also considered in some cases when dealing with very large images (up to about 44000×148000 pixels) to reduce the amounts of processed data at a time and enable parallel computing.

The main contribution of this work is to provide a set of fast algorithms for quantitative analysis of fluorescence TMA images which represents an actual need of pathologists in tissue-based researches but receives little attention from both academics and industry experts. Coupled with existing devices of the InnoScan range designed by Innopsys, these algorithms allow to envisage constructing an automated platform of imaging and pre-processing dedicated to TMAs: once the TMA slides are inserted into the scanner, the batch of inserted slides is automatically performed, and straightforwardly followed by the automated localization (segmentation) of tissue samples as well as the correction of scanning artifacts and the deconvolution without any human supervision. This workflow provides to final users (e.g., pathologists, researchers) not only artifact-free and high-resolution images of each TMA slide, but also structured data (composed of estimated coordinates of each sample, extracted regions of interest from the whole slide image, etc.) for further quantitative analysis. It will be a significant improvement in the automation of the present workflow for digital TMA image analysis where the majority of stages are still performed manually. Beyond the scope of tissue microarray, some of developed algorithms (e.g., segmentation, deconvolution) may have applications and impacts in other contexts, especially in optical microscopy and fluorescence imaging.

The remainder of this manuscript is structured as follows. First, in Chapter 2, we propose a fast and robust approach for TMA de-arraying by combining wavelet-based detection, active contours and thin-plate spline interpolation. In Chapter 3, the scanning artifacts (jitter) is addressed by considering an optical-flow-based variation approach to estimate the underlying displacement. Chapter 4 presents a regularization-based deconvolution method using novel convex regularizers called generalized Sparse Variation. Finally, Chapter 5 summarizes our contributions and results, and gives a perspective to future works.

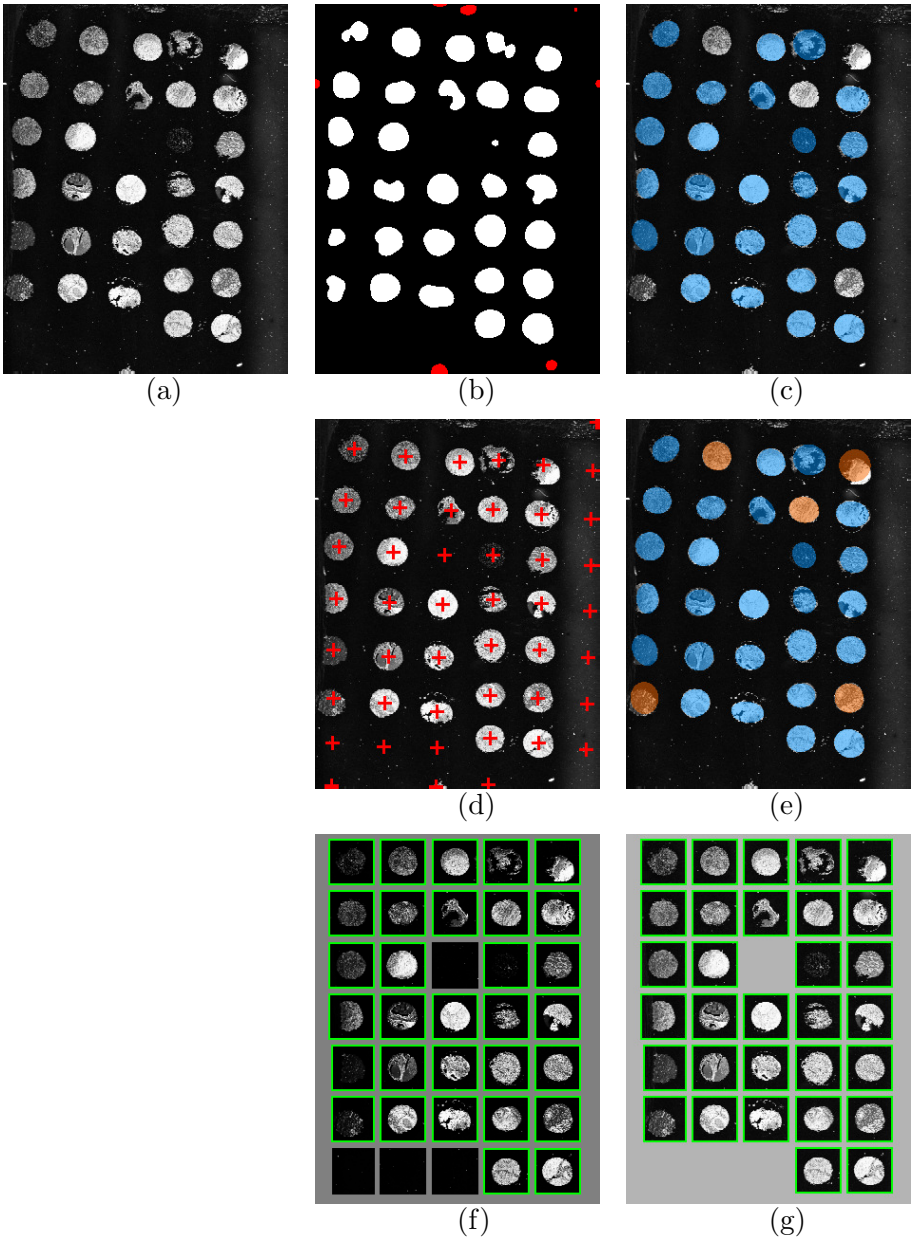

Figure 1.3: Example of TMA de-arraying. (a) Fluorescence image of a TMA, (b) detection result, (c) segmentation result, (d) estimation of the deformed TMA grid, (e) recognized TMA cores, (f) de-arraying result, (g) manual annotation.

Preview of chapters

Chapter 2 :

On a tissue microarray slide, tissue samples are collected from different donors, thus it is highly important to properly identify and associate each sample with its pathological and clinical metadata. More precisely, each sample needs to be accurately localized and to be assigned to relevant row and column coordinates according to a grid pattern. This process is the so-called TMA de-arraying. Although de-arraying seems to be easy at first glance due to the TMA grid pattern, it is much more diffi-

cult in practice because the TMA grid is often strongly deformed and tissue samples can be destroyed or split into several parts during the manufacturing process. To overcome these difficulties, we combine wavelet-based detection, parametric active contours and thin-plate spline interpolation, and propose an automated, fast and robust method for TMA de-arraying. Our method is robust not only to noise but also to non-linear deformation of the TMA grid. It is also adapted for both brightfield and fluorescence images.

Chapter 3 :

In this chapter, we address to scanning artifacts due to pixel mis-positioning (jitter) arising in dedicated scanners developed by Innopsys. Inspired by variation optical flow computation, we propose a variational method for the correction of this specific jitter. Our method consists in estimating a dense displacement field representing the jitter by minimizing an energy functional composed of a non-convex re-alignment criterion and a convex differential-based regularizer. In order to minimize this non-convex functional, we utilize the half-quadratic splitting approach to decouple convex and non-convex terms in such a way that the original minimization problem can be solved by alternating two optimization steps – one using a proximal algorithm for the convex part and the other using an exhaustive search for the non-convex part. Experimental results on artificial and large real fluorescence images demonstrate that our method is not only capable to handle large displacements but is also efficient in terms of sub-pixel precision without modifying image intensities when comparing with image regularization-based approaches.

Chapter 4 :

In this chapter, we generalize the sparse variation (SV), which combines the total-variation (TV) regularization and the L_1 regularization, and introduce a novel family of convex and non-quadratic regularizers for fast deconvolution of large 2D fluorescence images. These regularizers are defined as mixed L_ν-L_2 norms ($\nu \geq 1$) which group image intensity and spatial differentials, computed at each pixel of the image, to favor the co-localization of high-intensity pixels and high-magnitude gradients. By coupling a regularization term of this family with a quadratic data fidelity term, we propose a fast and efficient deconvolution method by using the primal-dual (proximal) algorithms to minimize the corresponding energy functional. Experiment results on both 2D simulated and real fluorescence scanner images demonstrate that the proposed deconvolution method is very competitive when compared to other existing regularization-based methods, specially TV-based deconvolution and Hessian-norm-based deconvolution.

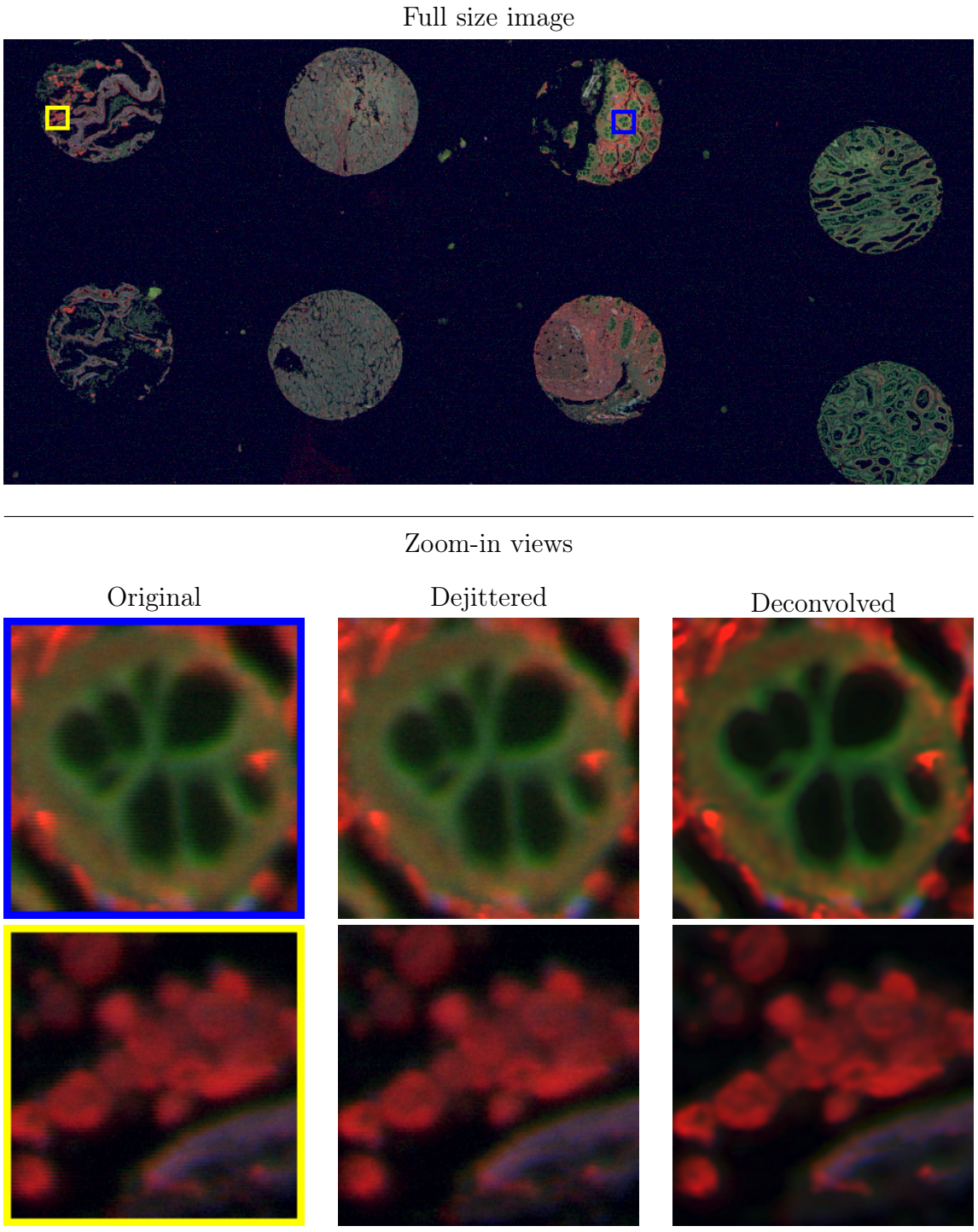

Figure 1.4: Example of dejittering and deconvolution on a fluorescence TMA image acquired in three colors.

Chapter 2

Tissue Microarray De-arraying

Related publications

H.-N. Nguyen, V. Paveau, C. Cauchois, C. Kervrann. Automatic core segmentation and registration for fast Tissue Microarray de-arraying[1]. Published in Proceedings of IEEE 12th International Symposium on Biomedical Imaging (ISBI), New York 2015
H.-N. Nguyen, V. Paveau, C. Cauchois, C. Kervrann. ATMAD: robust image analysis for Automatic Tissue MicroArray De-arraying[1]. Manuscript submitted for publication in BMC Bioinformatics, 2017

Abstract

In this chapter, we propose an Automatic, fast and robust TMA De-arraying (ATMAD) approach dedicated to images acquired with bright field and fluorescence microscopes (or scanners). First, tissue samples are localized in the large image by applying a locally adaptive thresholding on the isotropic wavelet transform of the input TMA image. To reduce false detections, a parametric shape model is considered for segmenting ellipse-shaped objects at each detected position. Segmented objects that do not meet the size and the roundness criteria are discarded from the list of tissue samples before being matched with the design grid. Sample matching is performed by estimating the TMA grid deformation under the thin-plate model. Finally, thanks to the estimated deformation, the true tissue samples that were preliminary rejected in the early image processing step are recognized by running a second segmentation step. By combining wavelet-based detection, active contour segmentation, and thin-plate spline interpolation, our approach is able to handle TMA images with high dynamic, poor signal-to-noise ratio, complex background and non-linear deformation of TMA grid. In addition, the deformation estimation produces quantitative information to asset the manufacturing quality of TMAs.
Keywords: tissue microarray, TMA de-arraying, detection, wavelet, segmentation, active contour, deformation, thin-plate spline

[1]These works were supported by Innopsys.

2.1 Introduction

2.1.1 Tissue MicroArray (TMA) history

The development of multi-tissue techniques was started at the mid-1980s in order to address the scarcity issue of diagnostic reagents and tissue samples. The pioneer work was contributed by Battifora (1986) who introduced the multi-tumor "sausage" tissue block. In this method, several rods of tissue, which were extracted from paraffin-embedded tissue blocks (or shortened as paraffin blocks), deparaffinized and rehydrated, were put together and reparaffinized after being tightly wrapped in small intestine of small mammals like a sausage. To avoid deparaffinization and reparaffinization procedures of Battifora's "sausage" technique, Wan et al. (1987) conceived the "punching" technique which used 16-gauge needle for retrieving cylinders of tissue (also tissue cores) from paraffin blocks and arraying them in a recognizable pattern. Although Wan's punching technique was a big footstep and was used in nearly all of today TMA techniques, its tissue pattern was not a grid one which is more structured and facilitates the identification of each tissue sample. The first multi-tissue grid pattern is described by Battifora and Mehta (1990) under the name of "checkerboard tissue block" in which tissue rods were manually aligned in a Cartesian coordinate system (checkerboard pattern).

By combining the punching technique of Wan and the "checkerboard" concept of Battifora and Mehta, Kononen et al. (1998) invented a machine for assembling efficiently and accurately extracted tissue cores in grid pattern. The proposed technique called "tissue microarray" (TMA) became therefore popular and widely used in most pathological laboratories. In the last decade, different TMA techniques were developed to improve manufacturing process and minimize manufacturing cost (e.g. [Gillett et al. 2000; Chan et al. 2000a; Fejzo and Slamon 2001; Packeisen et al. 2002; Badve et al. 2002; Hidalgo et al. 2003; Wang et al. 2003; Dan et al. 2004; Pan et al. 2004; Datta et al. 2005; Montgomery et al. 2005]), but all of them were based on Battifora's, Wan's and Kononen's previous works. Since in most TMA techniques, extracted tissue samples have cylinder form, in the following, we use the terms "tissue cores" or "TMA cores" (or even more shorter "cores") to refer TMA tissue samples.

2.1.2 Challenges of TMA de-arraying

In a TMA, assembled tissue cores are collected from different donor blocks. It is thus highly important to matching them with their proper meta-data for further clinical or pathological analysis. To this end, grid pattern was conceived to ease the localization of each TMA cores. However, in spite of numerous technique improvements [Dan et al. 2004; Pilla et al. 2012], TMAs manufactured recently by manual or automated (semi-automated) machine are still subjected to the deformation of the design tissue grid due to bad positioning of the tissue cores with respect to the design. Another main source of deformation is the heat deformation of the paraffin waxes – commonly used in TMA techniques – when embedding tissue cores into recipient block. Sectioning paraffin-embedded tissue blocks with a microtome to produce multiple slides may also produce additional deformation. In fact, the design grid may suffer geometric transformations such as translation, rotation and shear-

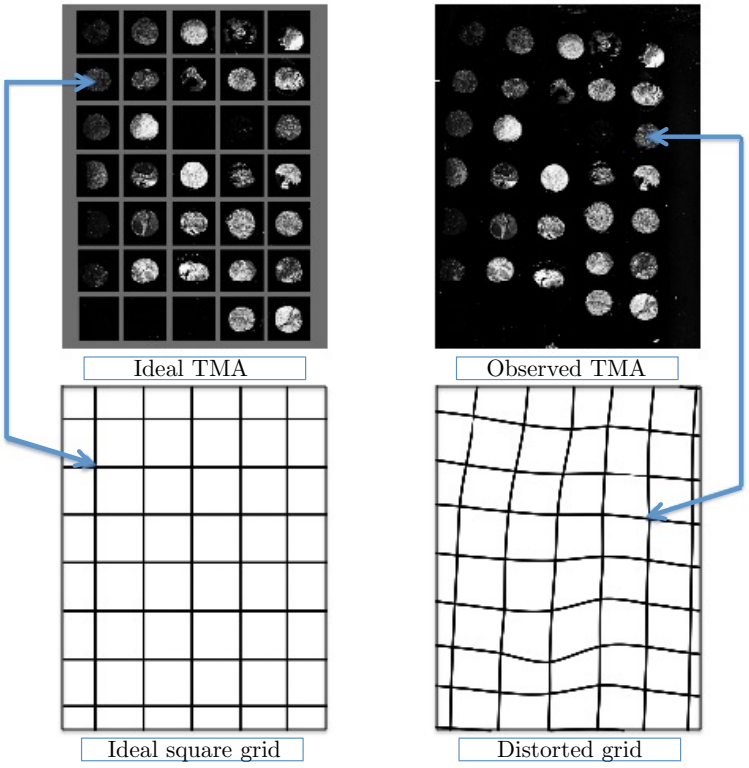

Figure 2.1: **Deformation of the TMA grid.** An ideal TMA (left top) has tissue cores perfectly aligned in vertical and horizontal directions with equal spacing according to a regular square grid (left bottom). The manufactured TMA (right top) is subjected to a non-linear deformation of the TMA grid resulting to a distorted grid (right bottom). We aim at de-arraying the observed TMA by estimating the deformation which transforms the ideal grid into the distorted grid.

ing (linear or affine deformations) combined with dilatation, distortion and random perturbations (non-linear deformations). In addition, some fragile tissue cores may be lost or split into several fragmented parts, making more difficulties to recognize them. Figure 2.1 illustrates a typical image of TMA imaged in fluorescence. We can clearly observe that the ideal TMA grid which is a square grid is significantly distorted after the manufacturing process and the present tissue cores do not have a perfectly circular shape as expected. These problems need to be taken into account to develop robust de-arraying methods.

2.1.3 State-of-the-art of TMA de-arraying methods

Closely similar to TMAs, DNA microarrays (also known as bio-chips) [Taub et al. 1983] are constructed by spotting DNA probes by robots with high precision according to a grid pattern. Numerous gridding methods for microarrays were used to localize each DNA probes and find its row and column coordinates with respect to the design grid. This procedure is called "de-arraying". Despite the similitude of these microarray concepts, existing "de-arraying" methods for microarrays are not adapted for TMAs because the grids are more highly deformed. Along with the

commercialization of digital imaging devices for TMA analysis over the last decade, several methods for TMA "de-arraying" have been developed (e.g [Vrolijk et al. 2003; Chen et al. 2004; Dell'Anna et al. 2005; Rabinovich et al. 2006; Lahrmann et al. 2010; Wang et al. 2011]). In general terms, a "de-arraying" approach consists in two steps: (i) segmentation and localization of assembled tissue cores; (ii) array coordinate (row and column coordinates) estimation of each core.

Firstly, for segmenting tissues, existing de-arraying methods usually assume that the histogram of a TMA image is bimodal. Under this assumption, these methods perform in general a thresholding by taking the local minimum between two highest peaks corresponding to the background and the foreground, of the image intensity histogram as global threshold. Various thresholding techniques were proposed from a simple thresholding as in [Vrolijk et al. 2003] to more sophisticated methods such as the moment-preserving thresholding in [Dell'Anna et al. 2005], the automatic thresholding based on Savitsky-Golay filtered histogram in [Rabinovich et al. 2006] or Otsu's method used in [Lahrmann et al. 2010; Wang et al. 2011]. To improve the segmentation result, pre-processing like contrast enhancement transform [Wang et al. 2011] or template matching [Dell'Anna et al. 2005] was applied. Morphological operators were also used as post-processing for removing outliers in the thresholded map as in [Vrolijk et al. 2003; Wang et al. 2011]. However, this underlying assumption is not satisfied in case of images acquired from novel fluorescence device because of their complex background. Due to the nature of fluorescence imaging, pixels corresponding to irrelevant objects – such as dusts, glue and washing stains – in the background have often high intensities resulting as a high peak in the intensity histogram; in contrast, the intensities of pixels corresponding to tissue cores could be relatively lower. Hence, as a consequence, most of cores fail to be detected with a high threshold and there is a number of outliers corresponding to a low threshold value.

Secondly, for estimating row and column coordinates of each TMA cores, the methods mentioned above were generally based on distance and angle criteria to define the average spacing between the cores and the orientation of the observed grid. These criteria were derived simply from the distance between neighbor tissue cores [Dell'Anna et al. 2005], or from sophisticated measures such as the histogram of distance and angle [Vrolijk et al. 2003] or the coefficients of the Hough transform [Chen et al. 2004] or even the Delaunay triangulation [Wang et al. 2011]. To deal with the case of missing tissue cores or the design of TMA grid in which some positions are left empty [Pilla et al. 2012], linear or local bilinear interpolation were used as in [Vrolijk et al. 2003; Wang et al. 2011] for completing the grid. Whereas these methods yield satisfactory results for further pathological analysis, they can not produce quantitative information about the deformation of the TMA grid which is an indicator for evaluating the quality of the manufactured input TMA. For that reason, we address this issue and develop a de-arraying method which is able to provide quantitative information about the deformation. Our approach allows management of traceability and quality control of the whole TMA manufacturing process.

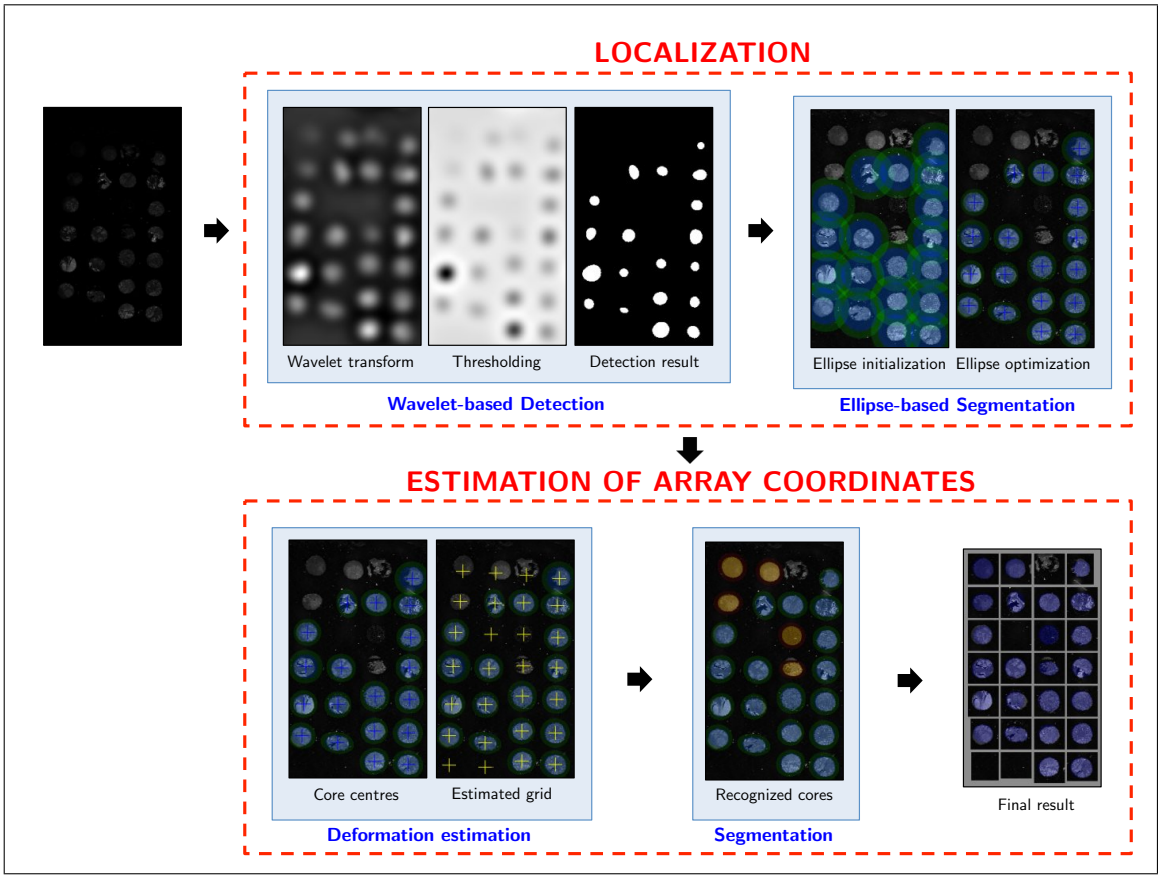

Figure 2.2: **Overview of our TMA de-arraying approach.** The proposed ATMAD approach consists in two steps : (i) tissue core localization; (ii) estimation of array coordinates of tissue cores. The localization step is performed by combining a fast wavelet-based detection and an ellipse-shaped active contour to produce accurate core positions for the second step. The second step is dedicated to the estimation of the deformation of the TMA grid. The objective is to refine the de-arraying result by providing additionally potential positions of tissue cores which were not recognized at the first step. The de-arraying result is presented as a regular array to facilitate the seeking of row and column coordinates of each core.

2.1.4 Overview of the method

In this chapter, we propose a fast and efficient approach for automated TMA de-arraying with the emphasis on fluorescence TMA images and modeling of TMA grid deformation. The proposed approach called ATMAD is based on the following image processing operations: core detection, core segmentation and estimation of the grid deformation. For the tissue localization step of the de-arraying procedure, we combine the detection and segmentation tasks to produce reliable inputs for the second step – the computation of the array coordinate of each tissue core. This second step is performed by using the deformation estimation module followed by a segmentation task to refine the result. The outline of our approach is shown in Fig. 2.2 which describes the two steps of the de-arraying procedure and the combination of the three image processing operations.

The "detection" operation (i.e. the detection) is based on a wavelet approach. In order to process images having large dynamic range, complex background and high

noise level such as fluorescence images, we compute a stationary wavelet transform of the input TMA image at an appropriate scale to the tissue size – the average tissue core radius given by the manufacturer. By choosing the mother wavelet as a difference of Gaussians, we can deduce the closed-form expression of the wavelet atom at any desired scale and use it to perform directly the wavelet decomposition. Our technique is faster and more accurate than the well-known "à trous" algorithm [Starck et al. 1994]. The wavelet transform map is then locally thresholded to spatially adapt to the contrast between the foreground – corresponding to TMA cores – and the inhomogeneous background. The position of potential tissue cores is defined as the center of the connected components in the thresholded wavelet transform map.

To delineate the boundary of each tissue core and improve detection result, an ellipse-shaped active contour [Thévenaz et al. 2011] is used for segmenting the detected object at each position obtained from previous step. The segmented objects, which are too large or too small than the given average size of tissue sample or too elongated, will be considered as false detection and be discarded from the list of potential positions. This removal is essential to discard potential outliers and enhance the reliability of the input for the estimation of row and column coordinates of TMA cores.

Instead of estimating directly the row and column coordinates of each core from the position list, we approximate the deformation of the TMA grid using the thin-plate model. In fact, the deformed grid is the image (in the sense of set theory) of the regular grid of design by the deformation. Given the deformation at some arbitrary points of the grid, the thin-plate interpolation allows to estimate it at other points [Bookstein 1989]. The more points we have known, the more precisely we estimate the deformation. Once the deformation is approximated, the computation of row and column coordinates of each tissue core is therefore straightforward. By reformulating as an approximation problem and solving it iteratively, our method is robust to high non-linear deformations which were observed in most real TMA images. Moreover, according to the thin-plate model, the approximation yields information such as the average translation, the rotation angle, the bending energies along the horizontal and vertical axes, etc. These information are useful to assess the quality of the manufactured TMAs.

The remainder of this chapter is organized as follows. In the next section, we describe the de-arraying approach including a technical presentation of the "detection, "segmentation", "deformation estimation" tasks. We also figure out how the proposed approach is adapted for TMA images acquired with bright field microscopes. In Section 2.2, we present the experimental results obtained from simulated and real data. Finally, the last section gathers the conclusions drawn from this research and details the future work.

2.2 Methodology

In our approach, the estimation of core positions on the input TMA image is subsequently refined in successive tasks by considering different image domains (i.e.

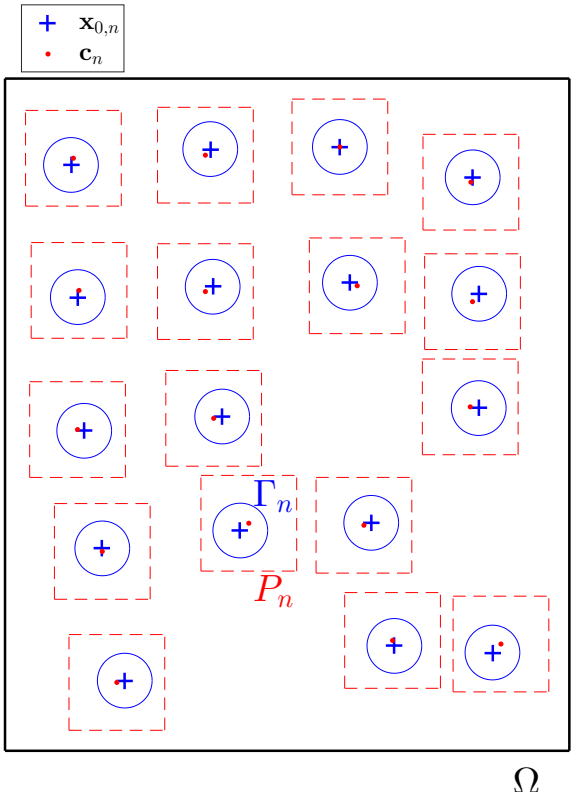

Figure 2.3: **Illustration of core positions and notations.** The image u is defined on a rectangular domain Ω (shown in black rectangle). For each detected position $\mathbf{c}_n$ (red small dots), a patch P_n (red dashed squares) centered at $\mathbf{c}_n$ is extracted. The ellipse Γ_n (blue ellipses) with center $\mathbf{x}_{0,n}$ (blue crosses) is optimized to fit the object of interest which is located inside the patch P_n.

patches or regions) in the input original image. Such a strategy allows not only to avoid unnecessary processing on non-content regions but also to reduce the acquisition time, storage and processing time of high resolution data. To distinguish the inputs and outputs of each task and facilitate the comprehension of the technical details, we present a diagram in Fig. 2.3 which illustrates a few notations which will be used throughout the chapter.

2.2.1 TMA core Detection

The detection of approximately circular TMA cores can be performed by spot detection algorithms. Spot detection is a well-known topic in image processing (see [Kervrann et al. 2016] for a recent review). Over past decades, number of spot detection methods have been proposed (e.g. [Breen et al. 1991; Olivo-Marin 2002; Sage et al. 2005; Zhang et al. 2007; Smal et al. 2008]). To produce satisfactory results, most of these methods require fine adjustment of a critical parameter: the detection scale corresponding to the size of the objects of interest. Automatic selection of the detection scale is a challenging problem since the objects of interest may have different sizes or they may have the same size as the irrelevant objects in the background. Few methods of automatic scale selection [Basset et al. 2014; Püspöki et al. 2015,

2016] have been proposed recently. However, in the context of tissue microarrays, the diameter of assembled TMA cores is defined by the size of the needle used for extracting cores from paraffin tissue blocks. The determination of the scale parameter used for spot detection is straightforward from this measure which is often given by the manufacturer. We propose here a fast algorithm for tissue core detection by performing directly the wavelet decomposition at the appropriate aforementioned scale and computing a locally-adaptive threshold of the wavelet coefficients.

2.2.1.1 Pre-processing

Wavelet-based detection techniques are known to be robust to noises with non-stationary distributions like Poisson noise or mixed-Poisson-Gaussian noise as in TMA images, acquired by brightfield or fluorescence. Pre-processing operations such as image denoising or variance stabilization transform are thus not mandatory. However, our algorithm is primarily designed for detecting bright spots over a dark background, and especially adapted for fluorescence images. brightfield TMA images, in which the tissue cores are darker than the background, are first inverted before further processing.

2.2.1.2 Scale selection

Nowadays, standard TMAs are manufactured with a diameter of tissue core typically from 0.6 to 1.5 millimeters. Given an imaging resolution (pixel size), the optimal scale of wavelet decomposition can be determined according to the core radius. If we denote r_{core} the expected average radius (in pixels) of TMA cores, the optimal scale index $\hat{j}$ of the wavelet decomposition that best fits the size of TMA cores is defined as:

$$\hat{j} = \underset{j \in \mathbb{N}^*}{\operatorname{argmin}} \left| r_{core} - 2^{j-1}\sigma_1 \right| \ , \tag{2.1}$$

where σ_1 is selected according to the pixel size.

2.2.1.3 Fast isotropic wavelet decomposition

In contrast to multiresolution approaches, our detection method requires only the wavelet decomposition at the appropriate selected scale. To compute the decomposition at a desired scale, usual wavelet transform techniques perform a sequence of successive convolutions which are used for computing iteratively the decomposition from the smallest scale to the coarsest scale. These techniques are time consuming when dealing with large images and high number of scales. Instead, to address to this computational issue, we build a dyadic isotropic wavelet frame $\{\psi_j\}_{j\geq 1}$ by choosing the scaling function ϕ_j as a Gaussian function whose variance v_j^2 is a function of scale $j \in \{1, \ldots, j_{\max}\}$ and $j_{\max}$ is the maximum index of the highest scale:

$$\phi_j(\mathbf{x}) = G_{v_j}(\mathbf{x}) = \frac{1}{2\pi v_j} \exp\left(-\frac{\|\mathbf{x}\|_2^2}{2v_j^2} \right), \tag{2.2}$$

where $\|\cdot\|_2$ denotes the Euclidean norm, $\mathbf{x} \in \Omega \subset \mathbb{R}^2$ is the pixel location in the rectangular domain Ω and

$$v_j^2 \;=\; \sum_{k=1}^{j} \sigma_k^2 \;=\; \sum_{k=1}^{j} 4^{k-1}\sigma_1^2 \;=\; \sigma_j^2 + v_{j-1}^2 \tag{2.3}$$

with $\sigma_k = 2^{k-1}\sigma_1$. Thanks to the semi-group property of Gaussian functions, the relationship between the scaling functions at subsequent scales can be expressed as:

$$\begin{aligned} \phi_j(\mathbf{x}) &= G_{\sqrt{\sigma_j^2+v_{j-1}^2}}(\mathbf{x}) \\ &= G_{\sigma_j} \star G_{v_{j-1}}(\mathbf{x}) \;=\; G_{\sigma_j} \star \phi_{j-1}(\mathbf{x}), \end{aligned} \tag{2.4}$$

where $\star$ denotes the convolution operator. Therefore, the wavelet decomposition $\Psi_j u$ of $u : \Omega \subset \mathbb{R}^2 \to \mathbb{R}$ at the scale $j \in \{1, \ldots, j_{\max}\}$ is obtained by convolution of u with the wavelet atom ψ_j as:

$$\begin{aligned} \Psi_j u(\mathbf{x}) \;=\; \psi_j \star u(\mathbf{x}) &= (\phi_{j-1} - \phi_j) \star u(\mathbf{x}) \\ &= (G_{v_{j-1}} - G_{v_j}) \star u(\mathbf{x}), \end{aligned}$$

with the conventions $v_0^2 = 0$ and $G_0(\cdot) = \delta(\cdot)$ (Dirac delta function). For more technical details on the proposed wavelet frame and the wavelet decomposition and reconstruction algorithms, please refer to the Appendices 2.A and 2.B.

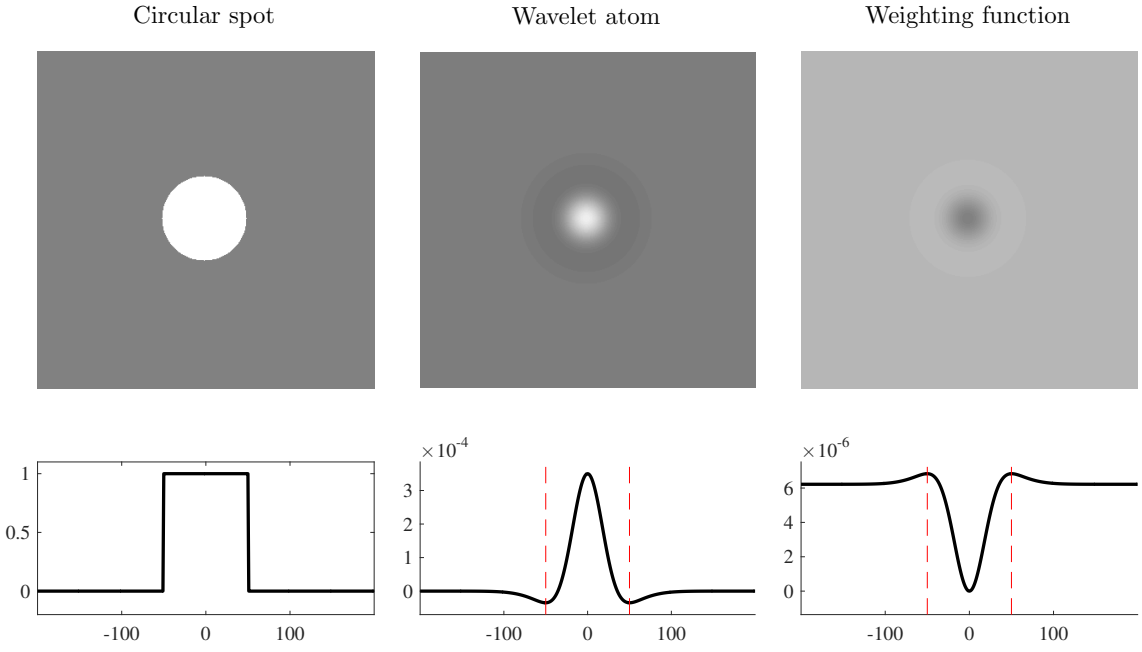

Figure 2.4: **Wavelet atom and corresponding weighting function used for estimating the local distribution wavelet transform of a circular spot image.** From left to right : the image of a circular spot, its wavelet atom at the appropriate scale and its corresponding weighting function on the top row; and their radial profile on the bottom row (red dashed lines delineate the radius of the spot).

2.2.1.4 Locally-adaptive thresholding

While the wavelet decomposition plays the role of a filtering which reduces the noise and enhances the objects of interest, a common way to detect objects is to threshold the filtered image – the wavelet decomposition of the input TMA image in our case. As depicted in [Basset et al. 2014], a global threshold is not appropriate to handle complex situations, especially when dealing with images acquired in fluorescence context because of their inhomogeneous background. To overcome this difficulty, we propose to define an adaptive threshold according to the local distribution of the wavelet decomposition $\Psi_{\hat{\jmath}} u$ previously computed. Accordingly, we consider the following statistical test at each point $\mathbf{x}$ of the TMA image u:

$$\begin{cases} \mathcal{H}_0 : & \mathbf{x} \text{ belongs to the background,} \\ \mathcal{H}_1 : & \mathbf{x} \text{ corresponds to tissue core (foreground).} \end{cases}$$

Pixels corresponding to tissue cores have strong positive responses in the wavelet decomposition. Under the null hypothesis $\mathcal{H}_0$, the wavelet coefficient $\Psi_{\hat{\jmath}} u(\mathbf{x})$, which follows the local distribution of the wavelet-decomposed-image background with mean $\mu(\mathbf{x})$ and variance $\nu^2(\mathbf{x})$, is lower than a certain value $\tau(\mathbf{x})$. Let $\mathbb{P}\left(\Psi_{\hat{\jmath}} u(\mathbf{x}) < \tau(\mathbf{x})\right)$ be the probability for a pixel $\mathbf{x}$ to be classified as "background" class. The threshold $\tau(\mathbf{x})$ is used to control the number of misclassification. Given a probability of false alarm $p_{\text{FA}} > 0$, the corresponding threshold τ_{FA} is selected such that the misclassification probability $\mathbb{P}\left(\Psi_{\hat{\jmath}} u(\mathbf{x}) \geq \tau_{\text{FA}}(\mathbf{x})\right)$ is lower than p_{FA}. By applying the conventional probabilistic Tchebychev's inequality, we get, $\forall \kappa(\mathbf{x}) > 0$:

$$\mathbb{P}\left(|\Psi_{\hat{\jmath}} u(\mathbf{x}) - \mu(\mathbf{x})| \geq \kappa(\mathbf{x})\right) \leq \frac{\nu^2(\mathbf{x})}{\kappa^2(\mathbf{x})}. \tag{2.5}$$

It follows that

$$\mathbb{P}\left(\Psi_{\hat{\jmath}} u(\mathbf{x}) \geq \mu(\mathbf{x}) + \kappa(\mathbf{x})\right) \leq \mathbb{P}\left(|\Psi_{\hat{\jmath}} u(\mathbf{x}) - \mu(\mathbf{x})| \geq \kappa(\mathbf{x})\right).$$

Now, let us define $\tau_{\text{FA}}(\mathbf{x}) = \mu(\mathbf{x}) + \kappa(\mathbf{x})$ and assume $(\nu^2(\mathbf{x})/\kappa^2(\mathbf{x})) \leq p_{\text{FA}}$ such that $\mathbb{P}\left(\Psi_{\hat{\jmath}} u(\mathbf{x}) \geq \tau_{\text{FA}}(\mathbf{x})\right) \leq p_{\text{FA}}$. Finally,

$$\tau_{\text{FA}}(\mathbf{x}) \geq \mu(\mathbf{x}) + \frac{\nu(\mathbf{x})}{\sqrt{p_{\text{FA}}}} \tag{2.6}$$

and the adaptive threshold $\tau_{\text{FA}}(\mathbf{x})$ is controlled by the p-value p_{FA} set by the user.

To determine the threshold $\tau_{\text{FA}}(\mathbf{x})$, the local mean $\mu(\mathbf{x})$ and the local variance $\nu^2(\mathbf{x})$ of the image background on the wavelet decomposition $\Psi_{\hat{\jmath}} u$ are required. However, prior knowledge about the image background distribution is unfortunately not available in most cases. We consider thus empirical estimations of μ and ν^2 at each point $\mathbf{x}$ from $\Psi_{\hat{\jmath}} u$:

$$\hat{\mu}(\mathbf{x}) = g \star \Psi_{\hat{\jmath}} u(\mathbf{x}) \,, \tag{2.7}$$

$$\hat{\nu}^2(\mathbf{x}) = g \star \left(\Psi_{\hat{\jmath}} u\right)^2(\mathbf{x}) - \hat{\mu}^2(\mathbf{x}) \,, \tag{2.8}$$

where $g(\cdot)$ is a weighting positive function (i.e. $\|g(\cdot)\|_1 = 1$, $\|\cdot\|_1$ is the L_1 norm and $g(\mathbf{x}) \geq 0, \forall \mathbf{x} \in \Omega$) mainly used to avoid the estimation of the background

distribution statistics being biased from coefficients corresponding to the foreground. By construction, $\hat{\mu}(\mathbf{x})$ and $\hat{\nu}^2(\mathbf{x})$ are weighted estimators derived from $\Psi_{\hat{\jmath}}u$ which is a filtered version of u by the band-pass filter $\psi_{\hat{\jmath}}$ in order to enhance the objects of radius r_{core}. It is thus convenient to define the weighting function g according to the wavelet atom $\psi_{\hat{\jmath}}$. By using an affine transform which implies the positivity and the normalization conditions, we propose a candidate for $g(\cdot)$ as follows :

$$\hat{g}(\mathbf{x}) = \frac{-\psi_{\hat{\jmath}}(\mathbf{x}) + \sup \psi_{\hat{\jmath}}}{\| -\psi_{\hat{\jmath}} + \sup \psi_{\hat{\jmath}} \|_1} \ , \tag{2.9}$$

where $\sup \psi_{\hat{\jmath}} = \|\psi_{\hat{\jmath}}\|_\infty$ denotes the supremum (L_∞ norm) of $\psi_{\hat{\jmath}}$ and $\| -\psi_{\hat{\jmath}} + \sup \psi_{\hat{\jmath}} \|_1$ is the normalization factor to ensure $\|\hat{g}(\cdot)\|_1 = 1$. The choice of this candidate is clarified in Fig. 2.4 showing the wavelet atom and its derived weighting function according to a given circular spot. The proposed weighting which is constructed from the wavelet atom has the same size of the considered spot and has a hollow shape at the center (see right column in Fig. 2.4). This specific shape allows to reduce the impact of high wavelet coefficients corresponding to foreground pixels on the estimation of the background statistics.

By substituting the empirical estimators to $\mu(\mathbf{x})$ and $\nu^2(\mathbf{x})$, we obtain the estimated detection threshold:

$$\hat{\tau}_{\text{FA}}(\mathbf{x}) = \hat{\mu}(\mathbf{x}) + \frac{\hat{\nu}(\mathbf{x})}{\sqrt{p_{\text{FA}}}} \ . \tag{2.10}$$

Thresholding the wavelet decomposition $\Psi_{\hat{\jmath}}u$ with respect to $\hat{\tau}_{\text{FA}}$ results in a binary image $I_{\text{FA}} : \Omega \to \{0, 1\}$:

$$I_{\text{FA}}(\mathbf{x}) \ = \ \begin{cases} 1 & \text{if } \ \Psi_{\hat{\jmath}}u(\mathbf{x}) \geq \tau_{\text{FA}}(\mathbf{x}) \\ 0 & \text{otherwise} \end{cases} \tag{2.11}$$

where each connected component in I_{FA} represents a region which is potentially a tissue core of the TMA image. The gravity centers of these regions (or detection position) will be used as inputs for estimating the array coordinates of TMA cores. However, the detection reliability has a great impact on the de-arraying outcome: few false detections may lead to severely inaccurate results. Removing false detections (i.e. outliers) is then crucial. To this end, the size of detected regions seems to be a relevant criterion since the core size is given in most cases by the TMA manufacturer. Although, due to the complexity of backgrounds, it may be highly different from the true core size. Instead of exploiting the imprecise information derived from the binary detection map I_{FA}, we perform an active-contour-based segmentation to delineate the objects at each detected position. Also, we re-use the segmentation results to confirm and improve the preliminary detection results.

2.2.2 Segmentation of TMA cores

As depicted in previous section, the detection binary image I_{FA} does not allow us to accurately determine the size of detected objects. Active contours are typically well appropriate in our context since they can evolve to closely delineate the object

borders and thus yield an estimation of the TMA core size. The family of parametric active contours presented below will help to refine the detected position and the size of TMA cores and eventually to determine the orientation of the potential core if it was deformed during the manufacturing process.

Since the seminal paper of Kass et al. (1988), active contour models (or snakes) have been successfully used to detect discontinuities, detect objects of interest or segment images, especially in bioimaging [Delgado-Gonzalo et al. 2015]. General purpose closed contours are generally controlled by elastic forces based on local curvature and image based potentials (e.g., [Kass et al. 1988; Zhu and Yuille 1996; Chan and Vese 2001; Kervrann and Trubuil 2002]). The curve evolves from its initial starting position towards the target object. The optimization of the underlying energy functional is traditionally performed using variational principles and finite differences techniques, which needs an appropriate initialization to converge to a relevant solution. At the end of the nineties and beginning of the 2000's, geodesic active contours [Caselles et al. 1997] based on the theory of surfaces evolution and geometric flows have been introduced to segment an arbitrary number of highly complex objects in the image. In our TMA context, the 2D shapes of tissue cores can be actually well estimated by ellipse-shaped active contours which belong to the family of parametric deformable templates.

Application-tailored parametrized templates introduced by Yuille et al. (1992) were proposed in cases where strong a priori knowledge about the shape being analyzed is available (e.g. eyes or lips in human faces [Yuille et al. 1992]). The models are hand-built using simple parametrized 2D geometric representations. Another line of research focused on models of random deformations for a given initial shape (deformable template). Grenander et al. obtained the first promising results in image segmentation by considering statistical deformable models which describe the statistics of local deformations applied to an original template (see [Amit et al. 1991; Grenander et al. 1991]). Markov models and Monte-Carlo techniques have been introduced in this context to derive optimal random deformations estimates from image data [Amit et al. 1991; Grenander et al. 1991; Grenander and Miller 1994; Kervrann and Heitz 1998; Descombes 2013]. In the approach initially proposed by Cootes et al. (1995) and successfully applied to object tracking [Kervrann and Heitz 1998], the shape structure and the parameters describing its deformations are learned from a training set of representative shapes. Meanwhile, Staib and Duncan (1992) proposed to combine parametric snakes (B-splines) to the standard decomposition on a Fourier basis to analyze deformable biomedical structures. All these methods are generally robust to noise but computationally demanding if stochastic iterative procedures are used to conduct the minimization and no initial guess close to the optimal solution is provided. Very recently "snakescules" [Thévenaz and Unser 2008] combined to fast algorithms and Markov point process [Descombes 2016] have been proposed along the same philosophy but dedicated to the detection of cells or nuclei in fluorescence microscopy images.

Finally, the ellipse fitting concept has been furthemore introduced by Thévenaz et al. (2011) as an extension of the simple circle-shaped active contour [Thévenaz and Unser 2008] which can be defined just by two points. As a consequence, a triplet of points is necessary to parametrize the ellipse-shaped version. However,

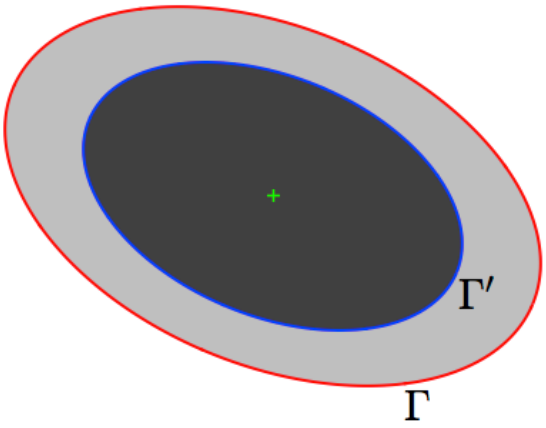

Figure 2.5: **Pair of concentric and coaxial ellipses.** The outer ellipse Γ (red curve) has an area twice larger than the inner ellipse Γ′ (blue curve). These ellipses determine two domains of the same area : an elliptical outer ring (shown in light gray) and an elliptical inner core (dark gray).

this parametrization which has an extra degree of freedom increases the complexity of the model and makes the optimization of ellipse parameters more challenging when compared to the circle-shaped model. To overcome these difficulties, an alternative way was proposed in [Pediredla and Seelamantula 2012]: the ellipses are configured by their center, their axes and the angle between their major axis and the horizontal. Under this configuration, the ellipse energy (also the cost function) which is defined as the contrast between the core and the ring delineated by the pair of ellipses (see Fig. 2.5), and the derivatives of the energy with respect to the ellipse parameters could be calculated efficiently by using the Green's theorem [Staib and Duncan 1992]. Nevertheless, the Green's theorem cannot be applied with no error in the discrete setting and digitized images. In order to handle properly the ellipse parametrization described in [Pediredla and Seelamantula 2012] instead of [Thévenaz et al. 2011] in the discrete setting, we propose a pixel-based smooth approximation of the underlying cost energy functional. Our approximation allows us to calculate properly the derivatives of the cost function with respect to the ellipse parameters and is not based on the Green's theorem also used in [Staib and Duncan 1992] for energy minimization.

2.2.2.1 Definition of the ellipse-based energy

More formally, let Γ be the outer ellipse with parameters $\{\mathbf{x}_0, a, b, \theta\}$ where $\mathbf{x}_0 = (x_0, y_0)$ is the center, a and b are the semi major and minor axes respectively, and θ is the angle of rotation. The inner ellipse Γ′ is defined as a concentric and coaxial ellipse of Γ such the latter has an area (denoted $|\Gamma|$) twice larger than the former: $|\Gamma| = 2|\Gamma'|$ (see Fig. 2.5). The factor 2 ensures that the area of the elliptical outer ring is equal to the area of the elliptical inner core. Let us consider a rectangular image patch P containing a potential TMA core associated to a connected component estimated by the detection method in the early stage. The ellipse energy is defined as a normalized image contrast between the two domains $\Gamma' \subset \Gamma \subset P$ where P is a rectangular

domain in the image domain Ω which contains a single TMA core [O'Sullivan and Qian 1994; Thévenaz et al. 2011]:

$$J(u,\Gamma) = \frac{1}{ab}\left(\int_{\Gamma\setminus\Gamma'} u(\mathbf{x})\ d\mathbf{x} - \int_{\Gamma'} u(\mathbf{x})\ d\mathbf{x}\right) \qquad (2.12)$$
$$= \frac{1}{ab}\left(\int_{\Gamma} u(\mathbf{x})\ d\mathbf{x} - 2\int_{\Gamma'} u(\mathbf{x})\ d\mathbf{x}\right)\ .$$

To handle discrete images, the continuous image u defined in (2.12) can be replaced by its sampled version as follows:

$$J(u,\Gamma) = \frac{1}{ab}\sum_{\mathbf{x}\in P\cap\mathbb{Z}^2} \left(\mathbb{1}_{\Gamma}[\mathbf{x}] - 2\ \mathbb{1}_{\Gamma'}[\mathbf{x}]\right) u[\mathbf{x}]\ , \qquad (2.13)$$

where $u[\mathbf{x}]$ is the discrete sample of $u(\mathbf{x})$ and $\mathbb{1}[\cdot]$ denotes the set indicator function such as $\mathbb{1}_{\Gamma}[\mathbf{x}] = 1$ if $\mathbf{x} \in \Gamma$ and 0 otherwise. However, there are two major drawbacks while considering this energy function. Firstly, the calculation of the energy gradient is not trivial in the discrete setting since the indicator functions in (2.13) are piecewise constant which are not differentiable at some points. Secondly, due to sampling effect, brutal switch of the membership of some points from a domain to another may happen just with an infinitesimal change in the ellipse parameters, giving rise to severe numerical instabilities. Smooth approximations of the underlying piecewise constant functions is recommended to overcome both discontinuity and sampling problems. The calculations of partial derivatives of the energy functional is facilitated if we can define a fuzzy membership to avoid abrupt domain switches (see Fig. 2.8a and 2.8b). Our goal is then to build an approximation which favors the computation of the partial derivative of the energy with respect to each ellipse parameter as much as possible. First, we consider the following quadratic form:

$$\|\mathbf{x}\|_{\Gamma}^2 = \left\| \begin{bmatrix} a^{-1} & 0 \\ 0 & b^{-1} \end{bmatrix} \begin{bmatrix} \cos\theta & \sin\theta \\ -\sin\theta & \cos\theta \end{bmatrix} \mathbf{x} \right\|_2^2 . \qquad (2.14)$$

For a given point $\mathbf{x}$, $\|\mathbf{x}-\mathbf{x}_0\|_{\Gamma}$ is a normalized metric between $\mathbf{x}$ and the ellipse center $\mathbf{x}_0$ induced by the geometry of the ellipse Γ. A pixel $\mathbf{x}$ belongs to the interior of the ellipse Γ if and only if $\|\mathbf{x}-\mathbf{x}_0\|_{\Gamma}^2 \leq 1$ since $\|\mathbf{x}-\mathbf{x}_0\|_{\Gamma}^2$ is always positive. The term $\mathbb{1}_{\Gamma}[\mathbf{x}]$ can be then expressed by a function of $\|\mathbf{x}-\mathbf{x}_0\|_{\Gamma}$ as $\mathbb{1}_{\Gamma}[\mathbf{x}] = \mathbb{1}_{]-\infty,1]}[\|\mathbf{x}-\mathbf{x}_0\|_{\Gamma}^2]$. Moreover, we need to find a smooth function which closely approximates $\mathbb{1}_{]-\infty,1]}$ as investigated in [Chan and Vese 2001; Thévenaz et al. 2011] and has simple derivative. We realized that the graph of $\mathbb{1}_{]-\infty,1]}$ looks similar to the C^{∞} S-shaped logistic curve whose the derivative is easy to compute. Let us consider therefore the following logistic function:

$$S_{\epsilon}(t) = \frac{1}{1+e^{\frac{t-1}{\epsilon}}} \ \underset{\epsilon\to 0}{\longrightarrow}\ \mathbb{1}_{]-\infty,1]}(t), \qquad (2.15)$$

where $\epsilon > 0$ controls the steepness of the curve (see the plot of $t \longmapsto S_{\epsilon}(t)$ in Fig. 2.6 for several values of ϵ). The smaller ϵ, the closer the curve S_{ϵ} approaches the graph of the indicator function $\mathbb{1}_{]-\infty,1]}$. Thanks to the property of logistic functions, the derivative of S_{ϵ} can be easily computed as $S'_{\epsilon}(t) = -\epsilon^{-1}S_{\epsilon}(t)\,(1-S_{\epsilon}(t))$.

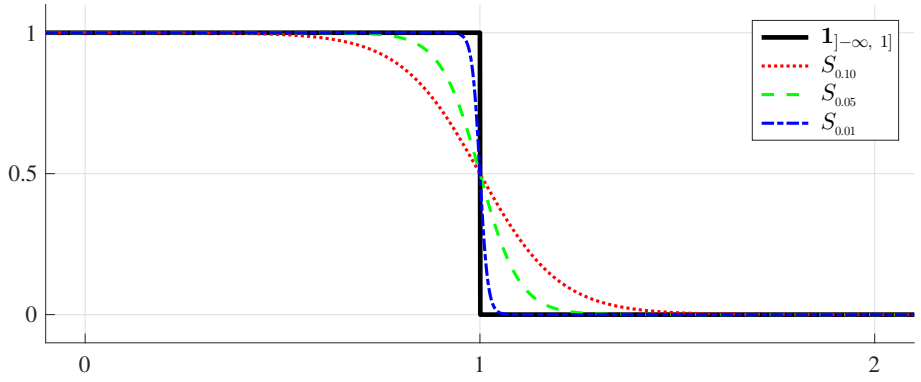

Figure 2.6: **Approximation of the indicator function by logistic curves.** The smaller ϵ, the closer the S-shaped curve S_ϵ approaches the graph of $\mathbb{1}_{]-\infty,1]}$.

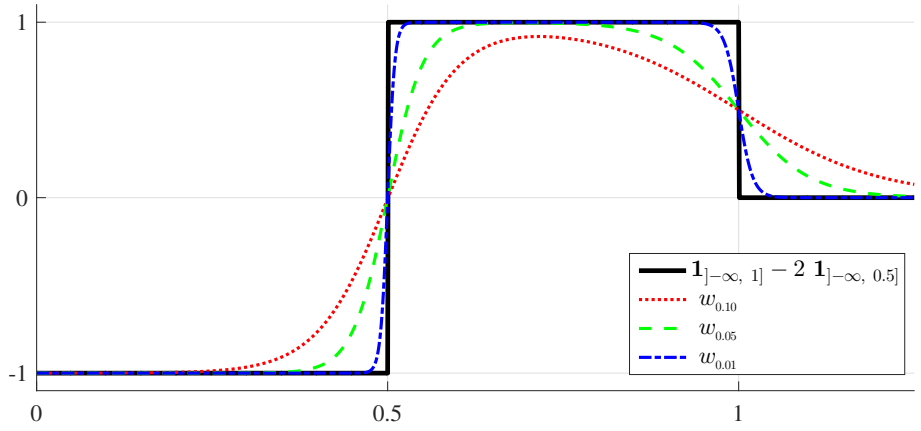

Figure 2.7: **The weights w_ϵ.** $w_\epsilon\left(\|\mathbf{x}-\mathbf{x}_0\|_\Gamma^2\right)$ approximates $\mathbb{1}_\Gamma[\mathbf{x}] - 2\ \mathbb{1}_{\Gamma'}[\mathbf{x}]$ whose the radial profile is represented by the graph of the step function $t \longmapsto \mathbb{1}_{]-\infty,\ 1]}(t) - 2\ \mathbb{1}_{]-\infty,\ 0.5]}(t)$.

Finally, the energy functional has the following form [Thévenaz et al. 2011]:

$$J(u,\Gamma) = \frac{1}{ab} \sum_{\mathbf{x}\in P\cap\mathbb{Z}^2} w_\epsilon(\|\mathbf{x}-\mathbf{x}_0\|_\Gamma^2)\, u[\mathbf{x}] \ , \tag{2.16}$$

with $w_\epsilon(t) = S_\epsilon(t) - 2S_\epsilon(2t) = \dfrac{1}{1+e^{\frac{t-1}{\epsilon}}} - \dfrac{2}{1+e^{\frac{2t-1}{\epsilon}}}$. For illustration, we present in Fig. 2.7 the plot of w_ϵ whose the term $w_\epsilon(\|\mathbf{x}-\mathbf{x}_0\|_\Gamma^2)$ is nothing else than a smooth approximation of the piecewise constant function $\mathbf{x}_0 \longmapsto \mathbb{1}_\Gamma[\mathbf{x}] - 2\ \mathbb{1}_{\Gamma'}[\mathbf{x}]$. These weights are very similar to those described in [Chan and Vese 2001] and based on the arctan function.

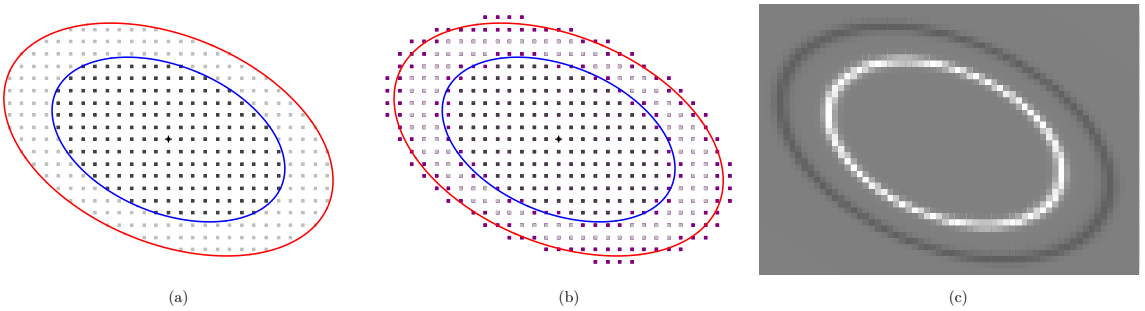

(a) (b) (c)

Figure 2.8: **Inner and outer domain membership under discrete setting.** Points in the inner core are marked by dark gray squares and those in the outer ring are marked by lighter gray squares. From left to right : (a) abrupt domain switch for points in the neighbor of ellipse boundaries (red and blue curves); (b) fuzzy membership with transition zones (marked by purple squares); and (c) first order derivative of the function w_ϵ (zero values are shown in gray).

2.2.2.2 Calculation of partial derivatives

By applying the derivation rules of composite functions, the partial derivatives of the energy with respect to each ellipse parameter $\{\mathbf{x}_0, a, b, \theta\}$ are given by:

$$\begin{cases} \frac{\partial J(u,\Gamma)}{\partial x_0} &= \frac{1}{ab}\sum_{\mathbf{x}} u[\mathbf{x}] w'_\epsilon\left(\|\mathbf{x}-\mathbf{x}_0\|^2_\Gamma\right) \frac{\partial \|\mathbf{x}-\mathbf{x}_0\|^2_\Gamma}{\partial x_0} \ , \\ \frac{\partial J(u,\Gamma)}{\partial y_0} &= \frac{1}{ab}\sum_{\mathbf{x}} u[\mathbf{x}] w'_\epsilon\left(\|\mathbf{x}-\mathbf{x}_0\|^2_\Gamma\right) \frac{\partial \|\mathbf{x}-\mathbf{x}_0\|^2_\Gamma}{\partial y_0} \ , \\ \frac{\partial J(u,\Gamma)}{\partial \theta} &= \frac{1}{ab}\sum_{\mathbf{x}} u[\mathbf{x}] w'_\epsilon\left(\|\mathbf{x}-\mathbf{x}_0\|^2_\Gamma\right) \frac{\partial \|\mathbf{x}-\mathbf{x}_0\|^2_\Gamma}{\partial \theta} \ , \\ \frac{\partial J(u,\Gamma)}{\partial a} &= \frac{1}{ab}\sum_{\mathbf{x}} u[\mathbf{x}] w'_\epsilon\left(\|\mathbf{x}-\mathbf{x}_0\|^2_\Gamma\right) \frac{\partial \|\mathbf{x}-\mathbf{x}_0\|^2_\Gamma}{\partial a} - \frac{J(u,\Gamma)}{a} \ , \\ \frac{\partial J(u,\Gamma)}{\partial b} &= \frac{1}{ab}\sum_{\mathbf{x}} u[\mathbf{x}] w'_\epsilon\left(\|\mathbf{x}-\mathbf{x}_0\|^2_\Gamma\right) \frac{\partial \|\mathbf{x}-\mathbf{x}_0\|^2_\Gamma}{\partial b} - \frac{J(u,\Gamma)}{b} \ , \end{cases} \tag{2.17}$$

$$\text{where} \quad w'_\epsilon(t) = \frac{4S_\epsilon(2t)\left(1-S_\epsilon(2t)\right) - S_\epsilon(t)\left(1-S_\epsilon(t)\right)}{\epsilon}$$

$$= \frac{1}{\epsilon}\left[\frac{4e^{\frac{2t-1}{\epsilon}}}{\left(1+e^{\frac{2t-1}{\epsilon}}\right)^2} - \frac{e^{\frac{t-1}{\epsilon}}}{\left(1+e^{\frac{t-1}{\epsilon}}\right)^2}\right] \ ,$$

and the calculation of partial derivatives of $\|\mathbf{x}-\mathbf{x}_0\|^2_\Gamma$ are detailed in the Appendix 2.C. As depicted in Fig. 2.8c, for a given parametrization $\{\mathbf{x}_0, a, b, \theta\}$, the term $w'_\epsilon\left(\|\mathbf{x}-\mathbf{x}_0\|^2_\Gamma\right)$ vanishes for most of points $\mathbf{x}$. Thus, the computation of the partial derivatives $J(u,\Gamma)$ takes account only few points near the ellipse boundaries where $w'_\epsilon\left(\|.-\mathbf{x}_0\|^2_\Gamma\right)$ is non-zero. Our smooth approximation which is adapted for discrete images produces similar expressions of the partial derivatives of the ellipse energy when comparing with those described in [Pediredla and Seelamantula 2012] for continuous images. It can be viewed as the expression of the Green's theorem in the discrete setting and an alternative to the optimization presented in [Grenander and Miller 1994].

2.2.2.3 Multi-ellipse segmentation for multi-tissue core analysis

Let $\{\mathbf{c}_n\}_{1\leq n\leq N}$ be the centroids of the connected components of the binary detection map I_{FA}. In the original image u, we extract a rectangular patch P_n centered at $\mathbf{c}_n$ with a radius ρ larger than the given tissue core radius r_{core} (for example, $\rho = 2r_{core}$). Let us define

$$\Pi_{\rho,\mathbf{c}_n} u = \{u[\mathbf{x}],\ \|\mathbf{x}-\mathbf{c}_n\|_\infty \leq \rho\}\,, \tag{2.18}$$

where $\mathbf{x} = (x, y) \in P_n$, $\|\mathbf{x}\|_\infty = \sup(|x|, |y|)$ and $\Pi_{\rho,\mathbf{c}_n}\cdot$ denotes the patch extraction operator with center $\mathbf{c}_n$ and radius ρ. In order to perform a multi-object segmentation, we consider the following multi-ellipse optimization problem:

$$\begin{aligned} &\underset{\Gamma_1,\ldots,\Gamma_N}{\arg\min}\ \sum_{n=1}^{N}\left\{\frac{1}{a_n b_n}\sum_{\mathbf{x}} w_\epsilon\Big(\|\mathbf{x}-\mathbf{x}_0^n\|^2_{\Gamma_n}\Big)\Pi_{\rho,\mathbf{c}_n}u[\mathbf{x}]\right\} \\ &\text{subject to } (\Gamma_1,\Gamma_2,\ldots,\Gamma_N)\in\Upsilon\ , \end{aligned} \tag{2.19}$$

where $\{\mathbf{x}_{0,n}, a_n, b_n, \theta_n\}$ are the parameters of the ellipse Γ_n and Υ is a set of constraints to ensure the ellipses fall into an acceptable range of configurations. In practice, we typically set

$$\begin{aligned} \Upsilon = \big\{\ &\|\mathbf{x}_{0,n}-\mathbf{x}_{0,n'}\|_2 > \rho;\quad \|\mathbf{x}_{0,n}-\mathbf{c}_n\|_\infty \leq \rho_{\max}; \\ &r_{\min}\leq a_n, b_n \leq r_{\max};\quad \theta_{\min}\leq\theta_n\leq\theta_{\max}\ \big\}_{1\leq n,n'\leq N}\ , \end{aligned}$$

for some predefined values $\rho_{\max}, r_{\min}, r_{\max}, \theta_{\min}, \theta_{\max}$ set according to the extracted patch positions and the allowed sizes and orientations of tissue cores. The constraint $\|\mathbf{x}_{0,n}-\mathbf{x}_{0,n'}\|_2 > \rho$ which prevents the distance between two ellipse centers being too close helps to avoid the overlapping of segmented tissue cores. In what follows, we denote $\mathcal{J}(u,\Gamma_1,\ldots,\Gamma_n)$ the global cost function associated with the optimization problem (2.19).

By construction, the function $\mathcal{J}(u,\Gamma_1,\ldots,\Gamma_n)$ is differentiable with respect to $(\Gamma_1,\ldots,\Gamma_N)$. The common way to minimize $\mathcal{J}(u,\Gamma_1,\ldots,\Gamma_n)$ under the constraint set Υ is to use a gradient method whose performance depends on how efficient is the computation of the gradient of $\mathcal{J}(u,\Gamma_1,\ldots,\Gamma_n)$. Since $\mathcal{J}(u,\Gamma_1,\ldots,\Gamma_n)$ is a linear combination of separable functions, therefore, the gradient can be simply obtained as:

$$\nabla\mathcal{J}(u,\Gamma_1,\ldots,\Gamma_n) = \begin{pmatrix} \nabla J(\Pi_{\rho,\mathbf{c}_1}u,\Gamma_1) \\ \vdots \\ \nabla J(\Pi_{\rho,\mathbf{c}_N}u,\Gamma_N) \end{pmatrix}, \tag{2.20}$$

where

$$J(\Pi_{\rho,\mathbf{c}_n}u,\Gamma_n) = \frac{1}{a_n b_n}\sum_{\mathbf{x}\in\Gamma_n} w_\epsilon\left(\|\mathbf{x}-\mathbf{x}_0^n\|^2_{\Gamma_n}\right)\Pi_{\rho,\mathbf{c}_n}u[\mathbf{x}]$$

and the expressions of its partial derivatives are given in (2.17).

The result of the multi-ellipse optimization problem (2.19) is a set of ellipses $\{\Gamma_n\}_{1\leq n\leq N}$ which fits the objects located in the regions of interest $\{\Pi_{\rho,\mathbf{c}_n}u\}_{1\leq n\leq N}$. Furthermore, given the major axes of these ellipses and the TMA core radius r_{core}, we discard the tiny, giant and flattened ellipses and we keep those which are most

similar to the expected tissue cores. The center of the selected ellipse allows us to determine the position of the recognized TMA core. This reference position will be used to determine the array coordinates of the corresponding tissue core. In the following, we denote $\mathcal{X}_0 = \{\mathbf{x}_{0,n}\}_{n\in\{1,\ldots,N\}}$ as the set of centers of the N reliable and selected ellipses.

2.2.3 Estimation of array coordinate and TMA core positions

An ideal TMA is the one which has tissue cores perfectly aligned in both horizontal and vertical directions and equally spaced according to a regular square grid. The array coordinate $\mathbf{p} = (k, l) \in \mathbb{Z}^2$ of a core can be simply obtained by drawing two orthogonal lines crossed at the considered core position. However, due to the deformation of the design TMA grid, the lines passing through tissue cores and their nearest neighbors may be slightly inclined with respect to the horizontal or vertical axes. Moreover, the direction of these lines may have a large spectrum of variations which makes more challenging the tracking of tissue cores over a given direction. To deal with this deformation, existing TMA de-arraying methods use usually distance-and-angle-based criteria for the purpose of defining the neighborhood of TMA cores. Although this approach estimates robustly the average core-to-core distance and the two principal directions of the deformed core grid, it may fail for some well-detected cores whose the position is strongly distorted with respect to their neighbors. In order to avoid this failure, we introduce an algorithm for estimating iteratively the deformation of the TMA grid in a way that the grid which is warped by the estimated deformation at an iteration gets closer to the observed TMA grid. To this end, we assume that the deformation of the TMA grid can be decomposed by linear and non-linear parts. Under this assumption, we estimate the linear part of the deformation by defining an oblique grid (affine warping) which is derived from the detected core positions as the initialization of the warped grid (see Fig. 2.9). The latter is used to find nearby cores that will be taken into account to compute an estimator of the grid deformation by using the thin-plate interpolation [Bookstein 1989] if we do an analogy with material deformation.

2.2.3.1 Estimation of the linear deformation

Our goal is to approximate the distorted TMA grid Λ (which is observed partially with the set of point $\mathcal{X}_0$) by an oblique grid Λ_0 which minimizes the distance between them in the way that the deformation of the grid is approximated by a 2D affine transform. For this purpose, we consider the set $\mathcal{C}_0$ of core pairs whose each pair $(\mathbf{x}_{0,n}, \mathbf{x}_{0,n'})$ is formed by an element of $\mathcal{X}_0$ and one of its four nearest neighbors with respect to the Euclidean distance

$$\mathcal{C}_0 = \{(\mathbf{x}_{0,n}, \mathbf{x}_{0,n'}) \in \mathcal{X}_0 \times \mathcal{X}_0,\, \mathbf{x}_{0,n'} \in \mathcal{N}(\mathbf{x}_{0,n})\}\,,$$

where $\mathcal{N}(\mathbf{x}_{0,n})$ denotes the 4-neighborhood of $\mathbf{x}_{0,n}$. To estimate the average core-to-core distance $\bar{d}_{cc}$, we compute the trimmed mean (denoted TM) of the length of the segment defined by the pair $(\mathbf{x}_{0,n}, \mathbf{x}_{0,n'})$ of $\mathcal{C}_0$ by discarding the most extreme values (typically 30%):

$$\bar{d} = \mathrm{TM}_{30\%}\left\{\|\mathbf{x}_{0,n} - \mathbf{x}_{0,n'}\|_2\right\}_{(\mathbf{x}_{0,n},\mathbf{x}_{0,n'})\in\mathcal{C}_0}\,. \tag{2.21}$$

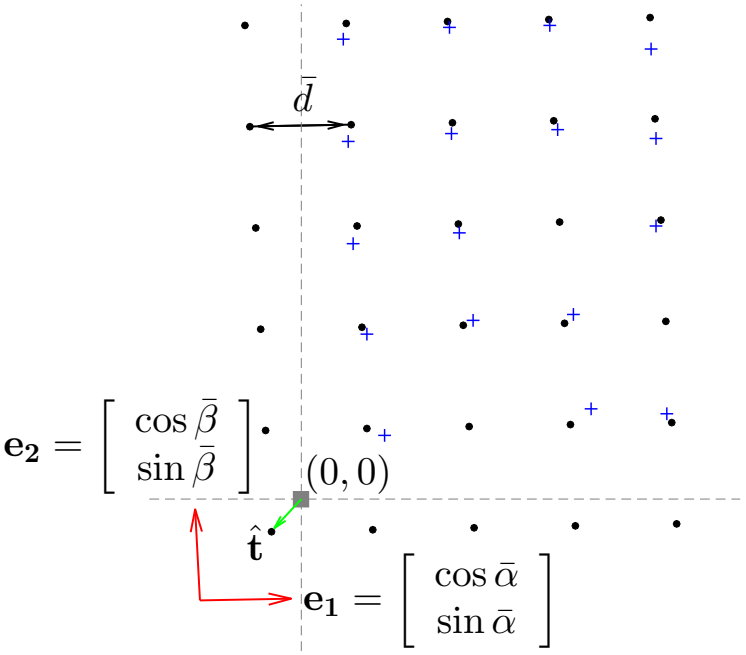

Figure 2.9: **Affine approximation of the grid deformation.** The distorted grid Λ which one only observe partially the set of point $\mathcal{X}_0 \subset \Lambda$ (shown in blue crosses) is approximated by the oblique (regular) grid Λ_0 (black circled dots). The latter is characterized by the average distance $\bar{d}$ between its points, two principal directions which are presented by two vectors $(\mathbf{e_1}, \mathbf{e_2})$ (red arrows), and the global translation $\hat{\mathbf{t}}$ (green arrow) of the grid with respect to the origin $(0,0)$ (gray square dot).

Let $\text{ang}(\mathbf{x}_{0,n}, \mathbf{x}_{0,n'})$ be the angle between the line passing through $(\mathbf{x}_{0,n}, \mathbf{x}_{0,n'})$ and the horizontal axis such that $-0.25\pi \leq \text{ang}(\mathbf{x}_{0,n}, \mathbf{x}_{0,n'}) \leq 0.75\pi$. By analogy, we define the two principal angles of the deformed TMA grid as follows:

$$\bar{\alpha} = \text{TM}_{30\%} \left\{ \text{ang}(\mathbf{x}_{0,n}, \mathbf{x}_{0,n'}) \leq \frac{\pi}{4} \right\},$$
$$\bar{\beta} = \text{TM}_{30\%} \left\{ \text{ang}(\mathbf{x}_{0,n}, \mathbf{x}_{0,n'}) \geq \frac{\pi}{4} \right\}.$$

Finally, we denote $\hat{\mathbf{t}}$ as the global translation of the distorted TMA grid with respect to the origin that minimizes the distance between the set $\mathcal{X}_0$ and the linearly-estimated grid Λ_0

$$\hat{\mathbf{t}} = \arg\min_{\mathbf{t}} \sum_{n=1}^{N} \min_{\mathbf{p} \in \mathbb{Z}^2} \|\mathbf{t} + \mathcal{F}(\mathbf{p}) - \mathbf{x}_{0,n}\|_2^2 \tag{2.22}$$

where $\mathcal{F}$ maps each array coordinates $\mathbf{p} \in \mathbb{Z}^2$ to a position of Λ_0 corrected by $\hat{\mathbf{t}}$ and

$$\mathcal{F}(\mathbf{p}) = \bar{d} \underbrace{\begin{bmatrix} \cos\bar{\alpha} & \cos\bar{\beta} \\ \sin\bar{\alpha} & \sin\bar{\beta} \end{bmatrix}}_{\mathbf{M}_{\bar{\alpha},\bar{\beta}}} \mathbf{p} \,. \tag{2.23}$$

Note that $\mathbf{M}_{\bar{\alpha},\bar{\beta}}$ is a change-of-basis matrix of unit column vectors and $\bar{d}$ is a scaling factor which transforms array coordinates (elements of $\mathbb{Z}^2$) to real spatial positions

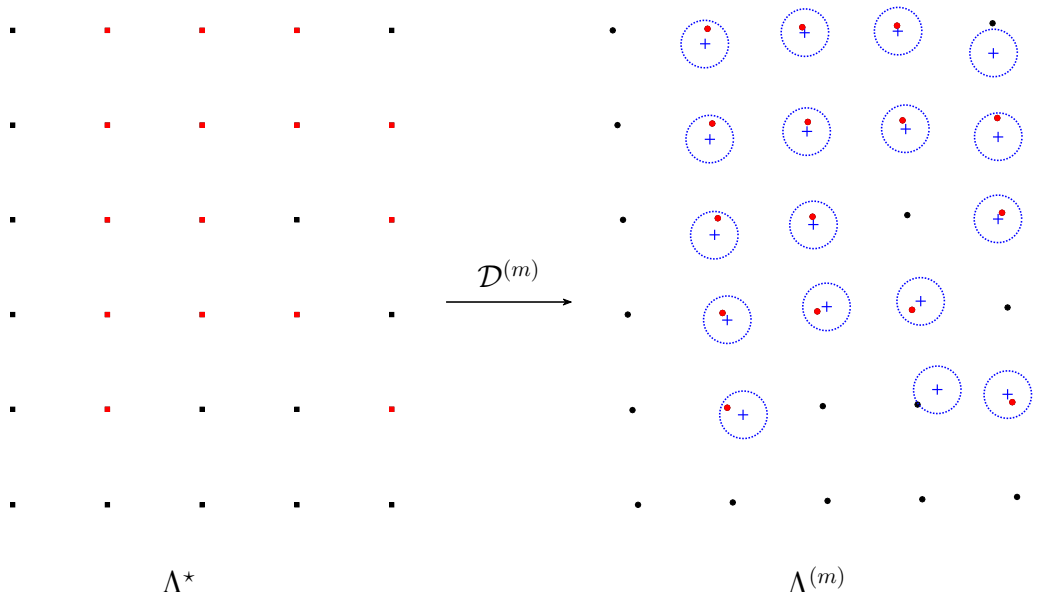

Figure 2.10: **Correspondence between the ideal grid and the observed distorted grid.** At an iteration m, the estimated deformation $\mathcal{D}^{(m)}$ maps each point $\mathbf{y}_\mathbf{p}^\star$ of the ideal square grid $\Lambda^\star$ (shown in square dots on the left) onto a point $\mathbf{y}_\mathbf{p}^{(m)} = \mathcal{D}^{(m)}(\mathbf{y}_\mathbf{p}^{(m)})$ in the warped grid $\Lambda^{(m)}$ (circled dots on the right) which manages to fit the observed set of points $\mathcal{X}_0$ (blue crosses). A position $\mathbf{x}_{0,n} \in \mathcal{X}_0$ is associated to a position $\mathbf{y}_\mathbf{p}^\star$ if $\mathbf{x}_{0,n}$ is located within a radius δ from $\mathbf{y}_\mathbf{p}^{(m)}$ (blue dotted circles). Associated positions are marked in red.

(in $\Omega \subset \mathbb{R}^2$). The resulting oblique grid is parametrized with four parameters $\{\bar{d}, \bar{\alpha}, \bar{\beta}, \hat{t}\}$ and represents the affine part of the grid deformation. We thus arrive at the affine mapping function: $\mathcal{A}(\mathbf{p}) = \hat{\mathbf{t}} + \mathcal{F}(\mathbf{p}) \in \Lambda_0$. The oblique grid Λ_0 will serve as initialization to estimate of the non-linear deformation of the grid. Figure 2.9 illustrates an example showing the oblique grid obtained from a given set of points as well as its estimated parameters.

2.2.3.2 Thin-plate-based estimation of the deformation

Let $\Lambda^\star$ be the ideal design TMA grid with $(0, 0)$ as origin and d the ideal distance between two neighboring cores along the horizontal and vertical axes. The mapping is then defined as:

$$\mathbf{y}_\mathbf{p}^\star = d\mathbf{p} \in \Lambda^\star, \forall \mathbf{p} \in \mathbb{Z}^2.$$

The deformation $\mathcal{D}$ maps each point $\mathbf{y}_\mathbf{p}^\star \in \Lambda^\star$ onto a point $\mathbf{y}_\mathbf{p} = \mathcal{D}(\mathbf{y}_\mathbf{p}^\star)$ in the distorted grid Λ. In order to estimate the deformation $\mathcal{D}$ at all points of the grid $\Lambda^\star$, we aim at approximating this set from the observed set $\mathcal{X}_0 = \{\mathbf{x}_{0,n}\}$ by using the thin-plate splines as an interpolant. Indeed, given a set of points $\mathcal{D}^{-1}\mathcal{X}_0 = \{\mathcal{D}^{-1}(\mathbf{x}_{0,n})\}_{n\in\{1,\dots,N\}}$, the coefficients of the interpolating thin-plate splines are the minimizers of a quadratic function which is the first approximation of the bending energy of the mapping from $\mathcal{D}^{-1}\mathcal{X}_0$ to the set of target points $\mathcal{X}_0$ (see [Bookstein 1989]). Nevertheless, unlike the usual framework [Bookstein 1989], the correspondence between the two sets of points is not established, that is $\mathcal{D}^{-1}\mathcal{X}_0$ is unknown. Instead of investigating a matching method to determine $\mathcal{D}^{-1}\mathcal{X}_0$, we pro-

pose to build a sequence of grids $\{\Lambda^{(m)}\}_{m\geq 0}$ which evolves iteratively to fit $\mathcal{X}_0$. We initialize this sequence with the oblique grid $\Lambda^{(0)} = \Lambda_0$ previously computed. The linear approximation of $\mathcal{D}$ is then as follows:

$$\begin{aligned} \mathbf{y}_{\mathbf{p}}^{(0)} &= \mathcal{D}^{(0)}(\mathbf{y}_{\mathbf{p}}^{\star}) \\ &= \hat{\mathbf{t}} + \frac{\bar{d}}{d}\begin{bmatrix}\cos\bar{\alpha} & \cos\bar{\beta} \\ \sin\bar{\alpha} & \sin\bar{\beta}\end{bmatrix}\mathbf{p}. \end{aligned} \tag{2.24}$$

At iteration m, a core position $\mathbf{x}_{0,n} \in \mathcal{X}_0$ is associated to a position $\mathbf{y}_{\mathbf{p}}^{\star}$ if the former is located within a radius δ from $\mathbf{y}_{\mathbf{p}}^{(m)} = \mathcal{D}^{(m)}(\mathbf{y}_{\mathbf{p}}^{\star})$. Pairs of associated positions establish therefore the correspondence between the ideal grid $\Lambda^{\star}$ and the set of observed point $\mathcal{X}_0$. We also note that all the positions of $\Lambda^{\star}$ do not have a corresponding position in $\mathcal{X}_0$ as shown in Fig. 2.10 mainly because the cardinality of sets are not the same. Let $\mathcal{P}^{(m)}$ be the set of pairs of associated positions:

$$\mathcal{P}^{(m)} = \left\{ \left(\mathbf{x}_{0,n}, \mathbf{y}_{\mathbf{p}}^{\star}\right),\ \|\mathcal{D}^{(m)}(\mathbf{y}_{\mathbf{p}}^{\star}) - \mathbf{x}_{0,n}\|_2 \leq \delta \right\}. \tag{2.25}$$

Assume that $N^{(m)}$ is the number of elements of $\mathcal{P}^{(m)}$. The objective is to estimate the deformation $\mathcal{D}^{(m)}$ from the set of $N^{(m)}$ associated pairs $(\mathbf{x}_{0,n}, \mathbf{y}_{\mathbf{p}}^{\star})$. According to [Bookstein 1989], we define the Gram's matrix $\left\{\mathbf{K}_{n,n'}^{(m)}\right\}_{1\leq n,n'\leq N^{(m)}}$ as follows:

$$\mathbf{K}_{n,n'}^{(m)} = \|\mathbf{x}_{0,n} - \mathbf{x}_{0,n'}\|_2^2 \log \|\mathbf{x}_{0,n} - \mathbf{x}_{0,n'}\|_2^2, \tag{2.26}$$

and the additional matrices as:

$$\mathbf{Y}^{(m)} = \begin{bmatrix} 1 & 1 & \dots & 1 \\ \mathbf{y}_{\mathbf{p}_1} & \mathbf{y}_{\mathbf{p}_2} & \cdots & \mathbf{y}_{\mathbf{p}_{N^{(m)}}} \end{bmatrix}, \tag{2.27}$$

$$\mathbf{L}^{(m)} = \left[\begin{array}{c|c} \mathbf{K}^{(m)} & \mathbf{Y}^{(m)} \\ \hline {\mathbf{Y}^{(m)}}^{\top} & 0 \end{array}\right], \tag{2.28}$$

$$\mathbf{X}^{(m)} = \begin{bmatrix} \mathbf{x}_{0,1} & \mathbf{x}_{0,2} & \dots & \mathbf{x}_{0,N^{(m)}} & 0 & 0 & 0 \end{bmatrix}, \tag{2.29}$$

$$\mathbf{W}^{(m)} = \left(\left(\mathbf{L}^{(m)}\right)^{-1}\left(\mathbf{X}^{(m)}\right)^{\top}\right)^{\top}, \tag{2.30}$$

with $\mathbf{W}^{(m)} = (\mathbf{w}_1^{(m)}, \mathbf{w}_2^{(m)}, \dots, \mathbf{w}_{N^{(m)}}^{(m)})^{\top}$. By using the entries of the matrix $\mathbf{W}^{(m)}$, the estimator of the deformation $\mathcal{D}$ and of the grid Λ at the next iteration $m+1$ are therefore defined as:

$$\mathbf{y}_{\mathbf{p}}^{(m+1)} = \mathbf{w}_{N^{(m)}+1}^{(m)} + \left[\mathbf{w}_{N^{(m)}+2}^{(m)} \,\middle|\, \mathbf{w}_{N^{(m)}+3}^{(m)}\right]\mathbf{y}_{\mathbf{p}}^{\star} + \sum_{n=1}^{N^{(m)}} \mathbf{w}_n^{(m)}(\|\mathbf{x}_{0,n} - \mathbf{y}_{\mathbf{p}}^{\star}\|_2^2 \log \|\mathbf{x}_{0,n} - \mathbf{y}_{\mathbf{p}}^{\star}\|_2^2). \tag{2.31}$$

This iterative scheme will be stopped at the iteration $m^* = m$ if there are no change between $\Lambda^{(m)}$ and $\Lambda^{(m+1)}$. At convergence, the row and column coordinates of a detected cores of position $\mathbf{x}_{0,n} \in \mathcal{X}_0$ is simply given by:

$$\hat{\mathbf{p}} = \underset{\mathbf{p}\in\mathbb{Z}^2}{\arg\min} \|\mathbf{x}_{0,n} - \mathcal{D}^{(m^*)}(\mathbf{y}_{\mathbf{p}}^{\star})\|_2^2. \tag{2.32}$$

Moreover, since the grid $\Lambda^{(m^*)}$ is an estimator of the deformed TMA grid Λ which is partially observed in $\mathcal{X}_0$, it can be used as approximated positions to recognize tissue cores which are missed during detection and segmentation processes. Indeed, to refine de-arraying result, we perform another multi-ellipse optimization at the position of remaining nodes of the grid $\Lambda^{(m^*)}$. If there are ellipses that meet the size and the roundness criteria of standard cores, we add them to the list of detected core position and adjust the coefficients of the thin-plate splines according to the new list. An example of TMA de-arraying is depicted in Fig. 2.14 showing the gain of our method in term of tissue core detection.

2.3 Results and discussion

2.3.1 Description of datasets

To evaluate our de-arraying ATMAD approach, we selected a number of DNA microarray and tissue microarray images including those which are artificially simulated and those which are acquired in both bright field and fluorescence modes. The selected images were collected from various sources and can be classified into three data sets.

The first set is a collection of binary images generated by Wang et al. (2011) as pseudo TMA slides. This data set was artificially created by taking account of different possible situations occurring during the TMA manufacturing process, including rotations and stretches of the design grid as well as irregularities in the size and the shape of tissue cores. The average core radius is approximately $r_{core} = 15$ pixels for all images. The whole set of all these simulated images and ground truths can be freely downloaded at `https://get.google.com/albumarchive/117531880452844036890`.

The second data set is composed of color TMA images from the AIDS and Cancer Specimen Resource (ACSR) Digital Library of the University of California San Francisco (`http://acsr.ucsf.edu`). This online library – managed and visualized by Aperio's WebScope software – contains several hundreds of tissue specimens which are mostly stained with H&E (Hematoxylin and Eosin) stain and are imaged by bright field microscopy technique. For this experiment, we considered downsampled version (with the magnification between 0.4X and 0.6X) of the original images hosted on ACSR's server in order to reduce the processing time. The considered resolutions correspond to images of approximately 1000×1000 pixels, on which the TMA cores have radius of only a few dozen pixels but it is sufficient for our approach to localize them.

The third set for the evaluation includes fluorescence high-dynamic-range (HDR) images showing DNA microarray and tissue microarray slides. Provided by the courtesy of Innopsys company, these HDR images which were saved in 16-bit-TIFF format were acquired using a scanner called InnoScan 1100 AL[2]. The latter which is equipped with three excitation lasers (488 nm, 532 nm and 625 nm compatible with

[2] see `https://www.innopsys.com/en/lifesciences-products/microarrays/innoscan/innoscan-1100-al` for more details.

cyanine dyes such as Cy2, Cy3 and Cy5 respectively). It can perform simultaneously the acquisition on each excitation channel and provides up to three color fluorescence images. The maximal scan area supported by the mentioned device is 22×74 mm^2 corresponding to the size of typical microscopy slides used in most biological laboratories nowadays. For the same reason with ACSR's images, we selected typical images acquired by this Innopsys's scanner with spatial resolutions varying in a range from 10 to 40 μm per pixel in this experiment instead of using those with higher resolution (up to 0.5 μm per pixel or a 20X magnification equivalently). Indeed, considering such images of low resolution and small size as input data not only enables efficient and low-memory-requirement processing but also requires very short scanning time – less than just five minutes with a resolution of 10 μm per pixel when compared with typically several hours of acquisition at sub-micrometer resolutions.

Regarding the complexity of the datasets, it contains difficult cases such as irregular and non-rounded shapes, fragmented cores as well as low contrasts between image background and foreground. Sophisticated array design with incomplete (missing cores) rows and columns is also present in the image set for the purpose of testing the robustness of our de-arraying approach (see Figs. 2.11-2.14).

2.3.2 Experimental results and algorithm evaluation

For the first and second data sets which contain images with dark spots and bright background, we performed first a color inversion before further processing. The de-arraying procedure was directly applied on binary and grayscale images. Multi-channel color images as in the case of ACSR's data require a conversion to grayscale such as a simple average over all channels which we used in these experiments.

In order to evaluate the performance of our ATMAD algorithm, we analyzed the obtained results by considering two criteria: (i) the rate of samples which are successfully localized and (ii) the rate of samples whose array coordinates are correctly estimated. To that end, the de-arraying ATMAD outcome was compared with the ground-truth provided by the simulated dataset or by manual annotation of real-world TMA images. The comparative similarity between the de-arraying results and ground-truths (simulation, annotation) is quantitatively measured by these six following metrics:

- Accuracy: $\mathrm{A} = \dfrac{\mathrm{TP}+\mathrm{TN}}{\mathrm{TP}+\mathrm{TN}+\mathrm{FP}+\mathrm{FN}}$,
- Precision: $\mathrm{P} = \dfrac{\mathrm{TP}}{\mathrm{TP}+\mathrm{FP}}$,
- Recall (sensitivity): $\mathrm{R} = \dfrac{\mathrm{TP}}{\mathrm{TP}+\mathrm{FN}}$,
- F-score: $\mathrm{F} = 2\dfrac{\mathrm{P}\,\mathrm{R}}{\mathrm{P}+\mathrm{R}}$,

	Ellipse-based segmentation	Non-linear registration
Option 1	–	–
Option 2	★	–
Option 3	–	★
Option 4	★	★

Table 2.1: Workflow options corresponding to the selection (activation/deactivation) of ellipse-based segmentation and non-linear registration modules.

- G-score: $\mathrm{G} = \sqrt{\mathrm{P}\,\mathrm{R}}$,
- Jaccard coefficient: $\mathrm{JSC} = \dfrac{\mathrm{TP}}{\mathrm{TP} + \mathrm{FP} + \mathrm{FN}}$.

"True Positive" (TP) denotes the number of true tissue samples (cores) which are correctly localized, or those whose array coordinates are correctly estimated. "False Negative" (FN) denotes the number of true cores which are not successfully localized (due to non detection or failed segmentation), or those whose array coordinates are not estimated. "False Positive" (FP) denotes the number of cores which are wrongly localized (due to false detection), or those whose array coordinates are wrongly estimated. "True Negative" (TN) denotes the number of "empty" spot positions (no core is placed) where no core is wrongly localized.

To better appreciate the impact of the components (or modules) of our de-arraying approach, the performance was evaluated under four different setting options (see also Table 2.1):

Option 1: deactivation of ellipse-based segmentation and non-linear registration modules,
Option 2: activation of ellipse-based segmentation module and deactivation of non-linear registration module,
Option 3: deactivation of ellipse-based segmentation module and activation of non-linear registration module,
Option 4: activation of ellipse-based segmentation and non-linear registration modules.

When the ellipse-based segmentation module is deactivated, the spot localization is performed only with the wavelet-based detection method. Consequently, the process of removal of unreliable detected cores based on the size and the shape criteria is then disable, and the refinement of de-arraying result using estimated positions of the deformed TMA grid can not be performed. Meanwhile, the deactivation of the non-linear registration module implies that the grid deformation is assumed to be approximated by an affine (linear) transform. It could result in a non-coincidence between core positions and estimated positions of the deformed grid for most of cores. A distance-based matching is thus necessary to establish the correspondence of each core position and its array coordinates. To allow a step-by-step evaluation of the performance, besides the final de-arraying result, intermediary results of the

		Localization						Estimation of array coordinates					
		A[a]	P[b]	R[c]	F[d]	G[e]	JSC[f]	A[a]	P[b]	R[c]	F[d]	G[e]	JSC[f]
Simulated													
Average on 31 images													
	Wang *et al.* Wang et al. (2011)	1	1	1	1	1	1	1	1	1	1	1	1
	ATMAD Opt. 1	1	1	1	1	1	1	0.93	1	0.93	0.96	0.96	0.93
	Opt. 2	0.95	1	0.95	0.98	0.98	0.95	0.85	1	0.84	0.91	0.91	0.84
	Opt. 3	1	1	1	1	1	1	1	1	1	1	1	1
	Opt. 4	0.95	1	0.95	0.98	0.98	0.95	0.95	1	0.95	0.98	0.98	0.95
Fig. 2.11a													
	ATMAD Opt. 1	1	1	1	1	1	1	1	1	1	1	1	1
	Opt. 2	0.97	1	0.96	0.98	0.98	0.96	0.97	1	0.96	0.98	0.98	0.96
	Opt. 3	1	1	1	1	1	1	1	1	1	1	1	1
	Opt. 4	0.97	1	0.96	0.98	0.98	0.96	0.97	1	0.96	0.98	0.98	0.96
Fig. 2.11b													
	ATMAD Opt. 1	1	1	1	1	1	1	0.93	1	0.92	0.96	0.96	0.92
	Opt. 2	0.93	1	0.92	0.96	0.96	0.92	0.90	1	0.89	0.94	0.95	0.89
	Opt. 3	1	1	1	1	1	1	1	1	1	1	1	1
	Opt. 4	0.93	1	0.92	0.96	0.96	0.92	0.93	1	0.92	0.96	0.96	0.92
Brightfield													
Average on 8 images													
	ATMAD Opt. 1	0.94	1	0.93	0.96	0.96	0.93	0.91	1	0.88	0.94	0.94	0.88
	Opt. 2	0.87	1	0.83	0.91	0.91	0.83	0.84	1	0.79	0.88	0.89	0.79
	Opt. 3	0.94	1	0.93	0.96	0.96	0.93	0.94	1	0.93	0.96	0.96	0.93
	Opt. 4	0.87	1	0.83	0.91	0.91	0.83	0.93	1	0.91	0.95	0.95	0.91
Fig. 2.12													
	ATMAD Opt. 1	0.96	1	0.94	0.97	0.97	0.94	0.91	1	0.89	0.94	0.94	0.89
	Opt. 2	0.87	1	0.83	0.91	0.91	0.83	0.84	1	0.80	0.89	0.89	0.80
	Opt. 3	0.96	1	0.94	0.97	0.97	0.94	0.96	1	0.94	0.97	0.97	0.94
	Opt. 4	0.87	1	0.83	0.91	0.91	0.83	0.93	1	0.91	0.95	0.95	0.91
Fluorescence													
Average on 8 DNA microarray images													
	ATMAD Opt. 1	1	1	1	1	1	1	1	1	1	1	1	1
	Opt. 2	1	1	1	1	1	1	1	1	1	1	1	1
	Opt. 3	1	1	1	1	1	1	1	1	1	1	1	1
	Opt. 4	1	1	1	1	1	1	1	1	1	1	1	1
Fig. 2.13													
	ATMAD Opt. 1	1	1	1	1	1	1	1	1	1	1	1	1
	Opt. 2	1	1	1	1	1	1	1	1	1	1	1	1
	Opt. 3	1	1	1	1	1	1	1	1	1	1	1	1
	Opt. 4	1	1	1	1	1	1	1	1	1	1	1	1
Average on 4 TMA images													
	ATMAD Opt. 1	0.79	0.77	1	0.87	0.88	0.77	0.92	0.98	0.93	0.95	0.95	0.91
	Opt. 2	0.91	0.99	0.90	0.94	0.95	0.89	0.73	1	0.69	0.82	0.83	0.69
	Opt. 3	0.79	0.77	1	0.87	0.88	0.77	-	-	-	-	-	-
	Opt. 4	0.91	0.99	0.90	0.94	0.95	0.89	0.92	0.98	0.93	0.96	0.96	0.91
Fig. 2.14													
	ATMAD Opt. 1	0.88	0.86	1	0.93	0.93	0.86	0.94	1	0.94	0.97	0.97	0.94
	Opt. 2	0.86	1	0.84	0.91	0.92	0.84	0.80	1	0.77	0.87	0.88	0.77
	Opt. 3	0.88	0.86	1	0.93	0.93	0.86	0.97	1	0.97	0.98	0.98	0.97
	Opt. 4	0.86	1	0.84	0.91	0.92	0.84	1	1	1	1	1	1

Table 2.2: Performance of the proposed de-arraying method on three datasets under four setting options: (1) both the segmentation and the non-linear estimation (for the deformation) modules are deactivated, (2) the segmentation is activated but the non-linear estimation is deactivated, (3) the segmentation is deactivated and the non-linear estimation is activated, and (4) both of them are activated. All considered performance scores range from 0 (worst) to 1 (best) and measure the similarity between the de-arraying results and their corresponding ground-truth or manual annotation. Notations: [a] accuracy (A), [b] precision (P), [c] recall (R), [d] F-score (F), [e] G-score (G) and [f] Jaccard coefficient (JSC).

de-arraying procedure were also carefully analyzed.

For a comparative evaluation, we also provide de-arraying results on simulated images (which are generated using the deformation model described in [Wang et al. 2011]) obtained with the method of Wang et al. (2011) – the state-of-the-art method for TMA brightfield image de-arraying, and compare these results to those obtained with the proposed ATMAD method. Unfortunately, it was not possible to apply the method Wang et al. (2011) on real-world images since the software and code are not available. In Table 2.2, the average performance obtained on each dataset as well as on each example is shown in Figs. 2.11-2.14. We notice that, except the precision and recall scores which are not in agreement in certain cases, the Accuracy, F-score, G-score and Jaccard metrics yield consistent results about the effectiveness of the de-arraying method. Accordingly, we will focus on the F-score metric in the next sections for the sake of simplicity. The results with all the metrics are reported in Table 2.2.

2.3.3 Simulated images

We evaluated our ATMAD method applied to the Wang's dataset and we compared the results with those obtained with the method described in [Wang et al. 2011]. An example of de-arraying result with different levels of deformation is illustrated in Fig. 2.11. The top row shows the original images. The two middle rows show the de-arraying outcomes obtained with deactivation and activation of the segmentation respectively (the non-linear estimation for the deformation is activated in both cases). These two cases correspond to the setting option 3 and 4 respectively, as reported in Table 2.2. The recognized spot positions are marked by green boxes and correctly aligned in a array to facilitate localization and identification. The bottom row of Fig. 2.11 shows the ground-truth provided by the authors of the dataset.

As expected, in the case of simulated images when the background is constant, our method provided a perfect F-score = 1 (corresponding to an accuracy of 100%) in average with the Option 3 even if the localization of spots is only performed with the wavelet-based detection method. On the second row of Fig. 2.11 showing the de-arraying results obtained on two typical examples with the deactivation of the ellipse-based segmentation method, we notice that all the spots are successfully recognized and the array coordinates are correctly estimated. The results are similar to those obtained with the method of Wang et al. (2011) (for more details, see Table 2.2). Meanwhile, the de-arraying results obtained with the Option 4 achieved a slightly lower F-score F = 0.98 (corresponding to an accuracy of 95%) in average. This score is a direct consequence of the fact that all existing spots were not recognized by the spot localizer due to segmentation failure or elimination, as depicted in Figs. 2.11e and 2.11f in which too small, too large and too elongated spots were not taken into account in the final de-arraying result. This behavior is confirmed by a lower Recall value which measures the sensitivity of the method (R = 0.95 in average compared with the perfect score R = 1 obtained with the Option 3). Although, despite a smaller number of correct spot positions, the estimation of the array coordinate yielded exact results for successfully recognized spots (Precision value P = 1 in average) comparing with the ground-truth. In terms of deformation estimation,

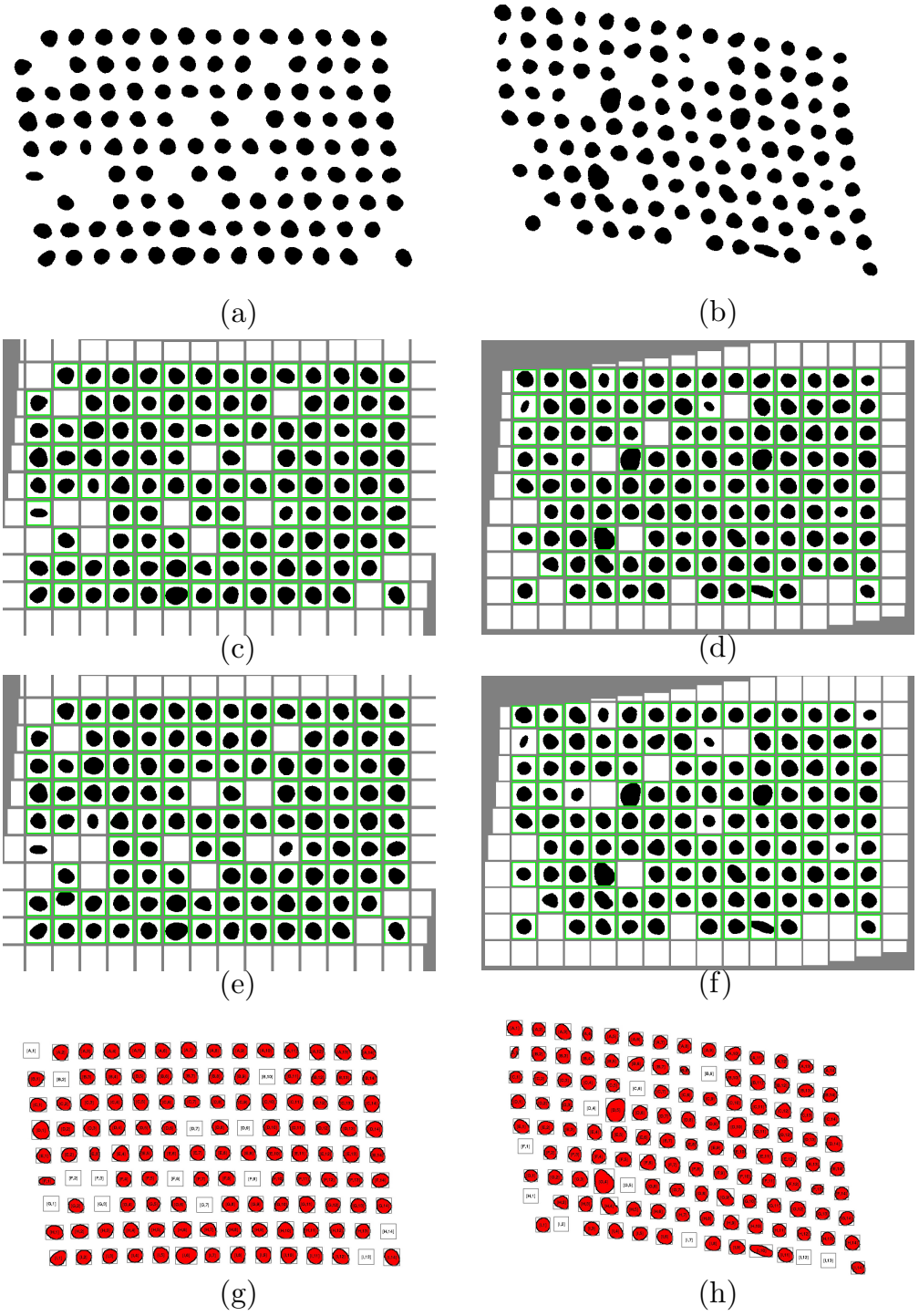

Figure 2.11: **Example of de-arraying on simulated images.** From left to right: TMAs with the grid deformation varying from low to high. From top to bottom: original images, de-arraying result by the proposed method with segmentation module deactivated/activated, ground truth given by Dr Jinhai Wang. The obtained de-arraying results are presented in array form with recognized spot positions marked by green boxes.

the estimated potential spot positions provided by the de-arraying with two setting options are almost identical. It thus allows us to localize spots which were not

recognized and demonstrates the robustness of our method for estimating the grid deformation.

Regarding the two remaining options (not illustrated in Fig. 2.11), when both the segmentation and non-linear estimation modules are deactivated (Option 1), ATMAD produced surprisingly decent de-arraying results with a F-score = 0.96 in average on this set of simulated images (see Table 2.2). This score which is slightly lower than those obtained with Option 4 is possibly contributed by the monotone and non-oscillating nature of the deformation model used to generate those test images, as described in [Wang et al. 2011] and illustrated in Figs. 2.11a and 2.11b. Meanwhile, the combination of the segmentation activated and the non-linear estimation deactivated (Option 2) yielded sharply inferior results. The F-score in average is barely 0.91 (corresponding to an accuracy level of 84%). It is mainly due to lower rate of correctly localized spots, implying less precise linear estimation for the deformation.

Moreover, we point out that when there is no false positive (i.e. FP = 0 implies P = 1), the Jaccard similarity coefficient (JSC) coincides with the Recall (R) value. This explains why we have obtained the same values for these two performance measures on this set of simulated images. We also observe similar behaviors in some cases on brightfield and fluorescence images when the method tends to eliminate all false detections during the localization step.

2.3.4 Bright field images

We have noticed that in the previous experiments with simulated data, our wavelet-based detection algorithm was able to localize all spots on images with constant background. In the case of brightfield TMA images whose background is not constant but generally homogeneous, this approach might still be efficient for spot localization since the situation is much more simpler than in fluorescence imaging. In this section, we focus on the evaluation of ATMAD applied to the ACRS dataset with the options 3 and 4 (see Table 2.1) to assess the impact of the ellipse-based segmentation algorithm. In Fig. 2.12, the de-arraying result with these two setting options on a H&E stained TMA image containing irregularities in the shape of tissue cores is illustrated. The original input image shown in Fig. 2.12a is the slide cut #9 of the TMA whose the ID is 550-T0011-01 on ACSR's database. The de-arraying results obtained with the option 3 and 4 are depicted in Fig. 2.12c and 2.12d respectively. To evaluate the accuracy of these results, we consider in Fig. 2.12b a reference de-arraying obtained by manual annotation. The latter is presented in the same format (*i.e.* an array representation) as those of the automated de-arraying outcomes to facilitate comparison.

Comparing with an accuracy of 100% obtained on simulated data, localization only based the wavelet method achieved in average approximately 94% of existing TMA cores on ACSR's data (corresponding to a F-score = 0.96 in average). Indeed, it failed generally to recognize cores with inner hole or cores which are split into parts (see Fig. 2.12c) since the shape of these cores implies that the wavelet coefficients at their position are lower than the detection threshold – resulting to non detection. Activating the segmentation module does not improve successful recognition rate

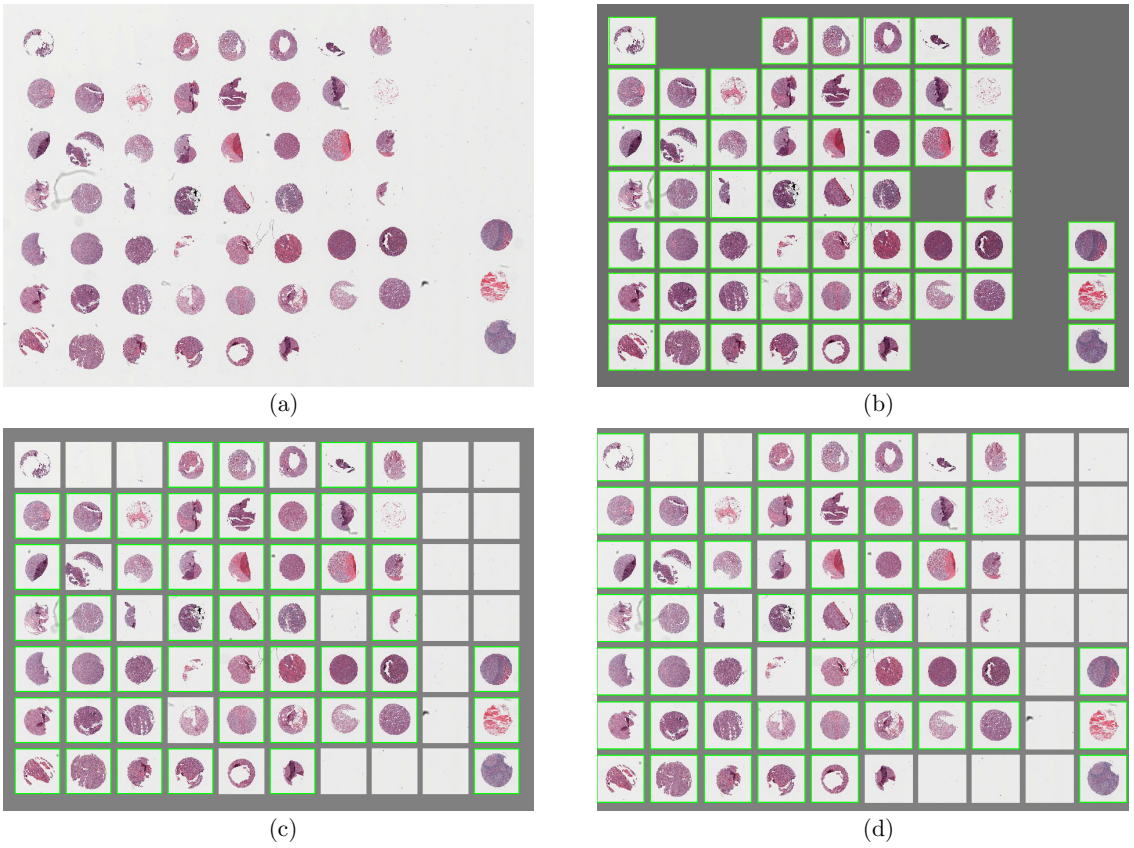

Figure 2.12: **Example of de-arraying on bright field TMA image.** (a) Original image : H&E stained TMA on ACSR's database with ID 550-T0011-01. (b) Manual annotation used for comparison with de-arraying results. (c)-(d) De-arraying results obtained with the deactivation/activation of the segmentation module (Option 3 and 4 respectively). These results and the manual annotation are represented in array format with recognized cores marked by green boxes.

of the localization step due to the use of detected core position for initializing the ellipse fitting. In our interest, the main role of this module in the localization step is to measure the size and the roundness of detected objects in order to eliminate false detection and to provide reliable input for the estimation of the grid deformation. For this reason, only about 87% of existing cores were correctly recognized during the localization step (corresponding to F-score = 0.91 in average) with the combination of the detection and the segmentation modules due to the segmentation failure and the elimination of outliers. In spite of the difference between the localization results obtained with the deactivation/activation of the segmentation module, the non-linear estimation of the grid deformation using these results however yielded similar de-arraying outcomes as illustrated in Fig. 2.12c and 2.12d. The overall accuracy of the de-arraying procedure with the activation of the ellipse-based segmentation module is approximately 93% (corresponding to F-score = 0.95 in average) compared to 87% (corresponding to F-score = 0.91 in average) if the module is activated (see Table 2.2). Under the latter setting options, the final recognition rate of tissue cores has increased by about 6% with respect to the rate obtained after the localization step. This improvement is due to the segmentation performed using the potential position which is provided by the estimation of the grid deformation to recognize

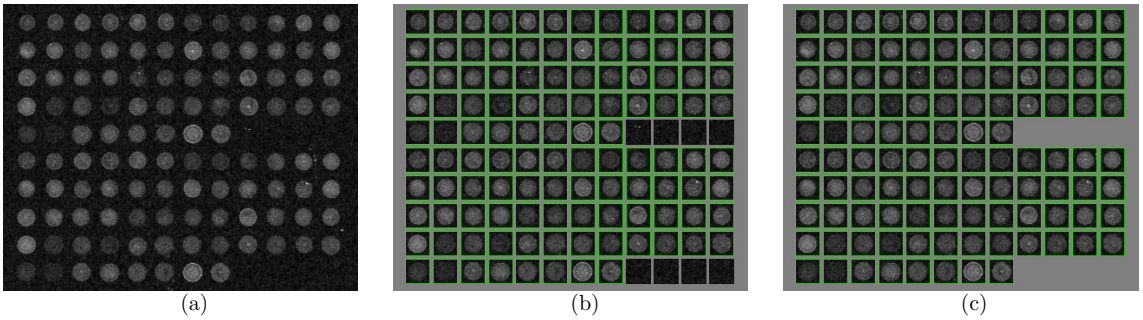

(a) (b) (c)

Figure 2.13: **Example of de-arraying on a fluorescence DNA microarray image with the deactivation of both the segmentation and of the non-linear estimation for the TMA grid deformation.** (a) Contrast-enhanced original image. (b) De-arraying result of the proposed method presented in array format. (c) Manual annotations in array format. For comparison purpose, recognized DNA spots are marked by green boxes.

missed cores during the first step of the de-arraying procedure (for example, some fragmented cores or cores with inner hole were additionally recognized as shown in Fig. 2.12d in comparison with Fig. 2.12c). This approach is useful, not only for brightfield images, but also in the case of fluorescence images, in which the contrast between the background and the foreground is often significantly weaker.

For the two remainder options (Options 1 and 2), ATMAD produced slightly inferior scores when compared to those obtained with the Options 3 and 4. It is due to the imprecise estimation of tissue core positions computed with affine registration of the grid. Quantitative similar results were observed in the case of simulated images as reported in Table 2.2.

2.3.5 Fluorescence images

In this section, we evaluated ATMAD on a more challenging image dataset which is acquired by fluorescence scanners and characterized by high noise level and non-homogeneous background. Unlike simulated and brightfield images depicting tissues, fluorescence images provided by Innopsys company, are composed of both DNA microarray and TMA images. Examples of DNA and TMA image de-arraying are respectively shown in Figs. 2.13 and 2.14. For the illustrated DNA microarray, we presented in Fig. 2.11 only the original image, the final de-arraying result and the corresponding manual annotations. Whereas, intermediate results were additionally illustrated in Fig. 2.12 besides the original image as well as the final result and the ground truth in the case of TMA image to allow step-by-step evaluation.

As expected, the proposed ATMAD method achieved 100% accuracy (corresponding to the perfect F-score = 1) in average on DNA microarray images under all four considered setting options (see Table 2.2 and Fig. 2.13). This perfect score was obtained due to the regularity of the size, the shape and the grid of spotted DNA samples which facilitates the localization and the estimation of the array coordinates of each spot.

It is however not possible to reach such performance scores on TMA images in most cases because of the deformation of TMA grid and the irregularities of TMA cores. Indeed, when the segmentation module is deactivated (Options 1 and 3), the

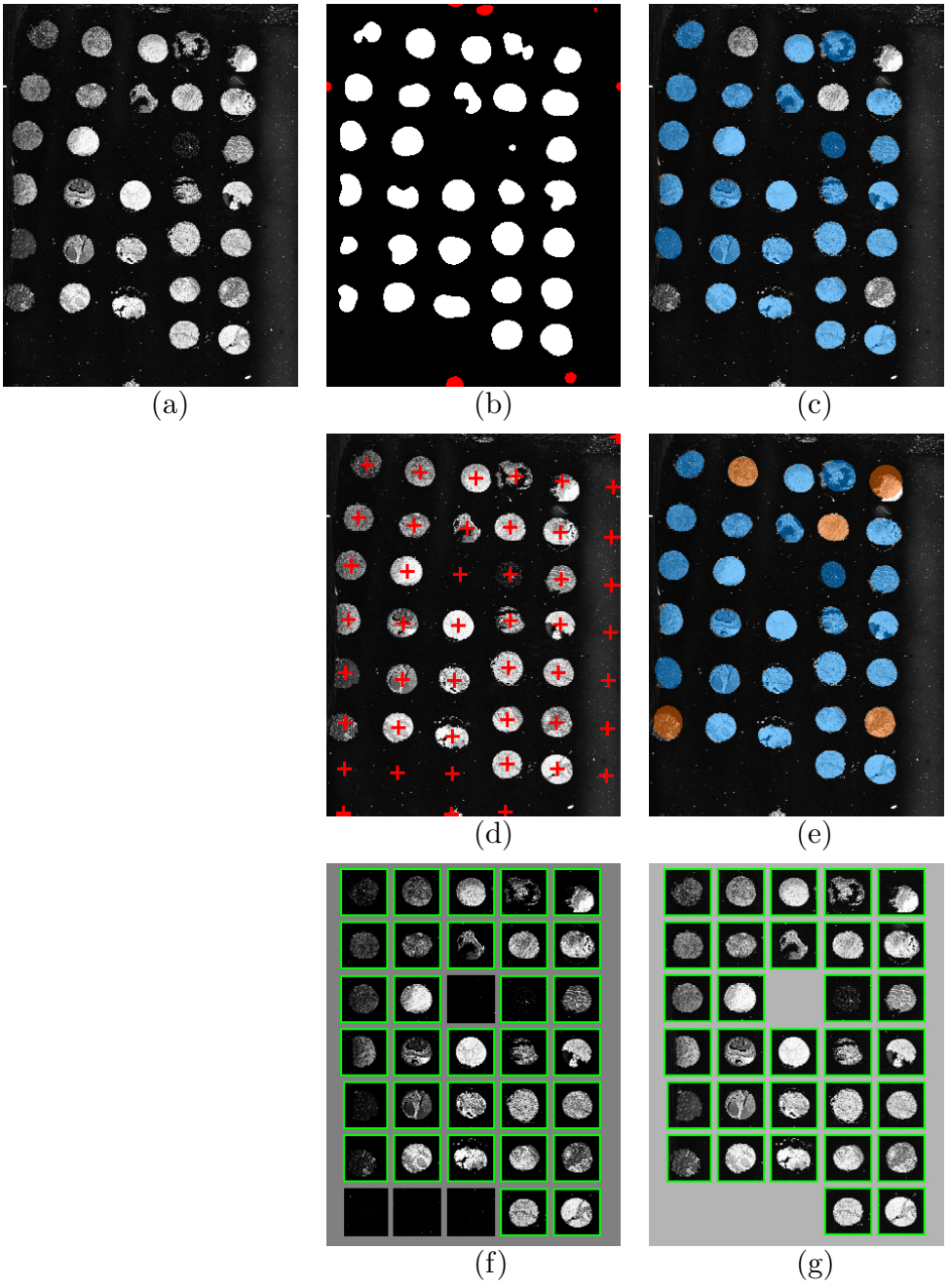

Figure 2.14: **Example of de-arraying on a fluorescence TMA image with the activation of both the segmentation and of the non-linear estimation for the TMA grid deformation.** (a) Contrast-enhanced original image. (b) Detection map (accurate detection is marked in white, wrong detection is marked in red). (c) Segmentation of TMA cores (recognized cores are colored by blue ellipses). (d) Estimated TMA grid (potential core position is marked by a red cross). (e) Recognized TMA cores (cores which are additionally recognized are colored by orange ellipses). (f) Final de-arraying result in array format (recognized core position is marked by green box). (g) Manual annotations for comparison.

localization of TMA cores estimated with only the wavelet-based detection method, often suffers from false positives because erroneous detection of irrelevant objects on the background is not eliminated. False detection mostly occurs in images with

complex background such as those illustrated in Figs. 2.14a and 2.14b. Note that in the case of fluorescence TMA images, the number of false positives is significantly larger than in the case of simulated and brightfield TMA images. On the other hand, tanks to the adaptive threshold derived from the wavelet transform, there is in general no false negative (i.e. all existing tissue cores were detected). These results demonstrate that the detection operation is not too sensitive (perfect recall score R = 1 in average), but also it is not precise enough (weak precision score P = 0.77 in average) in fluorescence imaging. Consequently, it lowered the overall performance of TMA core localization. In Table 2.2, the accuracy is only about 79% (corresponding to a F-score = 0.87) in average. Note that the linear transform estimation (Option 1) using the set of localizations with false positives, yielded satisfying de-arraying results (with an accuracy of 91% or F-score = 0.94 in average), mainly because robust estimators are used for TMA grid registration. Nevertheless, in some cases the non-linear transform estimation (Option 3) was unable to correctly handle erroneous inputs and to produce reliable de-arraying results.

In order to reduce the number of false positives during the localization step, we combined the wavelet-based detection method with the ellipse-based segmentation method. Despite low-light fluorescence imaging conditions and low contrast in images, the multi-core ellipse-based segmentation perfectly performed with a rate of 100% of successful segmentation over all detected positions. The segmentation procedure provided reliable features of the object found at each detected position (see Fig. 2.14c). By combining the detection and the segmentation modules, the localizer gave better results; in average, the overall accuracy is about 91% (F-score = 0.94) to be compared to only 79% when the ellipse-based segmentation module is not activated (see Table 2.2). Given these precise localization results, the non-linear transform estimation produced satisfactory outcomes; the row and column coordinates of most existing TMA cores were accurately computed (Fig. 2.14f). In average, the de-arraying with activation of both the ellipse-based segmentation and the non-linear transform estimation modules (Option 4) achieved a F-score = 0.96 (corresponding to an accuracy of 92%), which is sightly better than those obtained with option 1 (F-score = 0.95). We also notice a gain of about 1% in terms of overall accuracy (0.01 in terms of F-score performance) comparing to the localization step. The improvement between the two steps of the de-arraying procedure demonstrates the positive influence of the ellipse-based segmentation module on the overall performance of the proposed ATMAD method.

To sum up, the proposed de-arraying method rarely achieves perfect scores in the case of real (brightfield and fluorescence) images (except those obtained on DNA microarrays) in comparison to simulated images. This weaker performance is often due to the insufficient number of localized cores obtained on images with complex non-homogeneous background and/or highly irregular shapes of tissue cores. Consequently, we get imperfect de-arraying results which represent only array coordinates of each core. In spite of these imperfections, we have noticed that the spline approximation of the grid deformation yields, in most cases, accurate core position. More efficient segmentation algorithms can be used to further localize cores which were not recognized and thus to refine de-arraying results.

The majority of the time computing is spent on the detection task to compute

the wavelet transform. Overall, the computational cost is less than 5 seconds for de-arraying a 1000×1000 image. The experiments were performed on a Macbook Pro equipped with 2.7 Ghz Intel Core i7, 16 Gb of RAM and the Mac OS X v. 10.12.4 operating system. The algorithm was implemented in Matlab and we exploited the intrinsic parallelism of the CPU by performing many ellipse-based segmentation in parallel.

2.4 Conclusion

This chapter introduced a fast and efficient algorithm for de-arraying TMA by combining wavelet transform, active contour and thin-plate interpolation. The proposed ATMAD algorithm is adapted not only for bright field images but also for fluorescence images which are more challenging in terms of tissue localization due to complex backgrounds. This difficulty is carried out by a two-step approach: a fast detection followed by a careful segmentation to reduce the number of false alarms. The row and column coordinates of each localized tissue core are next computed by estimating the deformation of the design grid. Using the estimation of the deformation, tissue cores which are missed during localization can be later recognized and it refine thus the de-arraying result.

Acknowledgements

We would like to show our gratitude to Dr Jinhai Wang (Queen's University Belfast, Belfast, United Kingdom) and the AIDS and Cancer Specimen Resource Digital Library (University of California San Francisco) for sharing their valuable tissue microarray images which were used to evaluate the proposed TMA de-arraying approach.

Appendices

2.A Isotropic wavelet frame

Mathematically, a wavelet $\psi : \mathbb{R}^d \longrightarrow \mathbb{R}$ is a function of zero average:

$$\int \dots \int_{\mathbb{R}^d} \psi(\mathbf{x}) \; d\mathbf{x} \; = \; 0 \; ,$$

where d is the number of dimensions (usually, $d = 1,\ 2$ or 3). When the wavelet function ψ is isotropic (*i.e.* $\psi(-\mathbf{x}) = \psi(\mathbf{x}), \forall \mathbf{x} \in \mathbb{R}^d$), we deduce the wavelet atoms $\{\psi_{(\mathbf{t},s)}\}_{(\mathbf{t},s)\in\mathbb{R}^d\times\mathbb{R}_+^*}$ by dilation of ψ with factor s and translation by vector $\mathbf{t}$ as:

$$\psi_{(\mathbf{t},s)}(\mathbf{x}) = \frac{1}{s^d} \; \psi\left(\frac{1}{s}(\mathbf{x}-\mathbf{t})\right) \; .$$

The wavelet transform of a square-integrable function $u \in L^2(\mathbb{R}^d)$ is defined as the inner product (in $\mathbb{R}^d$) of u and the wavelet atom $\psi_{(\mathbf{t},s)}$ as follows:

$$\Psi u(\mathbf{t}, s) = \left\langle u, \psi_{(\mathbf{t},s)} \right\rangle = \int \ldots \int_{\mathbb{R}^d} u(\mathbf{x}) \; \bar{\psi}_{(\mathbf{t},s)}(\mathbf{x}) \; d\mathbf{x} \; ,$$

where $\bar{\psi}_{(\mathbf{t},s)}$ denotes the complex conjugate of $\psi_{(\mathbf{t},s)}$. To construct a shift-invariant representation, we consider the dyadic wavelets derived by discretizing the scale parameter along a dyadic sequence $\{2^j\}_{j\in\mathbb{Z}}$, while the translation parameter is not sampled as:

$$\left\{ \psi_j(\mathbf{x}) = \frac{1}{2^{dj}} \; \psi\left(\frac{\mathbf{x}}{2^j}\right) \right\}_{j\in\mathbb{Z}} \; . \tag{2.33}$$

The family $\{\psi_j\}_{j\in\mathbb{Z}}$ is a frame of $L^2(\mathbb{R}^d)$ according to [Mallat 2008]. Using this family, the isotropic wavelet transform of u at the scale (or resolution) 2^j and the position $\mathbf{x} \in \mathbb{R}^d$ is:

$$\begin{aligned} \Psi_j u(\mathbf{x}) &= \int \ldots \int_{\mathbb{R}^d} u(\mathbf{x}) \; \frac{1}{2^{dj}} \; \psi\left(\frac{1}{2^j}(\mathbf{x}-\mathbf{t})\right) d\mathbf{t} \\ &= u \star \check{\psi}_j(\mathbf{x}), \end{aligned} \tag{2.34}$$

where $\check{\psi}_j(\mathbf{x}) = \psi_j(-\mathbf{x}) = \psi_j(\mathbf{x})$ since ψ_j is isotropic. The wavelet coefficient $\Psi_j u(\mathbf{x})$ can also be expressed as the difference of approximations of u at subsequent scales as follows:

$$\Psi_j u(\mathbf{x}) = u_{j-1}(\mathbf{x}) - u_j(\mathbf{x}) \; , \tag{2.35}$$

$$u_j(\mathbf{x}) = \chi_j \star u_{j-1}(\mathbf{x}) = \lim_{k\to+\infty} (\chi_j \star \ldots \star \chi_{j-k}) \star u(\mathbf{x}) \; , \tag{2.36}$$

where u_j and χ_j denote respectively the approximation of u and the smoothing function at the scale 2^j.

The infinite convolution cascade $\phi_j = \lim_{k\to+\infty} (\chi_j \star \ldots \star \chi_{j-k})$ represents the approximation operator applied on u at the given resolution 2^j. In order to favor the simplest computation of the convolution sequence in (2.36), the selection of $(\chi_j)_{j\in\mathbb{Z}}$ is critical. Among many function families, Gaussian functions are convenient since it satisfies the semi-group property (i.e. the convolution of two Gaussians is also a Gaussian with variance being the sum of the original variances):

$$G_{\sigma_a} \star G_{\sigma_b}(\mathbf{x}) = G_{\sqrt{\sigma_a^2+\sigma_b^2}}(\mathbf{x}) \; ,$$

where G_σ is a Gaussian with standard deviation σ.

Therefore, if we choose χ_j being a Gaussian G_{σ_j} with standard deviation σ_j, the convolution sequence $(\chi_j \star \ldots \star \chi_{j-k})$ can be easily computed by summing $\sigma_j^2, \ldots, \sigma_{j-k}^2$. Since resolution decreases by a factor 2 between two consecutive scales, it is appropriate to set $\sigma_j = 2\sigma_{j-1} = 2^{j-1}\sigma_1$, where σ_1 is a reference standard deviation according to the Shannon-Nyquist sampling step. Thus, we have:

$$\sum_{k=0}^{+\infty} \sigma_{j-k}^2 = \sum_{k=0}^{+\infty} \left(2^{j-k-1}\sigma_1\right)^2 = \frac{4^j}{3}\sigma_1^2 \; .$$

Then, the approximation operator at the scale 2^j can be expressed as a convolution with a Gaussian of variance $(4^j/3)\sigma_1^2$:

$$\phi_j(\mathbf{x}) = \lim_{k \to +\infty} (\chi_j \star \ldots \star \chi_{j-k})(\mathbf{x}) = G_{\sqrt{(4^j/3)\sigma_1^2}}(\mathbf{x}) \ .$$

Additionally, from equations (2.34) to (2.36), we deduce:

$$\psi(\mathbf{x}) = 2^{dj}(\phi_{j-1}(2^j\mathbf{x}) - \phi_j(2^j\mathbf{x})) = \phi_{-1}(\mathbf{x}) - \phi_0(\mathbf{x}) \ . \tag{2.37}$$

By generalizing the equation expressed the relation of the mother wavelet ψ and its associate scaling function ϕ as described in [Starck and Murtagh 2006] as follows:

$$\frac{1}{2^d}\psi\left(\frac{\mathbf{x}}{2}\right) = \phi(\mathbf{x}) - \frac{1}{2^d}\phi\left(\frac{\mathbf{x}}{2}\right),$$

a closed-form solution of the scaling function ϕ (also known as father wavelet) is obtained as:

$$\phi(\mathbf{x}) = \phi_0(\mathbf{x}) = G_{\sigma_1/\sqrt{3}}(\mathbf{x}) = \frac{1}{(2\pi\sigma_1^2/3)^{d/2}} \exp\left(-\frac{3\|\mathbf{x}\|_2^2}{2\sigma_1^2}\right).$$

Since ϕ is Gaussian, ψ is defined as the difference of two Gaussians (DOG) with the first standard deviation equal to half of the second one. Given a value of σ_1 as input, the wavelet atoms ψ_j which are also DOGs are determined using the equations (2.33) and (2.37). Hence, a class of isotropic wavelets can be simply characterized by only one parameter.

2.B Direct wavelet decomposition algorithm and reconstruction

Starck et al. (2007) proposed a method for performing the isotropic undecimated wavelet transform. This algorithm is called the Starlet transform. Like the standard undecimated wavelet transforms, the Starlet transform uses the *à trous* algorithm [Starck et al. 1994] which inserts zeros (holes) in the discrete convolution kernel at each iteration. This kernel is a low-pass filter derived from the normalized cardinal B-spline of order 3:

$$\begin{aligned} h^{(1D)}[k] &= \frac{1}{16}[1,\ 4,\ 6,\ 4,\ 1], \quad k \in \{-2,-1,0,1,2\}, \\ B_3(u) &= \frac{1}{12}(|u-2|^3 - 4|u-1|^3 + 6|u|^3 \\ &\qquad - 4|u+1|^3 + |u+2|^3). \end{aligned}$$

Yet, as the order tends to infinite, the normalized cardinal B-spline tend to a Gaussian function The kernel used for wavelet decomposition is then an approximation of a Gaussian. To avoid the decimation at each level, the insertion of holes in the kernel leads to approximation errors, since the kernels with holes are far from their corresponding scaling functions. The error cumulation through iterations increases

Level (j)	**Std. of** χ_j (σ_j)	**Variance of** ϕ_j^0 (v_j^2)
1	σ_1	σ_1^2
2	$2\sigma_1$	$5\sigma_1^2$
3	$4\sigma_1$	$21\sigma_1^2$
4	$8\sigma_1$	$85\sigma_1^2$
5	$16\sigma_1$	$341\sigma_1^2$
6	$32\sigma_1$	$1365\sigma_1^2$

Table 2.3: Computation of the variance of the scaling function phi_j^0 at first few levels.

with the level of the decomposition. In addition, the iterative convolution process involves the dependence of the higher level of the decomposition on its previous levels. To sum up, the limits of *à trous* algorithm are its inaccuracy and computational cost.

To overcome these limits, the discrete wavelet decomposition of a function u at the desired scale 2^j can be obtained by performing the discrete convolution between u and the corresponding wavelet atom ψ_j. In practice, since all computations are performed over discrete signals, the input signal is not u but its discrete approximation counterpart. Without losing the generality, one can assume this approximation is u_0. In fact, using (2.35) and (2.36), we have:

$$\begin{aligned}\Psi_j u(\mathbf{x}) &= u_{j-1}(\mathbf{x}) - u_j(\mathbf{x}) \\ &= \begin{cases}(\chi_{j-1} * \ldots \star \chi_1 - \chi_j \star \ldots \star \chi_1) \star u_0(\mathbf{x}) \text{ if } j > 1 \\ u_0(\mathbf{x}) - \chi_1 \star u_0(\mathbf{x}) \text{ if } j = 1\end{cases} \\ &= (\phi_{j-1}^0 - \phi_j^0) \star u_0(\mathbf{x}) \\ &= \psi_j^0 \star u_0(\mathbf{x}),\end{aligned}$$

where $\phi_j^0 = \begin{cases} \chi_j \star \ldots \star \chi_1 & \text{if } j > 1 \ , \\ \delta & \text{if } j = 1 \ . \end{cases}$

The key idea of our method is the computation of the scaling function ϕ_j^0 which results the convolution sequence $\chi_j \star \ldots \star \chi_1$. Since χ_j is chosen as a Gaussian with variance $\sigma_j^2 = 4^{j-1}\sigma_1^2$, the function of interest ϕ_j^0 is also a Gaussian with variance:

$$v_j^2 = \begin{cases} \displaystyle\sum_{k=1}^{j} 4^{k-1}\sigma_1^2 & \text{if } j \geq 1, \\ 0 & \text{if } j = 0. \end{cases}$$

The values of v_j^2 at first few levels are reported in the Table 2.3.

Hence, there are two ways to compute $\Psi_j u$. The fastest way is to compute directly the wavelet atom $\psi_j^0(\mathbf{x}) = \phi_{j-1}^0(\mathbf{x}) - \phi_j^0(\mathbf{x}) = G_{v_{j-1}}(\mathbf{x}) - G_{v_j}(\mathbf{x})$ (with convention $G_0(\mathbf{x}) = \delta(\mathbf{x})$). Then, the wavelet decomposition map is the convolution product $\Psi_j u(\mathbf{x}) = \psi_j^0 \star u_0(\mathbf{x})$. The alternative way is to compute two convolutions

$u_{j-1}(\mathbf{x}) = \phi^0_{j-1} \star u_0(\mathbf{x})$ and $u_j(\mathbf{x}) = \phi^0_j \star u_0(\mathbf{x})$, thus the wavelet decomposition is derived by taking the difference of two computed results. This way is slower than the first one but it is useful to reconstruct the input signal u_0.

By construction, for any given level j, the formula of reconstruction of u_0 is:

$$\begin{aligned} u_0(\mathbf{x}) &= \sum_{k=1}^{j} \Psi u_k(\mathbf{x}) + u_j(\mathbf{x}) \\ &= \sum_{k=1}^{j-1} (u_{k-1} - u_k)(\mathbf{x}) + \Psi_j u(\mathbf{x}) + u_j(\mathbf{x}) \\ &= u_0(\mathbf{x}) - u_{j-1}(\mathbf{x}) + \Psi_j u(\mathbf{x}) + u_j(\mathbf{x}) \ . \end{aligned}$$

The perfect reconstruction of u_0 is therefore possible if $u_0 - u_{j-1}$ and u_j are known. Yet, u_{j-1} and u_j are computed by using the alternative way of the wavelet decomposition. Instead of returning only the wavelet decomposition $\Psi_j u$, $u_0 - u_{j-1}$ and u_j are also stored if the user needs to perform the reconstruction step. This approach can be extended for multi-scale reconstruction. In fact, if we have $(\Psi_j u)_{j \in J}$ where $J = \{j_1, j_2, \ldots, j_{|J|}\} \subset \mathbb{N}^*$, the reconstruction formula is written as:

$$u_0(\mathbf{x}) = \frac{1}{|J|} \sum_{k=1}^{|J|} (u_0 - u_{j_k - 1} + \Psi u_{j_k} + u_{j_k})(\mathbf{x}) \ .$$

In practice, wavelet-based algorithms compute over a set of subsequent scales (i.e. $J = \{j_0, j_0+1, \ldots, j_0+|J|-1\}$). In this case, the reconstruction formula is therefore:

$$u_0(\mathbf{x}) = u_0(\mathbf{x}) - u_{j_0-1}(\mathbf{x}) + \sum_{k=0}^{|J|-1} \Psi u_{j_0+k}(\mathbf{x}) + u_{j_0+|J|-1}(\mathbf{x}) \ .$$

2.C Partial derivatives of the ellipse quadratic form

Let $\{\mathbf{x}_0, a, b, \theta\}$ be the parameters of the ellipse Γ where $\mathbf{x}_0 = (x_0, y_0)$ is the center, a and b are the semi major and minor axes, and θ is the angle of rotation. We consider the quadratic form induced by Γ as:

$$\begin{aligned} \|\mathbf{x} - \mathbf{x}_0\|^2_\Gamma &= \left\| \begin{bmatrix} a^{-1} & 0 \\ 0 & b^{-1} \end{bmatrix} \begin{bmatrix} \cos\theta & \sin\theta \\ -\sin\theta & \cos\theta \end{bmatrix} (\mathbf{x} - \mathbf{x}_0) \right\|^2_2 \\ &= \left(\frac{\cos\theta}{a}(x - x_0) + \frac{\sin\theta}{a}(y - y_0) \right)^2 \\ &\quad + \left(-\frac{\sin\theta}{b}(x - x_0) + \frac{\cos\theta}{b}(y - y_0) \right)^2 \ . \end{aligned}$$

The partial derivatives of $\|\mathbf{x}-\mathbf{x}_0\|_\Gamma^2$ with respect to $\{\mathbf{x}_0, a, b, \theta\}$ are given by:

$$\frac{\partial \|\mathbf{x}-\mathbf{x}_0\|_\Gamma^2}{\partial x_0} = -2\left[\frac{\cos\theta}{a}\left(\frac{\cos\theta}{a}(x-x_0)+\frac{\sin\theta}{a}(y-y_0)\right) - \frac{\sin\theta}{b}\left(-\frac{\sin\theta}{b}(x-x_0)+\frac{\cos\theta}{b}(y-y_0)\right)\right]$$

$$\frac{\partial \|\mathbf{x}-\mathbf{x}_0\|_\Gamma^2}{\partial y_0} = -2\left[\frac{\sin\theta}{a}\left(\frac{\cos\theta}{a}(x-x_0)+\frac{\sin\theta}{a}(y-y_0)\right) + \frac{\cos\theta}{b}\left(-\frac{\sin\theta}{b}(x-x_0)+\frac{\cos\theta}{b}(y-y_0)\right)\right] ,$$

$$\frac{\partial \|\mathbf{x}-\mathbf{x}_0\|_\Gamma^2}{\partial a} = -\frac{1}{a}\left(\frac{\cos\theta}{a}(x-x_0)+\frac{\sin\theta}{a}(y-y_0)\right)^2 ,$$

$$\frac{\partial \|\mathbf{x}-\mathbf{x}_0\|_\Gamma^2}{\partial b} = -\frac{1}{b}\left(-\frac{\sin\theta}{b}(x-x_0)+\frac{\cos\theta}{b}(y-y_0)\right)^2 ,$$

$$\frac{\partial \|\mathbf{x}-\mathbf{x}_0\|_\Gamma^2}{\partial \theta} = 2\left(\frac{b}{a}-\frac{a}{b}\right)\left(\frac{\cos\theta}{a}(x-x_0)+\frac{\sin\theta}{a}(y-y_0)\right) \times \left(-\frac{\sin\theta}{b}(x-x_0)+\frac{\cos\theta}{b}(y-y_0)\right) .$$

Chapter 3

Dejittering of Scanned TMA Images

Related publication

H.-N. Nguyen, V. Paveau, C. Cauchois, C. Kervrann. A Variational Method for Dejittering Large Fluorescence Line Scanner Images[1]. Manuscript submitted for publication in IEEE Transactions on Computational Imaging, 2017

Abstract

We propose a variational method dedicated to jitter correction of large fluorescence scanner images. Our method consists in minimizing a regularization energy functional to estimate a dense displacement field representing the spatially-varying jitter. The computational approach is based on a half-quadratic splitting of the energy functional which decouples the re-alignment data term and the dedicated differential-based regularizer. The resulting problem amounts to alternatively solving two convex and non-convex optimization sub-problems with appropriate algorithms. Experimental results on artificial and large real fluorescence images demonstrate that our method is not only capable to handle large displacements but is also efficient in terms of sub-pixel precision without inducing additional intensity artifacts.

Keywords: Dejittering, fluorescence scannner, variational method, regularization, optimization, quadratic relaxation, proximal algorithm

3.1 Introduction

Over the past decades, the evolution of digital technology has radically changed the way in which images are handled, stored, visualized and transmitted. Nowadays, most of imaging devices are able to transform acquired images into digital form in order to allow not only the recording on electronic medium, but also the processing by computers. This transformation is called digitization which consists in generating a finite sequence of samples from the input (analog) signal. Despite number of advantages, digitization often suffers from undesirable artifacts during the acquisition,

[1]This work was supported by Innopsys.

transmission and recording processes due to imperfections of one or more components of the involved devices. One of those artifacts is *jitter*, a type of distortion characterized by the mispositioning of pixels in the image.

There are several situations where jittering frequently arises. A typical example is the analog-to-digital conversion of video from old magnetic tapes in which horizontal displacement of image lines (line jitter) might happen. As a result, edges appear to be jagged in vertical direction as illustrated in the first row of Fig. 3.1. It is mainly because the synchronization signals that contain the information of the relative position of image rows to each other, were corrupted with noise in the video signal and/or by degradation of the storage medium. Line jitter can also occur during wireless video transmission due to delayed and loss packets. Another case is the video interlacing technique that scans video images by recording two fields with half vertical resolution at two different times. Alternating lines of these two fields enables doubling the frame rate (temporal resolution) of the video while remaining the same bandwidth (amount of data). The temporal difference between the two recorded fields can lead to a rolling effect in both horizontal and vertical directions as a consequence of relative motions of the camera and the objects in the scene. Similarly, during long acquisition process, random displacement (vibration) of the imaging device and the imaged object is a major cause of jittering in biomedical equipment such as CT (computer tomography) and MRI (magnetic resonance imaging) scanners.

In this chapter, we do not address the problem of jittering in general, but we focus only on a particular case of jitter arising in dedicated fluorescence line scanners[2], as illustrated in the second row of Fig. 3.1. Here, the images are acquired pixel by pixel along each line with a change of scan direction between two subsequent lines (see Fig. 3.2). Such an acquisition system requires a very accurate positioning of each acquired pixel in order to provide output images with no distortion. Unfortunately, the resulting images are jiterred. The main sources of distortion are mainly due to:

- imperfect synchronization between mechanical and electronic components;
- small objective rotations induced by abrupt acceleration and deceleration during scanning;
- spatially-varying sinusoidal scan speed.

The pixels on subsequent lines are horizontally displaced in opposite directions, resulting in a structured jitter (see Figs. 3.1, 3.3 and 3.10). To our knowledge, there is no existing method to compensate the displacement errors in such jittered fluorescence images. Accordingly, we propose a computational approach inspired from variational optical flow methods, to restore images. Our approach consists in minimizing an energy functional which explicitly combines a non-convex data term with a convex spatial regularity term with respect to the horizontal displacement, while taking into account the particular structure of the jitter. The optimization problem

[2] InnoScan 1100 AL developed by Innopsys Inc., for more details of the product please refer to `https://www.innopsys.com/en/lifesciences-products/microarrays/innoscan/innoscan-1100-al`

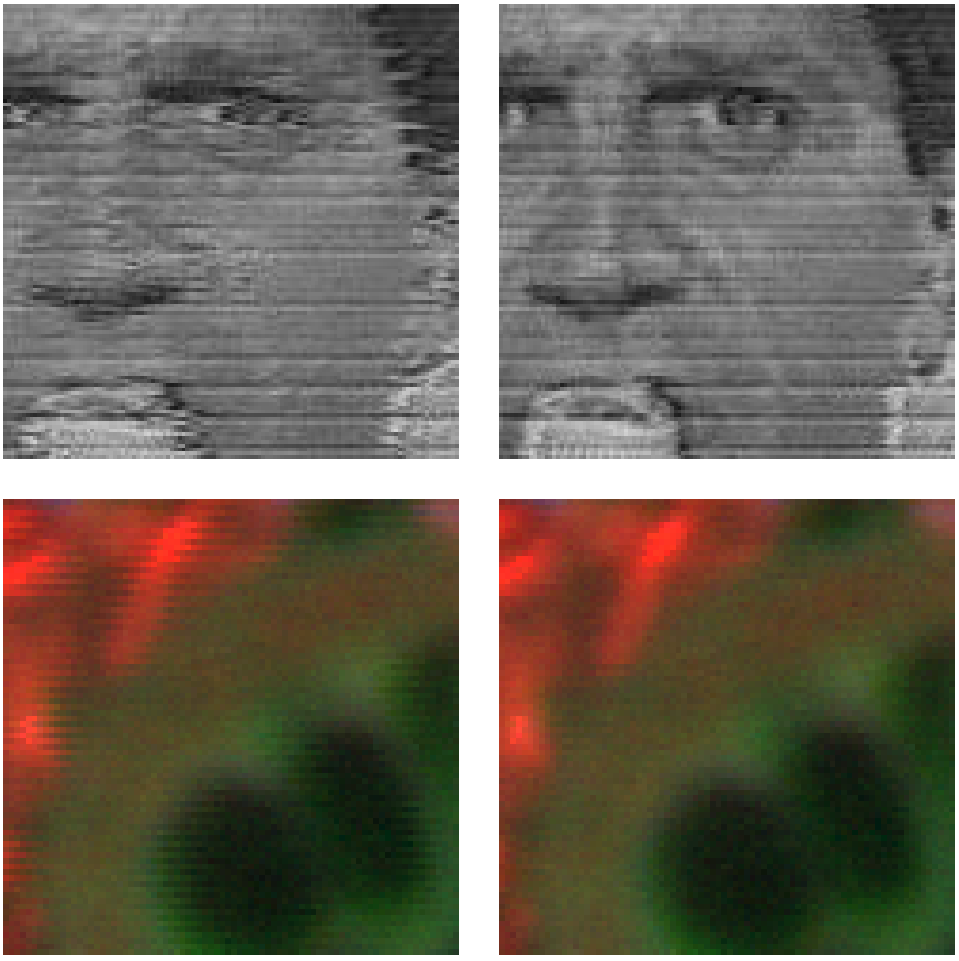

Figure 3.1: **Examples of jitters.** From top to bottom: jitter arising in analog-to-digital video conversion (Source `http://www.mee.tcd.ie/~ack/cd/linereg/linereg.htm`) and in fluorescence line scanner (by the courtesy of Innopsys). From left to right: jittered and dejittered image.

can be efficiently solved by introducing an auxiliary variable and a quadratic constraint to decouple the data term and the regularity term into two more tractable optimization sub-problems. The first sub-problem is convex while the second sub-problem is non-convex and does not exhibit spatial dependency between pixels. The proposed decoupling allows to solve each sub-problem separately with two appropriate algorithms: a proximal algorithm for the convex sub-problem and an exhaustive search for the non-convex sub-problem. The minimization of the proposed energy can be therefore performed by alternating the two optimization steps. Experiments on both simulated and real images show that our approach can handle large and non-integer displacements, while these two issues are not addressed by the majority of existing dejittering methods. Unlike image-regularization methods devoted to jitter correction, our approach does not smooth images but optimally register all the displaced lines.

The remainder of the chapter is organized as follows. In the next section, several existing methods for image dejittering and deinterlacing are reviewed. In Section 3.3, we present the proposed acquisition model based on the sampling theory. We explain the relationships between the ideal continuous image and its discrete jitter-

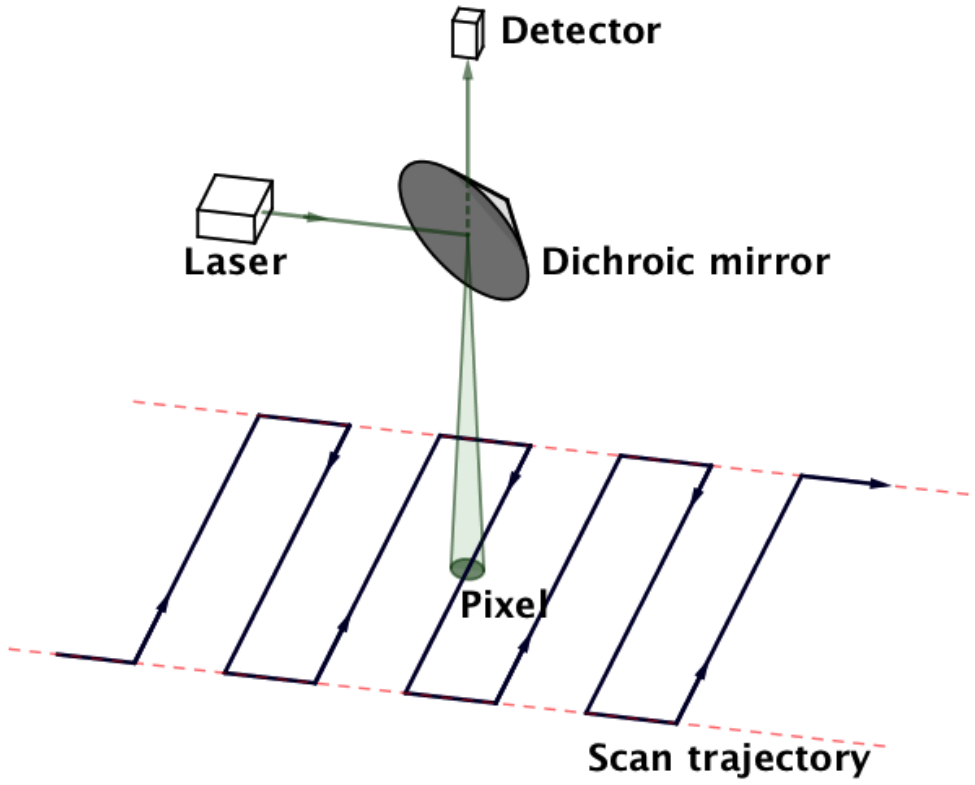

Figure 3.2: **Image acquisition process involved in fluorescence line scanners.** Images are acquired pixel by pixel along each line with a change of scan direction between two subsequent lines.

free as well as its jittered version. We also define a dedicated energy functional for dejittering. In Section 3.4, technical details of the proposed dejittering algorithm are given. Section 3.5 presents the experimental results obtained on simulated and real data. Finally, the last section gathers the conclusions drawn from this chapter and gives a perspective to further improvements.

3.2 Related works for image dejittering and deinterlacing

Analog video signals have a specific format that defines how the timing reference (also known as "time base") is embedded. It allows the receiving device to correctly extract the necessary synchronization information for reconstructing images and providing visual display. The corruption or even the loss of this timing reference consequently results in an extraction of incorrect synchronization information and thus introduces jitter. In the late of 80's, "time base correction" techniques were already used for restoring the embedded synchronization information in the analog signal. Noise was removed from the non-picture part of the signal in order to reproduce an accurate display of the input video. However, such a technique which is able to process solely analog signals cannot be applied to current digital videos. Over the

last two decades, intrinsic dejittering Kokaram (1998) techniques were introduced as an alternative solution. Indeed, these techniques which rely only on jittered image data are much more flexible and widely applicable when compared to conventional (non intrinsic) "time base correctors".

To perform (intrinsically) image dejittering, one can envisage simple approaches such as line averaging and correlation matching between two subsequent lines. Unfortunately, the former approach tends to produce blur and decreases the vertical resolution, whereas the latter tends to cause a bias in vertical direction due to its local property. At the end of 90's, Kokaram et al. (1997) invented the first intrinsic method, in which the authors assumed jitter-free images obey a 2D-AR (autoregressive) model. The unknown AR coefficients and the line displacements are jointly estimated by blocs using an iterative algorithm. Whitening of the estimated displacement can be performed in the case of drift (i.e. restored images are warped) to remove the low frequency component of the estimation.

Later, Laborelli (2003) proposed a different approach to estimate the line displacement by considering the L_1 norm of the difference of two or three consecutive shifted lines as a local criterion and using it to define a global cost which is optimized by dynamic programming. Right afterwards, Shen (2004) described a joint denoising and dejittering algorithm which consists in minimizing a energy functional in the Bayesian framework with respect to the original (unjittered) image and the associated displacement. The considered energy is derived from the posterior probability of the unjittered image and the displacement given the observed jittered image. This conditional probability is defined under the Gaussian distribution assumption of the displacement and of the noise, combined with the BV (bounded variation) image model. Instead of considering such a joint denoising and dejittering approach, Kang and Shen (2006) developed a two-step displacement-estimation method called "Bake and Shake" which relies on Perona-Malik diffusion [Perona and Malik 1990] to reduce the noise and the rolling effect of jittered images. The key idea of this method is that the intermediate diffused (baked) image – less noisy and less jittered – can guide the estimation of the displacement (i.e. the "shake" step). Later on, the "Bake and Shake" authors introduced in [Kang and Shen 2007] the notion of slicing moments of BV images – a measure to quantify how much the image is jittered. Using this notion, the displacement of image lines is obtained by minimizing a L_2-TV (total variation)-based functional of the vertical slicing moments.

In contrast to these continuous-optimization-based methods, Nikolova (2009a,b) proposed a fast algorithm for image dejittering by performing a complete search over a finite set of allowed integer values of shifts to optimize a non smooth and (eventually) non-convex local criterion. This local criterion is an extended version of the criterion mentioned in [Laborelli 2003] by using normalized L_p norms (with $p = 0.5$ or $p = 1$) and possibly higher order criteria (e.g. more than three adjacent lines). Recently, Lenzen and Scherzer (2011) introduced a PDE (partial differentiable equation) derived via semi-groups from a nonconvex energy functional for restoring directly jittered images without explicit estimation of the displacement. This model which is related to the mean curvature flow [Huisken 1984; Catté et al. 1992] corresponds to the minimization of an energy composed of a linearized realignment criterion and a TV regularization. Based on these previous works, Dong

et al. (2015) proposed a unified class of methods for different types of jitter by generalizing the Nikolova's algorithm to infinite dimensional framework and establishing its relation with the Lenzen's PDEs.

In the comparison with "line dejittering" which corrects the shift between consecutive lines of a jittered image, deinterlacing is the process of reconstructing a complete image frame from two recorded fields at half vertical resolution at two different times. It consists generally in compensating the motion between these recorded fields due to temporal difference. Inspired from optical flow models, the estimation of the underlying motion have been recently used in state-of-the-art deinterlacing methods. Most of these motion-estimation-based methods are defined in a variational framework with TV regularization [Ghodstinat et al. 2009; Keller et al. 2005, 2008].

Irrespective of deinterlacing or dejittering algorithms, we can classify the majority of them into three categories: (i) simultaneous methods such as [Shen 2004; Keller et al. 2008] which consist in jointly estimating the displacement and the jitter-free original image; (ii) methods, which aim at estimating the displacement represent the majority part on the literature as in [Kokaram et al. 1997; Kokaram 1998; Laborelli 2003; Kang and Shen 2006, 2007; Nikolova 2009a,b; Ghodstinat et al. 2009]; (iii) variational methods which consist in restoring the image without any estimation of the displacement as in [Keller et al. 2005; Lenzen and Scherzer 2011; Dong et al. 2015]. Note that there are a few problems which are not fully addressed in the literature such as large and non-integer displacement, over-fitting, or over-smoothing. Our approach belongs to the second category of methods since a displacement field is estimated by global energy minimization.

3.3 Jitter modeling: Application to fluorescence line scanner images

In this section, we present a general image acquisition model which explains the relationship between the ideal (undistorted) continuous image and its digitized versions. The digitized images are nothing else than finite sets of samples of the continuous image according to a sampling grid. In this chapter, we focus on gray-scale bidimensional (2D) images for the sake of clarity.

3.3.1 Notations and image sampling

Let $u : \Omega \to \mathbb{R}$ be an undistorted continuous image which is defined on a rectangular domain $\Omega = [0, M] \times [0, N] \subset \mathbb{R}^2$. Digitization consists in sampling the input continuous image with respect to a lattice (sampling grid) in order to provide an output discrete image. In the case of an ideal sampling, the sampling grid is a regular grid which is characterized by a couple of orthogonal unit vectors and a vertex-to-vertex distance (also sampling step). Without loss of generality, one can assume that this regular sampling grid is the Cartesian grid $\mathbb{Z}^2$ (i.e. the couple of characterized vectors is the canonical basis $(\mathbf{e}_1, \mathbf{e}_2)$ of the plane $\mathbb{R}^2$ and the sampling step equals to 1, implying that each vertex of the sampling grid is an integer point).

The sampled version of u according to $\mathbb{Z}^2$, defined as the set of finite samples $\{u_{i,j} \triangleq u[i,j]\}_{(i,j)\in\mathbb{Z}^2\cap\Omega}$, is called the (discrete) jitter-free image. For the sake of simplicity, we denote the image grid $\Lambda = \mathbb{Z}^2 \cap \Omega = \{0,1,\ldots,M\} \times \{0,1,\ldots,N\}$.

Let us denote $\boldsymbol{w} : (i,j) \in \Lambda \longmapsto (w_1(i,j), w_2(i,j)) \in \mathbb{R}^2$ the dense displacement field which represents the jitter, occurring during the image acquisition process. The jittered version of u with respect to the displacement field $\boldsymbol{w}$ is therefore defined as:

$$\Big\{ f_{i,j} \triangleq f[i,j] = u\left[i - w_1(i,j), j - w_2(i,j)\right] \Big\}_{(i,j)\in\Lambda} \ . \tag{3.1}$$

In other words, $\{f_{i,j}\}_{(i,j)\in\Lambda}$ is a sampled version of u according to a irregular sampling grid

$$\tilde{\Lambda} = \{(i - w_1(i,j), j - w_2(i,j)) \ , \ \forall (i,j) \in \Lambda\} \subset \mathbb{R}^2 \ . \tag{3.2}$$

The restoration of $\{u_{i,j}\}_{(i,j)\in\Lambda}$ from irregular samples $\{f_{i,j}\}_{(i,j)\in\Lambda}$ with unknown sampling position $\tilde{\Lambda}$ is the so-called *dejittering* procedure.

3.3.2 Alternating line pixel jitter

In contrast to a general irregular sampling case in which the perturbed sampling position $\tilde{\Lambda}$ does not need to have any particular structure (beyond a minimal sampling density) [Almansa et al. 2006; Facciolo et al. 2009], dejittering usually exploits the structure of the associated vector field $\boldsymbol{w}$ to compensate the displacement errors and re-align the jagged edges. In this chapter, we focus on a specific jitter arising in images acquired by fluorescence line scanners (InnoScan 1100 AL). A typical example of jittering is illustrated in Fig. 3.3, depicting a checkerboard pattern in which the displacement between two subsequent image lines is not constant along the horizontal axis. This situation is quite different from the usual case of line jitter which is well documented in the literature (e.g., [Kokaram 1998; Kokaram et al. 1997; Laborelli 2003; Shen 2004; Kang and Shen 2006, 2007; Nikolova 2009a,b; Lenzen and Scherzer 2011; Dong et al. 2015]).

In such jittered images, we notice that:

- the pixels on the even lines are shifted in the opposite direction with respect to those on the odd lines;
- there is no apparent displacement between lines of the same set of even lines or odd lines.

More specifically, the rolling effect appears only in the vertical direction and not in the horizontal direction. By measuring the gap between vertical contours on subsequent lines at difference positions in the jittered images, we also notice that the magnitude of displacement along horizontal axis varies smoothly according to a specific pattern depending on pixel positions (see Fig. 3.3). Consequently, the observed jitter can be named as "alternating line pixel jitter". Based on the described observations, we noticed that estimating the difference in displacement between the set of all odd lines and those of all even lines is sufficient to re-align jagged shapes. Without loss of generality, one can arbitrary assume that the displacement equals to zero on even lines (or odd lines). Under this assumption, we propose to

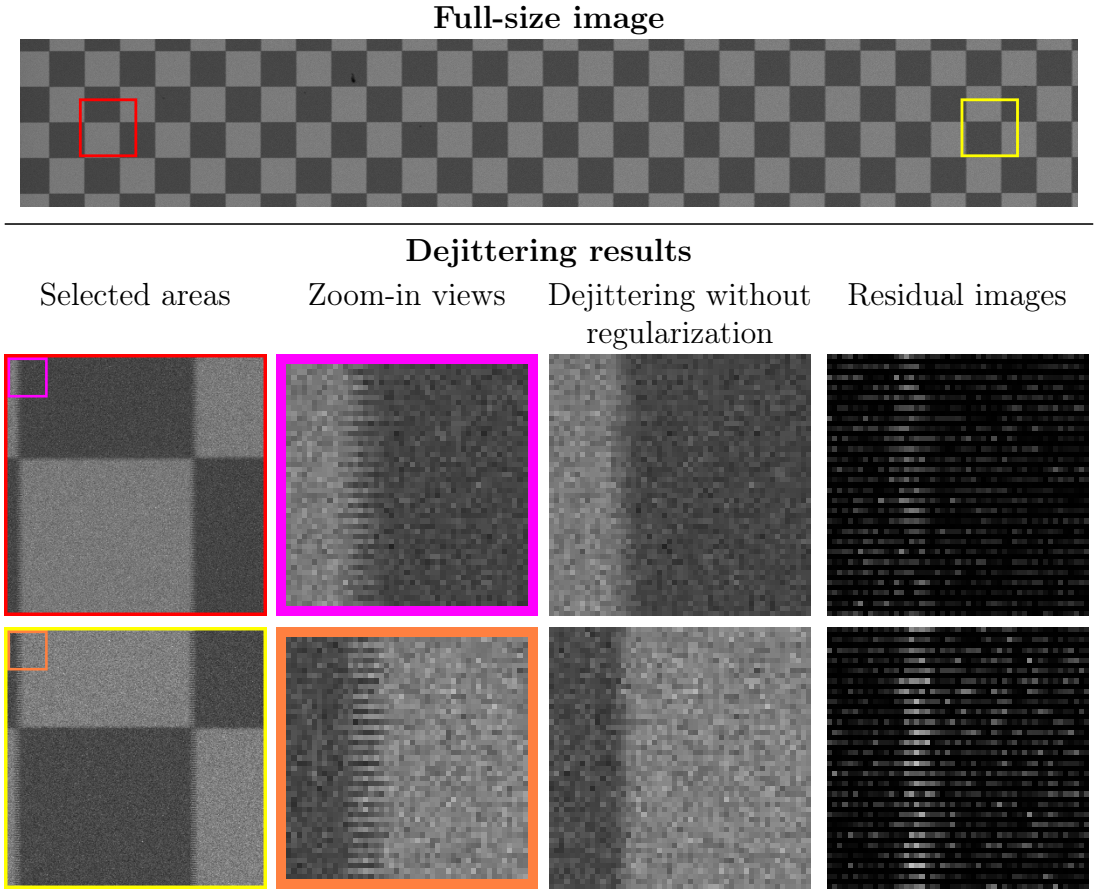

Figure 3.3: **Image of a tool slide used for scanner calibration before/after correction of the vertical rolling effect.** A tool slide depicting a checkerboard pattern is scanned over a region of interest of 6 millimeters in width (approximately a third of maximal scan width supported by the scanner). Two regions (marked by red/pink and yellow/orange boxes) are selected to illustrate the displacement variation along the horizontal direction. The average displacement in the pink and orange square boxes is about 3 pixels and 6 pixels respectively. Dejittering with and without regularization provided very similar results in terms of visual quality on this piecewise constant image. For visualization purposes, the results by setting $\lambda = 0$ (without regularization) are displayed, including the residual images between the jittered and restored images.

model the occurred jitter by a vector field $\boldsymbol{w} = \{\boldsymbol{w}(i,j) = (w_{i,j}, 0)\}_{(i,j)\in\Lambda}$ whose the vertical component is zero and the horizontal component satisfies the two following conditions associated to odd and even lines:

$$\begin{cases} w_{i,j} = 0 \text{ if } j \in 2\mathbb{Z} \ , \\ w_{i,j} w_{i',j} \geq 0 \text{ for any } (i,i') \in \mathbb{Z}^2 \ . \end{cases} \tag{3.3}$$

The first condition implies the alternating structure of the observed jitter (one line of every two lines is shifted). The second condition implies that the horizontal component of the displacement vector at a given point on a line has the same sign as those at another point on the same line – resulting in the same displacement direction on the same line. Since the vertical component of $\boldsymbol{w}$ is assumed to be constant, we estimate only the horizontal component $w : (i,j) \longmapsto w_{i,j}$ to perform image dejittering.

3.4 Variational method for displacement estimation

3.4.1 Energy functional

To deal with the "alternating line pixel jitter" occurring in fluorescence scanner images, we aim at estimating the scalar field w which represents the displacement along the horizontal direction by minimizing a global energy of the following form:

$$E(w) = \underbrace{\sum_{i=0}^{M}\sum_{j=0}^{N}\rho(i,j,f,w)}_{E_D(w,f)} + \underbrace{\sum_{i=0}^{M}\sum_{j=0}^{N}\phi\big((Lw)_{i,j}\big)}_{E_R(w)} , \tag{3.4}$$

where L is a linear operator used to control the spatial regularity of w. The energy (3.4) explicitly combines a data potential $\rho(\cdot)$, which penalizes irregular shapes in the image f with respect to neighboring pixels of (i,j), with a regularization potential $\phi(\cdot)$ which penalizes high values of the norm of $(Lw)_{i,j}$. A typical example of ϕ and L is the combination of the square L_2-norm ($\phi(\cdot) = \|\cdot\|_2^2$) and the gradient operator ($L = \nabla$) as $\phi\big((Lw)_{i,j}\big) = \|(\nabla w)_{i,j}\|_2^2 = (\partial_x w)_{i,j}^2 + (\partial_y w)_{i,j}^2$, where ∂_x and ∂_y denote the first-order derivatives along the horizontal (x-axis) and vertical (y-axis) directions respectively.

This reformulation is inspired from the concept of regularized vector field which is widely used in optical flow to compute the motion between a pair of frames in a video sequence [Brox and Malik 2011; Fortun et al. 2015]. In the context of dejittering, regularizing the displacement field allows to overcome two major problems: (i) data over-fitting as observed with unregularized approaches [Kokaram 1998; Nikolova 2009b]; (ii) discontinuity over-smoothing as observed when regularization-based approaches are applied to jittered images [Shen 2004; Lenzen and Scherzer 2011; Dong et al. 2015].

3.4.2 Data fidelity term

The corrected version of the jittered image f by the displacement w is defined as:

$$\{\tilde{u}_{i,j} = f[i + w_{i,j}, j]\}_{(i,j)\in\Lambda} . \tag{3.5}$$

By considering the vertical regularity of the corrected image $\tilde{u}$, a data potential $\rho(\cdot)$ is designed to re-align the jittered image f as:

$$\rho(i,j,f,w) = |(D^{(k)}\tilde{u})_{i,j}|^{\beta} , \tag{3.6}$$

where $D^{(k)}$ denotes the discrete k^{th} order vertical derivative operator and β is a positive parameter which controls the amount of non zero entries of $D^{(k)}\tilde{u}$. In other words, $\rho(\cdot)$ favors sparse $D^{(k)}\tilde{u}$ if $0 < \beta \leq 1$, otherwise this potential promotes non-

sparse configurations. If $k = 1, 2$ and 3, we have the following discrete derivatives:

$$\begin{aligned}(D^{(1)}\tilde{u})_{i,j} &= \tilde{u}_{i,j} - \tilde{u}_{i,j-1} \\ &= f[i + w_{i,j}, j] - f[i + w_{i,j-1}, j - 1] \ ,\end{aligned}$$

$$\begin{aligned}(D^{(2)}\tilde{u})_{i,j} &= \tilde{u}_{i,j+1} - 2\tilde{u}_{i,j} + \tilde{u}_{i,j-1} \\ &= f[i + w_{i,j+1}, j + 1] - 2f[i + w_{i,j}, j] + \ f[i + w_{i,j-1}, j - 1] \ ,\end{aligned}$$

$$\begin{aligned}(D^{(3)}\tilde{u})_{i,j} &= \tilde{u}_{i,j+1} - 3\tilde{u}_{i,j} + 3\tilde{u}_{i,j-1} - \tilde{u}_{i,j-2} \\ &= f[i + w_{i,j+1}, j + 1] - 3f[i + w_{i,j}, j] \\ &\quad + 3f[i + w_{i,j-1}, j - 1] - f[i + w_{i,j-2}, j - 2] \ ,\end{aligned}$$

with the symmetric boundary conditions in the vertical direction such that $\tilde{u}_{i,j} = \tilde{u}_{i,-j}$ if $j < 0$ and $\tilde{u}_{i,j} = \tilde{u}_{i,2N-j}$ if $j > N$. In what follows, we choose $k = 2$ and $\beta = 1$ since these values allow to recover images with nearly piece-wise linearity in the vertical direction (see Nikolova (2009a,b)). However, this potential exhibits spatial dependency on w since $\rho(i, j, f, w)$ not only depends on $w_{i,j}$ but also on other entries $w_{i,j'}$ where j' is a neighbor of j according to the order k of the derivative.

Instead of considering the potential (3.6), a point-wise term when no spatial dependency on w is desired to facilitate the optimization task. From the condition (3.3), the displacement field w is non zero on odd lines (i.e. the function $i \longmapsto w_{i,j} \neq 0$ for $j \notin 2\mathbb{Z}$). Therefore, let us consider the odd line translation $\mathcal{T}_{w_{i,j}}$ defined as:

$$(\mathcal{T}_{w_{i,j}} f)_{i',j'} = \begin{cases} f[i', j'] & \text{if } j' \in 2\mathbb{Z} \ , \\ f[i' + w_{i,j}, j'] & \text{otherwise} \ . \end{cases}$$

By assuming that the variation of the displacement between odd and even lines on a small neighborhood of a point is infinitesimal, we consider novel non-local potential $\rho_{\boldsymbol{\sigma}}$ defined as follows:

$$\rho_{\boldsymbol{\sigma}}(w_{i,j}, f) = \begin{cases} 0 & \text{if } j \in 2\mathbb{Z} \ , \\ \displaystyle\sum_{(i',j') \in \boldsymbol{\sigma}(i,j)} |D^{(k)}(\mathcal{T}_{w_{i,j}} f)_{i',j'}|^{\beta} & \text{otherwise} \ , \end{cases}$$

where $\boldsymbol{\sigma}(i, j) = \{i - \lfloor \frac{r}{2} \rfloor, \ldots, i + \lfloor \frac{r}{2} \rfloor\} \times \{j - \lfloor \frac{s}{2} \rfloor, \ldots, j + \lfloor \frac{s}{2} \rfloor\}$ is a patch of size $r \times s$ pixels centered at pixel (i, j). The new data term, defined as:

$$E_D(w, f) = \sum_{i=0}^{M} \sum_{j=0}^{N} \rho_{\boldsymbol{\sigma}}(w_{i,j}, f) \ , \tag{3.7}$$

is a generalization of the point-wise data term.

3.4.3 Regularization term

We consider the following regularization term which exploits the alternating structure of the displacement field:

$$E_R(w) = \sum_{i=1}^{M}\sum_{j=2}^{N}\left\{\lambda\big(w_{i,j} - w_{i-1,j}\big)^2 + \ \nu\big(w_{i,j} - w_{i,j-2}\big)^2\right\}. \tag{3.8}$$

Here, $\lambda, \nu \geq 0$ are regularity parameters which control the regularity of w along the horizontal and vertical directions respectively. Also, we impose that the restored image has no sharp discontinuity. If we denote $L_{\lambda,\mu}$ the discrete differential-based operator as:

$$(L_{\lambda,\mu}w)_{i,j} = \begin{bmatrix} \sqrt{\lambda}\big(w_{i,j} - w_{i-1,j}\big) \\ \\ \sqrt{\mu}\big(w_{i,j} - w_{i,j-2}\big) \end{bmatrix} \in \mathbb{R}^2 \ ,$$

for $1 \leq i \leq M$ and $2 \leq j \leq N$ (otherwise $(L_{\lambda,\mu}w)_{i,j}$ is a null vector), the regularization term (3.8) can be rewritten as:

$$E_R(w) = \sum_{i=0}^{M}\sum_{j=0}^{N} \|(L_{\lambda,\mu}w)_{i,j}\|_2^2 \ , \tag{3.9}$$

where $\|\cdot\|_2$ denotes the Euclidean norm.

3.4.4 Optimization of the energy functional

Considering the proposed data and regularization terms, the final energy functional has the following form:

$$E(w) = \sum_{i=0}^{M}\sum_{j=0}^{N} \rho_{\boldsymbol{\sigma}}(w_{i,j}, f) + \|(L_{\lambda,\mu}w)_{i,j}\|_2^2 \ , \tag{3.10}$$

in which the second term is convex with respect to w and the first term is non-convex. The combination of a convex term with a non-convex term makes the underlying optimization problem difficult to optimize in general. Existing algorithms (e.g., [Mercier 1979; Eckstein and Bertsekas 1992; Combettes 2004; Combettes and Pesquet 2011; Chambolle and Pock 2011; Condat 2014]) cannot be applied to minimize (3.10). This situation is closely similar to the variation formulation of the optical flow problem (see [Horn and Schunck 1981; Fortun et al. 2015]) in which the non-convex data term is usually coupled with a convex regularity term (see [Zach et al. 2007, Wedel et al. 2009]). In addition, the two terms eventually may be not continuously differentiable. One computational approach consists in linearizing the data term and replacing the non differentiable functions by smoothly approximated versions. Standard differentiable optimization techniques can be then used to minimize the new energy. To avoid any approximations, we adopt the approach of Steinbrücker et al. (2009) and propose to optimize a quadratically relaxed version of (3.10) of the

following form:

$$E_\epsilon(w) = \sum_{i=0}^{M}\sum_{j=0}^{N} \rho_{\boldsymbol{\sigma}}(w_{i,j}, f) + \frac{1}{2\epsilon}(w_{i,j} - v_{i,j})^2 + \|(L_{\lambda,\mu} v)_{i,j}\|_2^2 \,, \tag{3.11}$$

where ϵ is a small constant and $v : (i,j) \longmapsto v_{i,j}$ is an auxiliary variable used to approximate w. The use of auxiliary variable for decoupling convex and non-convex part is also known as the half-quadratic method which was originally introduced by Geman and Yang (1995). This splitting technique is widely used in both linearized and non-linearized optical flow models (e.g., [Zach et al. 2007; Wedel et al. 2009; Steinbrücker et al. 2009]) to decompose the original optimization problem into two more tractable sub-problems.

Moreover, since the magnitude of displacement does not exceed a certain bound, one can add the convex constraint $\{\|w\|_\infty = \max_{i,j} |w_{i,j}| \leq w_{\max}\}$ to the relaxed optimization problem (3.11) where $w_{\max}$ denotes the maximal absolute value of displacement. Finally, we consider the final optimization problem:

$$\begin{aligned}(\hat{w}, \hat{v}) = \underset{w,v}{\operatorname{argmin}} \sum_{i=0}^{M}\sum_{j=0}^{N} \Big\{ & \rho_{\boldsymbol{\sigma}}(w_{i,j}, f) + \imath_{\boldsymbol{\mathcal{C}}}(w_{i,j}) \\ & + \frac{1}{2\epsilon}(w_{i,j} - v_{i,j})^2 \\ & + \|(L_{\lambda,\mu} v)_{i,j}\|_2^2 + \imath_{\boldsymbol{\mathcal{C}}}(v_{i,j}) \Big\} \,,\end{aligned} \tag{3.12}$$

where $\imath_{\boldsymbol{\mathcal{C}}}$ denotes the characteristic function of the subset $\boldsymbol{\mathcal{C}} = [-w_{\max},\ w_{\max}] \subset \mathbb{R}$ defined as ($r \in \mathbb{R}$):

$$\imath_{\boldsymbol{\mathcal{C}}}(r) = \begin{cases} 0 & \text{if } r \in \boldsymbol{\mathcal{C}} \,, \\ +\infty & \text{otherwise} \,. \end{cases}$$

This problem can be solved by alternating two optimization steps to update either w or v at each iteration:

- For v being fixed, solve

$$\underset{w}{\operatorname{argmin}} \sum_{i=0}^{M}\sum_{j=0}^{N} \left\{ \imath_{\boldsymbol{\mathcal{C}}}(w_{i,j}) + \rho_{\boldsymbol{\sigma}}(w_{i,j}, f) + \frac{1}{2\epsilon}(w_{i,j} - v_{i,j})^2 \right\} . \tag{3.13}$$

  This problem can be solved point-wise, since there are no spatial dependency term for w in (3.13). Therefore, the optimal values for $w_{i,j}$ at every point (i,j) can be simply computed by an exhaustive search in the discrete set of possible displacements:

$$\boldsymbol{\mathcal{W}} = \{-w_{\max}, -w_{\max} + \delta, -w_{\max} + 2\delta, \ldots, w_{\max}\} \,,$$

  where the step δ can be chosen as small as possible to guarantee the sub-pixel precision of the estimated jitter. To handle these non-integer displacements, we use Fourier interpolation for fast computation. In practice, for each point

(i,j), we minimize the function $w_{i,j} \longmapsto \rho_{\boldsymbol{\sigma}}(w_{i,j}, f) + \frac{1}{2\epsilon}(w_{i,j} - v_{i,j})^2$ over the finite and countable set $\boldsymbol{\mathcal{W}}$ rather than $\boldsymbol{\mathcal{C}}$ which is finite but uncountable. This discrete minimization not only helps to avoid the linearization of the data term, which may yield inaccurate results, but also allows to deal with large and non-integer displacements.

- For w being fixed, solve

$$\underset{v}{\operatorname{argmin}} \sum_{i=0}^{M} \sum_{j=0}^{N} \left\{ \frac{1}{2\epsilon}(w_{i,j} - v_{i,j})^2 + \|(L_{\lambda,\mu} v)_{i,j}\|_2^2 + \imath_{\boldsymbol{\mathcal{C}}}(v_{i,j}) \right\} . \tag{3.14}$$

Since the constraint set $\boldsymbol{\mathcal{C}}$ is convex, this problem can be solved by a simple projected gradient descent algorithm summarized as follows:

$$\begin{cases} \tilde{v}_{i,j}^{(k)} & = \dfrac{1}{\epsilon}(v_{i,j}^{(k)} - w) + (L_{\lambda,\mu}^{\top} L_{\lambda,\mu} v^{(k)})_{i,j} \ , \\ \\ v_{i,j}^{(k+1)} & = \operatorname{proj}_{\boldsymbol{\mathcal{C}}}(v_{i,j}^{(k)} - \gamma_k \tilde{v}_{i,j}^{(k)}) \ , \end{cases} \tag{3.15}$$

where $L_{\lambda,\mu}^{\top}$ denotes the adjoint of $L_{\lambda,\mu}$ and $\operatorname{proj}_{\boldsymbol{\mathcal{C}}}$ denotes the projection to the set $\boldsymbol{\mathcal{C}}$. To ensure the convergence of projected gradient descent iterations, the descent step γ_k satisfies the usual condition

$$0 < \gamma_k < \frac{2}{4(\lambda + \mu)} \ . \tag{3.16}$$

Note that the projected gradient descent algorithm is a particular case of the forward-backward algorithm (see [Combettes and Wajs 2005; Combettes and Pesquet 2011]). This algorithm also belongs to the family of proximal algorithms as depicted in [Condat 2014].

3.5 Experiment results

In order to evaluate our variational method, we consider both true and simulated jittered images. The real images are acquired by fluorescence scanners of the series InnoScan commercialized by Innopsys company. The laser beam is moving according to a programmed trajectory to scan input microscopic slides. In the scanner design, the velocity of the laser beam is not constant during the scanning: it starts slowly at the beginning of a line, then accelerates from left to right before reaching the maximum value at the middle of the line, and decelerates smoothly until the right border. The scan direction is reverse on the subsequent line (scanning from right to left). The desynchronization between the mechanical system, which controls the movement of the scanning laser beam, and the electronic system, which converts analog signals to digital output, leads to the recording of pixels at wrong positions. Consequently, we observe a vertical rolling effect of odd and even lines with non-constant displacements along the horizontal direction, low at the left and right borders of the lines, and maximal at the middle. The typical spatially-varying jittering effect is illustrated in Fig. 3.3 (different magnitudes of displacement).

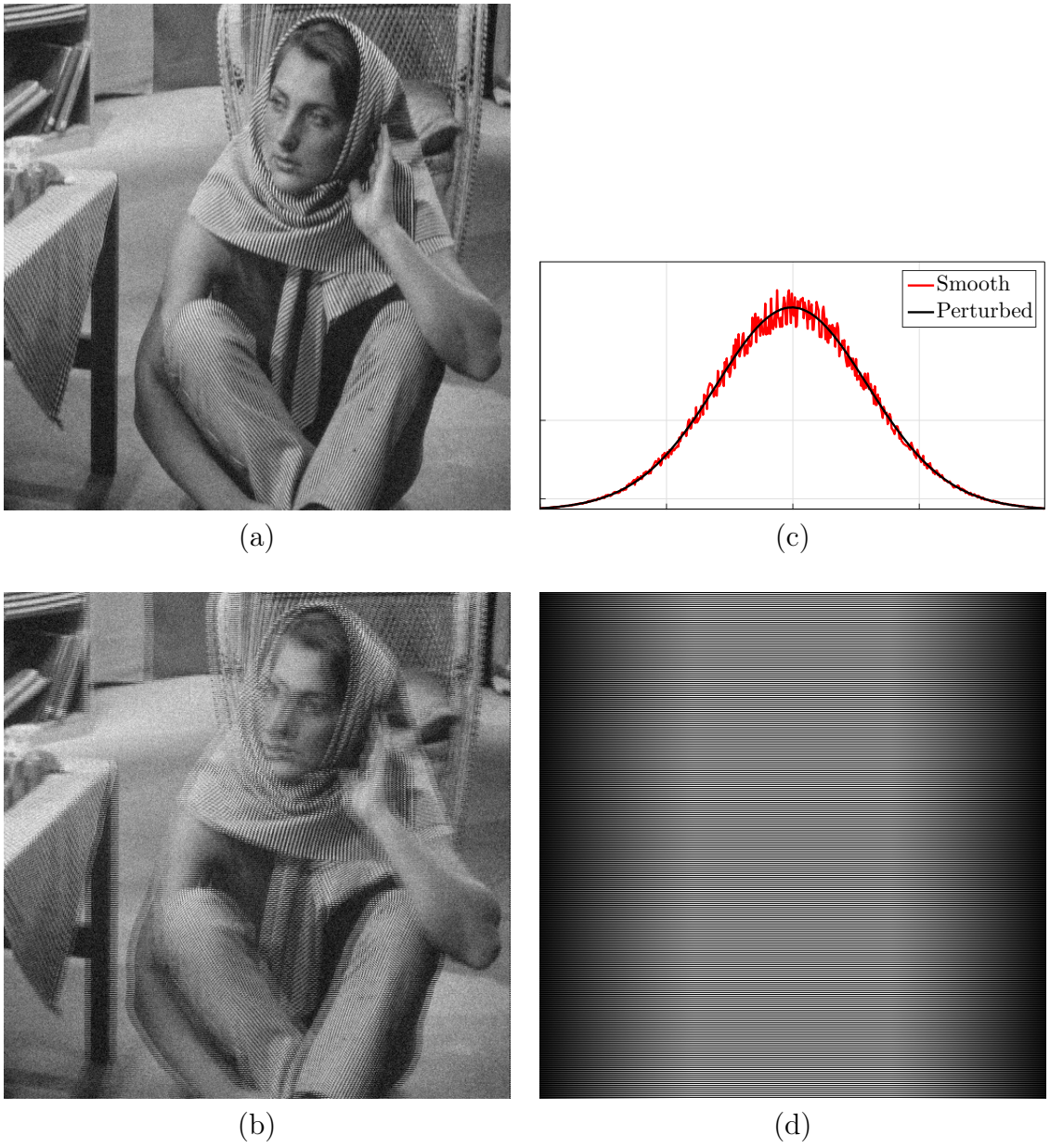

Figure 3.4: **Simulation of jittering on the *Barbara* 512 × 512 image by using a sinus function.** (a) Original image; (b) jittered image; (c) simulated displacement on even lines with respect to the horizontal axis (in pixels) plotted with an exponential scale: smooth displacement (red curve) is computed by using a sinus function and the perturbed version (black curve) is generated by adding small random values; (d) displacement field associated with (b) (black color represents zero value).

3.5.1 Evaluation on simulated images

To simulate the same jittering effect as in fluorescence scanner images, we first generated a dense displacement field which is zero on odd lines, and non-constant on even lines. The displacement with respect to the horizontal coordinate smoothly increases on the first half of the line and decreases on the second half according to a sinus function evolution. Random perturbation with small magnitude (less than one tenth of the pixel) was then added to the displacement field to model the micro-

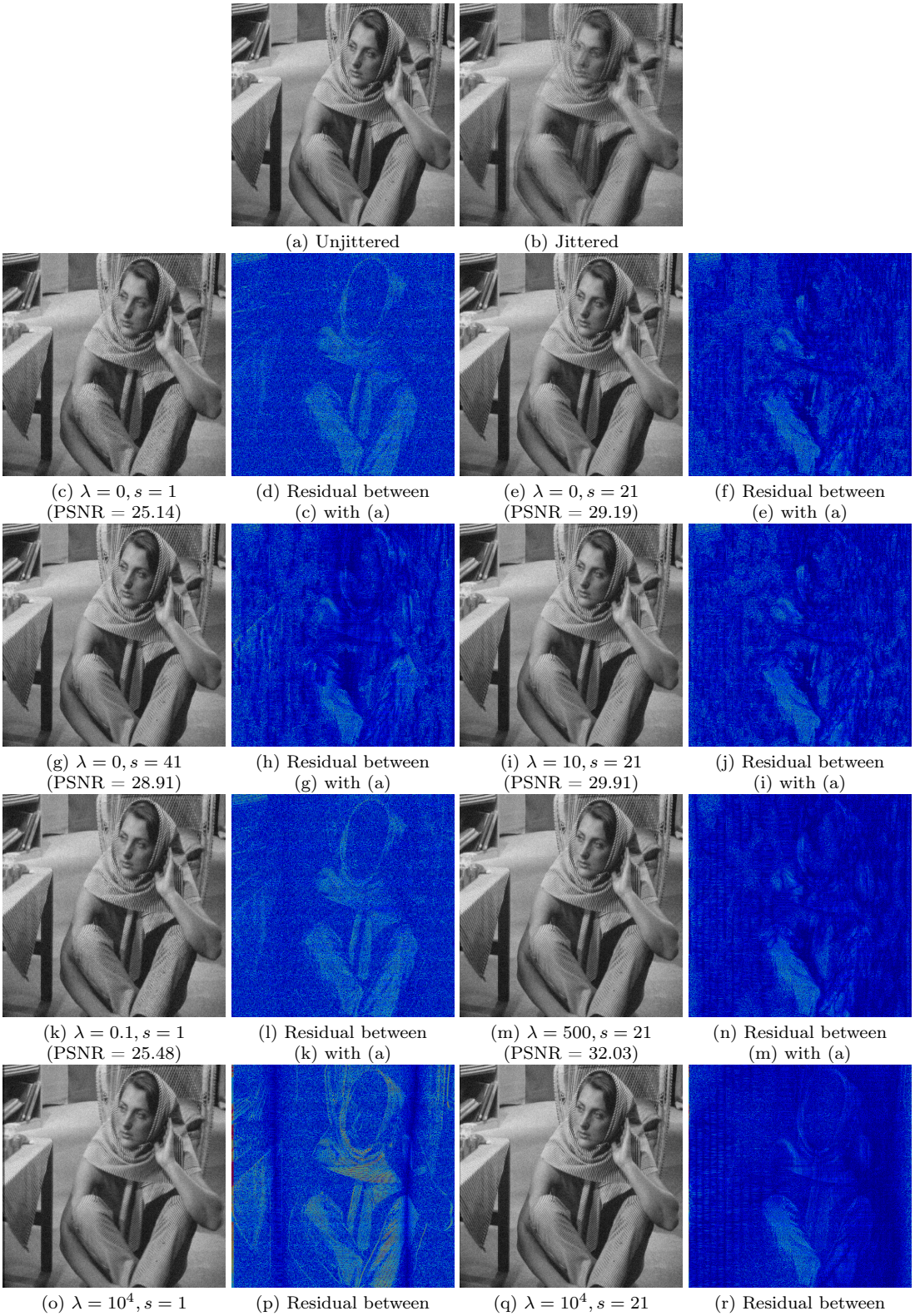

(a) Unjittered (b) Jittered

(c) $\lambda = 0, s = 1$ (PSNR = 25.14) (d) Residual between (c) with (a) (e) $\lambda = 0, s = 21$ (PSNR = 29.19) (f) Residual between (e) with (a)

(g) $\lambda = 0, s = 41$ (PSNR = 28.91) (h) Residual between (g) with (a) (i) $\lambda = 10, s = 21$ (PSNR = 29.91) (j) Residual between (i) with (a)

(k) $\lambda = 0.1, s = 1$ (PSNR = 25.48) (l) Residual between (k) with (a) (m) $\lambda = 500, s = 21$ (PSNR = 32.03) (n) Residual between (m) with (a)

(o) $\lambda = 10^4, s = 1$ (PSNR = 21.19) (p) Residual between (o) with (a) (q) $\lambda = 10^4, s = 21$ (PSNR = 31.32) (r) Residual between (q) with (a)

Figure 3.5: **Result of dejittering with different parameters of regularization λ and window size s on the *Barbara* image (512×512) corrupted with white Gaussian noise ($\sigma = 0.04$).** Residual images are shown in color where "cold" colors correspond to low residual values and "hot" colors correspond to high residual values.

vibration of the acquisition system. A set of eight images was selected and corrupted with the artificial jittering process. An example of jitter simulation applied to the *Barbara* image is shown in Fig. 3.4.

3.5.1.1 Robustness to noise

To analyze the robustness of our approach to noise, a zero-mean white Gaussian noise with variance σ^2 is first added to the original images before artificially jittering the images. The performance of our algorithm on these images is measured by the Peak Signal-to-Noise Ratio (PSNR) and by the Structural Similarity (SSIM) index between the dejittered images and their unjittered version in both noise-free and noisy cases. In the case of real data, the ground truth is not available and quantitative evaluation as described previously is not possible. Therefore, we display the dejittering outcome and visually compare in details the obtained results with the input images to highlight the effect of displacement correction. In all our experiments, we normalized the images in the range $[0, 1]$ to compare more objectively the results and to evaluate the influence of algorithm parameters. For the sake of simplicity, we focused on square windows ($s = r$) and isotropic regularization parameters ($\lambda = \nu$) when performing dejittering on simulated images.

A typical result of our dejittering method with different regularization parameters and estimation window sizes is illustrated in Fig. 3.5. On the second column of Fig. 3.5, the residual of dejittered images is also displayed to compare the results. In this example, the jitter-free image was corrupted with a white Gaussian noise with standard deviation $\sigma = 0.04$ (which corresponds to a value of PSNR = 26.77). The displacement field was estimated by setting the precision of displacement to $\delta = 0.1$ (in pixel) and $p = 0.5$. We can see that, even in the case of $s = 1$ (smallest estimation window) and $\lambda = 0$ (without regularization), the vertical rolling effect is significantly removed and most of large geometric structures and small details are well restored (see Figs. 3.5c, 3.5d and 3.6). However, we observe an aliasing effect on the restored image with these parameter settings (see the first column in Fig. 3.6). Aliasing typically occurs in regions near the left and right borders of the image where the displacement is relatively smaller than those observed in the middle of the image. Nevertheless, aliasing does not disturb the overall visual display. It is slightly reduced when increasing the size of the estimation window s and/or the regularization parameter λ as depicted in Fig. 3.6. In dense textured regions (see third column of Fig. 3.6), we notice that dejittering with parameters $s = 1$ and $\lambda = 0$ failed to properly recover very fine details. With these parameter settings, the orientation of the texture was wrongly estimated. It is mainly due to the repetition of patterns and the lack of regularity of the estimated displacement field.

We expected that dejittering with higher values of s and λ, both encouraging spatial regularities of the displacement field, would produce better reconstruction results. Surprisingly, setting $s = 21$ (large estimation window) and $\lambda = 0$ (no explicit regularization) yielded better restoration results than $s = 1$ and $\lambda = 0.1$ (highest value of SSIM with $s = 1$ among $\lambda \in \{0, 0.1, 1, 10, 500, 10000\}$, see Table 3.1). The final restoration result is very close to the result obtained with $s = 21$ and $\lambda = 10$ (see the third column of Fig. 3.6). This suggests that our method provides

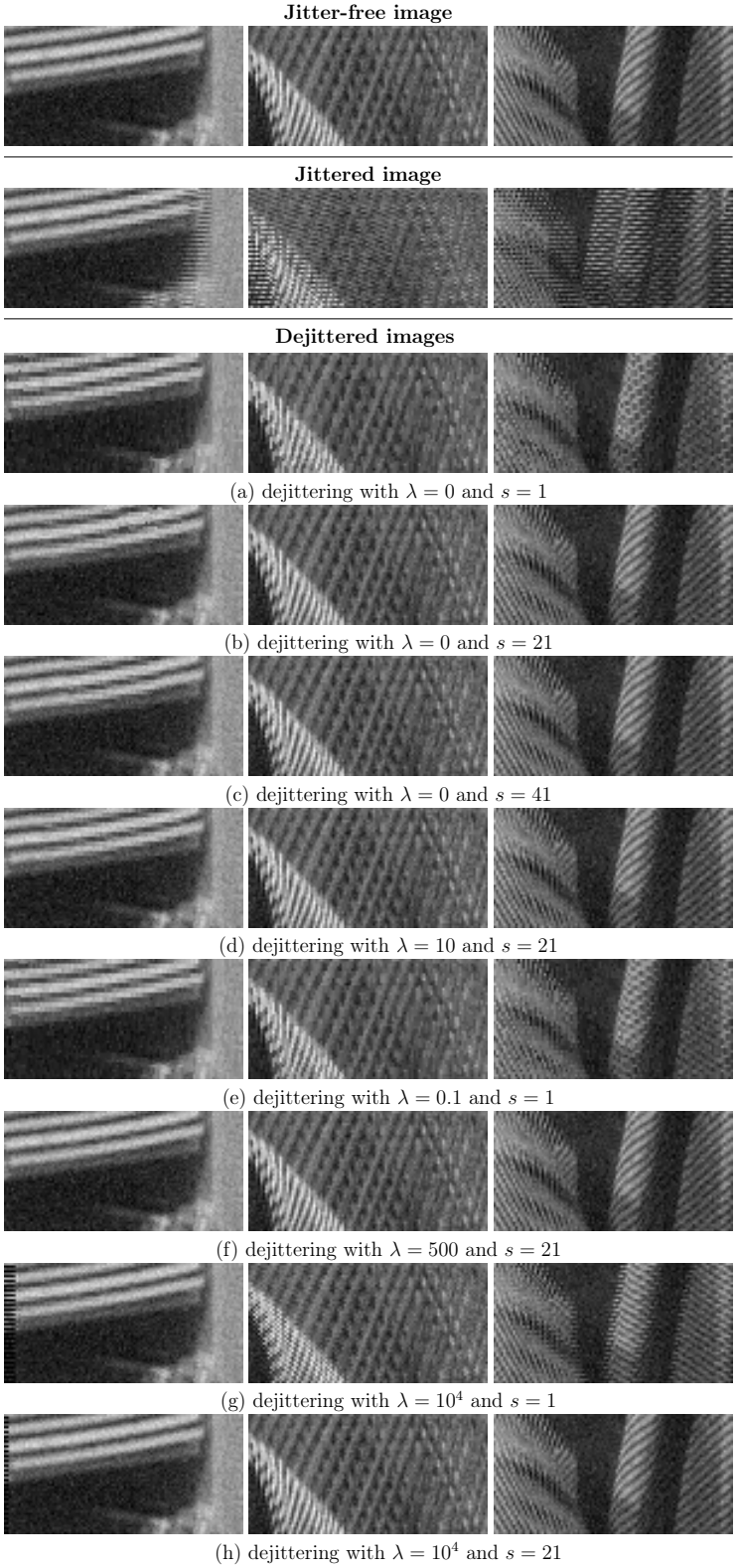

(a) dejittering with $\lambda = 0$ and $s = 1$

(b) dejittering with $\lambda = 0$ and $s = 21$

(c) dejittering with $\lambda = 0$ and $s = 41$

(d) dejittering with $\lambda = 10$ and $s = 21$

(e) dejittering with $\lambda = 0.1$ and $s = 1$

(f) dejittering with $\lambda = 500$ and $s = 21$

(g) dejittering with $\lambda = 10^4$ and $s = 1$

(h) dejittering with $\lambda = 10^4$ and $s = 21$

Figure 3.6: **Detail comparison of dejittering result with different parameters of regularization λ and window size s on the *Barbara* image (512×512) corrupted with white Gaussian noise ($\sigma = 0.04$).** First row: unjittered image. Second row: jittered image. Third row to ninth row: dejittered images with different values for λ and s.

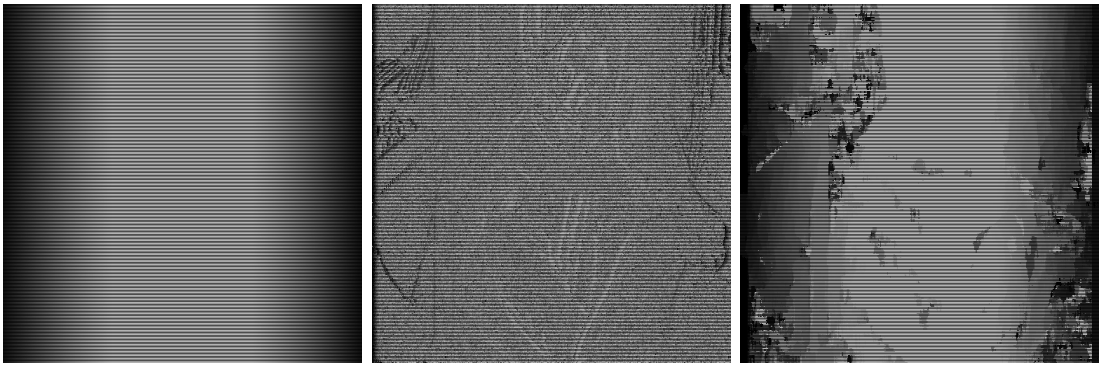

(a) Ground truth

(b) $\lambda = 0, s = 1$ (SSIM = 0.9088)

(c) $\lambda = 0, s = 21$ (SSIM = 0.9614)

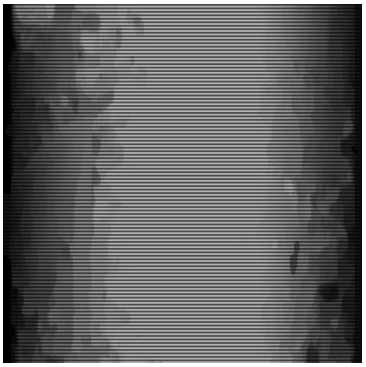

(d) $\lambda = 0, s = 41$ (SSIM = 0.9533)

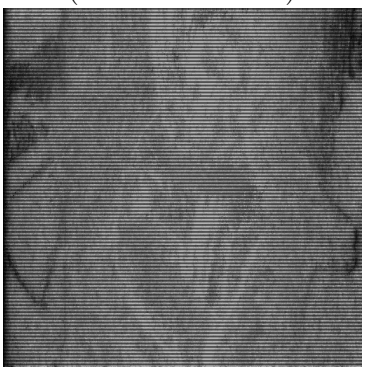

(e) $\lambda = 10, s = 21$ (SSIM = 0.9628)

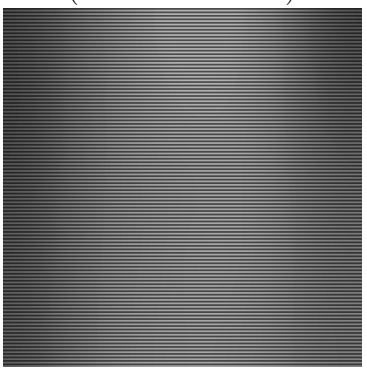

(f) $\lambda = 0.1, s = 1$ (SSIM = 0.9131)

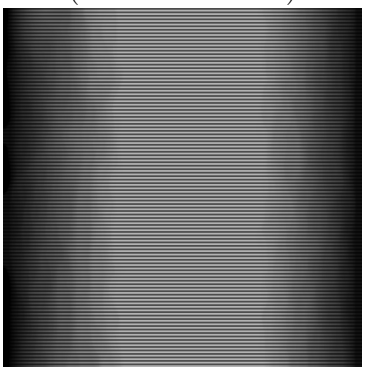

(g) $\lambda = 500, s = 21$ (SSIM = 0.9683)

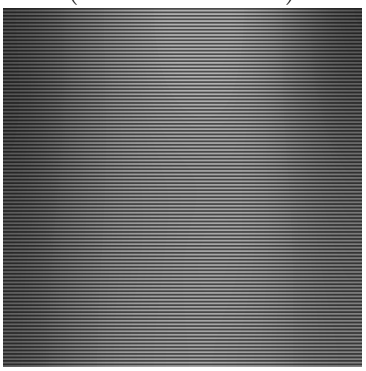

(h) $\lambda = 10^4, s = 1$ (SSIM = 0.7831)

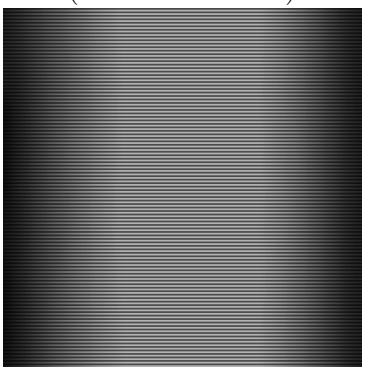

(i) $\lambda = 10^4, s = 21$ (SSIM = 0.9670)

Figure 3.7: **Comparison of estimated displacement fields with different parameters of regularization λ and window size s on the *Barbara* image corrupted with white Gaussian noise $\sigma = 0.04$.** Top left: Ground-truth. (b)-(h): Displacement fields estimated with different values of λ and s.

better results with larger estimation window sizes than with higher regularization parameters.

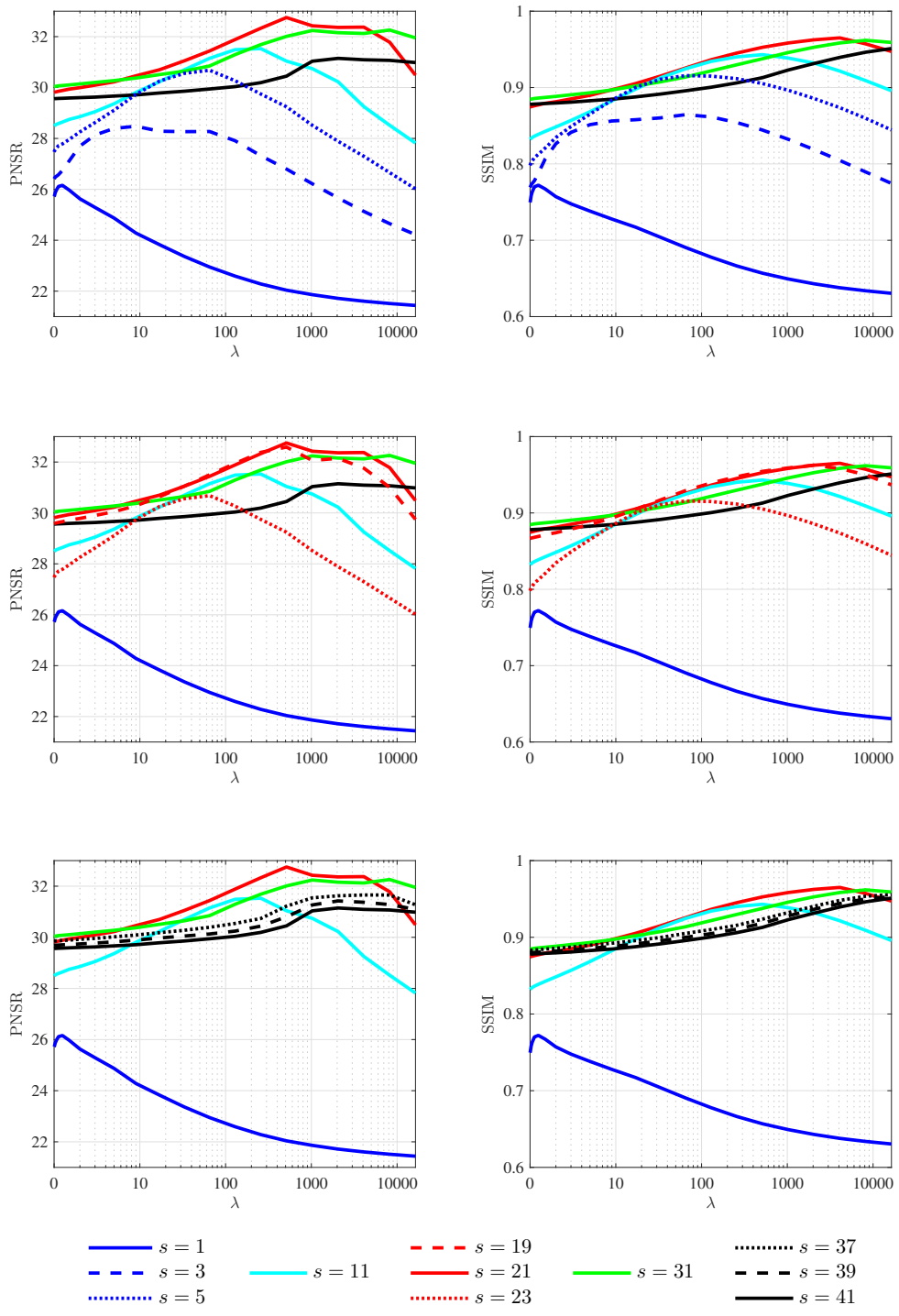

Figure 3.8: **Dejittering performance (PSNR and SSIM values) depending on λ for several values of s.** The scores are computed on the *Barbara* image corrupted with Gaussian white noise ($\sigma = 0.04$) and are plotted with a logarithmic scale for visualization purposes. We display the curves corresponding to three categories of window size: small windows (blue curves), medium windows (red curves) and large windows (black curves). The cyan and the green curves which correspond to $s = 11$ and $s = 31$ respectively are transitional between these three groups of windows.

3.5.1.2 Influence of regularization parameter and window size

To better understand the impact of λ and s in the estimation of the displacement field, the estimated displacement corresponding to the dejittering result in Fig. 3.5

are shown in Fig. 3.7. For comparison purpose, we also displayed in Fig. 3.7a the simulated displacement (ground truth) which was used to generate jittered images. Moreover, Fig. 3.7b shows the estimated displacement with $\lambda = 500$ and $s = 21$ which corresponds to the best value of SSIM scores (SSIM=0.9683) for all possible couples (λ, s). Finally, the displacement estimated with $\lambda = 10000$ is illustrated in the last row of Fig. 3.7 as may be considered as an extreme case. As expected, the larger estimation window and/or the higher regularization parameter, the more regular displacement field is obtained. Indeed, we can observe that image details visibly appear in the estimated field for $\lambda = 0$ and $s = 1$ (the smallest value of λ and s). For higher values of λ while the value s remains the same, these details are smoothed as shown in Figs. 3.7c, 3.7e and 3.7g. Meanwhile, the combination of larger s and $\lambda = 0$ provides piecewise-constant results (also known as staircasing effect). Sharp discontinuities are not expected, even though the dejittered image obtained with this parameter setting (Fig. 3.5g) provides very encouraging results. The staircasing effect can be reduced by setting a strictly positive value for λ to enforce the smoothness of the displacement (see Figs. 3.7d, 3.7f and 3.7h). In contrast, a high value of λ combined with a small value of s tends to over-smooth the displacement field as depicted in Fig. 3.7g ($\lambda = 10000$ and $s = 1$). Considering the same regularization parameter with large window sizes (e.g., $\lambda = 10000$ and $s = 21$) tends to produce results very close to the ground-truth as shown in Fig. 3.7h. This behavior emphasizes how the performance of our method depends on the regularization parameter λ and on the size s of the estimation window. Figure 3.8 shows plots of PSNR and SSIM values for different values of λ and s. In summary, the performance values vary as follows: for a given value of s, as λ increases, the performance (PSNR, SSIM) increases, reaches a maximum value, and decreases towards a limit value. From Fig. 3.8, it is recommended to combine a high value of the regularization parameter λ with a large estimation window size s.

For large scale comparison, we provide the SSIM values for all the tested images with different noise levels as well as several regularization parameters and window sizes in Table 3.1. It turns out that the performance of our method varies case by case and depends not only on the image itself but also on the amount of noise. In general, the higher the noise level is, the higher optimal values for λ and s are. To illustrate the performance obtained in case of strong noise, we display in Fig. 3.9 the three best dejittering results on *Mandrill* image (512×512) corrupted with a white Gaussian noise with standard deviation $\sigma = 0.1$. Even in the case of strong noise and complex texture, our method, which does not require any pre-processing (e.g., denoising), is able to restore fine details and vertical structures if appropriate values for λ and s are selected. In the three zoom-in views of Fig. 3.9 depicting reconstruction of eye, hair and beard regions in the *Mandrill* image, we notice that the occurred jitter is efficiently removed. The image details and textures are also well preserved in all cases.

3.5.2 Evaluation on real fluorescence scanner images

In this section, we evaluate the proposed algorithm on an fluorescence image of eight tissue microarray cores (see Fig. 3.10). This image, saved in 16-bit-TIFF format, was

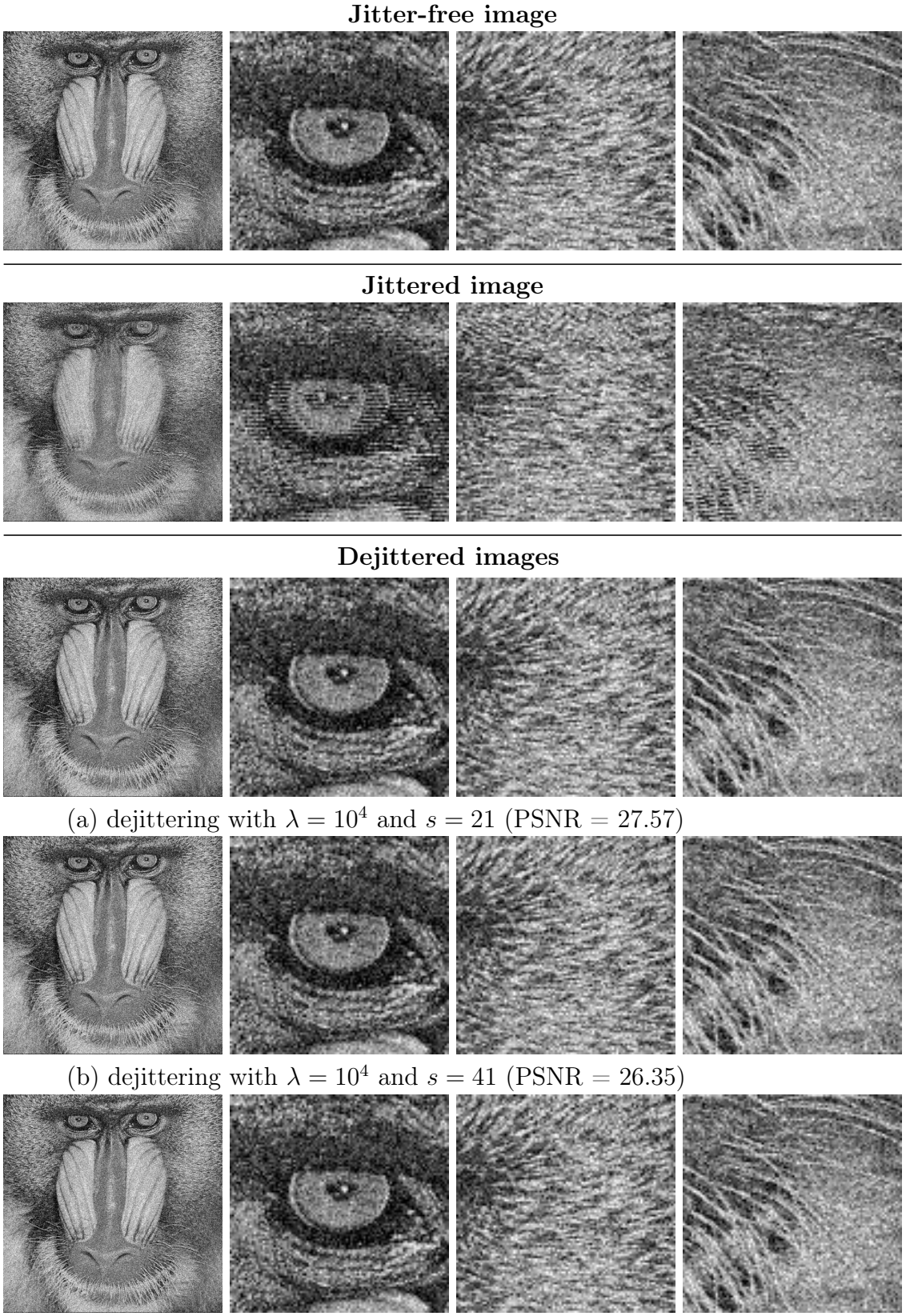

(a) dejittering with $\lambda = 10^4$ and $s = 21$ (PSNR = 27.57)

(b) dejittering with $\lambda = 10^4$ and $s = 41$ (PSNR = 26.35)

(c) dejittering with $\lambda = 10^3$ and $s = 21$ (PSNR = 25.31)

Figure 3.9: **Dejittering result on very noisy** *Mandrill* **image** (512×512) **(corrupted with white Gaussian noise** $\sigma = 0.1$**).** The first column contains full size images, all remaining columns display some regions of interest to compare in details. First row: jitter-free image. Second row: jittered image. Third row to fifth row: dejittering with different values for λ and s.

	$\lambda = 0$				$\lambda = 0.1$				$\lambda = 1$			
	$s = 1$	$s = 5$	$s = 21$	$s = 41$	$s = 1$	$s = 5$	$s = 21$	$s = 41$	$s = 1$	$s = 5$	$s = 21$	$s = 41$
$\sigma = 0$ (Noise-free)												
Barbara	0.9088	0.9419	0.9614	0.9533	0.9131	0.9456	0.9614	0.9533	0.9063	0.9518	0.9616	0.9534
Boat	0.9322	0.9624	0.9851	0.9771	0.9387	0.9683	0.9853	0.9771	0.9399	0.9812	0.9861	0.9772
Cameraman	0.9585	0.9846	0.9913	0.9851	0.9603	0.9888	0.9913	0.9851	0.9583	0.9930	0.9914	0.9852
Lena	0.9306	0.9576	0.9798	0.9742	0.9411	0.9621	0.9800	0.9742	0.9537	0.9750	0.9805	0.9743
Mandrill	0.7780	0.8295	0.9128	0.9302	0.8016	0.8471	0.9136	0.9303	0.8109	0.9024	0.9185	0.9313
Peppers	0.9018	0.9231	0.9533	0.9569	0.9161	0.9289	0.9537	0.9570	0.9187	0.9480	0.9554	0.9573
Phantom	0.9918	**0.9914**	0.9876	0.9868	0.9880	0.9908	0.9876	0.9868	0.9797	0.9888	0.9876	0.9867
Micro-tubule	0.9439	0.9827	0.9914	0.9911	0.9591	0.9845	0.9914	0.9911	0.9757	0.9888	0.9916	0.9912
$\sigma = 0.02$												
Barbara	0.8236	0.8647	0.9236	0.9166	0.8365	0.8722	0.9246	0.9168	0.8265	0.8965	0.9282	0.9174
Boat	0.8308	0.8629	0.9134	0.9140	0.8443	0.8698	0.9141	0.9144	0.8318	0.8902	0.9178	0.9155
Cameraman	0.8308	0.8450	0.8827	0.8894	0.8416	0.8525	0.8844	0.8900	0.8312	0.8702	0.8917	0.8926
Lena	0.8230	0.8515	0.9118	0.9170	0.8409	0.8590	0.9129	0.9171	0.8460	0.8887	0.9166	0.9179
Mandrill	0.7486	0.7962	0.8962	0.9177	0.7733	0.8127	0.8977	0.9179	0.7734	0.8738	0.9034	0.9190
Peppers	0.8068	0.8275	0.8885	0.9047	0.8275	0.8346	0.8893	0.9049	0.8255	0.8662	0.8947	0.9058
Phantom	0.7647	0.7620	0.7710	0.7895	0.7791	0.7574	0.7716	0.7895	0.7597	0.7553	0.7749	0.7909
Micro-tubule	0.8415	0.8842	0.9225	0.9321	0.8609	0.8891	0.9226	0.9321	0.8801	0.9064	0.9249	0.9331
$\sigma = 0.04$												
Barbara	0.7341	0.7815	0.8700	0.8729	0.7508	0.7911	0.8714	0.8731	0.7383	0.8229	0.8769	0.8745
Boat	0.7315	0.7604	0.8339	0.8423	0.7485	0.7666	0.8345	0.8423	0.7334	0.7928	0.8404	0.8441
Cameraman	0.7232	0.7309	0.7851	0.7938	0.7376	0.7343	0.7858	0.7942	0.7272	0.7583	0.7909	0.7967
Lena	0.7145	0.7407	0.8201	0.8452	0.7370	0.7456	0.8212	0.8455	0.7354	0.7790	0.8267	0.8466
Mandrill	0.7020	0.7416	0.8628	0.8944	0.7277	0.7558	0.8646	0.8947	0.7193	0.8224	0.8720	0.8961
Peppers	0.7046	0.7268	0.8051	0.8360	0.7291	0.7335	0.8067	0.8360	0.7261	0.7669	0.8140	0.8377
Phantom	0.5966	0.5991	0.6238	0.6485	0.6196	0.5973	0.6253	0.6495	0.6117	0.5997	0.6323	0.6522
Micro-tubule	0.7271	0.7644	0.8352	0.8595	0.7490	0.7715	0.8356	0.8594	0.7535	0.7976	0.8396	0.8607
$\sigma = 0.1$												
Barbara	0.7341	0.7815	0.8700	0.8729	0.7508	0.7911	0.8714	0.8731	0.7383	0.8229	0.8769	0.8745
Boat	0.7315	0.7604	0.8339	0.8423	0.7485	0.7666	0.8345	0.8423	0.7334	0.7928	0.8404	0.8441
Cameraman	0.7232	0.7309	0.7851	0.7938	0.7376	0.7343	0.7858	0.7942	0.7272	0.7583	0.7909	0.7967
Lena	0.7145	0.7407	0.8201	0.8452	0.7370	0.7456	0.8212	0.8455	0.7354	0.7790	0.8267	**0.8466**
Mandrill	0.7020	0.7416	0.8628	0.8944	0.7277	0.7558	0.8646	0.8947	0.7193	0.8224	0.8720	0.8961
Peppers	0.7046	0.7268	0.8051	0.8360	0.7291	0.7335	0.8067	0.8360	0.7261	0.7669	0.8140	0.8377
Phantom	0.5966	0.5991	0.6238	0.6485	0.6196	0.5973	0.6253	0.6495	0.6117	0.5997	0.6323	**0.6522**
Micro-tubule	0.7271	0.7644	0.8352	0.8595	0.7490	0.7715	0.8356	0.8594	0.7535	0.7976	0.8396	**0.8607**

	$\lambda = 10$				$\lambda = 500$				$\lambda = 10000$			
	$s = 1$	$s = 5$	$s = 21$	$s = 41$	$s = 1$	$s = 5$	$s = 21$	$s = 41$	$s = 1$	$s = 5$	$s = 21$	$s = 41$
$\sigma = 0$ (Noise-free)												
Barbara	0.8799	0.9597	0.9628	0.9542	0.8237	0.9549	**0.9683**	0.9577	0.7831	0.9313	0.9670	0.9663
Boat	0.9315	**0.9916**	0.9881	0.9778	0.9008	0.9857	**0.9916**	0.9806	0.8772	0.9665	0.9859	0.9847
Cameraman	0.9434	**0.9953**	0.9915	0.9854	0.9299	0.9846	0.9916	0.9867	0.9182	0.9740	0.9843	0.9872
Lena	0.9551	0.9864	0.9824	0.9748	0.9363	0.9825	**0.9876**	0.9773	0.9135	0.9669	0.9838	0.9812
Mandrill	0.8186	0.9536	0.9294	0.9351	0.8068	0.9678	0.9620	0.9547	0.7894	0.9416	0.9711	**0.9771**
Peppers	0.9114	0.9685	0.9607	0.9586	0.8874	0.9650	0.9720	0.9650	0.8696	0.9378	0.9696	**0.9737**
Phantom	0.9640	0.9851	0.9873	0.9868	0.9492	0.9734	0.9841	0.9863	0.9472	0.9619	0.9769	0.9851
Micro-tubule	0.9748	0.9934	0.9924	0.9915	0.9538	0.9914	**0.9955**	0.9938	0.9334	0.9781	0.9926	0.9937
$\sigma = 0.02$												
Barbara	0.7967	0.9357	0.9372	0.9201	0.7232	0.9401	**0.9606**	0.9353	0.6881	0.8984	0.9588	0.9573
Boat	0.8152	0.9243	0.9275	0.9192	0.7771	0.9357	0.9650	0.9400	0.7561	0.8987	**0.9714**	0.9626
Cameraman	0.8123	0.9019	0.9092	0.8998	0.7967	0.9163	0.9574	0.9311	0.7850	0.8909	**0.9652**	0.9603
Lena	0.8472	0.9326	0.9284	0.9210	0.8197	0.9303	**0.9669**	0.9435	0.7935	0.8911	0.9642	0.9629
Mandrill	0.7761	0.9393	0.9176	0.9229	0.7607	0.9589	0.9578	0.9472	0.7434	0.9230	0.9685	**0.9747**
Peppers	0.8119	0.9212	0.9086	0.9100	0.7858	0.9253	0.9500	0.9325	0.7697	0.8798	0.9490	**0.9548**
Phantom	0.7382	0.7576	0.7860	0.7983	0.7231	0.7428	0.8041	0.8211	0.7200	0.7396	0.7936	**0.8281**
Micro-tubule	0.8754	0.9327	0.9335	0.9356	0.8403	0.9315	**0.9594**	0.9553	0.8135	0.8974	0.9455	0.9586
$\sigma = 0.04$												
Barbara	0.7036	0.8852	0.8930	0.8803	0.6409	0.9058	0.9461	0.9137	0.6191	0.8525	**0.9512**	0.9495
Boat	0.7054	0.8483	0.8565	0.8511	0.6696	0.8524	0.9115	0.8842	0.6575	0.7894	0.9245	**0.9278**
Cameraman	0.7034	0.7949	0.8065	0.8040	0.6863	0.8163	0.8595	0.8452	0.6757	0.7754	**0.8790**	0.8656
Lena	0.7198	0.8463	0.8464	0.8534	0.6981	0.8442	0.9069	0.8930	0.6793	0.7819	0.9134	**0.9248**
Mandrill	0.7072	0.9121	0.8912	0.9011	0.6866	0.9416	0.9505	0.9302	0.6735	0.8907	0.9641	**0.9647**
Peppers	0.7034	0.8374	0.8400	0.8450	0.6840	0.8412	0.9240	0.8932	0.6733	0.7718	0.9218	**0.9390**
Phantom	0.5875	0.6074	0.6525	0.6612	0.5706	0.6024	0.7137	0.6939	0.5674	0.5957	0.6734	**0.7226**
Micro-tubule	0.7382	0.8390	0.8527	0.8658	0.7004	0.8297	0.8907	0.8968	0.6820	0.7744	0.8843	**0.9084**
$\sigma = 0.1$												
Barbara	0.6021	0.7752	0.8108	0.8177	0.5679	0.7888	0.8993	0.8703	0.5603	0.7038	0.9083	**0.9241**
Boat	0.6004	0.7289	0.7572	0.7680	0.5827	0.7378	0.8479	0.8176	0.5814	0.6606	0.8599	**0.8729**
Cameraman	0.6009	0.6602	0.7040	0.7167	0.5827	0.6666	0.7841	0.7722	0.5763	0.6207	0.8063	**0.8139**
Lena	0.6010	0.7265	0.7243	0.7472	0.5806	0.7177	0.8188	0.8005	0.5746	0.6606	0.8136	0.8250
Mandrill	0.6054	0.7924	0.7899	0.8085	0.5899	0.8158	0.8994	0.8676	0.5873	0.7456	**0.9549**	0.9377
Peppers	0.5799	0.6996	0.7186	0.7363	0.5662	0.6881	0.8267	0.8003	0.5610	0.6332	0.8224	**0.8626**
Phantom	0.4783	0.4974	0.5336	0.5498	0.4629	0.4919	0.5831	0.5961	0.4604	0.4813	0.5617	0.6138
Micro-tubule	0.5807	0.6954	0.7028	0.7243	0.5679	0.6609	0.7597	0.7715	0.5653	0.6095	0.7193	0.7721

Table 3.1: Dejittering result on simulated data with different noise levels, window sizes and regularization parameters. The SSIM values are computed using the dejittered images and their corresponding unjittered (eventually noisy) version.

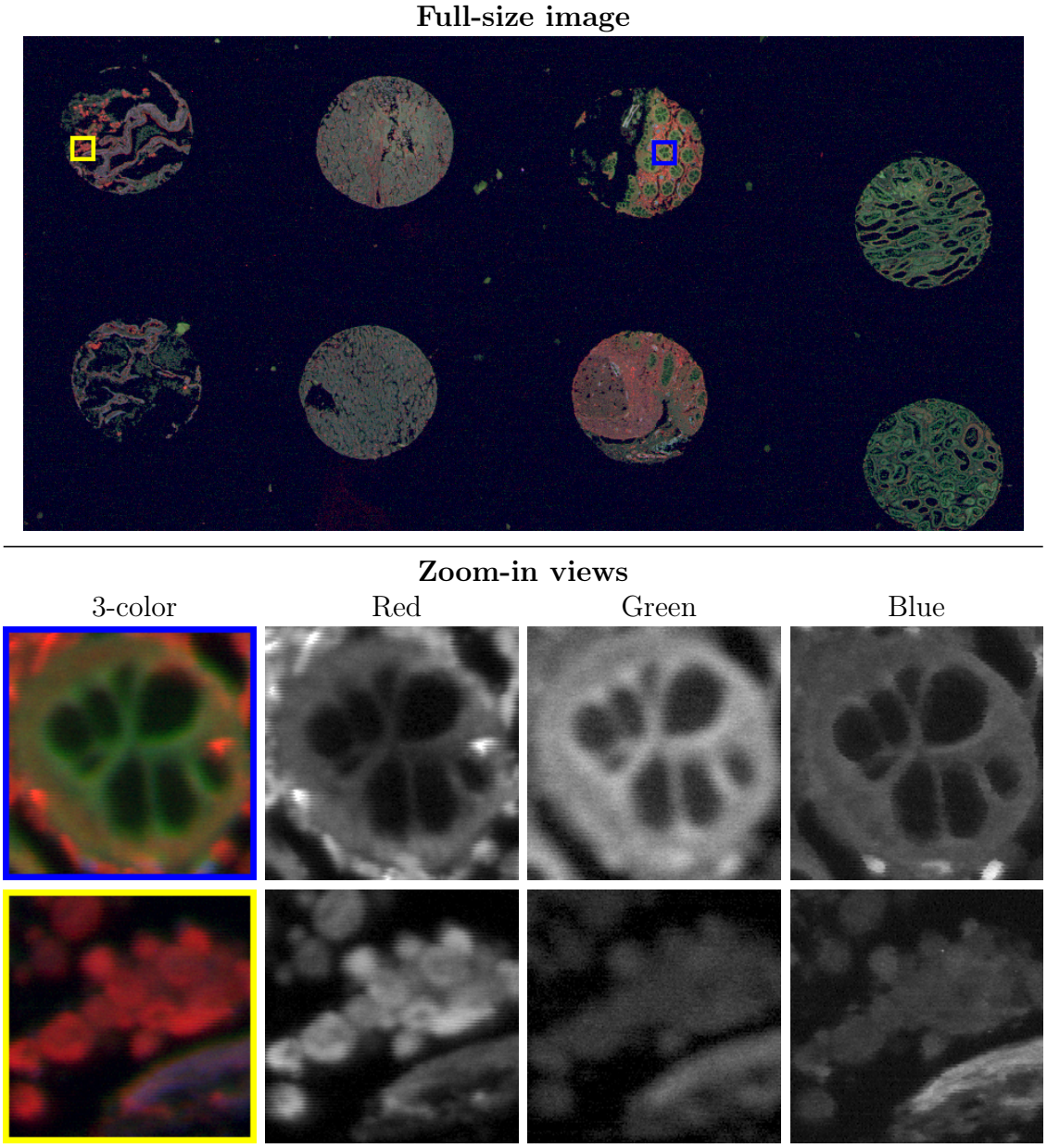

Figure 3.10: **Large jittered image depicting eight tissue microarray spots acquired by fluorescence scanner in three colors.** An region of interest of 4.7×2.8 mm^2 was scanned at spatial resolution of 0.5 μm/pixel, corresponding to an image of 9544 $\times$ 4704 pixels. Two areas which are marked by blue and yellow box are selected for comparison in details between the jittered input image and dejittering results. From top to bottom: full size image, zoom-in view of two selected areas (blue box and yellow box respectively). From left to right of two bottom rows: 3 colors at the same time, red (488 nm), green (532 nm) and blue (635 nm) channels displayed separately. We can clearly see that the vertical rolling effect in the red channel is stronger than in the two other channels.

acquired using the Innopsys fluorescence scanner named InnoScan 1100AL at the spatial resolution of 0.5 μm per pixel with three excitation wavelengths: 488 nm, 532 nm and 635 nm which are compatible with cyanine dye fluorophores such as Cy2, Cy3 and Cy5. In this experiment, the size of the acquired image is 9544×4704

pixels. Such a large image in which the absolute displacement between adjacent lines does not exceed 10 pixels requires huge computational resources if the dejittering is applied. In order to reduce the computational cost and to produce a satisfactory comparison between images before and after the correction of displacement error, we performed dejittering on non-background regions (i.e., tissue core regions) and we displayed several zoom-in views to better assess the results of the dejittering algorithm.

In this study, we first noticed that the vertical rolling effect on the jittered image (see two bottom rows of Figs. 3.10) in the red channel (488 nm) is visibly stronger than in green (532 nm) and blue (635 nm) channels. This suggests that the displacement is not the same for the three channels. To our knowledge, this is mainly due to the imperfection of the mechanical system which results in a trajectory difference of the three excitation beams. The dejittering was therefore performed separately on each channel and the result on the three channels was then merged to produce 3-color image as the original image. In this experiment, the values of λ and s are set as follows: $\lambda = 500$ and $s = 11$.

The dejittering result obtained with these parameters is reported in Fig. 3.11. We can notice that the jitter has been significantly reduced on the three channels. We observe however some regions where the jitter was not well corrected, especially in transition zones between bright and dark patches, but in overall the visual effect is sharply improved. Furthermore, in spite of the separate processing on each channel, the merged image of these dejittered versions does not suffer from decorrelation artifacts. Accordingly, no registration is required to re-align the dejittering results.

An example of dejittering result on image acquired over a large region of interest is also illustrated in Fig. 3.3 depicting a tool slide with checkerboard pattern used for scanner calibration. The width of the input image scanned at 1.0 μm per pixel, is about 6 thousand pixels corresponding to approximately 6 millimeters in real scale. Since the distance between two vertical lines of the images can reach several hundreds of pixels, large estimation windows (high value of s) are considered. As shown in the two bottom rows of Fig. 3.3, we can notice that dejittering without regularization provided satisfactory results in terms of visual quality on this piecewise constant image.

In general, the computational cost depends on the size of the input images as well as the parameter setting. The computing time is in average 3.8 ± 0.7 seconds in the case of dejittering without regularization and 26.9 ± 9.8 seconds with regularization on images of size 512×512 pixels. On real large images whose the width can reach several thousands of pixels as shown in this section, the computing time varies from less than 5 minutes to more than 10 minutes for dejittering without regularization and it is about more than one hour with regularization. The experiments were performed on a Macbook Pro equipped with 2.7 Ghz Intel Core i7, 16 Gb of RAM and the Mac OS X v. 10.12.4 operating system. The algorithm was implemented in C/C++ and we exploited the intrinsic parallelism of the CPU to solve large-scale problems.

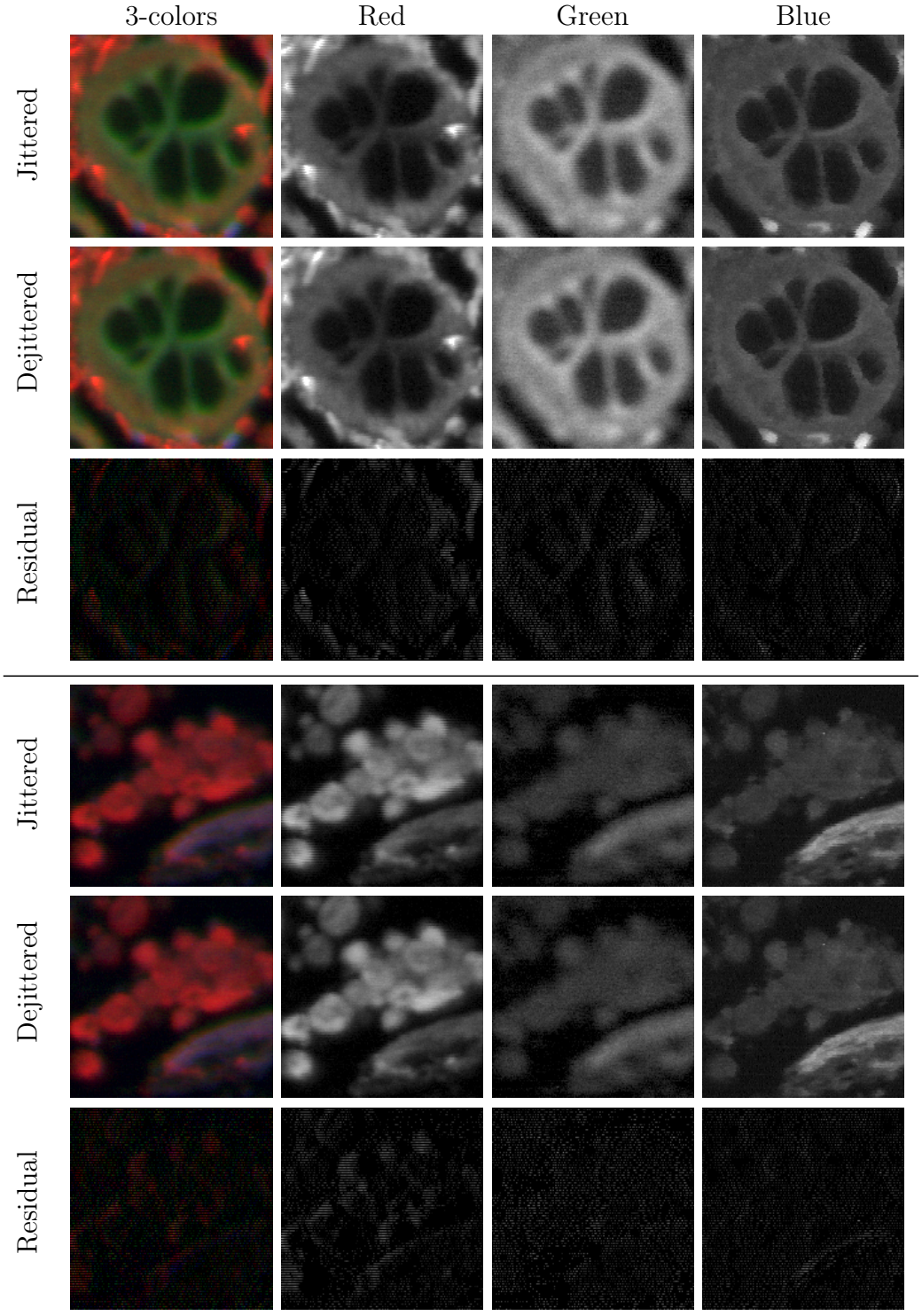

Figure 3.11: **Zoom-in views of the dejittering results obtained on two region of interest in the TMA image in Fig. 3.10.** Top panel: the area inside of the blue box. Bottom panel: the area inside of the yellow box. In each panel, from left to right: 3-color image, red (488 nm), green (532 nm) and blue (635 nm) channel; from top to bottom: jittered images, dejittered images, and residual images between the input and restored images.

3.5.3 Comparative studies

In this section, we compare our method to the approach proposed in [Nikolova

2009a,b], which will be named Nikolova's line dejittering (NLD) method in the sequel. The NLD method belongs to the class of displacement-estimation-based algorithms and may be considered as a state-of-the-art method for line jitter removal. In our experiments, we consider the standard version of NLD (i.e. Algorithm 1 in Nikolova (2009b) without denoising). In order to conduct a fair comparison of these two methods – one of which cannot handle non-constant displacements along the horizontal direction, and the other is not appropriate to random displacements along the vertical direction – we generated a specific structured jitter called "alternating line jitter": one line of every two lines is shifted but the displacement is constant along the horizontal direction. This jittering scenario fulfills the application conditions of each method, instead of those described in Section 3.5.1. Accordingly, jitter-free images (previously used for experiments in Section 3.5.1) are corrupted by the mentioned jittering process with both integer and non-integer displacements to evaluate the restoration performance. White Gaussian noise is also added to evaluate the robustness of the algorithms. Moreover, we have also performed comparisons on real fluorescence images: the two methods are applied on small regions of interest of Fig. 3.10, in which the displacement between two subsequent lines is quasi-constant along the horizontal direction. This situation is very close to the context of "alternating line jitter". Because strong regularity in both the vertical and horizontal directions is desired, one considers large estimation windows and high regularization values when applying our algorithm. Typically, we set $s = 81$ and $\lambda = 10^4$ in this experiment.

Examples of dejittering results on several simulated and real images corrupted with different signal-to-noise ratios, are illustrated in Fig. 3.12 showing zoom-in views of jittered and dejittered images obtained with the two methods. In the last column of Fig. 3.12, we can clearly notice that in the case of integer displacement, NLD produces results which are visually more pleasant while compared with jittered images. However, this method suffers from warping effect (distortion) appearing in regions depicting typically strong noise (e.g., *Barbara* image corrupted with Gaussian noise with standard deviation $\sigma = 0.04$) or noise-like textures (noise-free version of *Mandrill* image as shown in Fig. 3.12). These re-alignment artifacts are a direct consequence of the bias in the displacement estimation due to the lack of regularity of the estimated displacement along the vertical direction. Nikolova (2009b) then suggests to slightly modify the original NLD method by combining with a pre-denoising step when dealing with noisy images, especially in the case of strong noises. In contrast, our dejittering method is able to provide distortion-free results on jittered images with integer displacements (see the third row of Fig. 3.12) without any pre-processing, even when the noise is very strong. In the case of non-integer displacement, NLD performs poorly. It produces dejittered images which look highly warped in the vertical direction. In addition, the occurred jitter is not removed but replaced by another jitter, generating distorted images. In our opinion, this is because NLD, originally designed for integer displacement, does not support sub-pixel precision. Consequently, approximation errors on subsequent lines are accumulated, causing more severe errors. Strong distortion is also observed in the NLD dejittering results on real images (see bottom row of Fig. 3.12) as expected, due to infinitesimal variations and non-integer nature of the displacement field. In

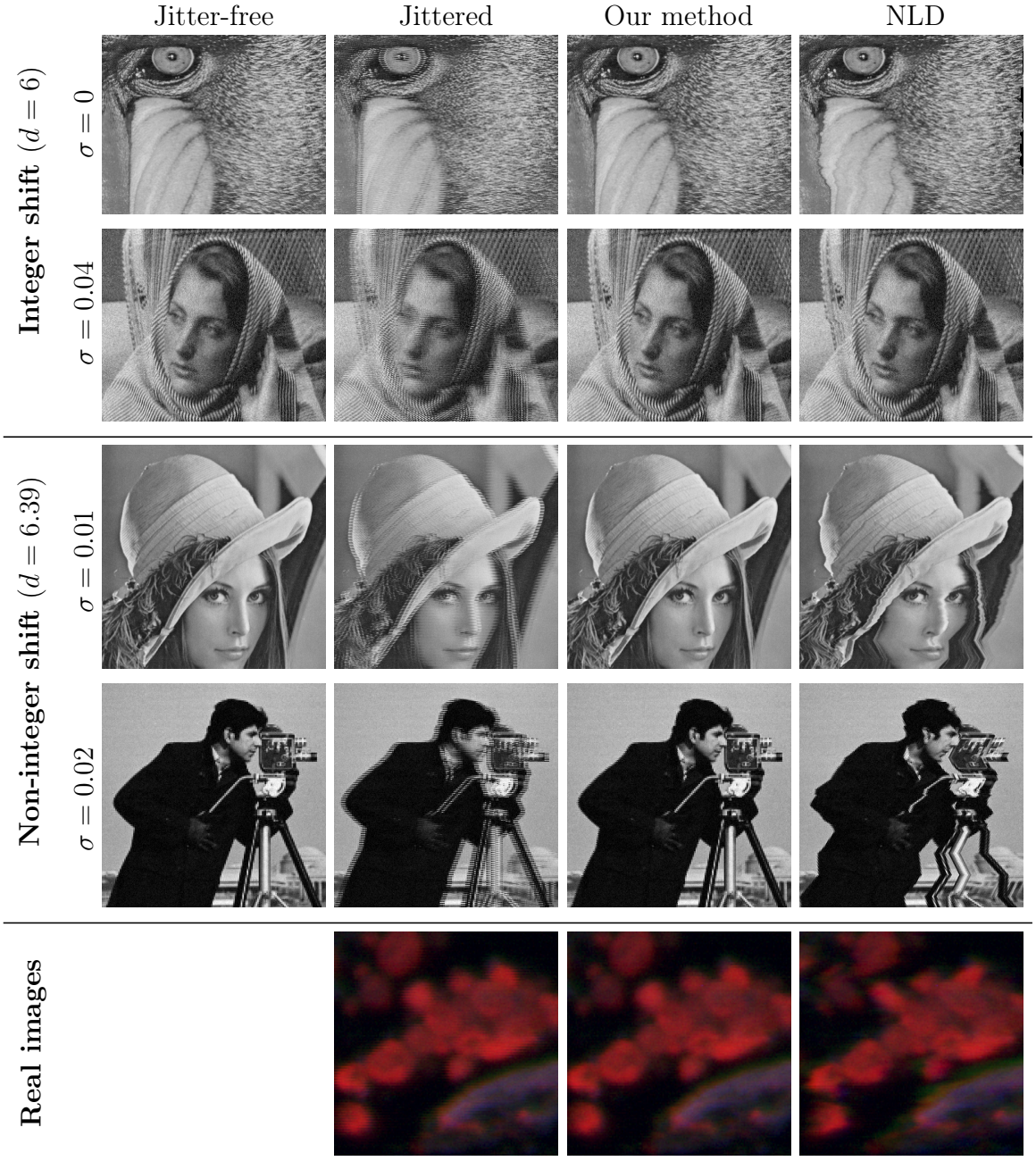

Figure 3.12: **Comparative dejittering results obtained with the proposed method and Nikolova's method (NLD) Nikolova (2009a,b).** From left to right: jitter-free images, jittered images, dejittered images obtained with our method, and dejittered images obtained with NLD. From top to bottom: zoom-in views of noisy-free *Mandrill* image (512×512) corrupted with integer line jitter ($d = 6$), *Barbara* image (512×512) corrupted with Gaussian noise ($\sigma = 0.04$) and integer line jitter ($d = 6$), *Lena* image (512×512) corrupted with Gaussian noise ($\sigma = 0.01$) and non-integer line jitter ($d = 6.39$), *Cameraman* image (512×512) corrupted with Gaussian noise ($\sigma = 0.02$) and non-integer line jitter ($d = 6.39$), and real fluorescence TMA image (see Fig. 3.10).

comparison to these unsatisfactory results, the dejittered images obtained with our algorithm are visibly much more better in all the three cases. On simulated images, the proposed method is able to restore very well fine details as well as large structures and produces results looking closely similar to the reference (jitter-free) images. Its

superior performance versus NLD emphasizes the necessity of taking into account of non-integer displacements and the influence of a dedicated regularization term when dealing with real-world structured jitter.

3.5.4 Denoising of jittered images

In many cases, it happens that image quality is degraded not only by jitter but also by noise during acquisition. The restoration task, therefore, aims at removing the occurred jitter as well as denoising the input acquired images. However, denoising without dejittering yields in general weak results since the existing denoising algorithms exploit contextual information from neighbor pixels which suffer from mispositioning due to jitter. It leads to unsatisfactory denoising results or, even worse, serious distortion of image details. To reduce these artifacts, several authors (e.g, [Shen 2004; Lenzen and Scherzer 2011; Dong et al. 2015]) recommend to jointly perform denoising and dejittering by iteratively estimating a jitter-free and noise-free image from the observed noisy and jittered image. These methods in principle incorporate a denoising step in the "global" restoration scheme, implying that a change of the denoising model requires major modifications in the resulting algorithm. While the performance of the latter on images, which are corrupted with "alternating line pixel jitter" and noise, still remains in question, it unfortunately is not practical if one envisages applying sophisticated denoising methods.

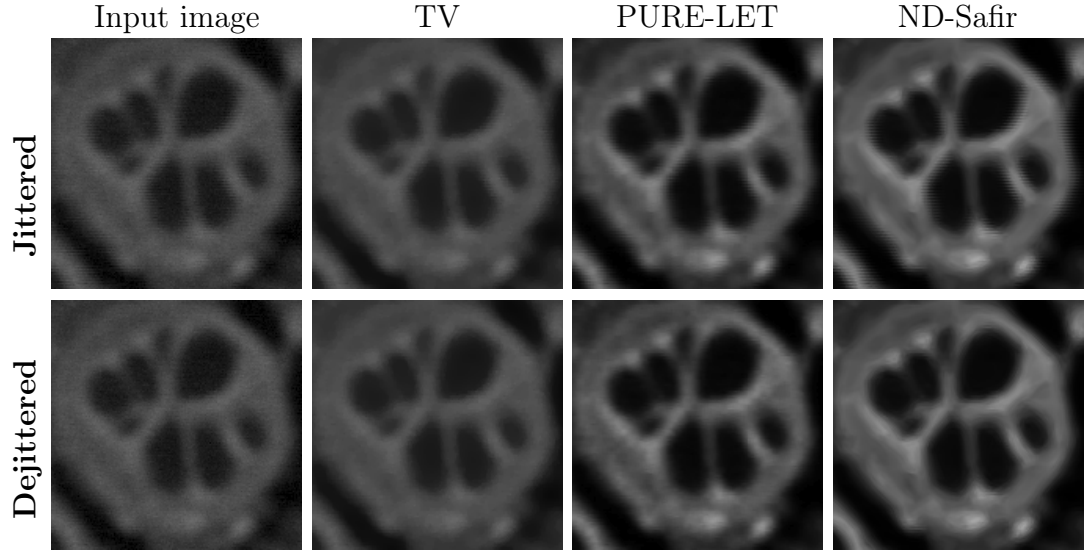

Figure 3.13: **Denoising results obtained with three different methods applied on a jittered and dejittered region of interest extracted from a real fluorescence TMA image shown in Fig. 3.10**. The jitter is not removed if denoising is applied on the jittered image (first row). For viusalization purposes, the original and restored images have been normalized in the range $[0, 1]$.

Accordingly, we consider here a more flexible two-step approach similar to those described in [Nikolova 2009b]. First, it consists dejittering the input images and then denoising the dejittered image. In comparison to Nikolova (2009b) which suggests two noise removal steps while dealing with jittered images with strong noise – i/ an

under-denoising step is applied before dejittering to improve the compensation of displacement errors; ii/ a full denoising step is applied on the dejittered images – we propose to denoise the jitter-corrected images, irrespective of the noise level. A variety of efficient denoising algorithms can be then combined with our dejittering method.

The two step approach is illustrated in Fig. 3.13 showing results obtained on one channel (Green component) of the fluorescence image in Fig. 3.10, using different advanced denoising methods, applied to jittered and dejittered images. In our experiments, we considered the Total Variation [Rudin et al. 1992], PURE-LET [Luisier et al. 2009, 2010] and ND-Safir [Kervrann and Boulanger 2006; Boulanger et al. 2010] algorithms. We can clearly notice that jitter cannot be removed if denoising is applied on the jittered images. Actually, noise is removed but jitter is visually emphasized. More satisfactory results are obtained if the dejittered images are denoised in a second step.

3.6 Conclusion

In this chapter, we have proposed a variational method to remove a specific jitter arising in large fluorescence scanner images. We formulate the dejittering problem as an estimation problem of the underlying displacement by minimizing an energy functional which combines convex regularization and non-convex non-local data terms. To solve the non-convex minimization problem, the half-quadratic splitting technique is used to decompose the energy functional into convex and and non-convex parts in such a way that the original minimization problem can be done by alternating two optimization steps. One step used the projected gradient algorithm to minimize the convex sub-problem. A fast exhaustive search is used to minimize the non-convex sub-problem in the second step. This approach allows us to approximate accurately the optimal solution of the original problem while avoiding the linearization of the data term. In numerous experiments, we show that our method is able not only to remove efficiently the rolling effect due to this jitter even in the case of huge images and large, non-integer displacements.

Chapter 4

Sparse variation based approach for fluorescence image deconvolution

Related publication

H.-N. Nguyen, V. Paveau, C. Cauchois, C. Kervrann. Generalized sparse variation regularization for large fluorescence image deconvolution[1]. Manuscript submitted for publication in IEEE Transactions on Image Processing, 2017

Abstract

In this chapter, we generalize the sparse variation (SV), which combines the total-variation (TV) regularization and the L_1 regularization, and introduce a novel family of convex and non-quadratic regularizers for fast deconvolution of large 2D fluorescence images. These regularizers are defined as mixed L_ν-L_2 norms ($\nu \geq 1$) which group image intensity and spatial differentials, computed at each pixel of the image. By coupling a regularization term of this family with a quadratic data fidelity term, we propose a fast and efficient deconvolution method by using the primal-dual (proximal) algorithms to minimize the corresponding energy functional. Experiment results on both 2D simulated and real fluorescence scanner images demonstrate the performance of our method in terms of restoration quality as well as computational time.
Keywords: Fluorescence imaging, image deconvolution, sparse variation, convex optimization, proximal algorithms

4.1 Introduction

Fluorescence microscopy is nowadays an imaging technique widely used in the field of biomedical sciences for cell biology research. The sample of interest is first labelled by fluorescent molecules before being excited by the illumination light of a given wavelength; upon the excitation, fluorophore re-emits light of relatively longer

[1]This work was supported by Innopsys.

wavelength which is then collected by photosensitive sensors to form the digitized image of the input sample. This imaging modality provides in practice a very powerful framework to biologists for observing, analyzing, and studying specific fluorescently-tagged structures at very high spatial and temporal resolutions.

Despite number of advantages, there are two major limitations of fluorescence microscopy. The first limitation is the presence of noise in acquired images. Similarly to other optical imaging techniques, the main contribution of noise here is the photon (shot) noise. The latter is mainly due to the quantum nature of light, implying that the arrival of a photon on a sensor is a random event and thus the number of incident photons over a period of time is a random variable depending on the brightness of the light source. In the context of fluorescence imaging, the image signal-to-noise-ratio (SNR) is usually very low because the low dose of illumination light is required to avoid photo-bleaching of fluorescent molecules and preserve specimen integrity (photo-toxicity). Additionally, the quality of acquired fluorescence images is worsened by the blurring effect. This second limitation (i.e. blur) is a consequence of various factors during acquisition process including optical diffraction, excitation wavelength, immersion medium refraction and specimen thickness. These limitations not only degrade the image quality in terms of overall visualization but also have a negative severe impact on specimen analysis since they reduce the ability to recognize the objects of interest from noisy background and to detect fine details.

To improve the quality of images acquired by fluorescence microscopes, deconvolution is frequently suggested as pre-processing step for noise removal and resolution enhancement before further analysis. It aims at restoring the original (noise-free and sharp) image from observed noisy and blurry image, which is in general an ill-posed inverse problem. Number of regularization-based methods have been proposed over the past few decades in order to stabilize numerically the solution of the underlying inverse problem as well as to produce better estimation in the sense that the latter looks more similar to real-world images. The choice of an appropriate regularization modelling prior knowledge about the imaged objects is thus highly important for high-quality deconvolution results.

In this chapter, we present a novel family of convex regularizers which are well-suited for fluorescence microscopy images by taking into account the characteristics of fluorescence imaging context. These regularizers are inspired from the concept of sparse variation (SV), originally introduced by Eickenberg et al. (2015) for MRI segmentation. Indeed, based on the observation of the sparse distribution and the co-localization of regions with high intensity and high-magnitude gradient on fluorescence images, we consider the mixed norm L_1-L_2 norm of a linear transform combining the image intensity and spatial differential coefficients into one feature vector, computed at each pixel of the image, to promote the spatial sparsity of bright objects over relatively darker background. Under the assumption of additive Gaussian noise, the image deconvolution problem then corresponds to the minimization of a convex functional which can be efficiently solved by primal-dual (proximal) algorithms. We evaluate furthermore the proposed SV-based deconvolution method on both simulated and real fluorescence images. Experimental results prove that our regularization approach outperforms total variation (TV) [Rudin et al. 1992] which is the most widely used regularizer in image processing, and is very competitive

when compared to the Hessian Schatten-norm regularizer [Lefkimmiatis et al. 2013].

The remainder of the chapter is organized as follows. In Section 4.2, we briefly review several existing deconvolution methods for bi-dimensional (2D) fluorescence microscopy images. In Section 4.3, we introduce the norm-based regularization approach which is frequently used in image processing. We derive a novel family of convex non-quadratic regularizers by generalizing the concept of sparse variation. In Section 4.4, given the family of regularizers, a general variational framework for image deconvolution is presented. We also describe an optimization algorithm to solve the underlying variational problem. Then, in Section 4.5, we assess the performance of our approach on simulated and real large fluorescence images. Finally, we conclude this chapter and propose some future work in Section 4.6.

4.2 Related works for deconvolution of fluorescence images

In fluorescence microscopy, the arising blur is mainly induced by the limited aperture of the objective which results in light diffraction through the optical system. The diffraction phenomenon implies that light emitted by an infinitely small point source appears wider at the focal plan and spreads into a specific pattern called "point spread function" (PSF). As a consequence, the obtained 2D image of an object is the superposition of these emitted light patterns from each point of the object. It can be mathematically modelled as the convolution product of the imaged object and the PSF of the microscope under the linear shift-invariance assumption of the imaging system. In contrast with hardware-assisted techniques that aim at adjusting the optical system to reduce the size of the PSF and/or reject out-of-focus light before it reaches the detector, hence improving the spatial resolution of acquired images, deconvolution is a computational post-processing technique which consists in restoring a sharper image of the object from its blurry digitized version.

In the last twenty years, many deconvolution methods have been investigated in order to deal with the steadily increasing amounts of microscopy data. The most popular deconvolution approach is the linear filtering method such as Wiener and Tikhonov-Miller (see [van der Voort and Strasters 1995; van Kempen et al. 1996, 1997]) filters. The former provides the minimizer of the mean squared error between the estimated (deconvolved) image and the true image, while the latter consists in minimizing an energy functional composed of a quadratic data term and a quadratic regularization term, resulting in linear operations on the acquired image. Both Wiener and Tikhonov-Miller filters assume that the acquired image is corrupted by additive Gaussian noise. Despite the simplicity and low-computation-requirement, such linear methods usually produce limited deconvolution results since they do not restore fine image details at frequency components that are beyond the bandwidth of the point spread function (*i.e.* the support of its Fourier transform). Moreover, the positivity of the results obtained with these filters can not be always guaranteed due to their linear nature. It presents therefore a major issue while dealing with fluorescence microscopy images in which pixel intensities have positive values by definition.

To handle this issue, several iterative non-linear algorithms have been proposed instead of previously mentioned one-step approaches. Among them, the iterative constrained Tikhonov-Miller algorithm [van der Voort and Strasters 1995; van Kempen et al. 1996, 1997] and a modified version of it which is called the Carrington algorithm [Carrington 1990; Carrington et al. 1995] consist in minimizing iteratively the Tikhonov functional. The only difference between them is in the way they integrate the constraint of non-negativity at each iteration. In contrast with these additive-form algorithm, the Gold-Meinel algorithm [Meinel 1986] implicitly incorporates the positivity by considering a multiplicative formulation. As an alternative, the Richardson-Lucy algorithm [Richardson 1972; Lucy 1974; Shepp and Vardi 1982] which is derived from the maximum likelihood estimation (MLE) under the assumption of Poisson noise involves similar multiplicative-form iterations. An important drawback of both Gold-Meinel and Richardson-Lucy algorithms is however their numerical instability, resulting in noise amplification after a small number of iterations. A further review of these classical deconvolution algorithms is given in [Sibarita 2005].

Later on, the total variation (TV) regularization approach, originally introduced by Rudin et al. (1992) for image denoising, was widely used for image deconvolution [Combettes and Pesquet 2004], including in microscopy imaging (see [Dey et al. 2006; Soulez et al. 2012]). The success of this well-known approach is mainly due to its ability to preserve sharp edges and smooth homogeneous areas in the underlying images. Although, its downside is the staircasing effect, resulting in images of contiguous regions with constant intensities [Chan et al. 2000b]. This effect is rather an artifact than a desired property on non-synthetic images. A family of non-quadratic functionals which involve Schatten norms of the Hessian matrix has been investigated in [Lefkimmiatis et al. 2013] as second-order extensions of TV in order to attenuate staircasing effect. Its performance was furthermore depicted in [Lefkimmiatis et al. 2012; Lefkimmiatis and Unser 2013] showing their effectiveness in biomedical applications, specially for fluorescence image deconvolution. Beside these Hessian-based regularizers, other second and higher-order regularization approaches were also proposed as alternatives, including the L_1 norm of the Laplacian operator, the modified Laplacian and the affine total-variation (see [Lefkimmiatis et al. 2013] for comprehensive comparison). Recently, a novel energy functional has been introduced using a specific non-convex regularization functional [Arigovindan et al. 2013] to cope with the relevant characteristics of fluorescence images. This functional tends to penalize jointly the pixel intensities and intensity variations to favor sparsely distributed bright objects over relatively darker background. However, its non-convex nature leads to complicated optimization problems and does not guarantee the convergence to global optimum. A gentle initialization of the algorithm is suggested in [Arigovindan et al. 2013] to overcome local minima of the energy functional. In our opinion, an appropriate regularizer which takes into account important characteristics of fluorescence imaging in a similar way as in [Arigovindan et al. 2013], and possesses interesting mathematical properties, including convexity, invariance to contrast, scale, rotation, and translation as total variation and Hessian Schatten norm regularizers, is highly recommended for fast and high-quality deconvolution of large fluorescence images.

4.3 Norm-based regularization

Most of commonly-used regularizers in imaging problems (such as denoising, deconvolution, inpainting, etc.) have the following form:

$$E_R(u) = \int_\Omega \Phi(Lu(\mathbf{x}))\ d\mathbf{x}\ , \tag{4.1}$$

where u is an image defined on a square domain $\Omega \subset \mathbb{R}^2$, L (called "regularization operator") is a linear operator used to control the spatial distribution of u and $\Phi(\cdot)$ is a positive potential function usually related to a norm distance. A typical example is the Tikhonov regularization using the squared Euclidean (L_2-) norm chosen as potential function ($\Phi = \|\cdot\|_2^2$), frequently combined with the identity operator ($L = \mathrm{Id}$) or a differentiation operator (such as the gradient and the Laplacian operators) or eventually an orthogonal projection operator in order to cope with particular structure of the desired solution. Due to their convex and differentiable properties, quadratic penalties are widely used for many years to numerically stabilize inverse problems arising in number of applications including astronomy [Gull and Daniell 1978; Starck and Murtagh 2006], ultrasound imaging [Zhao et al. 2016], scanning-tunneling microscopy [Kokaram et al. 1995], electrical tomography [Vauhkonen et al. 1998], magnetic resonance imaging [Ying et al. 2004] and atomic-force microscopy [Cidade et al. 2000]. Nevertheless, despite its mathematical tractability and implementation simplicity, Tikhonov regularization yields unsatisfactory results if the image transform (by the regularization operator L) does not have a small norm. In particular, when differentiation operator is used, it tends to produce blurred details in obtained images since images with low gradient magnitudes are encouraged.

4.3.1 Differential norm regularizers

To avoid over-smoothing caused by quadratic functionals, non-quadratic regularizers have been studied recently as alternative solutions. One of the most popular among them is total variation [Rudin et al. 1992] which considers the gradient operator and the Euclidean norm as the following:

$$\mathrm{TV}(u) = \int_\Omega \|\nabla u(\mathbf{x})\|_2\ d\mathbf{x}\ , \tag{4.2}$$

where $\nabla u(\mathbf{x}) \in \mathbb{R}^2$ denotes the gradient of u at the point $\mathbf{x}$. By definition, total variation can be interpreted as the L_1-norm of the image gradient magnitude $\|\nabla u\|_2$; or in other words, it corresponds to the mixed L_1-L_2 norm ($\|\cdot\|_{1,2}$) of the image gradient ∇u where the L_1-norm acts on the spatial domain Ω and the L_2-norm acts on the gradient vector components. The use of the L_1-norm, which promotes sparsity, favors images with vanishing gradients except at some points and thus allows to restore well-preserved and sharp edges, showing the superior performance of TV when compared to the Tikhonov approach. The convexity of such a norm enables to consider efficient optimization algorithms (see [Boyd and Vandenberghe 2004]) and explains the wide use of total variation in various imaging applications due to its computational simplicity. However, the drawback of TV is the staircasing

effect (also known as blocking artifact) since imposing vanishing gradients also leads to piecewise-constant reconstructions while the underlying images are not necessary piecewise-constant.

A way to prevent the blocking artifact is to "regularize" the TV functional by replacing the Euclidean norm of the image gradient by a smooth approximation [Nikolova 2004] of the following form:

$$\mathrm{TV}_{h_\epsilon}(u) = \int_\Omega h_\epsilon(\|\nabla u(\mathbf{x})\|_2)\ d\mathbf{x}\ , \tag{4.3}$$

where $h_\epsilon : \mathbb{R}_+ \to \mathbb{R}$ is a smooth and non-decreasing function on $\mathbb{R}_+$ and ϵ is a parameter controlling the smoothness of the approximation. A usual and convenient choice for h_ϵ is the Huber function

$$t \longmapsto \begin{cases} \frac{1}{2\epsilon}t^2 & \text{if } |t| \leq \epsilon\ , \\ |t| - \frac{\epsilon}{2} & \text{if } |t| > \epsilon\ , \end{cases} \tag{4.4}$$

which leads to the so-called "Huber norm". This "norm" has similar behavior as the Euclidean norm for high gradient (when $\|\nabla u\|_2 > \epsilon$) but is quadratic for small gradient and thus implies the property of avoiding the blocking artifact of the associated TV-Huber (TVH) regularizer. The performance of TV-Huber model has been proved in [Louchet and Moisan 2013] for image denoising.

Another way to overcome the issue of staircasing is to consider higher-order differentiation operators instead of first-order operators. By investigating the Hessian operator which is a second-order operator, Lefkimmiatis et al. (2013) proposed a family of convex regularizers as an extension of total variation. It is based on the matrix norm of the Hessian, computed at each point of the image

$$\mathrm{HV}_p(u) = \int_\Omega \|\mathcal{H}u(\mathbf{x})\|_{\boldsymbol{\mathcal{S}}_p}\ d\mathbf{x}\ , p \geq 1\ , \tag{4.5}$$

where $\mathcal{H}u(\mathbf{x})$ is the Hessian matrix of u at the point $\mathbf{x}$

$$\mathcal{H}u(\mathbf{x}) = \begin{bmatrix} \frac{\partial^2}{\partial x^2}u(\mathbf{x}) & \frac{\partial^2}{\partial x \partial y}u(\mathbf{x}) \\ \\ \frac{\partial^2}{\partial y \partial x}u(\mathbf{x}) & \frac{\partial^2}{\partial y^2}u(\mathbf{x}) \end{bmatrix}\ , \tag{4.6}$$

and $\|\mathcal{H}u(\mathbf{x})\|_{\boldsymbol{\mathcal{S}}_p}$ denotes its Schatten p-norm [Bhatia 1997] defined as

$$\|\mathcal{H}u(\mathbf{x})\|_{\boldsymbol{\mathcal{S}}_p} = \left(\sum_{l=1}^{2} \boldsymbol{\sigma}_l^p(\mathcal{H}u(\mathbf{x}))\right)^{\frac{1}{p}}\ , \tag{4.7}$$

with $\boldsymbol{\sigma}_l(\mathcal{H}u(\mathbf{x}))$ the l-th singular value of $\mathcal{H}u(\mathbf{x})$. The above-mentioned regularization functionals named Hessian variation (HV) favor vanishing second-order differentials, hence lead to piecewise-linear reconstructions in comparison with piecewise-constant reconstructions produced by total variation. They allow not only to prevent the undesired staircasing effect but also to provide better approximation of the spatial variation of image intensities.

In spite of the effectiveness of these Hessian-based regularizers, there are however few important characteristics of fluorescence imaging which were not considered by this approach, especially the sparsity of the spatial distribution of high-intensity regions and the colocalization between these regions and those with high magnitude gradients. In the next part, we introduce a novel regularization approach which exploits these interesting characteristics but preserves the desired properties of total variation as well as Hessian variation, such as convexity, contrast, rotation, translation, and scale invariance. It enables thus the application of convex optimization algorithms that are very efficient for large scale problems as in the context of fluorescence microscopy.

4.3.2 Generalized sparse variation

Originally introduced in [Eickenberg et al. 2015] for brain MRI segmentation, sparse variation (SV) is a non-quadratic penalty defined as

$$\mathrm{SV}_\rho(u) = \int_\Omega \underbrace{\sqrt{\rho^2 \|\nabla u(\mathbf{x})\|_2^2 + (1-\rho)^2 u(\mathbf{x})^2}}_{\|K_{1,\rho} u\|_2} \, d\mathbf{x} \quad , \tag{4.8}$$

where $\rho \in]0,1[$ is a parameter controlling the trade-off between spatial regularity and sparsity, and $K_{1,\rho}$ is the linear operator gathering the image gradient and the image intensity components:

$$K_{1,\rho} = \begin{bmatrix} (1-\rho)\,\mathrm{Id} \\ \rho\ \nabla \end{bmatrix} \text{ and } K_{1,\rho} u(\mathbf{x}) = \begin{pmatrix} (1-\rho) u(\mathbf{x}) \\ \rho\ \partial_x u(\mathbf{x}) \\ \rho\ \partial_y u(\mathbf{x}) \end{pmatrix} \in \mathbb{R}^3 \ , \tag{4.9}$$

with ∂_x and ∂_y denote the first order derivative in the horizontal and vertical direction respectively. From this point-of-view, sparse variation is closely similar to total variation and can also be expressed as a mixed L_1-L_2 norm as:

$$\mathrm{SV}_\rho(u) = \|K_{1,\rho} u\|_{1,2} \ , \tag{4.10}$$

where the operator $K_{1,\rho}$ is considered instead of the gradient operator. This regularizer has been proposed to reduce blocking artifacts by combining the L_1 penalty (on the image intensity), which enforces the sparsity of the images with TV penalty, which enforces the sparsity of image gradient. The idea behind this combination is to sparsify jointly the spatial distribution of image intensities and image gradients and to allow smooth variations between spatially-contiguous non-zero regions of the underlying image. Indeed, it promotes images with background with small intensity values and sparsely distributed bright objects since if a pixel is non-null, the gradient vector at this pixel is non-null as well, or otherwise both of them are null. Such images look like surprisingly to those which are typically obtained in fluorescence imaging.

Based on the concept of grouping image intensity and spatial differentials, we propose an extended version of sparse variation using the second order differentiation operator. The proposed regularization which is named as Hessian-based sparse

variation (HSV) is defined as the following:

$$\mathrm{HSV}_{\rho}(u) = \int_{\Omega} \sqrt{\rho^2 \|\mathcal{H}u(\mathbf{x})\|_F^2 + (1-\rho)^2 u(\mathbf{x})^2} \; d\mathbf{x} \; , \tag{4.11}$$

where $\|\cdot\|_F$ denotes for the matrix Frobenius norm and $\rho \in]0,1[$ is the weighting parameter. We also note that the Frobenius norm which is the square root of the sum of squared matrix entries coincides with the Schatten 2-norm ($\|\cdot\|_{\boldsymbol{\mathcal{S}}_2}$) in the case of the Hessian matrix due to its symmetry. More interestingly, by using the fact that the Frobenius norm of the Hessian matrix is equal to the Euclidean norm of its vectorized version, if we define

$$K_{_{2,\rho}} \triangleq \begin{bmatrix} (1-\rho)\,\mathrm{Id} \\ \rho\;\partial^2_{xx} \\ \rho\;\partial^2_{xy} \\ \rho\;\partial^2_{yx} \\ \rho\;\partial^2_{yy} \end{bmatrix} \; , \tag{4.12}$$

the expression of the Hessian-based sparse variation can be re-written as:

$$\mathrm{HSV}_{\rho}(u) = \int_{\Omega} \|K_{_{2,\rho}} u\|_2 \; d\mathbf{x} = \|K_{_{2,\rho}} u\|_{1,2} \; . \tag{4.13}$$

It recalls once again the famous mixed L_1-L_2 norm mentioned earlier. Our Hessian-based regularization is analogous to those introduced in [Arigovindan et al. 2013] which also combines image intensities and second-order differentials but a relaxed logarithm function is used for more sparsifying effect as

$$u \longmapsto \int_{\Omega} \log(\|K_{_{2,\frac{1}{2}}} u\|_2 + \varepsilon^2) \; d\mathbf{x} \; , \tag{4.14}$$

where $\varepsilon > 0$ is a control parameter to prevent the singularity at 0 of the logarithm.

From the definitions (4.8)–(4.13), we remark furthermore that the original sparse variation and its Hessian-based version correspond to convex regularizers since they are defined as the integration of linear operators. It is easy to verify that these regularizers are homogeneous, shift- and rotation-invariant as total variation. These properties not only are important in the sense of mathematical functional analysis but also allow the design of exact and efficient algorithms which are not possible for the smooth logarithm-based regularizer described in [Arigovindan et al. 2013]. In general, by using an arbitrary k-th order differentiation operator and by replacing the L_1-norm by a L_ν-norm ($\nu \geq 1$), we obtain a generalized version of sparse variation as the following:

$$\begin{aligned} \mathrm{GSV}^{(k)}_{\rho,\nu}(u) &\triangleq \|K_{_{k,\rho}} u\|^{\nu}_{\nu,2} \\ &\triangleq \int_{\Omega} \left[\rho^2 \|\mathcal{D}^{(k)} u(\mathbf{x})\|_2^2 + (1-\rho)^2 u(\mathbf{x})^2\right]^{\frac{\nu}{2}} d\mathbf{x} \; , \end{aligned} \tag{4.15}$$

where $\mathcal{D}^{(k)}$ denotes the corresponding vectorized version of a k-th order differentiation operator and ν is the parameter controlling the convexity degree of the functional. The family of convex regularizers $\mathrm{GSV}^{(k)}_{\rho,\nu}$ includes therefore sparse variation

$(k = 1, \nu = 1)$ and Hessian-based sparse variation $(k = 2, \nu = 1)$. In this work, we only consider $k = 1$ or 2 for the sake of simplicity, and we focus on the case of $\nu = 1$ to impose the sparsity of the image transform $K_{k,\rho}u$ which is the most important property to restore fluorescence images.

4.4 Variational image deconvolution

4.4.1 Continuous framework

Given an observed image $f : \Omega \to \mathbb{R}$ which is blurred and noisy, image deconvolution consists in restoring the underlying image $u : \Omega \to \mathbb{R}$ such that the following acquisition model holds:

$$f = \mathcal{T}(Hu) \ , \tag{4.16}$$

where H denotes the linear operator representing the blur related to the optical system (*e.g.*, point spread function) and $\mathcal{T}$ is a degradation operator modeling the measurement noise. In fluorescence microscopy, the arising shot noise is usually modeled by the Poisson distribution (or eventually by a mixed Poisson-Gaussian distribution) which is non-stationary and signal-dependent. Although this model is very convenient for modeling purpose, it also leads to practical computational difficulties since its associated data fidelity term is non-quadratic and is defined only for strictly positive images (not defined for images having zero-value pixels). To avoid the strict positivity issue, instead of considering the Poisson noise model, we assume, in this work, that the observed image f is corrupted by a Gaussian white noise as the following:

$$f = Hu + \eta \ , \tag{4.17}$$

where η denotes the additive Gaussian noise with zero-mean and standard deviation σ. Variance stabilization techniques (see [Starck and Murtagh 2006; Delpretti et al. 2008; Boulanger et al. 2010; Makitalo and Foi 2013]) can be used in the case of Poisson-Gaussian noise to approximately convert the mixed noise into a Gaussian noise [Dupe et al. 2009].

Under the assumption of additive Gaussian noise, the associated data fidelity term is a quadratic functional which corresponds to a least-squares fitting:

$$E_D(u) = \frac{1}{2}\int_\Omega \big(Hu(\mathbf{x}) - f(\mathbf{x})\big)^2 d\mathbf{x} \ . \tag{4.18}$$

Putting together this quadratic data term and the proposed regularization, the so-called SV (sparse variation) deconvolution can be reformulated as a minimization problem:

$$\begin{aligned} \hat{u} &= \arg\min_u \ \frac{1}{2}\|Hu - f\|_2^2 + \lambda\|K_{k,\rho}u\|_{1,2} \\ &= \arg\min_u \ \int_\Omega \Big[\frac{1}{2}(Hu(\mathbf{x}) - f(\mathbf{x}))^2 + \lambda\|K_{k,\rho}u(\mathbf{x})\|_2\Big] d\mathbf{x} \ , \end{aligned} \tag{4.19}$$

where $k = 1$ or 2, $0 \leq \rho \leq 1$ and $\lambda \geq 0$ is the regularization parameter. We remark that the problem (4.19) is convex since the underlying energy functional is sum of

convex terms, but it is non-smooth because of the singularity of the regularization term. Solving such a problem is not a trivial task due to its non-smoothness. Smooth approximation can be envisaged to overcome the non-differentiability of the underlying energy functional (objective) if we want to use standard differentiable optimization techniques (such as gradient descent or Newton-Raphson method). However, the solution of the approximated problem could be different from those of the original problem because the behavior of the objective is modified. To our knowledge, only primal-dual methods (e.g, [Chambolle and Pock 2011; Condat 2013]) allows to solve directly this kind of convex and non-smooth problem without any modification of the energy functional.

4.4.2 Discrete formulation

The observed noisy and blurry image f, which is obtained at the end of the acquisition process, is represented by its digitized (discrete) version and not by its continuously defined counterpart. The continuous model is not appropriate for discrete images even though the estimation of the continuous image u from discrete samples of f is in principle possible. For that reason, we propose to consider a discrete version of (4.19) by assuming that the images u and f are sampled according to the sampling grid

$$\Lambda = \mathbb{Z}^2 \cap \Omega = \{1, 2, \ldots, M\} \times \{1, 2, \ldots, N\} \ . \tag{4.20}$$

For a coordinate $\mathbf{p} = (i, j) \in \Lambda$, we denote by $u_{i,j} = u(\mathbf{p})$ (resp. $f_{i,j} = f(\mathbf{p})$) the value of u (resp. f) at the position (i, j). Discrete version of these images are therefore given by $\{u_{i,j}\}_{1\leq i\leq M, 1\leq j\leq N}$ and $\{f_{i,j}\}_{1\leq i\leq M, 1\leq j\leq N}$. Let us consider $\mathcal{X} = \mathbb{R}^{MN}$ a finite dimensional vector space equipped with a standard inner (scalar) product

$$\langle w, w' \rangle_{\mathcal{X}} = \sum_{i=1}^{M} \sum_{j=1}^{N} w_{i,j} w'_{i,j} \ . \tag{4.21}$$

The induced norm by the defined inner product is given by

$$\|w\|_{\mathcal{X}_2} = \sqrt{\langle w, w \rangle_{\mathcal{X}}} = \left(\sum_{i=1}^{M} \sum_{j=1}^{N} w_{i,j}^2 \right)^{\frac{1}{2}} \ . \tag{4.22}$$

It is easy to check that both $\{u_{i,j}\}_{i,j}$ and $\{f_{i,j}\}_{i,j}$ belong to the mentioned vector space $\mathcal{X}$.

In the following, without risk of ambiguity, we will consider the notations $K_{k,\rho} : \mathcal{X} \to \mathcal{X}^{2^k+1}$ and $H : \mathcal{X} \to \mathcal{X}$ for discrete versions associated with the intensity-differential-grouping and the blurring operator. In the discrete setting, the blurring operator H corresponds to a discrete convolution which can be efficiently computed by using fast Fourier transform (FFT) (see [Heideman et al. 1984; Van Loan 1992; Frigo and Johnson 1998, 2005]). To discretize $K_{k,\rho}$ (with $k = 1$ or 2), we use standard finite differences for the gradient and Hessian operators with Neumann conditions

on image boundaries

$$(K_{1,\rho}u)_{i,j} = \begin{pmatrix} (1-\rho)u_{i,j} \\ \rho(D_1^{(1)}u)_{i,j} \\ \rho(D_2^{(1)}u)_{i,j} \end{pmatrix} \in \mathbb{R}^3 \ , \tag{4.23}$$

and

$$(K_{2,\rho}u)_{i,j} = \begin{pmatrix} (1-\rho)u_{i,j} \\ \rho(D_{1,1}^{(2)}u)_{i,j} \\ \rho(D_{1,2}^{(2)}u)_{i,j} \\ \rho(D_{2,1}^{(2)}u)_{i,j} \\ \rho(D_{2,2}^{(2)}u)_{i,j} \end{pmatrix} \in \mathbb{R}^5 \ , \tag{4.24}$$

where

$$(D_1^{(1)}u)_{i,j} = \begin{cases} u_{i+1,j} - u_{i,j} & \text{if } i < M \ , \\ 0 & \text{if } i = M \ , \end{cases} \tag{4.25a}$$

$$(D_2^{(1)}u)_{i,j} = \begin{cases} u_{i,j+1} - u_{i,j} & \text{if } j < N \ , \\ 0 & \text{if } j = N \ , \end{cases} \tag{4.25b}$$

$$(D_{1,1}^{(2)}u)_{i,j} = \begin{cases} u_{i+1,j} - 2u_{i,j} - u_{i-1,j} & \text{if } 1 < i < M \ , \\ 0 & \text{otherwise} \quad , \end{cases} \tag{4.25c}$$

$$(D_{2,2}^{(2)}u)_{i,j} = \begin{cases} u_{i,j+1} - 2u_{i,j} - u_{i,j-1} & \text{if } 1 < j < N \ , \\ 0 & \text{otherwise} \quad , \end{cases} \tag{4.25d}$$

$$(D_{1,2}^{(2)}u)_{i,j} = (D_{2,1}^{(2)}u)_{i,j} = \begin{cases} u_{i+1,j+1} - u_{i+1,j} - u_{i,j+1} + u_{i,j} \\ \qquad \text{if } i < M \text{ and } j < N \ , \\ 0 \qquad \text{otherwise} \qquad . \end{cases} \tag{4.25e}$$

Let us consider these discrete operators and define the mixed L_1-L_2 norm of $\{(K_{k,\rho}u)_{i,j}\}_{i,j}$ as

$$\|K_{k,\rho}u\|_{\mathcal{X}_{1,2}} = \sum_{i=1}^{M}\sum_{j=1}^{N} \|(K_{k,\rho}u)_{i,j}\|_2 \ , \tag{4.26}$$

where the L_1-norm acts now on the discrete domain Λ. The energy functional associated with SV deconvolution problem in the discrete setting then reads, where $\lambda \geq 0$,

$$E(u) = \frac{1}{2}\|Hu - f\|_{\mathcal{X}_2}^2 + \lambda\|K_{2,\rho}u\|_{\mathcal{X}_{1,2}} \ . \tag{4.27}$$

Furthermore, due to the nature of photon-limited imaging in fluorescence microscopy which implies that image intensities are upper and lower bounded, range constraints on image intensities can also be added

$$\begin{aligned} \boldsymbol{\mathcal{C}} &= \{u : 0 \leq u_{i,j} \leq u_{\max}, 1 \leq i \leq M, 1 \leq j \leq N\} \\ &= [0,\ u_{\max}]^{MN} \subset \mathcal{X} \ , \end{aligned} \tag{4.28}$$

where the lower bound 0 guarantees to positivity of the solution and the upper bound $u_{\max} > 0$ is the maximal intensity value allowed. Finally, we consider the following minimization problem:

$$\hat{u} = \arg\min_u \ \frac{1}{2}\|Hu - f\|_{\mathcal{X}_2}^2 + \lambda\|K_{k,\rho}u\|_{\mathcal{X}_{1,2}} + \imath_{\boldsymbol{\mathcal{C}}}(u) \ , \tag{4.29}$$

where $\imath_{\boldsymbol{\mathcal{C}}}$ denotes the characteristic function of the convex subset $\boldsymbol{\mathcal{C}}$ defined as

$$\imath_{\boldsymbol{\mathcal{C}}}(u) = \begin{cases} 0 & \text{if } u \in \boldsymbol{\mathcal{C}} \\ +\infty & \text{otherwise} \end{cases} , \tag{4.30}$$

We notice that the objective function in (4.29) is a sum of linear composite functions as $u \mapsto \sum_{n=1}^{m} \mathscr{F}_n(L_n u)$, where each $\mathscr{F}_n$ is a convex function and each L_n is a linear bounded operator. Formally, we can write $m = 3$, $\mathscr{F}_1 = \imath_{\boldsymbol{\mathcal{C}}}$, $L_1 = \mathrm{Id}$, $\mathscr{F}_2 = \lambda\|\cdot\|_{\mathcal{X}_1,2}$, $L_2 = K_{k,\rho}$ and $\mathscr{F}_3 = \frac{1}{2}\|\cdot\|^2_{\mathcal{X}_2}$, $L_3 = H(\cdot) - f$. Generic primal-dual proximal approaches can be used to minimize this linear combination of convex functions as proposed in [Combettes et al. 2011, 2014], but it is not optimal since the smoothness of the quadratic terms $\frac{1}{2}\|Hu - f\|^2_{\mathcal{X}_2}$ is not exploited. In order to solve the problem (4.29), the design of an appropriate algorithm requires therefore to take into account the specific form of the corresponding energy, *i.e.* the sum of a simple convex function $\mathscr{F} = \imath_{\boldsymbol{\mathcal{C}}}$, a more sophisticated composite function $\mathscr{G} \circ L = \lambda\|K_{k,\rho}(\cdot)\|_{\mathcal{X}_1,2}$ (here, $\mathscr{G} = \lambda\|\cdot\|_{\mathcal{X}_1,2}$ and $L = K_{k,\rho}$) and a smooth function $\mathscr{H} = \frac{1}{2}\|H(\cdot) - f\|^2_{\mathcal{X}_2}$.

4.4.3 Minimization of the proposed energy

In this section, we present a first-order method to minimize the sum of convex functions in (4.29), based on the proximal splitting approaches (see [Mercier 1979; Eckstein and Bertsekas 1992; Combettes 2004; Combettes and Wajs 2005; Combettes and Pesquet 2011; Chambolle and Pock 2011; Condat 2013, 2014]). It consists in decomposing (splitting) the original problem into several simple sub-problems in the way that each single function of the sum can be processed separately. Indeed, smooth function involves its gradient operator, while non-smooth function implies its Moreau proximity operator [Moreau 1965]. These operators are well-suited for large-scale problems arising in signal and image processing, because they only exploit first-order information of the function and thus enable fast and efficient computation.

Let us recall first that the proximity operator of a convex function $\mathcal{J} : \mathcal{X} \to \mathbb{R}$ is defined as

$$\mathrm{prox}_{\tau\mathcal{J}}(u) = \arg\min_{w \in \mathcal{X}} \ \mathcal{J}(w) + \frac{1}{2\tau}\|u - w\|^2_{\mathcal{X}_2} , \tag{4.31}$$

where $\tau > 0$ is a control parameter. From this definition, it easy to verify that the proximity operator of the function $\mathscr{F}(u) = \imath_{\boldsymbol{\mathcal{C}}}(u)$ is nothing else than the projection (according to the norm $\|\cdot\|_{\mathcal{X}_2}$) onto the convex subset $\boldsymbol{\mathcal{C}} = [0,\ u_{\max}]^{MN}$ as the following

$$\begin{aligned} \mathrm{prox}_{\tau\mathscr{F}}(u) &= \arg\min_{w \in \mathcal{X}} \ \imath_{\boldsymbol{\mathcal{C}}}(w) + \frac{1}{2\tau}\|u - w\|^2_{\mathcal{X}_2} \\ &= \arg\min_{w \in \boldsymbol{\mathcal{C}}} \ \|u - w\|^2_{\mathcal{X}_2} . \end{aligned} \tag{4.32}$$

If we denote $\mathrm{proj}_{\boldsymbol{\mathcal{C}}}$ the projection operator on $\boldsymbol{\mathcal{C}}$, its closed-form expression is given by

$$\big(\mathrm{proj}_{\boldsymbol{\mathcal{C}}}(u)\big)_{i,j} = \max(0, \min(u_{\max}, u_{i,j})) , \tag{4.33}$$

which is completely simple and easy to compute. Meanwhile, the quadratic function $\mathscr{H}(u) = \frac{1}{2}\|Hu - f\|^2_{\mathcal{X}_2}$ possesses an analytic form for its associated proximity

operator but the latter is slightly complicated

$$\begin{aligned}\operatorname{prox}_{\tau\mathscr{H}}(u) &= \arg\min_{w\in\mathcal{X}} \frac{1}{2}\|Hw-f\|_{\mathcal{X}_2}^2 + \frac{1}{2\tau}\|u-w\|_{\mathcal{X}_2}^2 \\ &= (\tau H^\top H + \mathrm{Id})^{-1}(\tau H^\top H f + u)\ ,\end{aligned} \tag{4.34}$$

where the symbol $^\top$ denotes the adjoint of a linear operator and $H^\top : \mathcal{X} \to \mathcal{X}$ satisfies $\langle Hw, w'\rangle_{\mathcal{X}} = \langle w, H^\top w'\rangle_{\mathcal{X}}$. The evaluation of $\operatorname{prox}_{\tau\mathscr{H}}(u)$ corresponds to the inverse of a linear system that is not always possible in practice due to the high dimension of the problem. For this reason, optimization methods which involve the gradient of $\mathscr{H}$ are more appropriate since they do not require any inverse operator. In comparison with $\mathscr{F}$ and $\mathscr{H}$, the calculation of the proximity operator in the case of the composite function $\mathscr{G}\circ L(u) = \lambda\|K_{k,\rho}u\|_{\mathcal{X}_{1,2}}$ is theoretically possible but is challenging because of the presence of $K_{k,\rho}$ which is not diagonal.

To solve the minimization problem (4.29), we adopt the full splitting approach described in [Condat 2013, 2014]. The key idea of this approach is to evaluate the gradient, proximity and linear operators individually in order to avoid implicit operations such as inner loops or inverse of linear operators. Accordingly, only "simple" computations are considered such as the gradient $\nabla\mathscr{H}$, the proximity operators of $\mathscr{F}$ and $\mathscr{G}$, the linear mapping L and its adjoint operators $L^\top$. The corresponding proximal algorithm for the problem (4.29) is written under the following general form:

$$u^{(\ell+1)} = \operatorname{prox}_{\gamma\mathscr{F}}\Big\{u^{(\ell)} - \gamma\left(L^\top z^{(\ell)} + \nabla\mathscr{H}(u^{(\ell)})\right)\Big\}, \tag{4.35a}$$

$$z^{(\ell+1)} = \operatorname{prox}_{\zeta\mathscr{G}^\star}\Big\{z^{(\ell)} + \zeta L\left(2u^{(\ell+1)} - u^{(\ell)}\right)\Big\}, \tag{4.35b}$$

where $\gamma, \zeta > 0$ are proximal parameters, $\mathscr{G}^\star$ denotes the Legendre-Fenchel conjugate of $\mathscr{G}$ and its proximity operator $\operatorname{prox}_{\zeta\mathscr{G}^\star}$ can be directly computed from $\operatorname{prox}_{\frac{\mathscr{G}}{\zeta}}$ by using Moreau's identity $v = \zeta\operatorname{prox}_{\frac{\mathscr{G}}{\zeta}}(\frac{v}{\zeta}) + \operatorname{prox}_{\zeta\mathscr{G}^\star}(v)$. Following [Condat 2013, 2014], to guarantee the convergence of the proposed algorithm, the parameters γ and ζ must fulfill the condition

$$\gamma\left(\frac{1}{2} + \zeta|||L^\top L|||\right) < 1\ , \tag{4.36}$$

where $|||\cdot|||$ denotes the operator norm. The proofs of the convergence can be found in [Condat 2013]. We also note that the proposed algorithm belongs to the class of primal-dual algorithms which provide not only the solution of the primal problem (*a.k.a.* the original minimization problem) but also the solution of its dual problem.

Since the closed-form of $\operatorname{prox}_{\gamma\mathscr{F}}$ is already given, it remains to define the analytic expression of other terms in (4.35a) and (4.35b). We start with the gradient of the quadratic function $\mathscr{H}$ which is straightforwardly obtained by

$$\nabla\mathscr{H}(u) = H^\top(Hu - f)\ . \tag{4.37}$$

Next, we remark that the regularization operator $L = K_{k,\rho}$ is a linear mapping $u \in \mathcal{X} \mapsto K_{k,\rho}u = (v^t)_{1\le t\le 2^k+1} \in \mathcal{X}^{2^k+1}$, then its adjoint operator $L^\top = K_{k,\rho}{}^\top$ is

defined using the equation $\langle u, {K_{k,\rho}}^{\top} v\rangle_{\mathcal{X}} = \langle K_{k,\rho} u, v\rangle_{\mathcal{X}^{2^k+1}}$, which implies

$$\left({K_{1,\rho}}^{\top} v\right)_{i,j} = (1-\rho)v^1_{i,j} + \rho[(D^{(1)}_1)^{\top} v^2]_{i,j} + \rho[(D^{(1)}_2)^{\top} v^3]_{i,j} \tag{4.38}$$

and

$$\begin{aligned}\left({K_{2,\rho}}^{\top} v\right)_{i,j} = (1-\rho)v^1_{i,j} &+ \rho[(D^{(2)}_{1,1})^{\top} v^2]_{i,j} + \rho[(D^{(2)}_{1,2})^{\top} v^3]_{i,j} \\ &+ \rho[(D^{(2)}_{2,1})^{\top} v^4]_{i,j} + \rho[(D^{(2)}_{2,2})^{\top} v^5]_{i,j} \ ,\end{aligned} \tag{4.39}$$

where the involving adjoint operators $(D^{(1)}_1)^{\top}$, $(D^{(1)}_2)^{\top}$, $(D^{(2)}_{1,1})^{\top}$, $(D^{(2)}_{1,2})^{\top}$, $(D^{(2)}_{2,1})^{\top}$, and $(D^{(2)}_{2,2})^{\top}$ are given in the appendix section. From equations (4.38) and (4.39), one can deduce the following upper bounds:

$$\left\|\left\|{K_{1,\rho}}^{\top} K_{1,\rho}\right\|\right\| \leq (1-\rho)^2 + 8\rho^2 \ , \tag{4.40a}$$

$$\left\|\left\|{K_{2,\rho}}^{\top} K_{2,\rho}\right\|\right\| \leq (1-\rho)^2 + 64\rho^2 \ , \tag{4.40b}$$

that are used for choosing the proximal parameters γ and ζ.

The last term we want to deal with is the proximity operator $\mathrm{prox}_{\zeta\mathscr{G}^\star}$. We also note that the proposed primal-dual algorithm does not necessitate evaluating the proximity operator of the composite function $\mathscr{G} \circ L$ as in the case of generic proximal algorithms, but only $\mathrm{prox}_{\frac{\mathscr{G}}{\zeta}}$ is required. Since $\mathscr{G}$ is related to the mixed L_1-L_2 norm $\|\cdot\|_{\mathcal{X}_{1,2}}$ whose the proximity operator is defined as:

$$\left(\mathrm{prox}_{\tau\|\cdot\|_{\mathcal{X}_{1,2}}}(v)\right)^t_{i,j} = \max(0, \|L_{i,j} v\|_2 - \tau)\frac{v^t_{i,j}}{\|L_{i,j} v\|_2} \ , \tag{4.41}$$

where $L_{i,j} : v \in \mathcal{X}^{2^k+1} \mapsto \left(v^t_{i,j}\right)_{1\leq t\leq 2^k+1} \in \mathbb{R}^{2^k+1}$ is a linear operator; by using the Moreau's identity, we obtain the closed-form expression of $\mathrm{prox}_{\zeta\mathscr{G}^\star}$ as the following:

$$\left(\mathrm{prox}_{\zeta\mathscr{G}^\star}(v)\right)^t_{i,j} = \frac{v^t_{i,j}}{\max\left(1, \frac{\|L_{ij} v\|_2}{\lambda}\right)} \ , \tag{4.42}$$

which shows that $\mathrm{prox}_{\zeta\mathscr{G}^\star}$ is independent from ζ and moreover it is an pointwise operator. These properties allow therefore fast and efficient computation by exploiting the intrinsic parallelism of multicore processors.

4.5 Experimental results

To evaluate the performance of the sparse variation (SV) deconvolution approach, we provide experimental comparisons with classical deconvolution methods (see [Sage et al. 2017]), that are commonly used in fluorescence microscopy such as the Richarson-Lucy (RL) algorithm, the iterative constrained Tikhonov-Miller (ICTM) algorithm, and the Gold-Meinel (GM) algorithm, and with recent regularization-based deconvolution methods, including total variation (TV), Hessian variation (HV), GraphNet (GN) [Ng et al. 2010; Kandel et al. 2013; Grosenick et al. 2013], TV-L_1 [Chan and Esedoglu 2005; Michel et al. 2011], and specially the non-convex

Regularizer	**Differentiation order**	**Convexity**	**Smoothness**
Total Variation (TV)	1	Convex	Non smooth
Hessian Variation (HV)	2	Convex	Non smooth
TV-L_1	1	Convex	Non smooth
GraphNet (GN)	1	Convex	Non smooth
Sparse Variation (SV)	1	Convex	Non smooth
Hessian-based SV (HSV)	2	Convex	Non smooth
TV Huber (TVH)	1	Convex	Smooth
HV Huber (HVH)	2	Convex	Smooth
TV-L_1 Huber (TV-L_1H)	1	Convex	Smooth
HV-L_1	2	Convex	Non smooth
HV-L_1 Huber (HV-L_1H)	2	Convex	Smooth
GraphNet Huber (GNH)	1	Convex	Smooth
Hessian-based GN (HGN)	2	Convex	Non smooth
HGN Huber (HGNH)	2	Convex	Smooth
SV Huber (SVH)	1	Convex	Smooth
HSV Huber (HSVH)	2	Convex	Smooth
Arigovindan et al. (2013) (LHSV)	2	Non convex	Smooth

Table 4.1: Properties of regularizers which are used in the deconvolution experiments.

regularizer (4.14) introduced by Arigovindan et al. (2013). The latter involves second order differentiation operator and is based on the logarithm function. It is abbreviated as LHSV (Log-based Hessian Sparse Variation) due to its similarity with the concept of SV. We recall that GraphNet is the sum of the L_1 norm of the image intensity and the squared L_2 norm of the image gradient (i.e. the Tikhonov penalty), whereas TV-L_1 differs from GraphNet by replacing the Tikhonov penalty by TV penalty:

$$\mathrm{GN}_\rho(u) = \rho\|\nabla u\|_2^2 + (1-\rho)\|u\|_1 \ , \tag{4.43}$$

$$\mathrm{TVL1}_\rho(u) = \rho\|\nabla u\|_{1,2} + (1-\rho)\|u\|_1 \ . \tag{4.44}$$

To enrich the catalog of convex regularizers used in these experiments, by using the Hessian operator instead of the gradient operator, we consider also an extended version of GraphNet and TV-L_1 which can be named as Hessian-based GraphNet (HGN) and Hessian Variation-L_1 (HV-L_1) respectively. Furthermore, Huber-norm-based smooth approximations of non-smooth regularization functionals, which enable the use of smooth optimization techniques such as gradient-descent-based methods, are also considered in our study. For these smooth regularization functionals, we use the projected gradient method to minimize the underlying deconvolution energy. In contrast, a full-splitting-based primal-dual algorithm [Condat 2013, 2014] is used in the case of non-smooth regularization functionals.

One important motivation of this work was to investigate the impact of smooth and non-smooth regularizers for image deconvolution. In Table 4.1, we summarize the characteristics of the reguralizers mentioned above. The deconvolution experiments were performed on an image set composed of both synthetic and real fluorescence images depicting bright objects over dark backgrounds.

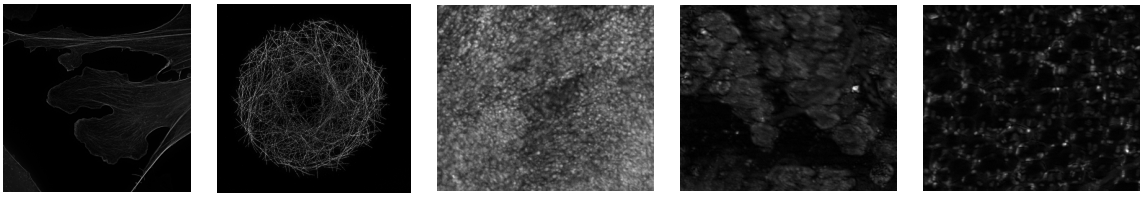

(a) (b) (c) (d) (e)

Figure 4.1: **Set of biological images acquired by SIM technology.** From left to right: (a) actin cytoskeleton, (b) microtubule, (c) tumor tissue, (d) muscle tissue, and (e) adipose tissue. The first two images are cell images collected from the Cell Image Library (`http://www.cellimagelibrary.org`) with id number CIL 7053 and CIL 36147 respectively (CIL stands for the Cell Image Library identifier). The last three images are tissue images in the dataset used in [Fu et al. 2016] (available at `https://dukespace.lib.duke.edu/dspace/handle/10161/10892`).

Image	**Type**	**Image size**	**Pixel size**	**Spatial resolution**
Actin cytoskeleton	Cell	1904×1900 px	0.04 μm	0.1 μm
Microtubule	Cell	1054×1028 px	0.04 μm	0.1 μm
Tumor	Tissue	350×300 px	1.50 μm	4.4 μm
Muscle	Tissue	350×300 px	1.50 μm	4.4 μm
Adipose	Tissue	350×300 px	1.50 μm	4.4 μm

Table 4.2: Information of test images (see Fig. 4.1).

4.5.1 Experiments on simulated image

We have selected several SIM (Structured Illumination Microscopy) images to serve as blur-free and noise-free reference images (*i.e.* ground-truth) in our experiments. SIM imaging allows to reconstruct very fine details at very high resolutions (up to 100 nm for standard SIM techniques) while removing noise from raw acquired measurements. These fluorescence images, shown in Fig. 4.1, were collected from two sources: the Cell Image Library (CIL) database (available at `http://www.cellimagelibrary.org`) and the training dataset used in [Fu et al. 2016] for the detection of positive margins in a pre-clinical genetically engineered mouse model of sarcoma. We note that, for the latter data set, the used SIM technique called widefield SIM is specially developed for tissue imaging which does not require sub-cellular resolution. For that reason, the resolution is much smaller than those of conventional SIM which is approximately 100 nm as in the case of CIL images. In Table 4.2, we provide detailed information of all test images, including specimen name, image size and spatial resolution.

To produce a homogeneous and fair comparison of different methods and to avoid bias induced by inhomogeneous dynamic ranges between the images, we first normalized the reference images in the range $[0, 1]$ before all further simulations. The normalized images are then blurred by considering a Gaussian point spread function with standard deviation $\sigma_{\text{PSF}} = 2$. A Gaussian noise with zero mean and variance σ^2 is also added to these images in order to generate observed noisy and blurry data. In these experiments, we consider three distinct noise levels corresponding to a standard deviation $\sigma \in \{0.02, 0.04, 0.08\}$ respectively. Quantitative evaluation of each deconvolution method is measured by the Peak Signal-to-Noise Ratio (PSNR) and by the Structural Similarity (SSIM) index between the deconvolved images and

the reference images.

For regularization-based methods which combine penalties on image intensity and on image differentiation operator (such as SV, TV-L_1, GraphNet and their variants), we set the trade-off parameter $\rho = 0.5$, implying the equal contribution of each component for simplification purpose. In the case of the Richardson-Lucy (RL) algorithm which is originally designed to deal with Poisson noise, the degraded images are re-scaled to the original dynamics of the underlying reference images by multiplying by a normalization factor. The RL deconvolution results are then re-normalized for a fair comparison with those obtained by the other methods. Before applying the Gold-Meinel algorithm, the noisy images are smoothed with a Gaussian filter as pre-processing step because this algorithm assumes that the noise is negligible.

Quantitative evaluation

In Table 4.3, we provide the comparative results of the proposed SV deconvolution with the tested methods for the set of fluorescence images shown in Fig. 4.1, for different degradation conditions. Note that the deconvolution outcome of each method was obtained using parameters which were tuned in the way that produces the best PSNR performance. Using these fine-tuned parameters, the SSIM score is computed for an additional quantitative criterion to evaluate the effectiveness of considered deconvolution methods.

According to the results reported in Table 4.3, we notice that the non-regularization methods such as RL and GM algorithms perform poorly, irrespectively of the images and the noise levels, showing their non-competitiveness when compared with regularization-based methods. The poor performance of these methods is mainly due to the lack of regularization on the solution, leading to noise amplification in deconvolved images. Among the regularization-based methods, the iterative constrained Tikhonov-Miller (ICTM) algorithm, based on the squared L_2 norm of the image gradient, generally produces encouraging results in terms of PNSR and SSIM performance. In some cases, it eventually outperforms other competitors. For example, on the image of tumor tissue (see Fig. 4.1c), ICTM solution achieves the best PSNR and SSIM scores in the case of medium and high noise levels (corresponding to $\sigma = 0.04$ and $\sigma = 0.08$ respectively); meanwhile, slightly inferior scores are obtained for low noise level ($\sigma = 0.02$) but the difference between them and the corresponding highest values is relatively small.

Regarding non-smooth regularizers, Hessian variation consistently gives superior PSNR scores than TV, for all considered images and noise levels. In terms of SSIM performance, it produces better results in most of cases. In comparison to TV that only penalizes image gradient norm, the TV-L_1 approach which introduces additionally the L_1 penalty on image intensities, yields slightly improved PSNR and SSIM values in some few cases. For the remaining cases, the obtained results using TV and TV-L_1 are very similar. The analogous behavior is also noticed when we compare the couple of HV and HV-L_1 regularizers, the second-order extension of TV and TV-L_1 respectively. The experimental results shows furthermore that the second-order regularizers achieve in general higher PSNR and SSIM scores than the

	Image	Actin cytoskeleton			Microtuble			Tumor			Muscle			Adipose		
		$\sigma=0.02$	$\sigma=0.04$	$\sigma=0.08$	$\sigma=0.02$	$\sigma=0.04$	$\sigma=0.08$	$\sigma=0.02$	$\sigma=0.04$	$\sigma=0.08$	$\sigma=0.02$	$\sigma=0.04$	$\sigma=0.08$	$\sigma=0.02$	$\sigma=0.04$	$\sigma=0.08$
PSNR	RL	-3.87	-3.88	-3.92	27.89	23.11	17.86	27.77	22.77	17.66	27.67	22.37	17.15	26.02	21.25	15.65
	ICTM	35.77	34.39	32.65	29.28	27.98	26.61	27.43	26.07	24.53	**34.19**	**32.74**	31.14	33.74	31.98	30.17
	GM	-4.02	-4.03	-4.05	28.92	24.82	19.79	29.44	24.15	18.80	29.26	23.94	18.51	27.12	22.85	17.42
	TV	35.46	34.32	32.92	29.17	27.88	26.61	26.61	25.41	24.05	33.72	32.38	31.14	33.28	31.81	30.17
	TV-L_1	35.45	33.96	31.84	29.25	27.93	26.62	26.67	25.40	23.94	33.67	32.07	30.13	33.29	31.58	29.45
	GN	33.84	31.15	28.07	29.82	28.26	26.22	27.31	25.49	22.83	32.12	29.12	26.07	32.39	29.69	27.08
	SV	35.71	33.41	30.44	30.34	28.82	27.07	**27.44**	25.75	23.31	33.85	31.48	28.72	34.55	32.19	29.37
	HV	**36.44**	**35.20**	**33.62**	29.98	28.57	27.09	27.39	26.01	24.41	34.43	32.94	**31.43**	**34.56**	**32.68**	**30.63**
	HV-L_1	36.36	34.87	32.55	29.99	28.61	27.16	27.39	25.99	24.32	34.38	32.67	30.51	34.53	32.54	30.17
	HGN	34.00	31.23	28.09	29.88	28.35	26.32	27.32	25.50	22.68	32.33	29.26	26.09	32.66	29.95	27.22
	HSV	35.71	33.24	30.09	**30.42**	**28.89**	**27.11**	**27.44**	25.70	23.08	33.73	31.21	28.35	34.52	32.14	29.34
	TVH	36.21	34.94	33.32	29.72	28.35	26.94	27.38	26.01	24.46	34.35	32.86	31.40	34.22	32.43	30.49
	TV-L_1H	36.26	34.87	32.85	29.76	28.41	27.03	27.38	26.01	24.42	34.33	32.71	30.89	34.22	32.41	30.28
	GNH	33.61	31.43	28.69	28.03	27.45	26.23	25.87	25.06	23.09	31.66	29.44	26.78	31.46	29.88	27.75
	SVH	35.88	33.72	30.84	30.13	28.70	27.09	**27.44**	25.83	23.49	34.01	31.74	29.16	34.47	32.37	29.85
	HVH	35.83	34.38	31.97	29.72	28.32	26.87	27.42	26.02	24.42	34.16	32.64	30.76	33.84	32.16	30.18
	HV-L_1H	35.88	34.17	31.33	29.75	28.38	26.98	27.42	26.01	24.24	34.14	32.24	29.53	33.87	32.06	29.69
	HGNH	34.55	32.56	29.36	28.28	27.84	26.54	26.21	25.52	23.42	32.72	30.57	27.41	32.36	30.67	28.22
	HSVH	35.73	33.65	30.64	29.88	28.47	26.90	27.36	**25.84**	**23.65**	33.96	31.72	28.88	33.93	31.93	29.42
	LHSV	34.82	32.18	28.11	28.56	27.78	25.47	26.21	24.61	20.96	33.23	30.49	26.83	33.93	30.71	27.38
SSIM	RL	0.434	0.432	0.422	0.624	0.363	0.156	0.546	0.301	0.128	0.521	0.265	0.102	0.694	0.449	0.201
	ICTM	0.867	0.823	0.765	0.714	0.647	0.586	0.776	0.696	0.591	0.840	0.796	0.741	0.859	0.809	0.743
	GM	0.425	0.424	0.418	0.728	0.563	0.370	0.637	0.377	0.177	0.610	0.347	0.149	0.745	0.540	0.276
	TV	**0.885**	**0.854**	**0.815**	0.819	0.756	0.677	0.734	0.646	0.536	0.830	0.787	0.741	0.866	0.820	0.755
	TV-L_1	0.866	0.792	0.675	0.828	0.778	0.720	0.736	0.649	0.546	0.828	0.770	0.677	0.863	0.799	0.680
	GN	0.714	0.608	0.492	0.850	0.795	0.719	0.777	0.696	0.576	0.753	0.609	0.436	0.769	0.619	0.453
	SV	0.861	0.790	0.683	**0.867**	**0.819**	**0.761**	**0.782**	0.704	**0.596**	0.837	0.759	0.632	0.878	0.801	0.668
	HV	0.883	0.846	0.802	0.832	0.765	0.679	0.770	0.693	0.581	**0.848**	**0.805**	**0.750**	0.882	**0.833**	**0.765**
	HV-L_1	0.869	0.798	0.704	0.837	0.782	0.725	0.770	0.692	0.588	0.846	0.792	0.699	0.879	0.816	0.708
	HGN	0.733	0.596	0.468	0.851	0.796	0.717	0.779	0.699	0.577	0.764	0.615	0.434	0.785	0.638	0.445
	HSV	0.872	0.797	0.679	0.856	0.818	0.754	**0.782**	**0.706**	0.594	0.836	0.752	0.612	0.874	0.794	0.661
	TVH	0.876	0.837	0.790	0.818	0.751	0.665	0.771	0.686	0.579	0.846	0.801	0.748	0.875	0.825	0.760
	TV-L_1H	0.876	0.827	0.761	0.825	0.769	0.706	0.771	0.686	0.579	0.846	0.796	0.725	0.873	0.821	0.735
	GNH	0.787	0.690	0.590	0.793	0.769	0.724	0.676	0.644	0.560	0.731	0.637	0.501	0.767	0.678	0.555
	SVH	0.876	0.813	0.722	0.846	0.796	0.740	0.780	0.701	0.593	0.842	0.771	0.665	**0.883**	0.821	0.716
	HVH	0.868	0.829	0.737	0.815	0.749	0.645	0.777	0.697	0.587	0.841	0.798	0.724	0.865	0.816	0.742
	HV-L_1H	0.868	0.806	0.706	0.820	0.766	0.717	0.777	0.697	0.594	0.841	0.781	0.667	0.864	0.802	0.691
	HGNH	0.823	0.736	0.612	0.804	0.772	0.719	0.696	0.662	0.571	0.789	0.696	0.534	0.817	0.717	0.585
	HSVH	0.869	0.801	0.695	0.830	0.773	0.716	0.776	0.691	0.579	0.838	0.762	0.637	0.863	0.800	0.680
	LHSV	0.836	0.687	0.528	0.817	0.757	0.587	0.697	0.609	0.368	0.804	0.671	0.469	0.847	0.724	0.523

Table 4.3: Performance of considered deconvolution methods in terms of PSNR and SSIM on the set of biomedical test images for three different noise levels.

corresponding first-order version. In contrast with first-tier performance obtained with these TV-based regularizations, GraphNet and its Hessian-based variant fail to be competitive for many selected images and signal-to-noise ratios. Their PSNR performance falls behind by more than 2 dB in average and even more than 3 dB in some cases, resulting in lower SSIM scores when compared to TV-related approaches that consider non-quadratic penalty on image differential components. Meanwhile, the results provided by sparse variation are almost comparable to those obtained with TV and HV in terms of both PSNR and SSIM performance. Specially, in the case of microtubule image (CIL 36147) which represents sparsely distributed fine filament structures over dark background, SV leaves these two competing regularizers behind on SSIM benchmark, whereas its PSNR score is higher for two noise levels and slightly lower (only 0.02 dB) than HV for the remaining noise level. In contrast to the supremacy of HV with respect to TV, Hessian-based sparse variation, the second-order extension of SV, does not achieve higher performance than its first-order version over half of cases and the difference between results obtained with these two versions are almost insignificant.

Comparing with these convex but non-smooth regularization functionals, the Huber-norm-based approximations yield in general satisfying results. In a few cases, the PSNR and SSIM score are slightly improved by using the smooth approximated version instead of the original counterpart, but slightly inferior performances are also observed in some other cases. More interestingly, the improvement is frequently noticed for first-order regularizers including TV Huber, TV-L_1 Huber, GraphNet Huber and SV Huber, whereas, second-order regularizers usually suffer from a lowering of PSNR score as well as SSIM value. Another smooth regularizer that we wished to investigate is the so-called LHSV which considers a regularization operator gathering the image intensity and the Hessian matrix coefficients as Hessian-based SV, but replaces the square root in the L_2 norm by a smooth approximation of the logarithm. Using the logarithm function enables to enforce the sparsifying effect, LHSV is able to efficiently remove noise in extremely noisy images while preserving essential details. In our experiments, this sophisticated approach produces however disappointing results on artificially degraded images. Indeed, the PSNR and SSIM scores are barely in the same grade of GraphNet and sharply inferior than those obtained with HV, SV or even TV in most cases.

Visual inspection and assessment

Based on our observations, the PSNR and SSIM benchmark do not yield a consistent ranking on the performance of each deconvolution approach, and thus it is not possible to definitely conclude which method works best among the considered methods. Their effectiveness needs to be assessed visually in local regions. Actually, there are chances that an obtained result with outstanding PSNR and SSIM scores is unacceptable in terms of visual quality, simply due to over-smoothing which results in the loss of fine details in deconvolved images or due to over-sharpening which leads to unrealistic reconstructions. For that reason, we provide in Fig. 4.2, a comparison showing the example of deconvolution results obtained with different methods on the microtubule image (CIL 36147) degraded by a Gaussian PSF ($\sigma_{\text{PSF}} = 2$) and

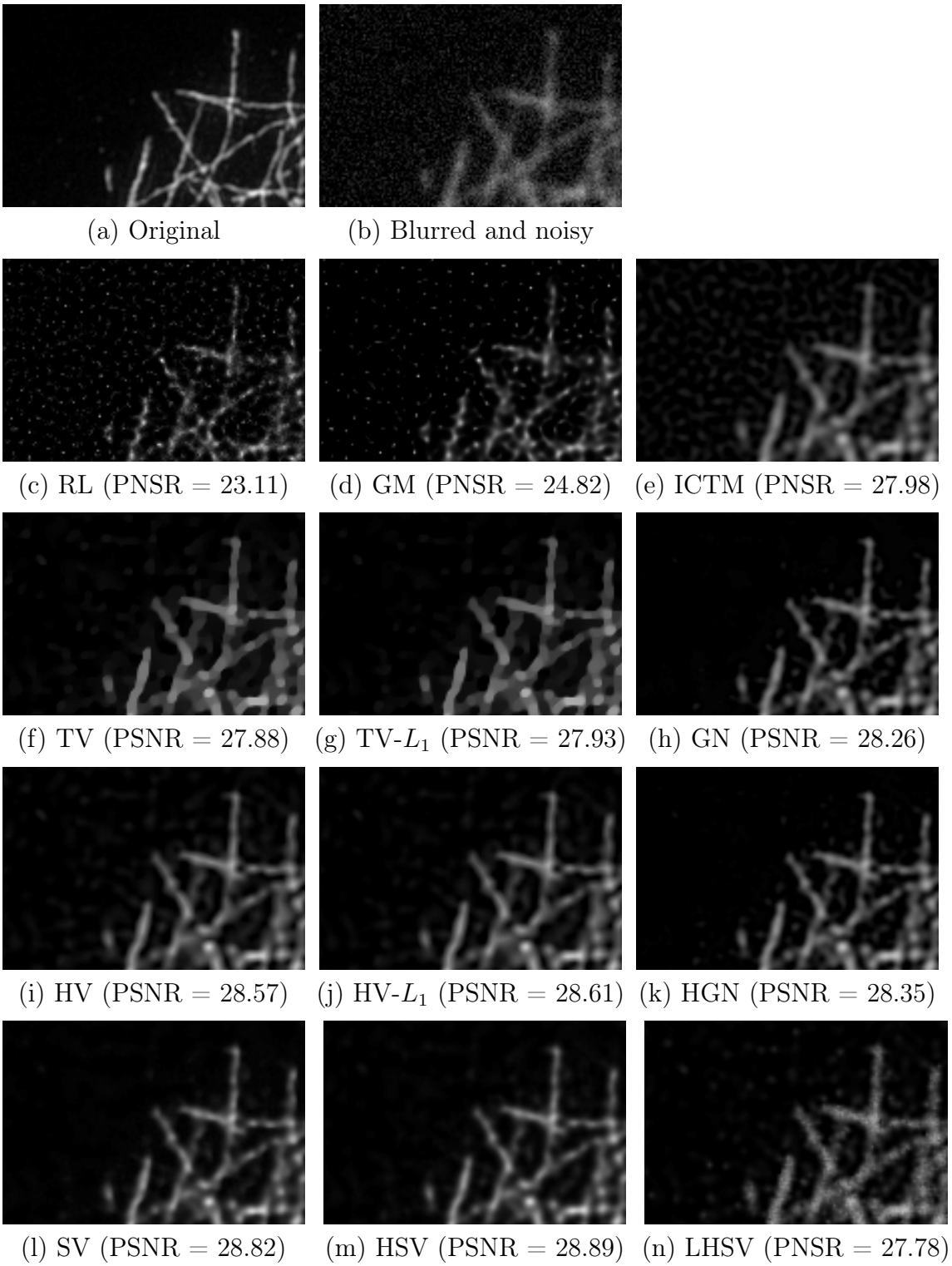

(a) Original (b) Blurred and noisy

(c) RL (PNSR = 23.11) (d) GM (PNSR = 24.82) (e) ICTM (PNSR = 27.98)

(f) TV (PSNR = 27.88) (g) TV-L_1 (PSNR = 27.93) (h) GN (PSNR = 28.26)

(i) HV (PSNR = 28.57) (j) HV-L_1 (PSNR = 28.61) (k) HGN (PSNR = 28.35)

(l) SV (PSNR = 28.82) (m) HSV (PSNR = 28.89) (n) LHSV (PNSR = 27.78)

Figure 4.2: **Deconvolution results on the microtubule image obtained with different methods in comparison to the proposed SV-based approach**. The original image (available at `http://www.cellimagelibrary.org/` with identifier CIL 36147) is degraded by a Gaussian PSF with standard deviation $\sigma_{\text{PSF}} = 2$ and a additive Gaussian noise with zero mean and standard deviation $\sigma = 0.04$. Zoom on filament details is shown in order to compare the performance of each method. The SV and Hessian-based SV solutions are very competitive when compared to those obtained with the other methods.

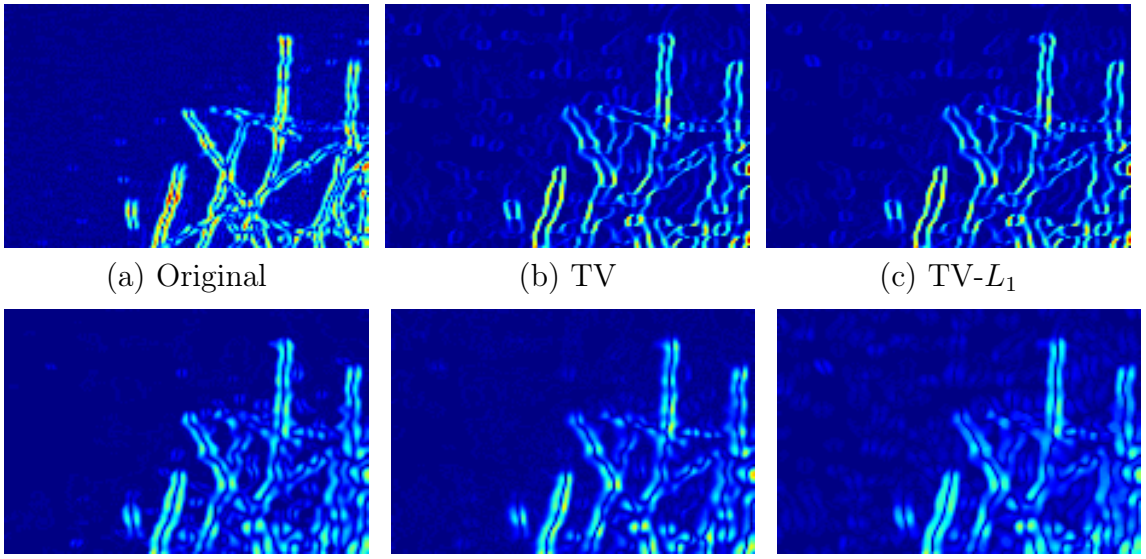

(a) Original (b) TV (c) TV-L_1

(d) GN (e) SV (f) HV

Figure 4.3: **Gradient magnitude of deconvolution results obtained with several convex regularizers**. The "hot" colors correspond to high gradients and "cold" colors to low gradients.

an additive Gaussian white noise with standard deviation $\sigma = 0.04$. The original image, showing microtubule structures on a *Drosophila S2* cell, was acquired by a Zeiss Elyra Super-resolution microscope equipped with SIM imaging technique and is collected as part of the Marine Biological Laboratory Neurobiology Course in summer 2011.

First, Fig. 4.2c and 4.2d clearly show that the GM and RL algorithms give very poor results. The ICTM algorithm produces, in contrast, more pleasant visual results, but it tends to over-smooth (blur) important structural details in the images (see Fig. 4.2e) due to the quadratic form of the Tikhonov regularizer. Comparing with the blurred ICTM solution, the deconvolved imaged obtained with LHSV has sharper details over a uniform background (see Fig. 4.2n). However, noise is not sufficiently removed, especially in non-background regions. It not only disturbs the visual effect but also makes the detection of fine details more difficult.

Meanwhile, the result provided by TV in Fig. 4.2f, is visually unrealistic in spite of its competitive PSNR and SSIM scores against other regularizers. As expected, it suffers from undesirable staircasing effect characterized by sharp edges and contiguous flat regions (also known as piecewise constant image). The staircasing artifacts can be easily observed in bright regions, notably those corresponding to filament structures which represent smooth changes of intensities. A particular consequence of staircasing effect that we want to figure out in the case of TV, is the presence of number of light-shaded spots with constant intensity over relatively darker surrounding areas. Most of these spots correspond generally to high peaks of noise in the blurred image background and do not represent any relevant structure of the original image. A deconvolved image with more homogeneous background is obtained using the TV-L_1 regularization that combines TV with the L_1 norm of the image intensity to prevent pixels having intensity smaller than a certain threshold, and controlled by the weight ρ and the regularization parameter λ. This thresholding which imposes

vanishing of low-intensity regions is also known as the feature selection property the TV-L_1 model as reported in [Chan and Esedoglu 2005]. However, this model does not remove staircasing artifacts related to TV regularization. In comparison with the latter, GraphNet addresses both staircasing and light-shaded spot issues by combining the quadratic Tikhonov functional with the L_1 penalty. The deconvolved image has indeed a uniform background (with less light-shaded spots) and a foreground with no apparent contiguous regions of constant intensity, as shown in Fig. 4.2h. It is visually more pleasant than TV and TV-L_1 solutions. It however produces slightly blurred image details due to the Tikhonov penalty which promotes smooth changes of intensities. However, it does not suffer from over-smoothing as in the ICTM solution due to the L_1 penalty which prevents nearly-zero intensity pixels, and hence enhances the contrast between bright objects and darker background. This is consistent with the high PSNR and SSIM values. In the particular example of microtubule image, GraphNet outperforms the ICTM, TV and TV-L_1 algorithms.

By examining the comparative results reported in Fig. 4.2, it turns out that SV gives similar results to GraphNet and outperforms all other regularizers which are first-order, convex and non-smooth, in terms of visual quality. The effectiveness of SV approach for fluorescence images, especially in the case of the microtubule image, can be justified by the way that this regularization affects the form of obtained solutions. In contrast with TV (penalty on image gradients), or with TV-L_1 and GraphNet that simply sum two penalties acting separately, one on image intensities and the other on image gradients, SV penalizes jointly image intensities and gradients by introducing structured sparsity on a specific linear transform which maps each pixel to an unique vector composed of its intensity and its directional derivatives in order to favor the co-localization of non-zero pixels and gradients. Therefore, it allows to obtain non-zero regions of eventually high-magnitude gradients, in opposition to relatively small-magnitude gradients in the case of GraphNet or vanishing gradients for TV and TV-L_1. This behavior results in better reconstruction of the image foreground, in which large intensity variation between pixels at the object boundaries and those in the middle, as well as sharp contrast between different objects may occur, while avoiding undesirable over-smoothing or over-sharpening effect. As an alternative, HV based on the norm of second-order differentiation operator leading to piecewise linear solutions, also permits the reconstruction of high-magnitude gradients not only at the edge of the objects but also inside objects. HV solution shown in Fig. 4.2i, is able to restore smooth intensity variations of filament structures and is visually comparable to the GraphNet and SV solutions. The background with some visible light-shaded spots is however non-homogeneous, as expected. Hence, in the example of microtubule image, SV represents so far the best deconvolution result with well-restored fine details and homogeneous background in comparison with existing regularizers including TV, TV-L_1, GraphNet and HV.

To better appreciate the behavior of the regularization approaches, Fig. 4.3 depicts the gradient magnitude of several deconvolution results shown in Fig. 4.2. We can clearly notice that, in the case of TV and TV-L_1 solution (see Figs. 4.3b and 4.3c respectively), the gradient vanishes for most of pixels except along object edges, thus implying blocking artifacts. The gradient of HV solution shown in Fig.

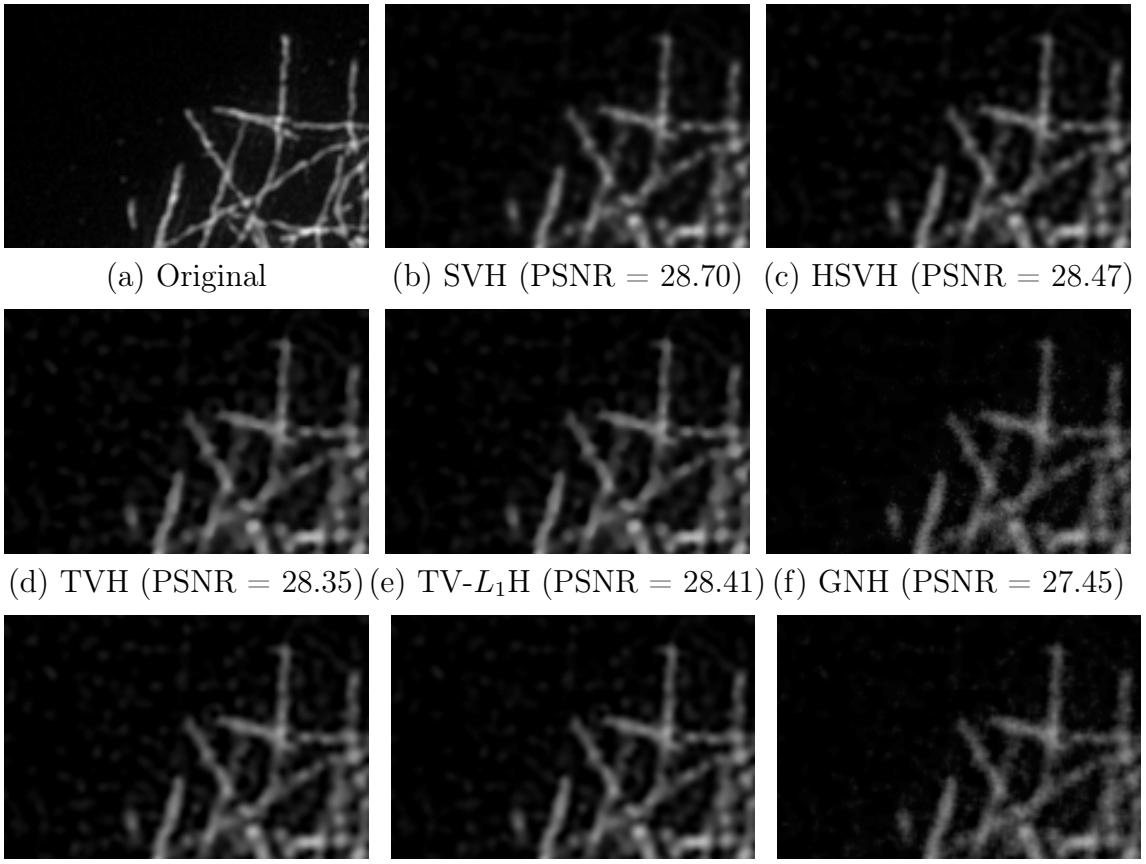

(a) Original (b) SVH (PSNR = 28.70) (c) HSVH (PSNR = 28.47)

(d) TVH (PSNR = 28.35) (e) TV-L_1H (PSNR = 28.41) (f) GNH (PSNR = 27.45)

(g) HVH (PSNR = 28.32) (h) HV-L_1H (PSNR = 28.38) (i) HGNH (PSNR = 27.84)

Figure 4.4: **Deconvolution results on the microtubule image obtained with Huber-based smooth approximation of some convex regularizers**. The original image (available at `http://www.cellimagelibrary.org/` with identifier CIL 36147) is degraded by a Gaussian PSF with standard deviation $\sigma_{\text{PSF}} = 2$ and an additive zero-mean Gaussian noise ($\sigma = 0.04$). Zoom on filament details is shown in order to compare the performance of each method.

4.3f possesses piecewise constant magnitude, or in other words, HV pushes the well-known staircasing effect to the image first-order differentials instead of the image itself. Unlike these regularizers, SV approach, which produces results with smoothly varied gradients as depicted in Fig. 4.3e, allows to handle smooth intensity changes and then restore a wider class of images than piecewise constant or piecewise linear images. In comparison, the spatial gradient of GraphNet solution (see Fig. 4.3d) is rather similar to SV, but the magnitude is slightly smaller at some points, resulting in slightly more blurred details.

Regarding second-order regularization, HV-L_1 solution shown in Fig. 4.2j is visually similar to HV, but with less light-shaded spots when compared to TV and TV-L_1. Hessian-based GraphNet produces quasi-identical results to those obtained with its first-order version (see Figs. 4.2k and 4.2h respectively). This is probably due to the quadratic nature of the squared norms (the L_2 norm for GraphNet and the Frobenius norm for the Hessian-based variant), regardless of the order of considered differentiation operator. In addition, insignificantly different results are also observed in the case of sparse variation and its Hessian-based version (see Figs. 4.2l

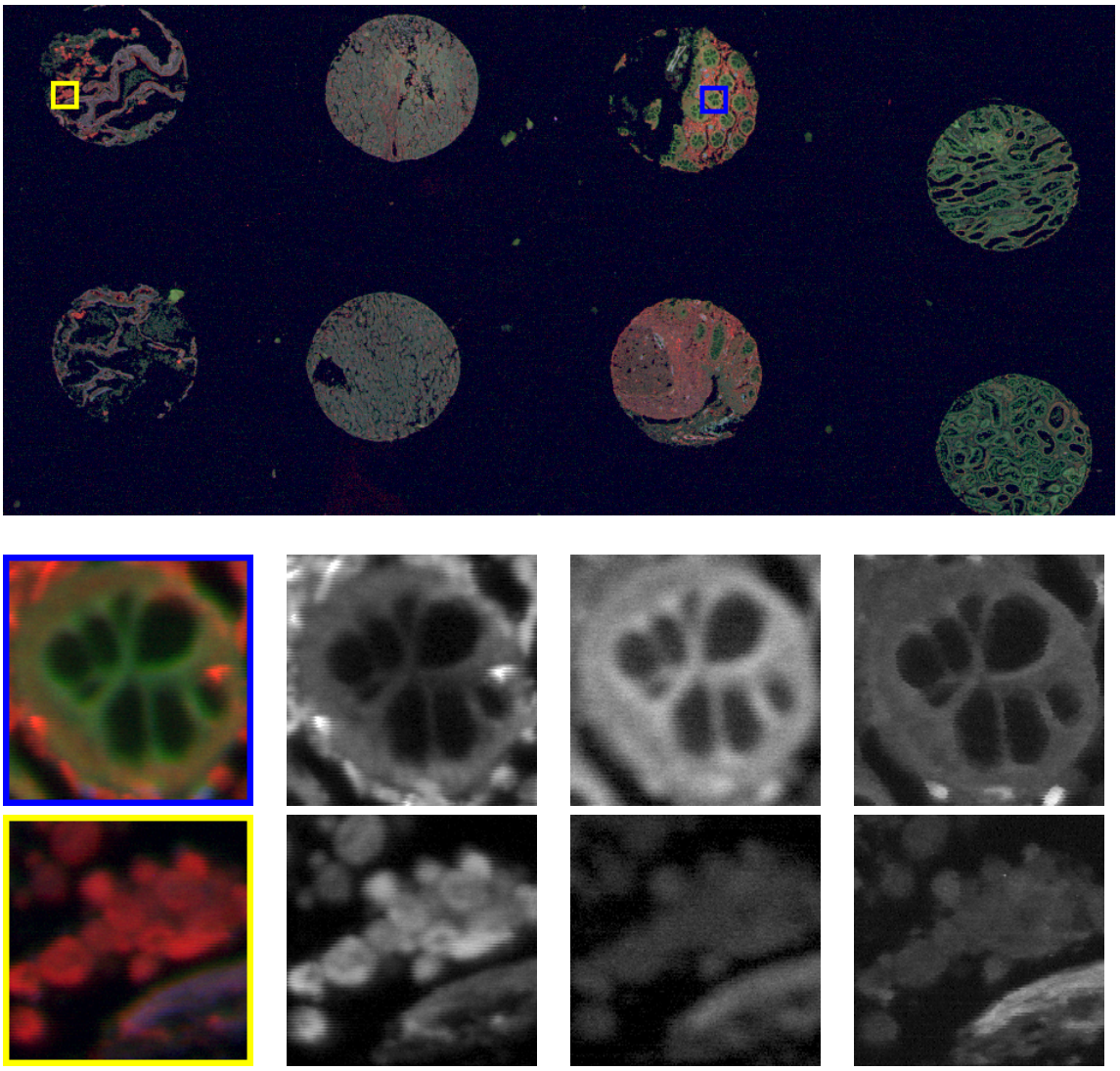

Figure 4.5: **Three-color fluorescence image of 8 tissue microarray cores**. A region of interest of 4.7 $\times$ 2.8 mm^2 was scanned using the fluorescence scanner named InnoScan 1100AL equipped with three excitation wavelengths (488 nm, 532 nm and 635 nm) at the spatial resolution 0.5 μm/pixel, corresponding to an image of 9544 $\times$ 4704 pixels. Two areas which are bordered by a blue and a yellow boxes are selected for comparison in details. First row: full size image. Second and third rows: zoom-in views of two selected areas; from left to right: 3 colors at the same time, red (488 nm), green (532 nm) and blue (635 nm) channels displayed separately.

for SV solution and 4.2m for those obtained with HSV). We note that the difference between them in terms of quantitative evaluation is negligible: only 0.07 dB of difference between the PSNR scores and 0.001 for their SSIM performances.

Finally, we compare the original non-smooth regularizers with the corresponding Huber-norm-based smooth approximation. Figure 4.4 shows the deconvolution results obtained with these smooth regularization functionals on the microtubule image CIL 36147 degraded by Gaussian PSF ($\sigma_{\text{PSF}} = 2$) and additive Gaussian noise ($\sigma = 0.04$). As depicted in Fig. 4.4c, TV-Huber prevents blocking artifact and provides visibly better result than the original TV model, as expected. The main drawback is the light-shaded spot issue that we have previously observed in the case of TV, TV-L_1 and HV solution (see Figs. 4.2f, 4.2g, and 4.2i respectively). In comparison, the TV-L_1 Huber solution shown in Fig. 4.4d, is indistinguishable from those obtained with TV-Huber in terms of fine detail reconstruction as well as non-homogeneous background. We notice that this regularization does not preserve the feature selection property of TV-L_1, maybe because the Huber norm disables the sparsity induced by the L_1 norm. Concerning second-order approaches, HV-Huber and HV-L_1 Huber give results (see Figs. 4.4f and 4.4g respectively) which are visually similar to their first-order versions. Nevertheless, they tend to worsen the problem of light-shaded spots by making these spots more pronounced. Similarly, undesirable light-shaded spots are also observed in the case of SV-Huber and HSV-Huber solution (see Figs. 4.4b and 4.4c). It degrades sharply the visual quality of these deconvolution results although fine details, such as filament structures are adequately restored. Solutions obtained with GraphNet-Huber and its Hessian-based variant (Figs. 4.4e and 4.4h) do not severely suffer from light-shaded spot issue and have more homogeneous background. However, they can not be considered as reliable solution due to the noisy reconstruction of relevant details in the image foreground. In our opinion, the Huber-norm-based approximation of convex non-smooth regularizers may improve deconvolution results in some aspects as we have observed, but it also modifies the properties of its corresponding original version.

To sum up, the proposed SV-based deconvolution approach yields better results in overall in comparison to those obtained with the tested methods. Not only achieving competitive PSNR and SSIM performance in most of cases, the SV and HV solutions are also very encouraging in terms of visual quality. According to our observations, they avoid in general over-smoothing and over-sharpening effect arising when using other regularizers, while being able to well restore image details with smooth changes of intensities and to efficiently eliminate strong noise from the background.

4.5.2 Application to real large fluorescence images

We present in this section the deconvolution results obtained with our method on real fluorescence images of tissue microarray (TMA) These TMA images, shown in Fig. 4.5 and 4.7, are acquired using dedicated scanner called InnoScan 1100AL[2].

[2] InnoScan 1100AL is developed and commercialized by Innopsys, see `https://www.innopsys.com/en/lifesciences-products/microarrays/innoscan/innoscan-1100-al` for more technical details.

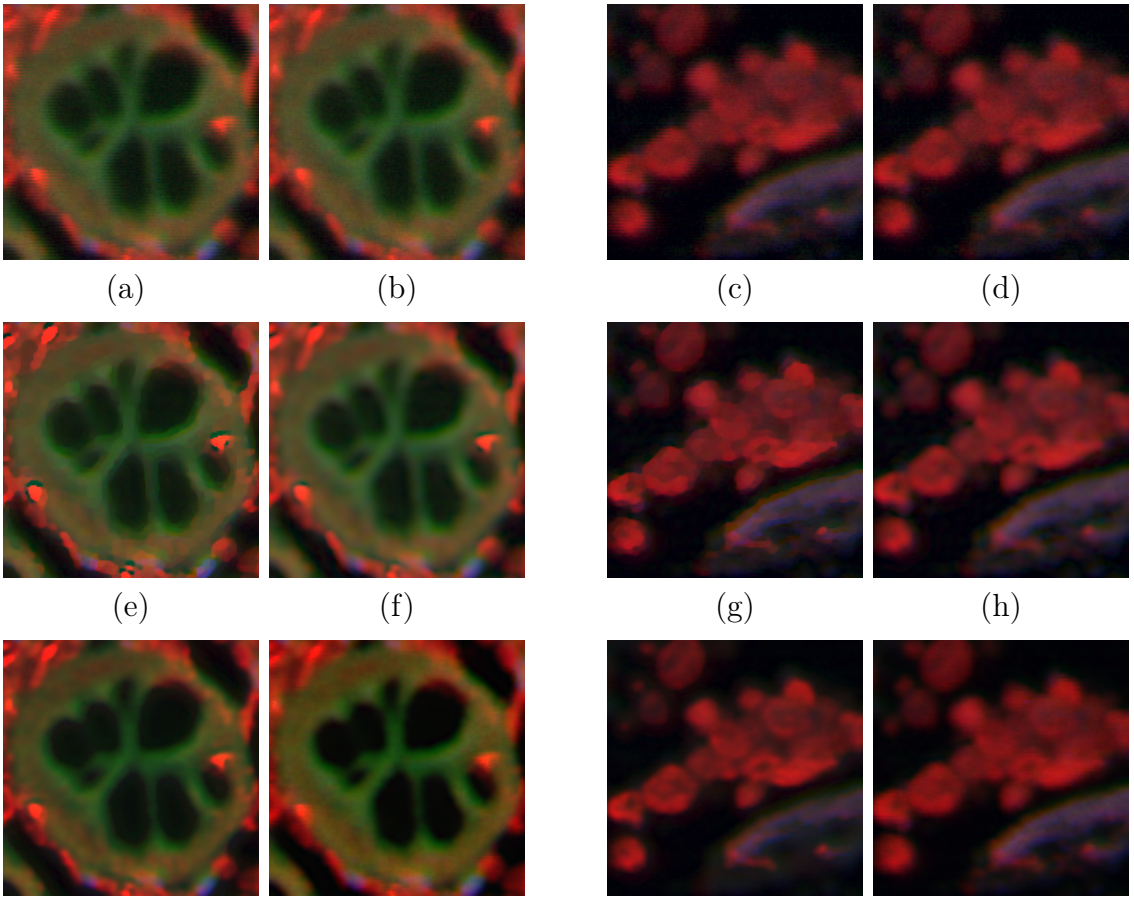

Figure 4.6: **Deconvolution results on the three-color TMA image obtained with different regularizers**. Zoom-in view on two selected areas are displayed for comparison purposes. (a) and (c): original acquired image; (b) and (d): dejittered image; (e) and (g): TV solution; (f) and (h): HV solution; (i) and (k): SV solution; (j) and (l): LHSV solution.

Equipped with three excitation lasers with corresponding wavelength 488 nm (red), 532 nm (green) and 635 nm (blue) respectively, this fluorescence scanner is able to provide single-color as well as multi-color (up to three color) images at very high resolutions. The highest resolution can reach to 0.5 μm per pixel (or a 20X objective equivalently) for normal users and eventually 0.2 μm per pixel in advanced mode for developers.

According to the scanner design, the acquisition on each color channel is performed pixel by pixel, by moving the excitation laser beam with respect to a programmed scanning trajectory and collecting re-emitted light at specific positions on the scanning trajectory. Due to the beam divergence, the intensity of a pixel does not measure the emitted fluorescence signals at its spatial positions but the integral of signals over a wider area defined by the laser pattern which has in theory the shape of an isotropic Gaussian spot. Given that, the diameter of laser spots configured for this fluorescence scanner is typically set to more than 1 μm, in the case of high-precision scanning which requires sub-micrometer pixel size, the optical resolution (in the sense of the shortest distance between two points that can still be distinguished) is then limited by the laser spot size, resulting in blurred details on acquired images. If the image pixels are correctly positioned, each channel of an acquired image can be modeled as the convolution product of the underlying fluorescently-tagged specimen and the corresponding laser spot. The latter is therefore called the PSF of the associated color channel. Due to its Gaussian nature, this PSF can be parametrized by its FWHM (Full Width at Half Maximum) value which is usually empirically measured during the scanner calibration process. The relation between the FWHM and the standard deviation σ_{PSF} of a Gaussian PSF is given by $\text{FWHM} = 2\sigma_{\text{PSF}}\sqrt{2\log 2}$.

As depicted in the second and third rows of Fig. 4.5, we notice that the acquired TMA images for this experiment suffer not only from blur, but also from rolling effect (jitter) in vertical direction due to the bad positioning of pixels. A dejittering step is thus required as pre-processing in order to re-align jagged shapes and produce less jittered input images for deconvolution step. To that end, we utilized the algorithm described in chapter 3 to compensate the specific jitter arising on these fluorescence images. In Figs. 4.6b and 4.6d, we provide zoom-in views of two selected areas on result obtained with this dejittering algorithm on the three-color TMA image shown in Fig. 4.5 for illustration purpose. We can clearly see that the rolling effect is significantly reduced when compared to the original jittered images.

4.5.2.1 Comparison with existing regularizers

We visually compared the results obtained with SV to those obtained with existing state-of-the-art regularizers such as TV, TV-L_1, GraphNet, HV, and LHSV on a fluorescence image showing eight tissue microarray cores (see Fig. 4.5). The considered TMA image, saved in 16-bit-TIFF format, was acquired in three colors at the resolution of 0.5 μm per pixel with a total size of 9544×4704 pixels. Since we notice that the vertical rolling effect is not the same on the three color channels, as shown in the two bottom rows of Fig. 4.5, the experiment is performed as the following. Each channel is first dejittered separately for an appropriate removal of the jitter

arising on it. Second, the dejittered outcome on each channel served as the input image for deconvolution. The deconvolution results are finally merged to produce a three-color image as the original image for comparison purposes. According to the scanner calibration, the measured FWHM value of the Gaussian laser spot is approximately 0.703 μm for all three channels, corresponding to a standard deviation $\sigma_{\text{PSF}} \simeq 0.5971$ μm which is slightly larger than the image pixel size.

The deconvolution results are shown in Fig. 4.6 (zoom-in view) on two selected areas for comparison in details. The regularization parameter for each regularization approach is tuned to get the most pleasant visual effect. As shown in Figs. 4.6e and 4.6g, TV produces piecewise constant reconstruction which wipes out details in areas with small changes of intensities and over-sharpens the transition between contiguous regions. The restored images look like cartoon images and are not natural visually. HV is able to restore better these fine details with smooth variations while preserving the contrast between structures in the foreground and the background (see Figs. 4.6f and 4.6h). The resulting image seems however slightly blurred when comparing with the SV and LHSV solution. Up to our knowledge, it may be due to the piecewise linear nature of the HV solution which does not fit the smooth nature of structures on the underlying image.

Both LHSV and SV which penalize jointly image intensities and image differential components, provide sharper reconstruction than HV based on the second-order differentiation operator. Because of this joint penalization concept, they also tend to unfortunately over-sparsify the distribution of non-zero pixels, resulting in vanishing nearly-zero-intensity details, as noticeable in Fig. 4.6i and 4.6j where several green color features are nearly disappeared. We remark that the over-sparsifying effect on LHSV solution is slightly stronger than those obtained with SV. In our opinion, it is mainly due to the combination of the logarithm function and the squared L_2 norm in the LHSV functional in comparison to the L_2 norm in the case of SV. Note that the jittering was not completely removed on the example shown in Figs. 4.6b and 4.6d, but SV handles these imperfect input images and produces nearly jitter-free solutions (see Figs. 4.6i, and 4.6k). It was not possible to get such a result with LHSV (see Figs. 4.6j, and 4.6l).

4.5.2.2 Sensitivity to PSF parameters

As previously reported, when the PSF of the imaging system is known, SV approach appears to be the best solution for deconvolution of real fluorescence images. There is unfortunately a small chance that the PSF is known with a very high precision. In practice, the PSF is rather estimated by direct estimation on acquired images or by calibration using small point-like objects to get PSF measures at different location. In fluorescence microscopy, one usually considers microbeads to estimate the PSF of the underlying microscope. However, this estimation may in some cases suffer from severe errors due to the measurement conditions and can lead to poor deconvolution results if the used deconvolution method is too sensitive to errors in the estimation of the PSF.

Consequently, our interest here is to evaluate the sensitivity of SV deconvolution to the PSF parameters. To that end, we consider a TMA image, shown in Fig. 4.7,

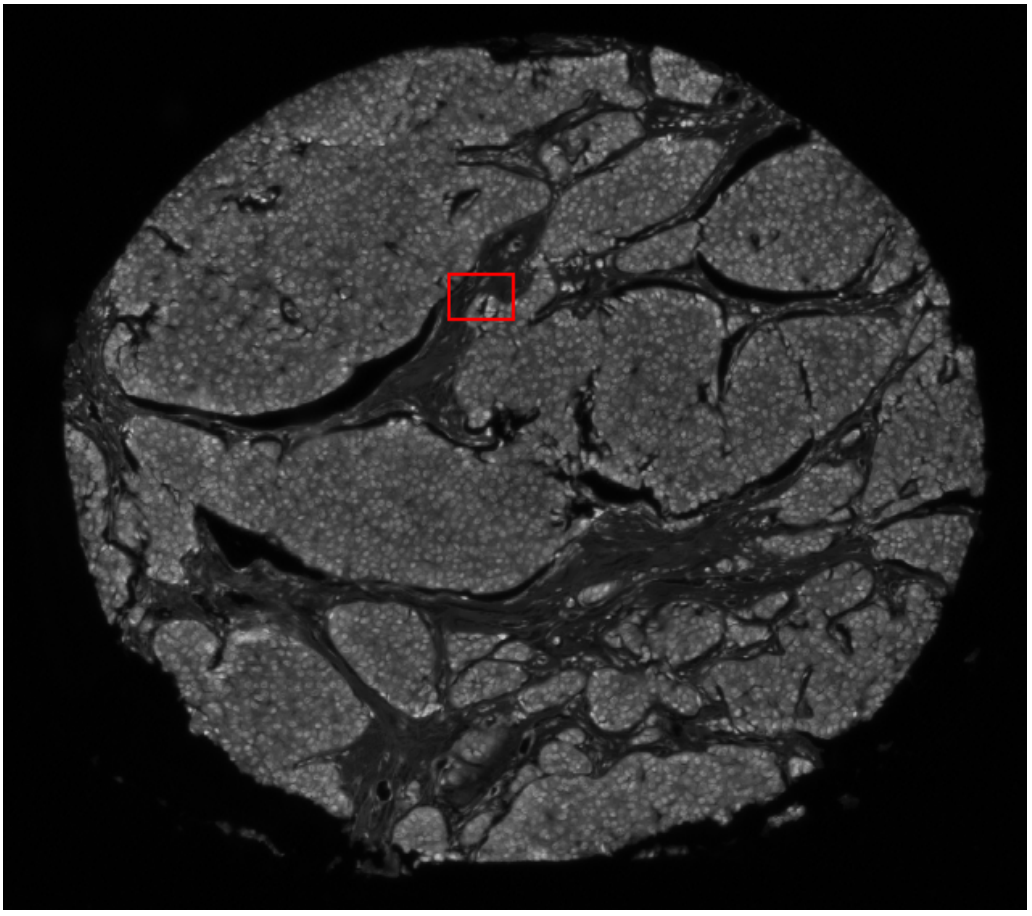

Figure 4.7: **Single-color fluorescence TMA image**. Image of a TMA core is acquired on the green channel (532 nm) at the resolution 0.2 μm per pixel. The size of the acquired image is 7580×6870 pixels. A region (bordered by rex box) is selected for comparison in details of deconvolution results obtained with different PSFs.

which was acquired on the green channel (532 nm) at the resolution of 0.2 μm per pixel using InnoScan 1100AL scanner. In this experiment, we note that the PSF of the scanner was not measured before acquisition. In Fig. 4.8, we provide then comparative results obtained on this single-color image with different PSFs to better appreciate the impact of PSF change on the deconvolution results. In this particular study, it has been experimentally established that the PSF can be approximated by an isotropic Gaussian function. Hence, we generated several Gaussian PSFs by varying the FWHM value in the range of $\{0.6,\ 0.7,\ 0.8,\ 0.9,\ 1.0\}$ (in μm). Regarding the regularization parameter λ, we selected four typical values to control the regularization level: $\lambda \in \{0.002,\ 0.003,\ 0.005,\ 0.008\}$.

In Fig. 4.8, we remark first that, for all the considered FWHM values and regularization parameters, our algorithm produced encouraging deconvolution results in terms of visual quality. However, we realize that some results still suffer from vertical rolling effect because jitter is not completely removed after pre-processing, as shown in the first row of Fig. 4.8. This effect is typically observed on deconvolved images obtained with low FWHM values. In the special case where FWHM $= 0.6$, all the four deconvolved images are concerned (see the second row of Fig. 4.8). The

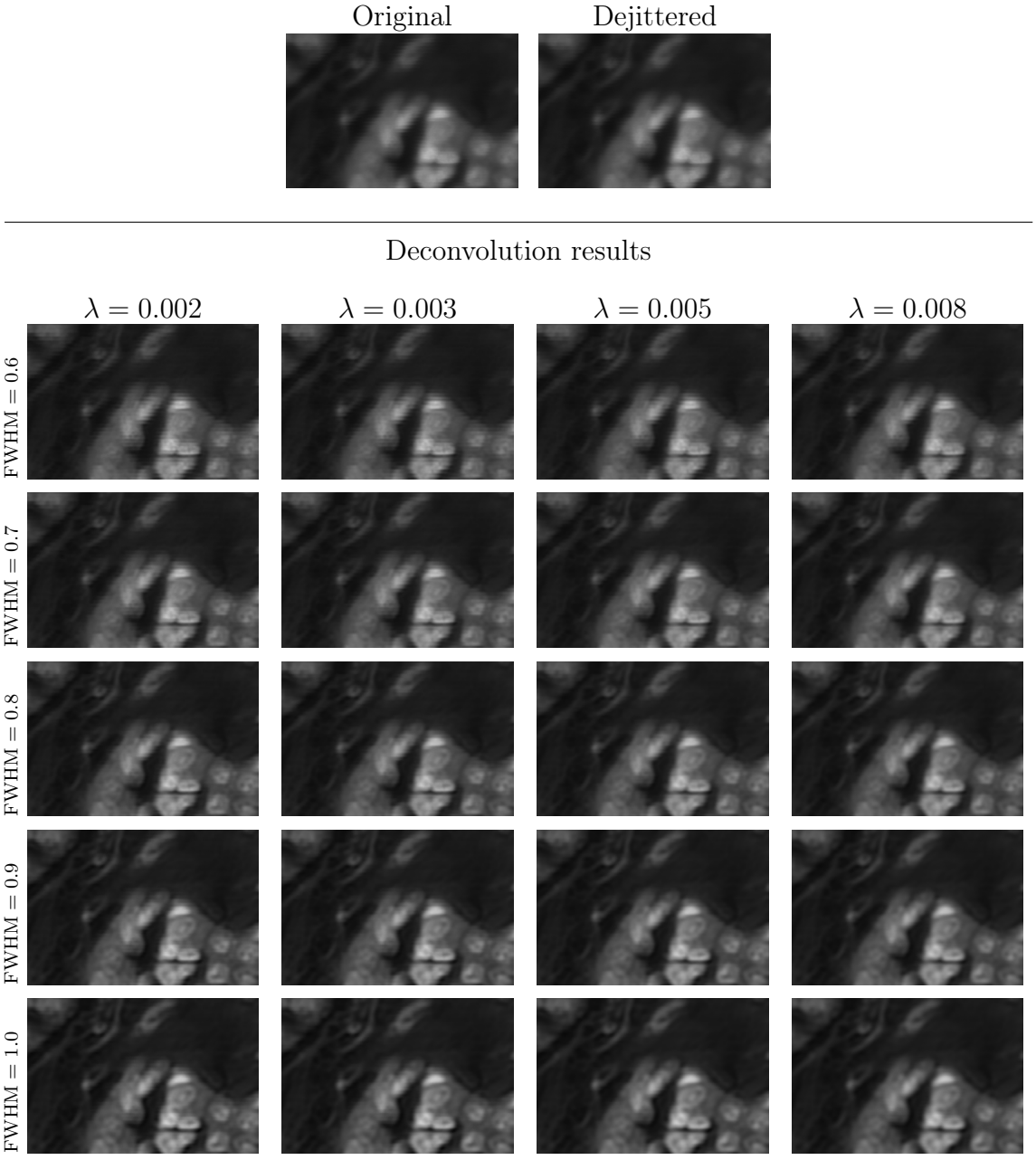

Figure 4.8: **Comparison of deconvolution results obtained on the single-color TMA image with different PSFs and regularization parameters**. Zoom-in view on the selected area (bordered by red box in Fig. 4.7) to compare in details before/after deconvolution differences as well as results obtained with different parameters. We consider Gaussian PSFs with FWHM values varying in the range $\{0.6, 0.7, 0.8, 0.9, 1.0\}$ and several regularization parameters $\lambda \in \{0.002, 0.003, 0.005, 0.008\}$. The two values, FWHM = 1.0 and $\lambda = 0.008$, yield the best result in terms of visual quality compared to the other combinations of parameters.

jittering artifacts are less visible with larger FWHM or when increasing the regularization parameters. The setting FWHM = 1.0 and $\lambda = 0.008$ yields the best visual results in comparison to those obtained with the other combinations of parameters. Although, very similar results are obtained for FWHM > 0.8, irrespectively to the choice of λ. This experiments revealed that the SV-based deconvolution method is not sensitive to small errors in PSF estimation and to non-stationarities induced by mixed Poisson-Gaussian noise.

In terms of computational performance, the proposed SV-based deconvolution algorithm takes only 0.5-0.7 second, for both first-order and second-order variants, on a standard image of 512×512 pixels. This processing time is comparable to TV with about 0.6 second and is much faster than HV with more than 1.3 seconds. Regarding LHSV approach, the computational time can reach more than 2.4 seconds, due to the non-convex nature of the regularization functional. The method was applied to large fluorescence images (7590×6870 pixels) and the computation time is about 80 seconds. The experiments were performed on a Macbook Pro equipped with 2.7 Ghz Intel Core i7, 16 Gb of RAM and the Mac OS X v.10.12.4 operating system. All the tested algorithms were implemented in Matlab and we exploited the intrinsic parallelism of the CPU to deal with large-scale inverse problems.

4.6 Conclusion

In this chapter, we have presented a deconvolution method for 2D fluorescence imaging using a novel family of convex regularizers. The proposed regularization functionals are based on the concept of sparse variation, that consists in penalizing jointly the image intensity and gradient at each pixel to favor the co-localization of non-zero intensities and gradients, by considering eventually higher-order differentiation operators. By construction, these regularizers possess interesting mathematical properties, namely convexity, invariance to scale, rotation, and translation as the well-known total variation regularization approach. It allows therefore to design efficient algorithms to solve the underlying deconvolution problem which is in general large-scale in the context of fluorescence microscopy. We reformulated the deconvolution as a minimization problem of a convex energy function composed of a quadratic data fidelity term and a sparse-variation-based regularity term under the constrain of positivity and maximum intensity value. In order to minimize this energy, we considered a primal-dual (proximal) algorithm based on the full-splitting technique which only involves first-order operators to cope with the large-scale nature of the problem. Experimental results on both synthetic and real fluorescence images demonstrated that our method was able to produce very competitive deconvolution results when compared to several competing methods in terms of quantitative performance as well as visual quality and computational time. A possible improvement is to accelerate the deconvolution of very large images (up to about 44000×148000 pixels in the case of images acquired by InnoScan 1100 AL) by applying the proposed method on overlapping patches. An extension of the method to 3D images can be also envisaged in short-term. Moreover, based on the parametric model of the PSF, the automatic estimation of the PSF will be an interesting approach for

further studies.

Chapter 5

Conclusion

This thesis, in the context of the development of a novel platform for quantitative analysis of tissue microarrays, brings us to concrete problems, dedicated to digital TMA image analysis on the one hand, and on the other, related to the imaging devices (more precisely, those of the InnoScan range designed by Innopsys). These specific problems which have no pre-existing solution require thus substantial developments in both theory and application. Besides the theoretical aspects which concern in general the modeling, the reformulation and the resolving of the underlying problems, the large-scale nature of acquired TMA images (up to about 44000×148000 pixels) also leads to some practical questions, namely computational complexity. This issue has been addressed in this work mostly by considering "first-order" algorithms, in the sense that they only involve simple linear operators (such as convolution, gradient, projection operator, etc.) which facilitate the implementation and allow parallel computing. In some other cases, subsampling (in the image domain as well as in the solution space) can be used as a pragmatic approach to reduce the amount of processing data at a time and provide a first estimation of the solution.

The first contribution of the thesis was to provide an automated and robust method for TMA de-arraying (Chapter 2) which is highly requested by pathologists and scientists working in tissue-based researches, but not too much interested within the scope of image processing. The proposed method has shown its effectiveness for both conventional bright-field and fluorescence images without any assumption on noise and dynamic range. By relying on a two-step approach in which result from a step can be refined by the following step to improve accuracy, our method is able to eliminate false detection of TMA cores due to outliers and to recover cores that are not recognized through the detection and segmentation steps, thus improving the final de-arraying results. Another improvement comparing to existing de-arraying methods is that not only the de-arraying result (i.e. the row and column coordinates of each TMA core) is provided, but also some quantitative measurements of the TMA grid deformation are estimated, thanks to the use of thin-plate splines to estimate the underlying deformation. These measurements can serve as quality indicators helping TMA constructors to adjust their techniques.

In Chapter 3, the problem of pixel mispositioning (jitter) arising in dedicated scanners has been addressed. While similar scanning artifacts have been reported in

the context of satellite imaging (push-broom and whiskbroom scanners) and modeled by irregular sampling, the existing solutions are not adapted for TMA images, mainly because it is not always possible to get accurate sampling (scanning) positions and biological images are much more complex than satellite images (containing in general piece-wise constant regions). Regarding general dejittering approaches (i.e. correction of random displacements of pixels), those based on image regularization may produce less jittered results but usually over-smoothed due to regularization. Inspired from variational optical flow formalism, we have proposed a variational method to estimate a dense displacement field modeling the arising jitter instead of directly estimating the (unknown) unjittered image in order to avoid oversmoothing effect. Our method consists in minimizing an energy function composed of a non-convex data fidelity term and a convex regularity term derived from the specific structure of the jitter. It leads to the application of half-quadratic splitting technique to decouple the original problem into simpler convex and non-convex subproblems which can be solved by appropriate optimization methods. Experiments on both simulated and real images showed that the proposed method produces very encouraging results in terms of visual quality, while avoiding over-smoothing effect or linearizing of non-convex term.

In contrast to the two previous chapters which concern little-known problems in image processing, we covered in Chapter 4 a more common problem: fluorescence image deconvolution. We have investigated the characteristics of fluorescence imaging modality, where few bright objects are observed over a relatively darker background, to define an appropriate regularization-based method. The contributions of this chapter were two-fold: (i) we have introduced a novel family of convex regularizers, based on Sparse Variation which combines total variation and the L_1 penalty on image intensities to enhance co-localization of pixels with high intensity and high-magnitude gradient in fluorescence images; (ii) we have proposed the so-called SV-based deconvolution method by considering this family of regularizers and primal-dual (proximal) algorithms combined with full-splitting technique for fast deconvolution of large fluorescence images. Simple but rapid and efficient, our deconvolution method produces competitive results both in terms of visual and quantitative quality when compared with existing regularization-based methods, including total variation and the Schatten norms of Hessian matrix.

In summary, this manuscript have presented few efficient algorithms for fluorescence TMA image analysis. In the continuation of this work, the short-term objective is to complete the analysis platform by integrating the developed algorithms into existing and future scanner systems. In our discussion, more pragmatic strategies need to be considered to accelerate the processing flow and reduce the hardware requirements. In long-term, machine-learning-based approaches can be envisaged in order to reinforce the automation level of the platform. Another point is to accelerate the deconvolution method by applying the method on overlapping patches. The method can be easily extended to 3D as well. Another issue will be the automatic estimation of the PSF size which can be spatially variant in the image.

Bibliography

A. Almansa, V. Caselles, G. Haro, and B. Rougé. Restoration and Zoom of Irregularly Sampled, Blurred, and Noisy Images by Accurate Total Variation Minimization with Local Constraints. *SIAM Multiscale Modeling & Simulation*, 5(1): 235–272, Jan 2006.

Y. Amit, U. Grenander, and M. Piccioni. Structural Image Restoration Through Deformable Templates. *Journal of the American Statistical Association*, 86(414): 376–387, June 1991.

M. Arigovindan, J. C. Fung, D. Elnatan, V. Mennella, Y.-H. M. Chan, M. Pollard, E. Branlund, J. W. Sedat, and D. A. Agard. High-resolution restoration of 3D structures from widefield images with extreme low signal-to-noise-ratio. *Proceedings of the National Academy of Sciences*, 110(43):17344–17349, 2013.

S. Badve, C. Deshpande, Z. Hua, and L. Lögdberg. Expression of Invariant Chain (CD 74) and Major Histocompatibility Complex (MHC) Class II Antigens in the Human Fetus. *Journal of Histochemistry and Cytochemistry*, 50(4):473–482, April 2002.

A. Basset, J. Boulanger, P. Bouthemy, C. Kervrann, and J. Salamero. SLT-LoG: A Vesicle Segmentation Method with Automatic Scale Selection and Local Thresholding Applied to TIRF Microscopy. In *IEEE 11th International Symposium on Biomedical Imaging 2014 (ISBI 2014)*, pages 533–536, April 2014.

H. Battifora. The Multitumor (Sausage) Tissue Block: Novel Method for Immunohistochemical Antibody Testing. *Laboratory Investigation; a Journal of Technical Methods and Pathology*, 55(2):244–248, August 1986.

H. Battifora and P. Mehta. The Checkerboard Tissue Block. An Improved Multitissue Control Block. *Laboratory Investigation; a Journal of Technical Methods and Pathology*, 63(5):722–724, November 1990.

R. Bhatia. *A Review of Linear Algebra*, pages 1–27. Springer New York, New York, NY, 1997.

F. L. Bookstein. Principal Warps: Thin-Plate Splines and the Decomposition of Deformations. *IEEE Transactions on Pattern Analysis and Machine Intelligence*, 11(6):567–585, June 1989.

J. Boulanger, C. Kervrann, P. Bouthemy, P. Elbau, J. B. Sibarita, and J. Salamero. Patch-based nonlocal functional for denoising fluorescence microscopy image sequences. *IEEE Transactions on Medical Imaging*, 29(2):442–454, February 2010.

S. Boyd and L. Vandenberghe. *Convex Optimization*. Cambridge University Press, New York, NY, USA, 2004. ISBN 0521833787.

E. J. Breen, G. H. Joss, and K. L. Williams. Locating Objects of Interest within Biological Images: The Top Hat Box Filter. *Journal of Computer-Assisted Microscopy*, 3(2):97–102, 1991.

T. Brox and J. Malik. Large displacement optical flow: Descriptor matching in variational motion estimation. *IEEE Transactions on Pattern Analysis and Machine Intelligence*, 33(3):500–513, 2011.

W. A. Carrington. Image restoration in 3-D microscopy with limited data. In *Proc. SPIE*, volume 1205, 1990.

W. A. Carrington, R. M. Lynch, E. D. Moore, G. Isenberg, K. E. Fogarty, and F. S. Fay. Superresolution three-dimensional images of fluorescence in cells with minimal light exposure. *Science*, 268(5216):1483–1487, 1995.

V. Caselles, R. Kimmel, and G. Sapiro. Geodesic Active Contours. *International Journal of Computer Vision*, 22(1):61–79, February 1997.

F. Catté, P.-L. Lions, J.-M. Morel, and T. Coll. Image selective smoothing and edge detection by nonlinear diffusion. *SIAM Journal on Numerical Analysis*, 29(1): 182–193, 1992.

A. Chambolle and T. Pock. A first-order primal-dual algorithm for convex problems with applications to imaging. *Journal of Mathematical Imaging and Vision*, 40 (1):120–145, 2011.

J. K. Chan, C. S. Wong, W. T. Ku, and M. Y. Kwan. Reflections on the Use of Controls in Immunohistochemistry and Proposal for Application of a Multitissue Spring-roll Control Block. *Annals of Diagnostic Pathology*, 4(5):329–336, October 2000a.

T. Chan, A. Marquina, and P. Mulet. High-order total variation-based image restoration. *SIAM Journal on Scientific Computing*, 22(2):503–516, 2000b.

T. F. Chan and S. Esedoglu. Aspects of total variation regularized L1 function approximation. *SIAM Journal on Applied Mathematics*, 65(5):1817–1837, 2005.

T. F. Chan and L. A. Vese. Active Contours without Edges. *IEEE Transactions on Image Processing*, 10(2):266–277, February 2001.

W. Chen, M. Reiss, and D. J. Foran. A Prototype for Unsupervised Analysis of Tissue Microarrays for Cancer Research and Diagnostics. *IEEE Transactions on Information Technology in Biomedicine*, 8(2):89–96, June 2004.

G. A. G. Cidade, C. Anteneodo, N. C. Roberty, and A. J. S. Neto. A generalized approach for atomic force microscopy image restoration with Bregman distances as Tikhonov regularization terms. *Inverse Problems in Engineering*, 8(5):457–472, 2000.

P. L. Combettes. Solving monotone inclusions via compositions of nonexpansive averaged operators. *Optimization*, 53:475–504, 2004.

P. L. Combettes and J. C. Pesquet. Image restoration subject to a total variation constraint. *IEEE Transactions on Image Processing*, 13(9):1213–1222, 2004.

P. L. Combettes and J.-C. Pesquet. *Proximal Splitting Methods in Signal Processing*, pages 185–212. Springer New York, New York, NY, 2011.

P. L. Combettes and V. R. Wajs. Signal recovery by proximal forward-backward splitting. *SIAM Multiscale Modeling & Simulation*, 4(4):1168–1200, 2005.

P. L. Combettes, Đ. Dũng, and B. C. Vũ. Proximity for sums of composite functions. *Journal of Mathematical Analysis and Applications*, 380(2):680 – 688, 2011.

P. L. Combettes, L. Condat, J. C. Pesquet, and B. C. Vũ. A forward-backward view of some primal-dual optimization methods in image recovery. In *2014 IEEE International Conference on Image Processing (ICIP)*, pages 4141–4145, October 2014.

L. Condat. A primal–dual splitting method for convex optimization involving lipschitzian, proximable and linear composite terms. *Journal of Optimization Theory and Applications*, 158(2):460–479, August 2013.

L. Condat. A generic proximal algorithm for convex optimization – application to total variation minimization. *IEEE Signal Processing Letters*, 21(8):985–989, 2014.

T. Cootes, C. Taylor, D. Cooper, and J. Graham. Active Shape Models-Their Training and Application. *Computer Vision and Image Understanding*, 61(1): 38–59, January 1995.

H.-L. Dan, Y.-L. Zhang, Y. Zhang, Y.-D. Wang, Z.-S. Lai, Y.-J. Yang, H.-H. Cui, Y.-T. Jian, J. Geng, Y.-Q. Ding, C.-H. Guo, and D.-Y. Zhou. A novel method for preparation of tissue microarray. *World Journal of Gastroenterology*, 10(4): 579–582, February 2004.

M. W. Datta, A. Kahler, V. Macias, T. Brodzeller, and A. Kajdacsy-Balla. A Simple Inexpensive Method for the Production of Tissue Microarrays from Needle Biopsy Specimens: Examples with Prostate Cancer. *Applied Immunohistochemistry & Molecular Morphology*, 13(1):96–103, March 2005.

R. Delgado-Gonzalo, V. Uhlmann, D. Schmitter, and M. Unser. Snakes on a Plane: A Perfect Snap for Bioimage Analysis. *IEEE Signal Processing Magazine*, 32(1): 41–48, January 2015.

R. Dell'Anna, F. Demichelis, M. Barbareschi, and A. Sboner. An Automated Procedure to Properly Handle Digital Images in Large Scale Tissue Microarray Experiments. *Computer Methods and Programs in Biomedicine*, 79(3):197–208, September 2005.

S. Delpretti, F. Luisier, s. Ramani, T. Blu, and M. Unser. Multiframe sure-let denoising of timelapse fluorescence microscopy images. In *2008 IEEE 13th International Symposium on Biomedical Imaging (ISBI)*, pages 149–152, Paris, France, May 2008.

X. Descombes. *Stochastic Geometry for Image Analysis*. John Wiley & Sons Inc., 2013.

X. Descombes. Multiple Objects Detection in Biological Images Using a Marked Point Process Framework. *Methods*, 115(Supplement C):2–8, September 2016. Image Processing for Biologists.

N. Dey, L. Blanc-Feraud, C. Zimmer, P. Roux, Z. Kam, J.-C. Olivo-Marin, and J. Zerubia. Richardson-lucy algorithm with total variation regularization for 3d confocal microscope deconvolution. *Microscopy Research Technique*, 69(4):260–266, 2006.

G. Dong, A. R. Patrone, O. Scherzer, and O. Öktem. Infinite dimensional optimization models and pdes for dejittering. In J.-F. Aujol, M. Nikolova, and N. Papadakis, editors, *Scale Space and Variational Methods in Computer Vision: 5th International Conference, SSVM 2015, Lège-Cap Ferret, France, May 31 - June 4, 2015, Proceedings*, pages 678–689. Springer International Publishing, Cham, 2015.

F. Dupe, J. Fadili, and J. Starck. A proximal iteration for deconvolving poisson noisy images using sparse representations. *IEEE Transactions on Image Processing*, 18 (2):310–321, 2009.

J. Eckstein and D. P. Bertsekas. On the douglas–rachford splitting method and the proximal point algorithm for maximal monotone operators. *Mathematical Programming*, 55(1):293–318, 1992.

M. Eickenberg, E. Dohmatob, B. Thirion, and G. Varoquaux. Grouping total variation and sparsity: Statistical learning with segmenting penalties. In N. Navab, J. Hornegger, W. M. Wells, and A. Frangi, editors, *Medical Image Computing and Computer-Assisted Intervention – MICCAI 2015: 18th International Conference, Munich, Germany, October 5-9, 2015, Proceedings, Part I*, pages 685–693, Cham, 2015. Springer International Publishing.

G. Facciolo, A. Almansa, J.-F. Aujol, and V. Caselles. Irregular to Regular Sampling, Denoising, and Deconvolution. *SIAM Multiscale Modeling & Simulation*, 7(4): 1574–1608, Jan 2009.

M. S. Fejzo and D. J. Slamon. Frozen Tumor Tissue Microarray Technology for Analysis of Tumor RNA, DNA and Proteins. *The American Journal of Pathology*, 159(5):1645–1650, November 2001.

D. Fortun, P. Bouthemy, and C. Kervrann. Optical flow modeling and computation: A survey. *Computer Vision and Image Understanding*, 134:1–21, 2015.

M. Frigo and S. G. Johnson. FFTW: an adaptive software architecture for the FFT. In *Proceedings of the 1998 IEEE International Conference on Acoustics, Speech and Signal Processing*, volume 3, pages 1381–1384, May 1998.

M. Frigo and S. G. Johnson. The design and implementation of FFTW3. *Proceedings of the IEEE*, 93(2):216–231, February 2005.

H. L. Fu, J. L. Mueller, M. J. Whitley, D. M. Cardona, R. M. Willett, D. G. Kirsch, J. Q. Brown, and N. Ramanujam. Structured illumination microscopy and a quantitative image analysis for the detection of positive margins in a pre-clinical genetically engineered mouse model of sarcoma. *PLOS ONE*, 11(1):1–19, January 2016.

D. Geman and C. Yang. Nonlinear image recovery with half-quadratic regularization. *IEEE Transactions on Image Processing*, 4(7):932–946, 1995.

M. Ghodstinat, A. Bruhn, and J. Weickert. Deinterlacing with motion-compensated anisotropic diffusion. In D. Cremers, B. Rosenhahn, A. L. Yuille, and F. R. Schmidt, editors, *Statistical and Geometrical Approaches to Visual Motion Analysis: International Dagstuhl Seminar, Dagstuhl Castle, Germany, July 13-18, 2008. Revised Papers*, pages 91–106. Springer Berlin Heidelberg, Berlin, Heidelberg, 2009.

C. E. Gillett, R. J. Springall, D. M. Barnes, and A. M. Hanby. Multiple Tissue Core Arrays in Histopathology Research: a Validation Study. *The Journal of Pathology*, 192(4):549–553, December 2000.

U. Grenander and M. I. Miller. Representations of Knowledge in Complex Systems. *Journal of the Royal Statistical Society. Series B (Methodological)*, 56(4):549–603, 1994.

U. Grenander, Y. Chow, and D. M. Keenan. *Hands: A Pattern Theoretic Study of Biological Shapes*. Springer-Verlag New York, Inc., New York, NY, USA, 1991.

L. Grosenick, B. Klingenberg, K. Katovich, B. Knutson, and J. E. Taylor. Interpretable whole-brain prediction analysis with GraphNet. *NeuroImage*, 72:304–321, 2013.

S. F. Gull and G. J. Daniell. Image reconstruction from incomplete and noisy data. *Nature*, 272(5655):686–690, April 1978.

M. Heideman, D. Johnson, and C. Burrus. Gauss and the history of the fast Fourier transform. *IEEE ASSP Magazine*, 1(4):14–21, October 1984.

A. Hidalgo, P. Piña, G. Guerrero, M. Lazos, and M. Salcedo. A Simple Method for the Construction of Small Format Tissue Arrays. *Journal of Clinical Pathology*, 56(2):144–146, February 2003.

B. K. Horn and B. G. Schunck. Determining optical flow. *Artificial Intelligence*, 17 (1):185–203, 1981.

G. Huisken. Flow by mean curvature of convex surfaces into spheres. *Journal of Differential Geometry*, 20(1):237–266, 1984.

B. M. Kandel, D. A. Wolk, J. C. Gee, and B. Avants. Predicting cognitive data from medical images using sparse linear regression. In J. C. Gee, S. Joshi, K. M. Pohl, W. M. Wells, and L. Zöllei, editors, *Proceedings of the 23rd International Conference on Information Processing in Medical Imaging (IPMI 2013), Asilomar, CA, USA,*, pages 86–97, Berlin, Heidelberg, 2013. Springer Berlin Heidelberg.

S. H. Kang and J. Shen. Video dejittering by bake and shake. *Image and Vision Computing*, 24(2):143–152, 2006.

S. H. Kang and J. Shen. Image dejittering based on slicing moments. In X.-C. Tai, K.-A. Lie, T. F. Chan, and S. Osher, editors, *Image Processing Based on Partial Differential Equations: Proceedings of the International Conference on PDE-Based Image Processing and Related Inverse Problems, CMA, Oslo, August 8–12, 2005*, pages 35–55. Springer Berlin Heidelberg, Berlin, Heidelberg, 2007.

M. Kass, A. Witkin, and D. Terzopoulos. Snakes: Active Contour Models. *International Journal of Computer Vision*, 1(4):321–331, January 1988.

S. Keller, F. Lauze, and M. Nielsen. A total variation motion adaptive deinterlacing scheme. In R. Kimmel, N. A. Sochen, and J. Weickert, editors, *Scale Space and PDE Methods in Computer Vision: 5th International Conference, Scale-Space 2005, Hofgeismar, Germany, April 7-9, 2005. Proceedings*, pages 408–418. Springer Berlin Heidelberg, Berlin, Heidelberg, 2005.

S. H. Keller, F. Lauze, and M. Nielsen. Deinterlacing using variational methods. *IEEE Transactions on Image Processing*, 17(11):2015–2028, 2008.

C. Kervrann and J. Boulanger. Optimal spatial adaptation for patch-based image denoising. *IEEE Transactions on Image Processing*, 15(10):2866–2878, Oct 2006.

C. Kervrann and F. Heitz. A Hierarchical Markov Modeling Approach for the Segmentation and Tracking of Deformable Shapes. *Graphical Models and Image Processing*, 60(3):173–195, May 1998.

C. Kervrann and A. Trubuil. Optimal Level Curves and Global Minimizers of Cost Functionals in Image Segmentation. *Journal of Mathematical Imaging and Vision*, 17(2):153–174, September 2002.

C. Kervrann, C. O. S. Sorzano, S. T. Acton, J.-C. Olivo-Marin, and M. Unser. A Guided Tour of Selected Image Processing and Analysis Methods for Fluorescence and Electron Microscopy. *IEEE Journal of Selected Topics in Signal Processing*, 10(1):6–30, February 2016.

A. Kokaram, P. Rayner, P. van Roosmalen, and J. Biemond. Line registration of jittered video. In *Proc. IEEE International Conference on Acoustics, Speech, and Signal Processing (ICASSP'97)*, volume 4, pages 2553–2556, 1997.

A. C. Kokaram. Line registration for jittered video. In *Motion Picture Restoration: Digital Algorithms for Artefact Suppression in Degraded Motion Picture Film and Video*, pages 99–118. Springer London, London, 1998.

A. C. Kokaram, N. Persad, J. Lasenby, W. J. Fitzgerald, A. McKinnon, and M. Welland. Restoration of images from the scanning-tunneling microscope. *Applied Optics*, 34(23):5121–5132, August 1995.

J. Kononen, L. Bubendorf, A. Kallionimeni, M. Bärlund, P. Schraml, S. Leighton, J. Torhorst, M. J. Mihatsch, G. Sauter, and O. P. Kallionimeni. Tissue Microarrays for High-Throughput Molecular Profiling of Tumor Specimens. *Nature Medicine*, 4(7):844–847, July 1998.

L. Laborelli. Removal of video line jitter using a dynamic programming approach. In *Proc. IEEE International Conference on Image Processing (ICIP 2003)*, volume 2, pages II–331–4 vol.3, 2003.

B. Lahrmann, N. Halama, K. Westphal, C. Ernst, Z. Elsawaf, P. Sinn, F. X. Bosch, H. Dickhaus, D. Jäger, P. Schirmacher, and N. Grabe. Robust Gridding of TMAs After Whole-Slide Imaging Using Template Matching. *Cytometry A*, 77(12):1169–1176, December 2010.

S. Lefkimmiatis and M. Unser. Poisson image reconstruction with Hessian Schatten-norm regularization. *IEEE Transactions on Image Processing*, 22(11):4314–4327, November 2013.

S. Lefkimmiatis, A. Bourquard, and M. Unser. Hessian-based norm regularization for image restoration with biomedical applications. *IEEE Transactions on Image Processing*, 21(3):983–995, 2012.

S. Lefkimmiatis, J. P. Ward, and M. Unser. Hessian Schatten-norm regularization for linear inverse problems. *IEEE Transactions on Image Processing*, 22(5):1873–1888, May 2013.

F. Lenzen and O. Scherzer. Partial differential equations for zooming, deinterlacing and dejittering. *International Journal of Computer Vision*, 92(2):162–176, 2011.

C. Louchet and L. Moisan. Posterior expectation of the total variation model: Properties and experiments. *SIAM Journal on Imaging Sciences*, 6(4):2640–2684, 2013.

L. B. Lucy. An iterative technique for the rectification of observed distributions. *The Astronomical Journal*, 79(6):745–754, June 1974.

F. Luisier, C. Vonesch, T. Blu, and M. Unser. Fast Haar-wavelet denoising of multidimensional fluorescence microscopy data. In *IEEE International Symposium on Biomedical Imaging: From Nano to Macro 2009 (ISBI 2009)*, pages 310–313, June 2009.

F. Luisier, C. Vonesch, T. Blu, and M. Unser. Fast interscale wavelet denoising of poisson-corrupted images. *Signal Processing*, 90(2):415–427, 2010.

M. Makitalo and A. Foi. Optimal inversion of the generalized anscombe transformation for poisson-gaussian noise. *IEEE Transactions on Image Processing*, 22(1): 91–103, 2013.

S. Mallat. *A Wavelet Tour of Signal Processing, Third Edition: The Sparse Way*. Academic Press, Boston, 3rd edition, 2008.

E. S. Meinel. Origins of linear and nonlinear recursive restoration algorithms. *Journal of the Optical Society of America A*, 3(6):787–799, June 1986.

B. Mercier. *Lectures on Topics in Finite Element Solution of Elliptic Problems*. Springer-Verlag Berlin Heidelberg, 1979.

V. Michel, A. Gramfort, G. Varoquaux, E. Eger, and B. Thirion. Total variation regularization for fMRI-based prediction of behavior. *IEEE Transactions on Medical Imaging*, 30(7):1328–1340, 2011.

K. Montgomery, S. Zhao, M. van de Rijn, and Y. Natkunam. A Novel Method for Making "Tissue" Microarrays From Small Numbers of Suspension Cells. *Applied Immunohistochemistry & Molecular Morphology*, 13(1):80–84, March 2005.

J. J. Moreau. Proximité et dualité dans un espace hilbertien. *Bulletin de la Société Mathématique de France*, 93:273–299, 1965.

B. Ng, A. Vahdat, G. Hamarneh, and R. Abugharbieh. Generalized sparse classifiers for decoding cognitive states in fMRI. In F. Wang, P. Yan, K. Suzuki, and D. Shen, editors, *Proceedings of the First International Workshop on Machine Learning in Medical Imaging: (MLMI 2010), Held in Conjunction with MICCAI 2010, Beijing, China,*, pages 108–115, Berlin, Heidelberg, 2010. Springer Berlin Heidelberg.

M. Nikolova. Weakly constrained minimization: Application to the estimation of images and signals involving constant regions. *Journal of Mathematical Imaging and Vision*, 21(2):155–175, September 2004.

M. Nikolova. One-iteration dejittering of digital video images. *Journal of Visual Communication and Image Representation*, (4):254–274, 2009a.

M. Nikolova. Fast dejittering for digital video frames. In X.-C. Tai, K. Mørken, M. Lysaker, and K.-A. Lie, editors, *Scale Space and Variational Methods in Computer Vision: Second International Conference, SSVM 2009, Voss, Norway, June 1-5, 2009. Proceedings*, pages 439–451. Springer Berlin Heidelberg, Berlin, Heidelberg, 2009b.

J.-C. Olivo-Marin. Extraction of Spots in Biological Images Using Multiscale Products. *Pattern Recognition*, 35(9):1989 – 1996, September 2002.

F. O'Sullivan and M. Qian. A Regularized Contrast Statistic for Object Boundary Estimation – Implementation and Statistical Evaluation. *IEEE Transactions on Pattern Analysis and Machine Intelligence*, 16(6):561–570, June 1994.

J. Packeisen, H. Buerger, R. Krech, and W. Boecker. Tissue Microarrays: a New Approach for Quality Control in Immunohistochemistry. *Journal of Clinical Pathology*, 55(8):613–615, August 2002.

C.-C. Pan, P. C.-H. Chen, and H. Chiang. An Easy Method for Manual Construction of High-Density Tissue Arrays. *Applied Immunohistochemistry & Molecular Morphology*, 12(4):370–372, December 2004.

A. K. Pediredla and C. S. Seelamantula. A unified approach for optimization of snakuscules and ovuscules. In *IEEE International Conference on Acoustics, Speech and Signal Processing 2012 (ICASSP 2012)*, pages 681–684, March 2012.

P. Perona and J. Malik. Scale-space and edge detection using anisotropic diffusion. *IEEE Transactions on Pattern Analysis and Machine Intelligence*, 12(7):629–639, 1990.

D. Pilla, F. Bosisio, R. Marotta, S. Faggi, P. Forlani, M. Falavigna, I. Biunno, E. Martella, P. De Blasio, S. Borghesi, and G. Cattoretti. Tissue Microarray Design and Construction for Scientific, Industrial and Diagnostic Use. *Journal of Pathology Informatics*, 3(1):42, December 2012.

Z. Püspöki, J. P. Ward, D. Sage, and M. Unser. Fast Detection and Refined Scale Estimation Using Complex Isotropic Wavelets. In *IEEE 12th International Symposium on Biomedical Imaging 2015 (ISBI 2015)*, pages 512–515, April 2015.

Z. Püspöki, D. Sage, J. P. Ward, and M. Unser. SpotCaliper: Fast Wavelet-Based Spot Detection with Accurate Size Estimation. *Bioinformatics*, 32(8):1278–1280, April 2016.

A. Rabinovich, S. Krajewski, M. Krajewska, A. Shabaik, S. M. Hewitt, S. Belongie, J. C. Reed, and J. H. Price. Framework for Parsing, Visualizing and Scoring Tissue Microarray Images. *IEEE Transactions on Information Technology in Biomedicine*, 10(2):209–219, April 2006.

W. H. Richardson. Bayesian-based iterative method of image restoration. *Journal of the Optical Society of America*, 62(1):55–59, January 1972.

L. I. Rudin, S. Osher, and E. Fatemi. Nonlinear total variation based noise removal algorithms. *Physica D: Nonlinear Phenomena*, 60(1):259 – 268, 1992.

D. Sage, F. R. Neumann, F. Hediger, S. M. Gasser, and M. Unser. Automatic Tracking of Individual Fluorescence Particles: Application to the Study of Chromosome Dynamics. *IEEE Transactions on Image Processing*, 14(9):1372–1383, September 2005.

D. Sage, L. Donati, F. Soulez, D. Fortun, G. Schmit, A. Seitz, R. Guiet, C. Vonesch, and M. Unser. DeconvolutionLab2: an open-source software for deconvolution microscopy. *Methods*, 115:28–41, 2017.

J. Shen. Bayesian video dejittering by the BV image model. *SIAM Journal on Applied Mathematics*, 64(5):1691–1708, 2004.

L. A. Shepp and Y. Vardi. Maximum likelihood reconstruction for emission tomography. *IEEE Transactions on Medical Imaging*, 1(2):113–122, October 1982.

J.-B. Sibarita. *Deconvolution Microscopy*, pages 201–243. Springer Berlin Heidelberg, Berlin, Heidelberg, 2005.

I. Smal, W. Niessen, and E. Meijering. A New Detection Scheme for Multiple Object Tracking in Fluorescence Microscopy by Joint Probabilistic Data Association Filtering. In *IEEE 5th International Symposium on Biomedical Imaging: From Nano to Macro 2008 (ISBI 2008)*, pages 264–267, May 2008.

F. Soulez, L. Denis, Y. Tourneur, and É. Thiébaut. Blind deconvolution of 3D data in wide field fluorescence microscopy. In *International Symposium on Biomedical Imaging*, Barcelone, Spain, May 2012.

L. H. Staib and J. S. Duncan. Boundary finding with parametrically deformable models. *IEEE Transactions on Pattern Analysis and Machine Intelligence*, 14 (11):1061–1075, November 1992.

J.-L. Starck and F. Murtagh. *Astronomical Image and Data Analysis*. Springer Berlin Heidelberg, Berlin, Heidelberg, 2006.

J.-L. Starck, F. D. Murtagh, and A. Bijaoui. Image Restoration with Noise Suppression Using a Wavelet Transform and a Multiresolution Support Constraint. In *SPIE's 1994 International Symposium on Optics, Imaging, and Instrumentation*, pages 132–143, September 1994.

J. L. Starck, J. Fadili, and F. Murtagh. The Undecimated Wavelet Decomposition and its Reconstruction. *IEEE Transactions on Image Processing*, 16(2):297–309, February 2007.

F. Steinbrücker, T. Pock, and D. Cremers. Large displacement optical flow computation without warping. In *Proc. IEEE 12th International Conference on Computer Vision (ICCV 2009)*, pages 1609–1614, 2009.

E. Taub, Floyd, J. M. DeLeo, and E. B. Thompson. Sequential Comparative Hybridizations Analyzed by Computerized Image Processing Can Identify and Quantitate Regulated RNAs. *DNA*, 2(4):309–327, December 1983.

P. Thévenaz and M. Unser. Snakuscules. *IEEE Transactions on Image Processing*, 17(4):585–593, April 2008.

P. Thévenaz, R. Delgado-Gonzalo, and M. Unser. The Ovuscule. *IEEE Transactions on Pattern Analysis and Machine Intelligence*, 33(2):382–393, February 2011.

H. T. M. van der Voort and K. C. Strasters. Restoration of confocal images for quantitative image analysis. *Journal of Microscopy*, 178(2):165–181, 1995.

G. M. P. van Kempen, H. T. M. van der Voort, J. G. J. Bauman, and K. C. Strasters. Comparing maximum likelihood estimation and constrained Tikhonov-Miller restoration. *IEEE Engineering in Medicine and Biology Magazine*, 15(1): 76–83, Jan 1996.

G. M. P. van Kempen, L. J. van Vliet, P. J. Verveer, and H. T. M. van der Voort. A quantitative comparison of image restoration methods for confocal microscopy. *Journal of Microscopy*, 185(3):354–365, 1997.

C. Van Loan. *Computational Frameworks for the Fast Fourier Transform.* Society for Industrial and Applied Mathematics, 1992.

M. Vauhkonen, D. Vadasz, P. A. Karjalainen, E. Somersalo, and J. P. Kaipio. Tikhonov regularization and prior information in electrical impedance tomography. *IEEE Transactions on Medical Imaging*, 17(2):285–293, April 1998.

H. Vrolijk, W. Sloos, W. Mesker, P. Franken, R. Fodde, H. Morreau, and H. Tanke. Automated Acquisition of Stained Tissue Microarrays for High-Throughput Evaluation of Molecular Targets. *The Journal of Molecular Diagnostics*, 5(3):160–167, August 2003.

W.-H. Wan, M. B. Fortuna, and P. Furmanski. A Rapid and Efficient Method for Testing Immunohistochemical Reactivity of Monoclonal Antibodies against Multiple Tissue Samples Simultaneously. *Journal of Immunological Methods*, 103 (1):121–129, October 1987.

L. Wang, M. T. Deavers, A. Malpica, E. G. Silva, and J. Liu. Tissue Macroarray: A Simple and Cost-effective Method for High-Throughput Studies. *Applied Immunohistochemistry & Molecular Morphology*, 11(2):174–176, June 2003.

Y. Wang, K. Savage, C. Grills, A. McCavigan, J. A. James, D. A. Fennell, and P. W. Hamilton. A TMA De-Arraying Method for High Throughput Biomarker Discovery in Tissue Research. *PLOS ONE*, 6(10):1–15, October 2011.

A. Wedel, T. Pock, C. Zach, H. Bischof, and D. Cremers. *An Improved Algorithm for TV-L^1 Optical Flow*, pages 23–45. Springer Berlin Heidelberg, Berlin, Heidelberg, 2009.

L. Ying, D. Xu, and Z. P. Liang. On Tikhonov regularization for image reconstruction in parallel MRI. In *The 26th Annual International Conference of the IEEE Engineering in Medicine and Biology Society*, volume 1, pages 1056–1059, September 2004.

A. L. Yuille, P. W. Hallinan, and D. S. Cohen. Feature Extraction from Faces Using Deformable Templates. *International Journal of Computer Vision*, 8(2):99–111, August 1992.

C. Zach, T. Pock, and H. Bischof. *A Duality Based Approach for Realtime TV-L^1 Optical Flow*, pages 214–223. Springer Berlin Heidelberg, Berlin, Heidelberg, 2007.

B. Zhang, M. J. Fadili, J. L. Starck, and J.-C. Olivo-Marin. Multiscale Variance-Stabilizing Transform for Mixed-Poisson-Gaussian Processes and its Applications in Bioimaging. In *IEEE International Conference on Image Processing 2007 (ICIP 2007)*, volume 6, pages 233–236, September 2007.

N. Zhao, Q. Wei, A. Basarab, D. Kouamé, and J. Y. Tourneret. Single image super-resolution of medical ultrasound images using a fast algorithm. In *2016 IEEE 13th International Symposium on Biomedical Imaging (ISBI)*, pages 473–476, April 2016.

S. C. Zhu and A. Yuille. Region Competition: Unifying Snakes, Region Growing, and Bayes/MDL for Multiband Image Segmentation. *IEEE Transactions on Pattern Analysis and Machine Intelligence*, 18(9):884–900, September 1996.

Abstract

This thesis aims at developing dedicated methods for quantitative analysis of Tissue Microarray (TMA) images acquired by fluorescence scanners. We addressed there issues in biomedical image processing, including segmentation of objects of interest (i.e. tissue samples), correction of acquisition artifacts during scanning process and improvement of acquired image resolution while taking into account imaging modality and scanner design. The developed algorithms allow to envisage a novel automated platform for TMA analysis, which is highly required in cancer research nowadays.

On a TMA slide, multiple tissue samples which are collected from different donors are assembled according to a grid structure to facilitate their identification. In order to establish the link between each sample and its corresponding clinical data, we are not only interested in the localization of these samples but also in the computation of their array (row and column) coordinates according to the design grid because the latter is often very deformed during the manufacturing of TMA slides. However, instead of directly computing array coordinates as existing approach, we proposed to reformulate this problem as the approximation of the deformation of the theoretical TMA grid using "thin plate splines" given the result of tissue sample localization. We combined a wavelet-based detection and a ellipse-based segmentation to eliminate false alarms and thus improving the localization result of tissue samples.

According to the scanner design, images are acquired pixel by pixel along each line, with a change of scan direction between two subsequent lines. Such scanning system often suffers from pixel mis-positioning (jitter) due to imperfect synchronization of mechanical and electronic components. To correct these scanning artifacts, we proposed a variational method based on the estimation of pixel displacements on subsequent lines. This method, inspired from optical flow methods, consists in estimating a dense displacement field by minimizing an energy function composed of a nonconvex data fidelity term and a convex regularization term. We used half-quadratic splitting technique to decouple the original problem into two small sub-problems: one is convex and can be solved by standard optimization algorithm, the other is non-convex but can be solved by a complete search.

To improve the resolution of acquired fluorescence images, we introduced a method of image deconvolution by considering a family of convex regularizers. The considered regularizers are generalized from the concept of Sparse Variation which combines the L_1 norm and Total Variation (TV) to favors the co-localization of high-intensity pixels and high-magnitude gradient. The experiments showed that the proposed regularization approach produces competitive deconvolution results on fluorescence images, compared to those obtained with other approaches such as TV or the Schatten norm of Hessian matrix.

Résumé

Ce travail de thèse a pour objectif de développer les méthodes originales pour l'analyse quantitative des images de Tissue Microarrays (TMAs) acquises en fluorescence par des scanners dédiés. Nous avons proposé des contributions en traitement d'images portant sur la segmentation des objets d'intérêts (i.e. des échantillons de tissus sur la lame de TMA scannée), la correction des artéfacts d'acquisition liés aux scanners en question ainsi que l'amélioration de la résolution spatiale des images acquises en tenant compte des modalités d'acquisition (imagerie en fluorescence) et la conception des scanners. Les développements permettent d'envisager une nouvelle plateforme d'analyse de TMAs automatisée, qui représente aujourd'hui une forte demande dans la recherche contre les cancers.

Les TMAs (ou "puces à tissus") sont les lames histologiques sur lesquelles de nombreux échantillons tissulaires venant de différents donneurs sont déposés selon une structure de grille afin de faciliter leur identification. Pour pouvoir établir le lien entre chaque échantillon et ses données cliniques correspondantes, on s'intéresse non seulement à segmenter ces échantillons mais encore à retrouver leur position théorique (les indices de ligne et de colonne) sur la grille TMA car cette dernière est souvent très déformée pendant la fabrication des lames. Au lieu de calculer directement les indices de ligne et de colonne (des échantillons), nous avons reformulé ce problème comme un problème d'estimation de la déformation de la grille de TMA théorique à partir du résultat de segmentation en utilisant l'interpolation par splines "plaques mincse". Nous avons combiné les ondelettes et un modèle d'ellipses paramétriques pour éliminer les fausses alarmes, donc améliorer les résultats de segmentation.

Selon la conception des scanners, les images sont acquises pixel par pixel le long de chaque ligne, avec un change de direction lors du balayage entre les deux lignes. Un problème fréquent est le mauvais positionnement des pixels dû à la mauvaise synchronisation des modules mécaniques et électroniques. Nous avons donc proposé une méthode variationnelle pour la correction de ces artéfacts en estimant le décalage entre les pixels sur les lignes consécutives. Cette méthode, inspirée du calcul du flot optique, consiste à estimer un champ de vecteurs en minimisant une fonction d'énergie composée d'un terme d'attache aux données non convexe et d'un terme de régularisation convexe. La relaxation quadratique est ainsi utilisée pour découpler le problème original en deux sous-problèmes plus simples à résoudre.

Enfin, pour améliorer la résolution spatiale des images acquises qui dépend de la PSF (*point spread function*) elle-même variant selon le faisceau laser d'excitation, nous avons introduit une méthode de déconvolution d'images en considérant une famille de régulariseurs convexes. Les régulariseurs considérés sont généralisés du concept de la variation parcimonieuses (*Sparse Variation*) combinant la norme L_1 de l'image et la variation totale (*Total Variation*) pour rehausser les pixels dont l'intensité et le gradient sont non-nuls. Les expériences montrent que l'utilisation de cette régularisation produit des résultats de déconvolution d'images très satisfaisants en comparaison avec d'autres approches telles que la variation totale ou la norme de Schatten de la matrice Hessienne.